Karlsruhe Institute of Technology

Detector optimization based on studies of charge migration in the high purity germanium crystals of the EDELWEISS dark matter experiment

Zur Erlangung des akademischen Grades eines
DOKTORS DER NATURWISSENSCHAFTEN
der Fakultät für Physik
des Karlsruher Instituts für Technologie

genehmigte

DISSERTATION

von

Dipl.-Phys.
Nadine Foerster
aus Stuttgart

Tag der mündlichen Prüfung:	03.02.2017
Referent:	Prof. Dr. Dr. h.c. Johannes Blümer
Korreferent:	Prof. Dr. Christian Enss
	(Universität Heidelberg, Kirchhoff-Institut für Physik)

Abstract

Cosmological observations on all scales of the universe have shown that 86 % of the matter in the universe consists of non-luminous, gravitating, dark matter, whereas the known baryonic matter only accounts for 14 %. Although Weakly Interacting Massive Particles (WIMPs) have not been detected so far, they are very attractive dark matter particle candidates as they naturally explain the observed dark matter density and satisfy the basic properties of dark matter, i.e. they are collisionless, stable, low self-interacting, neutral and weakly interacting with normal matter. Originally, WIMPs were assumed to be heavy with masses in the range from $100\,\mathrm{GeV/c^2}$ to $1\,\mathrm{TeV/c^2}$, however nowadays also low-mass WIMPs with masses of a few $\mathrm{GeV/c^2}$ are considered as potential candidates. Direct dark matter experiments try to measure the signature of an elastic scattering event of a WIMP with a target nucleon. The associated energy transfer is small, therefore dark matter detectors have to provide excellent background suppression together with very low detection thresholds. Especially for low-mass WIMPs, thresholds have to be in the sub-keV range.

This thesis was performed in the framework of the EDELWEISS experiment, which aims to detect WIMP interactions in High Purity Germanium (HPGe) detectors. The excellent performance of these detectors was proven in the EDELWEISS-III phase, setting limits on the WIMP-nucleon cross-section down to WIMP masses of $4\,\mathrm{GeV/c^2}$. The success was based on the hybrid detection of ionization (electron/hole-pairs) and heat (phonons) signals of a particle interaction, which allows to discriminate nuclear recoils, caused by WIMPs, from electron recoils, which are created by background γ- and β-rays. In addition, the special Fully Inter Digitized (FID) electrode design allowed to reject surface events, which are often affected by trapping and compromise a full measurement of the ionization energy.

In the next phase, having started in December 2016, EDELWEISS aims to increase its sensitivity down to low-mass WIMPs with $m_\chi \approx 1\,\mathrm{GeV/c^2}$. To reach this goal, detection thresholds in the sub-keV range are required. This can be achieved by operating the HPGe detectors at high electric fields, typically up to $100\,\mathrm{V/cm}$. This leads to the so-called Neganov-Trofimov-Luke (NTL) amplification of the heat signal: Drifting electrons and holes lead to secondary phonons, where the number of phonons is proportional to the applied electrode voltage. This technology allows to lower the detection threshold in the heat channel to the 100 eV-range. However, the discrimination power of electron and nuclear recoils and surface events is lost.

This thesis is centered on the study of the HPGe crystals, and especially on the charge migration properties of electrons and holes at low and high electric fields. These properties and their understanding are essential to make proper use of the NTL amplification. Therefore, we performed an extensive calibration experiment with a prototype FID HPGe detector at ground level. We focus on the characterization and understanding of the charge migration processes in the detector, which are crucial for a reliable detector performance. The analysis makes use of the comparison of experimental data with simulations based on modeling the hot carrier transport in the EDELWEISS detectors.

The first part of this work focuses on the pulse-shape analysis of the ionization signals. Pulse-shape analysis allows to study charge transport properties as the shapes of the ionization signals are a direct consequence of electron and hole migration in the HPGe crystal. We use the rise time of ionization signals at low and high electric fields and show that simulation and data are in very good agreement. Further we show that the rise time for surface events is clearly distinguishable from bulk events. We subsequently perform a rise time cut which allows us to reject surface events. Eventually, we show that the rise time parameter can be used to characterize the degradation and space-charge build-up in the detector.

The second part of this thesis is dedicated to the study of the detector performance at high electric fields. The heat signals at high biases are dominated by phonons which are created by drifting electrons and holes. Hence, charge migration processes like trapping are influencing both ionization and heat signals. We show that also at high electric fields, simulation and data are in good agreement. We find that the detector signals are heavily affected by trapping, leading to incomplete charge collection and reduced heat signals. Especially interactions close to the surface and in-between the ring electrodes are limiting the detector performance. Therefore, we optimize the electrode configuration to reduce poor charge collection in the surface region. In case the detectors are operated at high biases, the detection thresholds are low, and therefore low energy backgrounds interacting close to the surface become dominant. This requires an optimization focused on energy deposits in a layer $d \in [200\,\mathrm{nm}, 1\,\mu\mathrm{m}]$ close to the surface. We show that for an electrode design, which consists of only two electrodes, which fully cover the top, bottom and lateral surface of the detector with a small gap (3 mm) on the lateral surfaces, the number of events with reduced heat amplitude due to trapping can be reduced significantly compared to a FID-type detector.

In the searches for low-mass WIMPs with semiconductor detectors, voltage-assisted calorimetric amplification of heat signals will lead the path to higher sensitivity. Thus, understanding the charge transport and avoiding charge trapping becomes an even more important issue. This work proves that charge migration is very well understood for HPGe detectors at cryogenic temperature and bias electric fields ranging from $2\,\mathrm{V/cm}$ to $50\,\mathrm{V/cm}$ and even higher. This allows us to make the next experimental step towards low-mass WIMP searches with a reliable reconstruction of energy deposits in HPGe detectors.

Zusammenfassung

Kosmologische Beobachtungen auf allen Größenskalen des Universums haben gezeigt, dass 86 % der gesamten Masse im Universum aus nicht-leuchtender, gravitativ wechselwirkender Dunkler Materie besteht, wohingegen die bekannte baryonische Materie nur 14 % ausmacht. Obwohl schwach wechselwirkende massive Teilchen (*Weakly Interacting Massive Particles*, WIMPs) bisher noch nicht nachgewiesen wurden, stellen sie attraktive Anwärter auf ein Dunkle Materie Teilchen dar, weil sie zum einen auf natürliche Weise die heute beobachtete Dichte von Dunkler Materie erklären und zum anderen stabil und neutral sind, selten mit normaler Materie wechselwirken und auch eine niedrige Selbstwechselwirkungsrate aufweisen. Ursprünglich wurde angenommen, dass WIMPs hohe Massen im Bereich zwischen $100\,\mathrm{GeV/c^2}$ und $1\,\mathrm{TeV/c^2}$ haben sollten, allerdings gehören heutzutage auch WIMPs mit niedrigen Massen (*low-mass* WIMPs) von einigen $\mathrm{GeV/c^2}$ zu den potentiellen Anwärtern. Die Experimente zur direkten Suche nach Dunkler Materie versuchen, den elastischen Stoß eines WIMPs mit einem Target-Nukleon nachzuweisen. Da der Energieübertrag bei so einem Stoß sehr klein ist, müssen Dunkler Materie Detektoren eine exzellente Unterdrückung von Untergrundereignissen und sehr niedrige Detektionsschwellen aufweisen. Insbesondere für die Messung von low-mass WIMPs sind Detektionsschwellen im sub-keV Bereich notwendig.

Diese Arbeit wurde im Rahmen des EDELWEISS Experiments angefertigt, welches als Ziel hat, Wechselwirkungen von WIMPs in hochreinen Germanium Kristallen (*High Purity Germanium*, HPGe) zu messen. Die ausgezeichnete Funktionsweise dieser Detektoren wurde bereits in der 3. Phase des Experiments gezeigt und erlaubte Ausschlusswerte für den WIMP-Nukleon Streuwirkungsquerschnitt bis zu niedrigen WIMP Teilchenmassen von $4\,\mathrm{GeV/c^2}$ zu bestimmen. Dieser Erfolg basiert auf der gleichzeitigen Messung des Ionisierungs- (Elektron und Loch Paare) und Wärmesignals (Phononen) eines gestoßenen Teilchens. Über das Verhältnis von Ionisationsenergie zu Wärmesignal können Kernrückstöße und Elektronenrückstöße unterschieden werden, wobei erstere durch WIMPs verursacht werden und letztere durch γ- und β- Untergrundstrahlung. Zusätzlich besitzen die Detektoren ein spezielles Elektrodendesign (*Fully Inter Digitized*, FID), das die Identifizierung und Verwerfung von oberflächennahen Ereignissen erlaubt, welche oft vom Einfang von Ladungsträgern betroffen sind, was wiederum zu einer unvollständigen Messung der Ionisationsenergie führt.

Die nächste Phase des EDELWEISS Experiments begann im Dezember 2016 und hat zum Ziel, die Sensitivität für low-mass WIMPs mit $m_\chi \approx 1\,\mathrm{GeV/c^2}$ zu erreichen. Dies bedingt niedrige Detektionsschwellen im sub-keV Bereich. Erreicht werden kann dies, indem die HPGe Kristalle mit hohen elektrischen Feldern von bis zu $100\,\mathrm{V/cm}$ betrieben werden. Dies führt zu einer Verstärkung des Wärmesignal basierend auf dem Neganov-Trofimov-Luke (NTL) Effekt. Während Elektronen und Löcher durch den Kristall driften, werden sekundäre Phononen erzeugt, deren Anzahl mit dem angelegten elektrischen Feld ansteigt. Das ermöglicht eine Reduzierung der Detektionsschwelle im Wärmekanal auf unter $100\,\mathrm{eV}$. Allerdings geht die Diskriminierung von Elektronen- und Kernrückstößen, sowie die Identifizierung von oberflächennahen Ereignissen verloren.

Im Fokus dieser Arbeit stehen die Ladungstransporteigenschaften von Elektronen und Löchern in den HPGe Kristallen bei niedrigen und hohen elektrischen Feldern, da das Verständnis dieser Eigenschaften wesentlich ist, um die NTL Verstärkung wirkungsvoll zu nutzen. Zu diesem Zweck wurde ein umfangreiches Kalibrierungsexperiment mit einem FID HPGe Detektor in einem Oberflächenlabor durchgeführt und die experimentellen Ergebnisse mit Ladungstransportsimulationen in den EDELWEISS Detektoren verglichen.

Der erste Teil dieser Arbeit beschäftigt sich mit der Analyse der Pulsformen der Ionisationssignale. Diese Analyse erlaubt, Ladungtransporteigenschaften zu untersuchen, da die Form der Ionisationssignale eine direkte Konsequenz aus dem Transport von Elektronen und Löchern in den HPGe Kristallen ist. Die Analyse der Anstiegszeiten der Ionisationssignale bei hohen und niedrigen elektrischen Feldern zeigt, dass Simulationen und Messergebnisse gut übereinstimmen. Zusätzlich zeigt sich, dass oberflächennahe Ereignisse kürzere Anstiegszeiten als Ereignisse im Inneren des Detektors haben und folglich eine Diskriminierung von oberflächennahen Ereignissen möglich ist. Abschließend wird gezeigt, dass die Anstiegszeiten geeignet sind, frühzeitig das Entstehen von Raumladung und somit eine Verschlechterung der Ladungssammlung zu erkennen.

Der zweite Teil dieser Arbeit beschäftigt sich mit der Funktionsweise der HPGe Detektoren bei hohen elektrischen Feldern. In diesem Fall sind nicht nur die Ionisationssignale sondern auch das Wärmesignal stark von Ladungstransportprozessen beeinträchtigt, da das Wärmesignal von sekundären Phononen, die durch driftende Elektronen und Löchern entstehen, dominiert wird. Auch hier zeigte sich, dass Simulation und Messung gut übereinstimmen. Es stellte sich heraus, dass die Detektorsignale stark von Ladungseinfang beeinträchtigt sind, was zu unvollständiger Ladungssammlung und reduzierten Wärmesignalen führt. Davon betroffen sind vor allem Ereignisse, die nahe der Oberfläche und zwischen den Ringelektroden auftreten. Um den Einfluss von reduzierter Ladungssammlung für oberflächennahe Ereignisse zu minimieren, führen wir eine Optimierung der Elektrodenkonfiguration durch. Da im Falle von hohen elektrischen Feldern, die Detektionsschwelle niedrig ist, dominiert niedrigenergetische Untergrundstrahlung im oberflächennahen Bereich. Deswegen liegt der Schwerpunkt der Optimierung auf Energieeinträgen, die nahe der Oberfläche einer Schicht $d \in [200\,\mathrm{nm}, 1\,\mu\mathrm{m}]$ stattfinden. Vor allem ein geändertes Design der Elektroden, das nur noch aus 2 großflächigen Elektroden besteht, erlaubt im Vergleich zu einem FID Detektor eine signifikante Reduktion der Ereignisse, die von unvollständiger Ladungssammlung beeinflusst werden.

Die spannungsunterstützte Messung von Ionisierung als Wärmesignal in Halbleiterdetektoren ist ein vielversprechender und zukunftsweisender Weg um höhere Sensitivität für low-mass WIMPs zu erreichen. Dies macht ein gutes Verständnis von Ladungstransportprozessen und die Vermeidung von Signalreduzierung durch Ladungseinfang um so wichtiger. Diese Arbeit zeigt, dass der Ladungstransport in HPGe Detektoren bei tiefen Temperaturen und für elektrische Felder zwischen 2 V/cm und 50 V/cm und höher gut verstanden ist. Dadurch wird eine zuverlässige Rekonstruktion der Energieeinträge im Detektor auch bei hohen elektrischen Feldern möglich. Diese in dieser Arbeit gezeigte Verlässlichkeit der Energieskala erlaubt, den nächsten Schritt in Richtung der Detektion von low-mass WIMPs anzugehen.

Contents

1. Dark matter and detection

Cosmological observations in the last 100 years have shown that 26 % of the energy in the universe consists of non-luminous gravitating dark matter, whereas known baryonic matter only accounts for 5 % of the energy. Although dark matter is well established today, e.g. from measurements of the temperature fluctuations of the Cosmic Microwave Background (CMB) or the rotation curves of galaxies, its particle nature is still unknown. Many theories about dark matter particle candidates exist, where theories with Weakly Interacting Massive Particles (WIMPs) as dark matter candidates are very attractive. WIMPs naturally explain the nowadays observed dark matter density in the universe and fullfill all requirements for a dark matter particle candidate: They are heavy, cold, stable, highly collisionless and low self-interacting. In addition, WIMPs can be easily motivated by the Super Symmetric (SUSY) extension of the Standard Model (SM) of particles. Hence, WIMPs are expected to couple via the weak force to SM particles, they provide different detection channels.

In this chapter, we will present evidence for dark matter in the universe, followed by a discussion of dark matter particle candidates. As this thesis was performed within the EDELWEISS experiment, we will focus on WIMP dark matter candidates and direct dark matter searches.

1.1 Evidence for dark matter

The first to name a new kind of matter, which contributes about a factor 5 more to the matter density in the universe than the known baryonic matter, was F. Zwicky [2]. In 1933, he studied the velocities of galaxies in the Coma Cluster and found that the gravitational

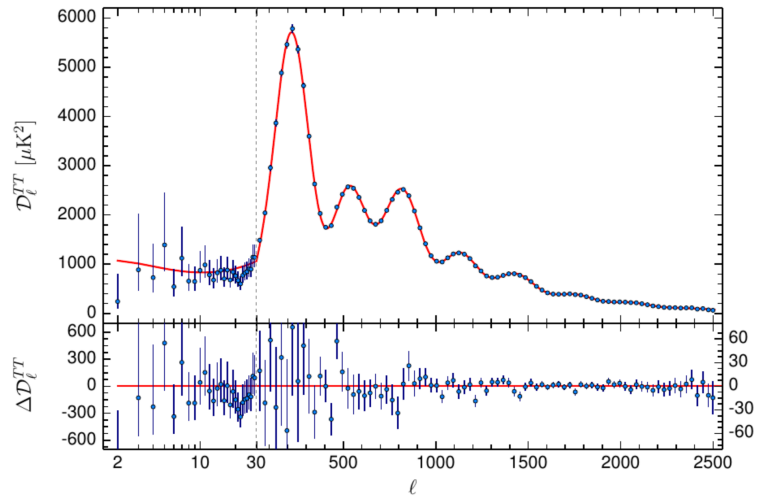

Figure 1.1: Power spectrum of the CMB in dependence of the multipole moment as measured by the Planck satellite [1]. The *red* curve marks the results from a best fit according to the ΛCDM model.

mass must be 400 times higher as expected from the gravity of the luminous mass in order to provide a stable system according to the virial theorem. As this additional mass was of an unknown kind and non-luminous, he named it *Dunkle Materie* (dark matter).

Since then a lot of additional observations have formed our picture of the universe and revealed that the energy densities in the universe can be constrained into baryonic matter Ω_{B}, non-baryonic dark matter Ω_{DM} and dark energy Ω_{Λ}, with

$$\Omega_{\mathrm{B}} = 0.049 \pm 0.001 \tag{1.1}$$

$$\Omega_{\mathrm{DM}} = 0.264 \pm 0.005 \tag{1.2}$$

$$\Omega_{\Lambda} = 0.686 \pm 0.005 \quad . \tag{1.3}$$

These values are extracted from measurements of the temperature fluctuations of the Cosmic Microwave Background (CMB) radiation with the Planck satellite [3], which provides the most convincing evidence for dark matter on the scale of the universe.

The CMB background is a close to perfect black body radiation with a temperature of $T = 2.72548\,\mathrm{K} \pm 0.00057\,\mathrm{K}$ and angular temperature fluctuations on the order of 10^{-5}. It was first measured in 1965 by Penzias and Wilson [4], although its existence was already predicted in 1948 by Gamow [5]. The interpretation of the CMB and its fluctuations is standardly performed within the nowadays established Standard Model of Cosmology (ΛCDM)[1]. This model is based on Big Bang physics and correctly predicts the CMB temperature fluctuations, the large scale structures in the distribution of galaxies, the abundance of the light baryonic particles H, He and Li, and the accelerating expansion of the universe.

In the framework of the ΛCDM model, the CMB can be explained as follows: Shortly after the Big Bang the universe consisted of a hot dense plasma, which contained electrons, baryons (protons and neutrons) and photons. Since the plasma was hot photons could not travel far as they interacted often, especially with the charged components in the plasma. With the expansion of the universe, the hot plasma cooled down. About 380,000 years after the Big Bang, it was cold enough to allow the formation of stable neutral atoms (H, He and Li). Thus, the interaction rate of photons with neutral atoms became much smaller than for charged particles, so the photons decoupled from baryonic matter in the plasma. The early universe became transparent to this so-called relic radiation, which is nowadays measured as the CMB. At the time the CMB decoupled, structure formation in the universe had not yet started. Therefore we expect the CMB temperature to be isotropic and homogeneous at every localization in the universe. However, already before structure formation slight temperature fluctuations existed. They were caused by small variations of gravity, originating from regions with slight over densities of matter and regions with higher radiation pressure, and are today measured as angular temperature fluctuations of the CMB on the order of 10^{-5}.

[1] Λ refers to the cosmological constant, which is assumed to be the dark energy content in the universe. CDM refers to cold dark matter, which moved with non-relativistic speed at the time of structure formation in the universe.

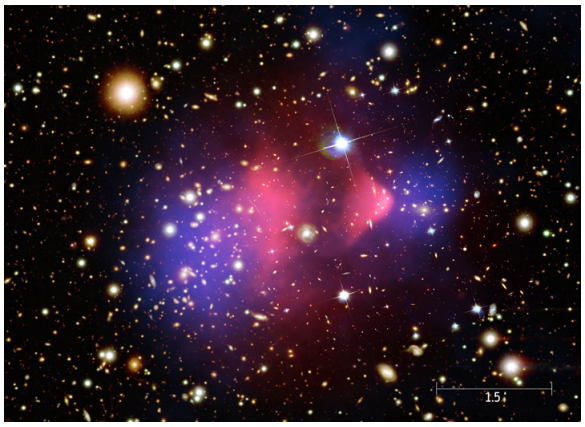

Figure 1.2: Image of the collision of two galaxies in the Bullet cluster [6]. The *red* color marks the luminous matter as measured by X-ray spectroscopy. The *blue* color marks the mass distribution, measured by gravitational lensing. Clearly the luminous mass is centered in the overlap region of both cluster, whereas two separated gravitational centers show up.

Results from measurements of the CMB with the Planck satellite are shown in fig. 1.1. The *red* curve is a fit to the temperature spectrum based on the ΛCDM model and allows to determine the baryonic and dark matter densities. The ΛCDM model is based on six parameters, which besides the baryonic and dark matter density (see eq. 1.1 - 1.3), includes the expansion rate of the universe (Hubble parameter) and the age of the universe [3].

Beside the original evidence presented by Zwicky, additional indications for the presence of dark matter on the scale of galaxy clusters originate from observations of gravitational lensing. If a light source is separated from the observer by a large distribution of matter, the light from the source can be bend on its way to the observer, according to Einstein's theory of general relativity. The strength of the bending allows one to reconstruct the total mass M of the gravitational lens. If in addition, the luminous mass L is measured, the ratio L/M reveals the amount of dark matter contributing to the gravitational lens. In general, we distinguish between strong gravitational lensing, where the foreground mass leads to multiple images of the source or Einstein rings, and weak gravitational lensing, where the distortion of the images around a foreground mass does not allow to reconstruct individual sources but the calculation of the foreground mass is still possible.

Gravitational lensing and X-ray measurements of the collision of two galaxies in the Bullet cluster (see fig. 1.2) strikingly show the different interaction mechanisms for luminous and dark matter. The baryonic matter in the two colliding galaxies interacts electromagnetically and leads to a strong deceleration of the baryonic clouds. Therefore the baryonic cloud after the collision is centered in the overlap region of both galaxies. The dark matter clouds only interact via the much weaker gravitational force. As a consequence the dark matter clouds pass through each other without much deceleration leading to two separated mass centers. The amount of gravitational mass in the Bullet Cluster is measured to be five times higher than the luminous mass.

On the galactic scale, the rotation curves of disk galaxies provide evidence for dark matter. In equivalence to planets orbiting around the sun, the rotation velocity v of objects inside the galaxy is expected to depend on the distance between the center and orbiting object R via

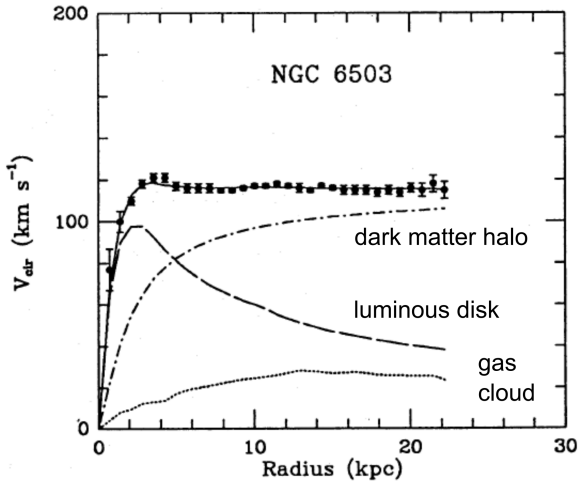

Figure 1.3: Rotation curve for spiral galaxy NGC 6503 [7]. The points represent the measured velocity distributions of the objects in the galaxy. The *dashed* and *dotted* curves represent the expected rotation curves from measurements of the luminous mass of disk and gas cloud. The *solid* line combines luminous and dark matter mass from a halo and describes correctly the measured rotation curve.

$$v = \sqrt{\frac{GM(R)}{R}} \quad , \tag{1.4}$$

where G is the gravitational constant and $M(R)$ is the mass of the orbit system. In spiral galaxies, the luminous mass can be determined by measuring the light emission and is found to be located in the center region of the galaxies. Thus, based on eq. 1.4 the rotation velocity of objects in the outer regions of a disk galaxy should decrease with $V \propto 1/\sqrt{R}$. However this behavior is not observed. An example for the velocity distribution of objects in galaxy NGC 6503 is shown in fig. 1.3. The so-called rotation curve shows that the orbital speed stays constant with distance from the center. The expected rotation curve based on measurements of the luminous mass is marked by the *dashed* curve. The discrepancy can be solved by introducing dark matter. It enhances the gravitational mass of the galaxy but it is non-luminous and can not be measured via the light emission of the galaxy. Since V. Rubin in 1970 [8] first observed the rotation curves of galaxies in the Andromeda Nebula, measurements of many other galaxies have been added.

Based on N-body simulations of structure formation in the universe, we nowadays assume dark matter is clumped in a spherical dark matter halo around the galaxy centers. Following Navarro, Frenk and White [9], the dark matter density ρ in such a halo can be parametrized by

$$\rho_\chi = \frac{\rho_{\mathrm{crit}}\delta_{\mathrm{c}}}{R/R_{\mathrm{s}}\,(1+R/R_{\mathrm{s}})} \quad , \tag{1.5}$$

where $\rho_{\mathrm{crit}} = 3H^2/(8\pi G)$ is the critical density of the universe that depends on the actual value of the Hubble parameter H. δ_{c} is the characteristic over-density of the halo and R_{s} the scale radius, which is determined by the halo mass. The analysis of rotation curves for the Milky Way and the parametrization of the dark matter halo according to eq. 1.5 allows one to determine the dark matter density at the localization of our solar system. The resulting dark matter density is $\rho(R_{\mathrm{Sun}}) \approx 0.3\,(\,\mathrm{GeV/c^2}\,)/\mathrm{cm}^3$ [10].

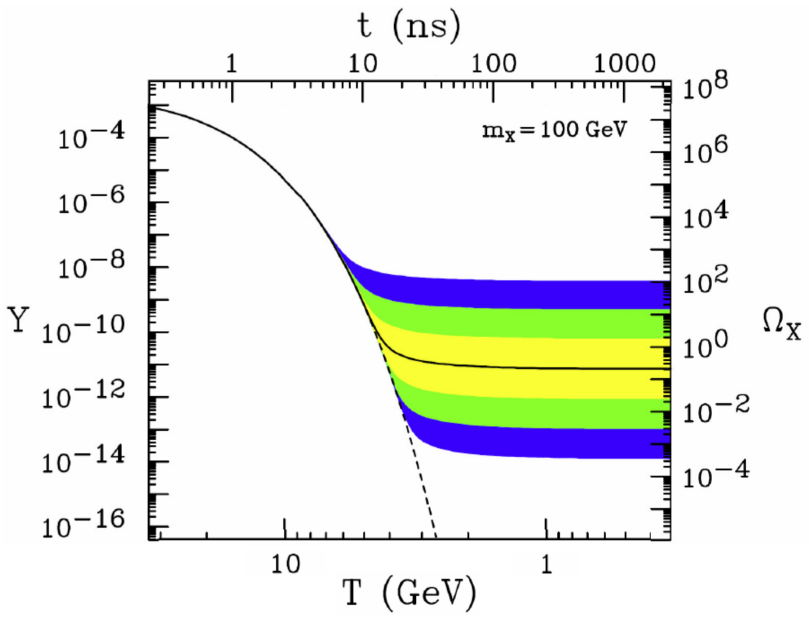

Figure 1.4: Thermal freeze out of a WIMP dark matter particle with a mass of $100\,\mathrm{GeV/c^2}$. The comoving number density (Y) as well as the resulting thermal relic density Ω_χ in dependence of the temperature and life time of the universe are shown. The *solid* line marks the annihilation cross-section, which provides the dark matter density observed today. The *yellow*, *green* and *blue* regions mark cross-sections that differ a factor 10, 100, 1000 from this value. Picture from [11].

1.2 Dark matter candidates

Although many cosmological observations have established the existence of dark matter, its nature is still unknown. Standardly, we assume nowadays that the majority of dark matter in the universe consists of non-baryonic and non-luminous matter.

Actually also dark matter models based on baryonic matter exist. A class of baryonic matter are Massive Astrophysical Compact Halo Objects (MACHOs), which contains objects like brown dwarfs, neutron stars, and also black holes, which are also non-luminous. However, recent observations conclude that MACHOs can not account for more than 20 % of the dark matter content in the universe [12].

Besides of being non-baryonic nature and non-luminous, dark matter particle candidates have to have additional properties following from the cosmological observations (see sec.1.1): A dark matter particle has to be electrically neutral, stable on the time scale of the universe, highly collisionless and weakly self-interacting. In the following, an overview of different dark matter particle models is given.

An attractive dark matter theory is based on Weakly Interacting Massive Particles (WIMPs). WIMPs naturally explain the observed dark matter density in the universe. In addition, they are expected to interact weakly with particles of the Standard Model (SM) and therefore allow the detection via different channels (see. 1.3). WIMPs are expected to be produced as thermal relic of the Big Bang. The early universe consisted of a hot

and dense plasma, where all particles, also WIMPs, were in a thermal equilibrium[2]. With the cooling of the universe, the annihilation rate of the SM particles creating dark matter particles is decreased. For a temperature $T < m_\chi$, where m_χ is the dark matter particle mass, the production of dark matter particles becomes Boltzmann suppressed according to $\propto \exp(-m_\chi/T)$. This is marked by the *dashed* curve in fig. 1.4. We see, that in this case the dark matter particles stay in thermal equilibrium and the dark matter density drops to zero. However, in addition to the cooling, the universe expands. At some time it became so dilute, that annihilation of dark matter particles become negligible. This *freeze-out* fixes the number density of the dark matter in the universe (*solid* line in fig. 1.4). Although this decoupling stops the annihilation of WIMPs into SM particles, interactions and energy transfers with SM particles may still be possible. The freeze-out of WIMP dark matter can be described by the Boltzmann equation

$$\frac{\mathrm{d}n}{\mathrm{d}t} = -3Hn - \langle \sigma_\mathrm{A} v \rangle \left(n^2 - n_\mathrm{eq}^2\right) \quad , \tag{1.6}$$

where n is the number density of the dark matter particle χ, H the expansion rate of the universe (Hubble parameter), $\langle \sigma_\mathrm{A} v \rangle$ the average annihilation cross-section for WIMPs and n_eq the equilibrium number density of dark matter. To be more precise, n relates to the loss of dark matter particles via $\chi\ \chi \rightarrow$ SM SM, and n_eq relates to the production of dark matter particles via SM SM $\rightarrow \chi\ \chi$. A numerical solution of eq. 1.6 connects the thermal relic density Ω_χ with the annihilation cross-section σ_A via

$$\Omega_\chi \propto \frac{T_0^3}{\rho_\mathrm{c} M_\mathrm{Pl}} \langle \sigma_\mathrm{A} v \rangle^{-1} \quad , \tag{1.7}$$

where ρ_c is the critical density of the universe, M_Pl the Planck mass and T_0 todays temperature of the universe. Eq. 1.7 shows that the dark matter density we observe today, can be retrieved by adjusting the annihilation cross-section of dark matter. In WIMP theory the annihilation cross-section is connected to the dark matter particle mass m_χ via

$$\langle \sigma_\mathrm{A} v \rangle = k \frac{g_\mathrm{weak}^4}{16\pi^2 m_{\chi^2}} \quad , \tag{1.8}$$

where k is used for parametrization and g_weak is the weak coupling constant. The typical mass of a weak-scale WIMP dark matter candidate, which provides the correct annihilation cross-section to explain the observed dark matter density is then predicted to be in the range $m_\chi \in \left[100\,\mathrm{GeV/c^2}, 1\,\mathrm{TeV/c^2}\right]$. However, several direct dark matter experiments have found hints for signatures of WIMPs with masses below $100\,\mathrm{GeV/c^2}$ (see sec. 1.4.4). Accompanied by possible dark matter annihilation signals from the Galactic Center [13], which also favor low mass dark matter candidates, additionally low-mass WIMP are nowadays considered as dark matter candidates. According to eq. 1.8, a lower WIMP mass leads to a higher annihilation rate and therefore to an earlier freeze out of dark matter WIMPs.

[2] Annihilation of SM particles creates dark matter particles χ and vice versa

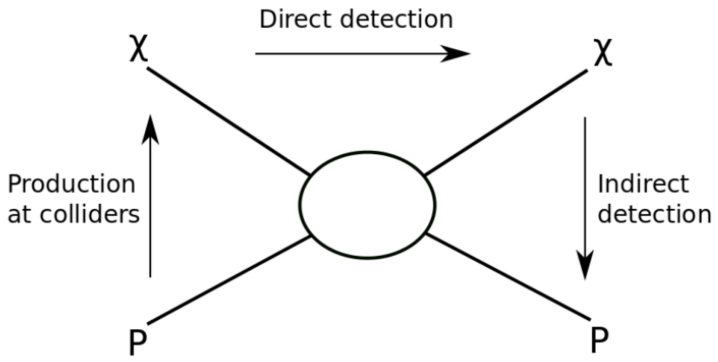

Figure 1.5: Schematic overview of different detection channels for WIMP dark matter [17].

The lowest limit for the mass of a WIMP that still provides a thermal relic density in agreement with cosmological observations is about $2\,\mathrm{GeV/c^2}$ (Lee-Weinberg bound [14]).

A WIMP dark matter particle candidate is provided by the Super Symmetric extension of the Standard Model of particles, which provides a very elegant solution to the gauge hierarchy problem. In SUSY models, every particle of the SM has a super partner. These super partners have the same quantum numbers and gauge interactions as the SM particles, but differ in spin by 1/2. The 4 neutral fermions with spin 1/2 form 4 mass eigenstates, so-called neutralinos, where the lightest neutralino provides a good WIMP dark matter candidate. The requirement of stability for dark matter particles on the time scale of the universe is solved by introducing a new quantum number, the R-parity, which prevents the neutralino from decaying into SM particles. For an overview of WIMP dark matter candidates see [11] or [13].

Other possible dark matter candidates are axions, which were originally postulated to solve the strong CP-problem in quantum chromodynamics (QCD). In comparison to WIMP dark matter candidates, axions are produced non-thermally and can have very small masses (μeV). However, they also fullfill the basic requirements for a dark matter candidate: They are sufficiently cold to allow structure formation, lead to the correct dark matter density and are highly collisionless. For an introduction to axion dark matter see [15].

Another explanation for dark matter, which also allows low-mass dark matter candidates, is given by asymmetric dark matter (ADM) models (see e.g. [16]). ADM models are based on the observation that dark matter and baryonic matter density are very similar, only differing about a factor 5 (see eq. 1.1 - 1.3). The baryonic matter density we observe nowadays is a consequence of the asymmetry in the number density of particles and anti particles. The ADM models assume that a similar particle - antiparticle asymmetry explains the dark matter density. Dark matter candidates based on ADM models favor low-masses in a typical range of $m_\chi \in [1, 15]$ GeV/c^2.

1.3 Detection of WIMP dark matter

WIMPs are very attractive candidates for particle dark matter as they are expected to interact with standard particles via the weak force, and can be studied via different processes: They can either scatter with SM particles (direct search) or they can be produced in collider experiments or they annihilate to SM particles (indirect search) (see fig. 1.5). We briefly discuss the different detection channels in this section. However, we focus on the direct detection channel, as this thesis was performed within the direct dark matter search experiment EDELWEISS.

1.3.1 Direct detection principle

Experiments like EDELWEISS are primarily interested in the search of WIMP dark matter, although most of them also provide sensitivity for other types of dark matter such as axions [18, 19]. In this section, we will focus on WIMP dark matter. The goal of experiments, which search for WIMPs, is to extract the WIMP-nucleon cross-section $\sigma_{\chi A}$ in dependence of the WIMP mass m_χ. In order to extract these parameters several assumptions are necessary, which are discussed here. WIMP dark matter candidates are expected to elastically scatter with the detector target nuclei. As the WIMP-nucleon cross-section is expected to be very small, $\sigma_{\chi A}\left(m_\chi = 100\,\mathrm{GeV/c^2}\right) < 10^{-45}\,\mathrm{cm}^2$ (see sec. 1.4.4), multiple scattering events in the detectors can be excluded. According to [20] the differential recoil spectrum for WIMP interactions in a target can be written as

$$\frac{\mathrm{d}R}{\mathrm{d}E_{\mathrm{rec}}}\left(E_{\mathrm{rec}},t\right) = \frac{\rho_0}{m_\chi m_{\mathrm{A}}} \int_{v_{\mathrm{min}}}^{v_{\mathrm{max}}} v \cdot f\left(\boldsymbol{v},t\right) \cdot \frac{\mathrm{d}\sigma_{\chi A}}{\mathrm{d}E_{\mathrm{rec}}}\left(E_{\mathrm{rec}},v\right) \mathrm{d}^3 v \quad , \tag{1.9}$$

where $\mathrm{d}\sigma_{\chi A}/\mathrm{d}E_{\mathrm{rec}}\left(E_{\mathrm{rec}},v\right)$ is the differential cross-section, m_{A} the target nucleon mass, v the dark matter velocity and ρ_0 and $f\left(\boldsymbol{v},t\right)$ the local density and velocity distribution of dark matter. The local velocity density depends on time, as the earth rotates around the sun. This offers two detection channels: The WIMP scattering rate can either be measured in dependence of the recoil energy E_{rec}, which is done in the EDELWEISS [21] experiment, or as an annual modulation [22], as it is done by the DAMA [23] experiment.

In order to extract the WIMP-nucleon cross-section from eq. 1.9, the velocity distribution of dark matter in the Milky Way has to be known. Normally the standard halo model (SHM) is used, which assumes an isotropic and isothermal spheric distribution of dark matter around the galaxy center with a density $\rho(R) \propto R^{-2}$ (see eq. 1.5), where R is the distance from the galactic center. The numerical solution of the collisionless Boltzmann equation then lead to a velocity distribution [24] described by

$$f\left(\boldsymbol{v},t\right) = N \cdot \exp\left(-\frac{3\left|\boldsymbol{v}\right|^2}{2\sigma^2}\right) \quad , \tag{1.10}$$

where N is a normalization parameter and $\sigma = \sqrt{3/2}v_c$ is defined by the speed v_c of objects orbiting around the galactic center. For the position of the earth in the Milky Way the SHM uses the local dark matter density $\rho = 0.3\,\mathrm{GeV/cm^3}$ and the local circular speed $v_c = 220\,\mathrm{km/s}$ [25]. An additional mandatory parameter is the escape velocity, up to which objects are bound in the Milky Way. The escape velocity was measured to be $v_{esc} = 544\,\mathrm{km/s}$ by the RAVE survey [26]. It provides the upper bound of the integral in eq. 1.9 with $v_{esc} = v_{max}$.

In order to calculate the WIMP-nucleon cross-section $\sigma_{\chi A}$ in dependence of the WIMP mass m_χ from the measured recoil spectrum (see eq. 1.9) further assumptions have to be made, concerning the particle-physics model for WIMP interactions with SM particles. Standardly, the differential cross-section $\mathrm{d}\sigma_{\chi A}/\mathrm{d}E_{rec}$ can be expressed as the sum of a spin-independent (SI) and a spin-dependent (SD) part

$$\frac{\mathrm{d}\sigma_{\chi A}}{\mathrm{d}E_{rec}} = \frac{m_A}{2\mu_A^2} \cdot \left(\sigma_0^{SI} \cdot F_{SI}^2(E) + \sigma_0^{SD} \cdot F_{SD}^2(E)\right) \quad , \tag{1.11}$$

where μ_A describes the reduced WIMP-nucleus mass, and F_{SI} and F_{SD} are the nucleus form factors of SI and SD interactions. To the spin-independent cross-section, protons and neutrons of the target nuclei contribute equally via

$$\sigma_0^{SI} = \frac{\mu_A^2}{\mu_p^2} \cdot (Z \cdot f_p + (A - Z) \cdot f_n)^2 \quad , \tag{1.12}$$

where μ_p is the reduced WIMP-proton mass and f_p and f_n are the contributions of protons and neutrons to the coupling strength. Standardly $f_p = f_n$ is assumed and the SI cross-section becomes proportional to the number of nucleons A^2. The spin-dependent cross-section is given by

$$\sigma_0^{SD} = \frac{32}{\pi}\mu_A^2 \cdot G_F^2 \cdot (a_p \cdot \langle S_p \rangle + a_n \cdot \langle S_n \rangle)^2 \cdot \frac{J+1}{J} \quad , \tag{1.13}$$

where G_F is the Fermi coupling constant and J the total nuclear spin. The SD cross-section is further determined by the effective coupling strengths of WIMPs to protons a_p and neutrons a_n and the expectation values for the nuclear spin contributions of protons $\langle S_p \rangle$ and neutrons $\langle S_n \rangle$. If we assume a WIMP-nucleon cross-section of $\sigma_{\chi A} = 10^{-45}\,\mathrm{cm^2}$ and a WIMP mass of $100\,\mathrm{GeV/c^2}$, the expected WIMP rate in a detector with germanium target is $< 10^{-5}\,\mathrm{events/(kg\ days\ keV)}$ [17].

1.3.2 Collider experiments and indirect searches

In fig. 1.5 it was illustrated, that in addition to the elastic scattering, WIMPs can be produced in collisions of SM particles or can annihilate to SM particles. In this section, we will briefly discuss the potential of dark matter searches resulting from these two channels.

The production of WIMPs in SM particle collisions can be studied with the CMS [27] and the ATLAS [28] detectors of the Large Hadron Collider (LHC) at CERN. The LHC

searches for signatures of new particles in proton-proton collisions with a center-mass energy of 7 TeV and higher, and already allowed the discovery of the Higgs particle [29, 30]. The production of dark matter particles would lead to a signature

$$pp \rightarrow \chi\bar{\chi} + x \quad , \tag{1.14}$$

where x could be a hadronic jet, a photon or also a decay of Z and W bosons into leptons. Although the produced WIMPs can not be detected directly, a dark matter signature would show up as missing momentum and energy in the jet x. So far no signatures of the production of dark matter at LHC have been found by ATLAS and CMS, but further searches will be performed with increasing center-mass energies.

Indirect searches are looking for the annihilation signal of dark matter via channels like

$$\chi\bar{\chi} \rightarrow \gamma\gamma, \gamma Z, \gamma H, q\bar{q}, W^-W^+, ZZ \quad , \tag{1.15}$$

which can even decay further into e^-e^+-, $p\bar{p}$, γ-rays or neutrinos. The idea is to use telescopes, point them at structures in the universe which contain a large amount of dark matter like stars, galaxies, the galactic center etc. and measure the emitted particle flux. If this flux is larger than expected from luminous-matter, this could be caused by annihilating dark matter particles. For example imaging atmospheric telescopes like HESS [31], MAGIC [32] or VERITAS [33] are scanning the sky and measure the γ-ray flux in the TeV-range for different directions. Other experiments like IceCube [34] or Super-Kamiokande [35] can measure excesses in the neutrino flux. Neutrinos produced by annihilating dark matter are attractive signals, as they interact only weakly and the direction of their flux can point back to the source. In comparison to that, charge particles are deflected by magnetic fields and γ-rays can interact with cosmic dust, which makes a reconstruction of the location of the source very difficult. So far no significant dark matter signal have been detected. However, satellite experiments like PAMELA [36] or AMS [37] have measured an increased positron flux in the galactic halo for energies in the range of 10 GeV to 250 GeV, which could be interpreted as a dark matter signal but is also consistent with an unknown population of millisecond pulsars or interactions of cosmic rays with cosmic dust. A good review on indirect and collider dark matter searches can be found in [38].

1.4 Direct detection techniques

Dark matter experiments which aim to detect WIMPs face in general two challenges: Firstly, the energy transfer in an elastic scattering event of a WIMP and a target nucleon is small. For standard WIMPs, the recoil energies are in the keV-range and for low-mass WIMPs even in the sub-keV range. Therefore appropriate detectors have to provide a low detection threshold. In fig. 1.6 the possible signatures of a WIMP scattering in different types of detectors are illustrated. Depending on the target material, phonons (heat), ionization (electron/hole pairs) or scintillation light are produced, and provide the mandatory low detection thresholds.

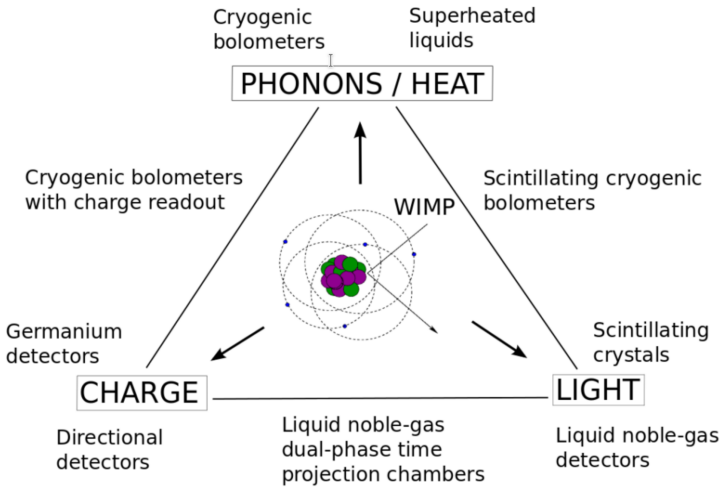

Figure 1.6: Direct detection techniques [17].

Secondly, the expected scattering rate of WIMPs with baryonic matter is low. As a consequence detectors need excellent shielding and discrimination methods for background events. Standardly, shielding against cosmic muons is provided by an operation in an underground laboratory. In addition, low radioactive materials are used for the experimental set-up in order to reduce the amount of γ- and β-backgrounds. Still, background interactions dominate the event rate in the detectors. Therefore many experiments rely on the simultaneous measurement of two signals. The hybrid detection of ionization/scintillation and heat allows to discriminate electron recoils, mainly caused by β- and γ-background radiation, from nuclear recoil (neutrons, WIMPs) and provide a significant background reduction. Hence β- and α-radiation, as well as low energy γ-rays (30 keV) do not penetrate very deep into a detector. Thus, many experiments use surface event discrimination techniques and only consider the inner (*fiducial*) volume of their detectors for the dark matter search.

In this section, we will focus on dark matter experiments based on the techniques presented in fig. 1.6. An overview of other techniques like bubble and drift chambers can be found in [17].

1.4.1 Scintillating and ionizing crystals

Scintillating crystals made of NaI(Tl) and Cs(Tl) operated at room temperature are used in the dark matter experiments DAMA [39] and KIM [40]. Nuclear recoils expected from WIMPs excite atoms or molecules in the crystals. Thus, the de-excitation leads to the emission of light. Thallium (Tl) atoms are placed in the crystals by purpose and act as luminescence centers. They shift the primary photon wavelengths to longer values, typically about 400 nm to 600 nm, at which photon sensors are more efficient. Based on their high density, scintillating crystals have a large stopping power. In addition, the can also be operated in stable manner stable over long terms and provide high exposures. However, these experiments can not discriminate between electron and nuclear recoils, and therefore these backgrounds have to be considered during the analysis.

Ionizing detectors are mainly made of High Purity Germanium (HPGe) crystals. They can be produced with the smallest impurity density of all semiconductor crystals, reaching even impurity densities below $10^{10}\,\mathrm{cm}^{-3}$. Furthermore, they can easily provide detection thresholds of a few keV, as the energy to produce an electron/hole-pair in Ge crystals is small (about 3 eV). However, HPGe detectors have to be at least operated at a liquid nitrogen temperature (77 K), in order to avoid significant noise contributions from thermally activated e^-/h^+-pairs. The exclusive measurement of ionization signals is used by the CoGent [41] experiment. With a 443 g HPGe crystal they were able to reach a detection threshold of 500 eV. In addition their detector is a p-type (acceptor atoms dominate the impurity density) point contact detector, which benefits from an increased dead layer that shields α- and β-background radiation. In addition, rise time analysis of ionization signals are used to discriminate surface events, which are typically more affected by incomplete charge collection due to trapping and recombination (see sec. 3.3.4) than bulk events.

1.4.2 Hybrid detection of ionization/scintillation and heat with calorimetric detectors

Calorimetric dark matter detectors are massive solid state crystals operated at cryogenic temperatures $T < 100\,\mathrm{mK}$. At these temperatures the heat capacities of the detectors are low enough to allow the measurement of recoil energies in the keV-range as a significant temperature rise in the μK-range (see sec. 2.4). In general calorimeters provide very low energy thresholds as the energy to produce a phonon is very small, typically a few meV. However, most dark matter experiments measure the ionization or scintillating signal in addition to the heat signal. This allows to discriminate electron and nuclear recoils, as the amount of ionization or scintillation light produced per unit energy deposit depends on the recoil type.

The EDELWEISS experiment uses HPGe crystals as dark matter targets. The HPGe detectors are operated in an electric field, and energy deposits are simultaneously measured as heat and ionization signals. The heat signals are measured with a Neutron Transmutation Doped (NTD) Ge thermistor, which allows to measure thermal phonons. Supplementary, since the EDELWEISS-II phase, the charge collecting electrodes have an interleaved electrode design. This allows to discriminate surface events by measuring the ionization signals on different sets of electrodes (see [42]). A detailed description of the HPGe detectors in EDELWEISS is given in chap. 2.

Another dark matter experiment based on semiconductor detectors is the CDMS experiment. In its first and second phase, the experiment was based on 19 HPGe and 11 silicon detectors [43, 44]. Like EDELWEISS, the detectors measure simultaneously heat and ionization in order to provide discrimination of electron and nuclear recoils. The heat signal is read-out with Transition Edge Sensors (TES), which allow to detect athermal phonons. Athermal phonons are high energy phonons with long mean free paths, which allow to localize energy deposits by the timing of the heat signals. The z-sensitive ionization and phonon-mediated (ZIP) detectors originally measured phonons with 4 TES, each covering

one quarter of the detector. Pulse-shape analysis of the phonon signals [45] allowed to reject 1 surface event in 10^6. The iZIP technology of the next phase (SuperCDMS experiments) used in addition interleaved electrodes, which allowed to discriminate surface event based on the asymmetry of the charge signal on these electrodes [46]. The next phase CDMSLite, as in EDELWEISS (see sec. 2.6.3), is dedicated to reduction of the energy threshold of the detectors, in order to increase sensitivity for low-mass WIMPs. This is done by applying high electric fields to the detector. The heat signal is then enhanced by secondary phonons produced by drifting electrons and holes (Neganov-Trofimov-Luke effect). In this case electron and nuclear recoil discrimination is not possible anymore. However, the CDMS collaboration has already successfully operated a detector with an energy threshold of only 56 eV [47].

The CRESST experiment [48] uses $CaWO_4$ tungsten crystals and simultaneously measures heat and scintillating light, which also allows to discriminate electron and nuclear recoils. Both signals are readout as heat signals with two tungsten TES. The scintillation light is absorbed in a semiconductor target, which is glued to a TES. Using the NTL effect for the scintillation light measurement can reduce the detection threshold for the scintillating light significantly [49]. Even without NTL amplification CRESST detectors have very low detection thresholds. This allowed them to set limits on the WIMP-nucleon cross-section for WIMP masses $m_\chi < 1\,\mathrm{GeV/c^2}$ [50].

1.4.3 Liquid noble gas detectors

Liquid noble gas detectors are either based on Ar (LAr) or Xe (LXe). This allows to construct detectors with large volumes and homogeneous targets. In addition, LAr and LXe provide high ionization and scintillation yields. Liquid noble gas detectors can be classified in two categories: Single phase detectors like DEAP [51] or XMASS [52] contain only liquid noble gas. The liquid is stored in a spherical container and surrounded by PMTs, which measure the scintillation light. A discrimination of electron and nuclear recoils can be performed via pulse-shape analysis. Especially for Ar, the states that provide the luminescence have different life-times (6 ns and 1.6μs) and are populated differently depending on the type of the interacting primary particle [53].

Double phase liquid noble gas detectors, like XENON10/100 [54, 55], LUX [56], PandaX [57], measure scintillation and ionization signals. Typically, the liquid Xe or Ar is stored in a cylindrical vessel. The scintillation signal is measured as a prompt signal with PMTs on the top and bottom of the tank. Ionized electrons are drift upwards in an electric field and enter a gas phase, where their signals are amplified and also measured with the PMTs. The time difference of ionization and scintillation signal defines the z-axis of the energy deposit and the pattern of the PMTs allows to reconstruct the (x,y)-position.

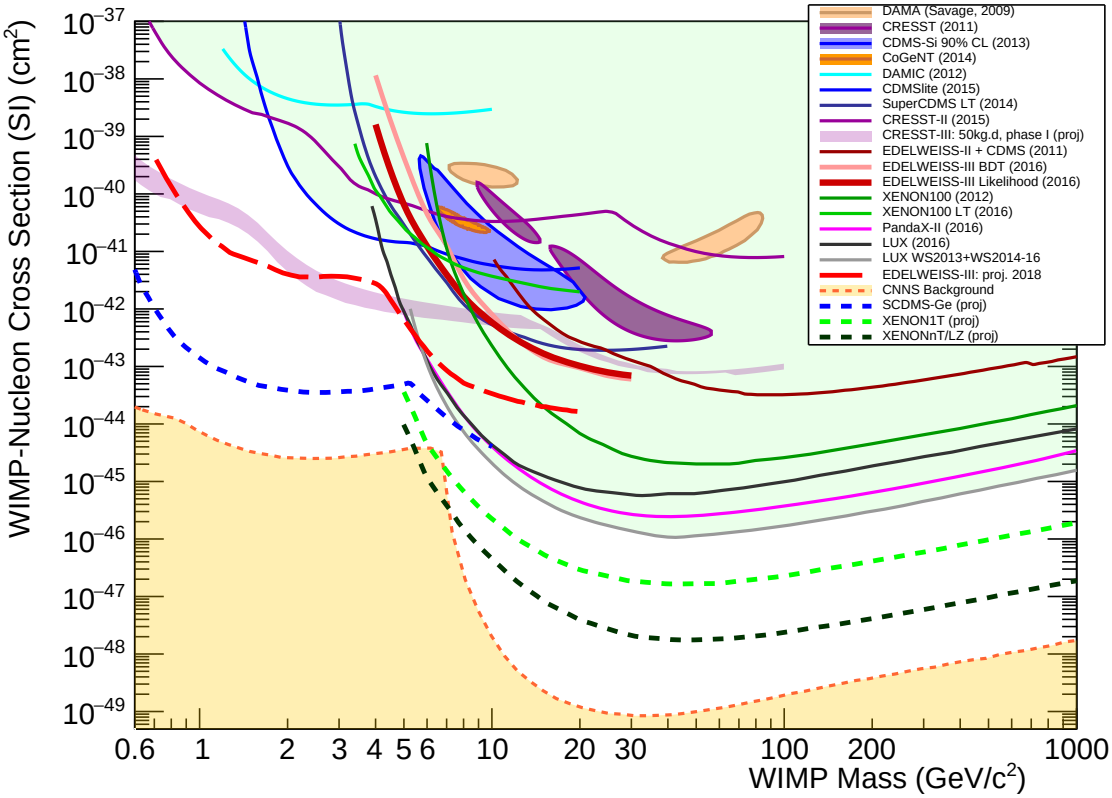

Figure 1.7: Spin-independent WIMP-nucleon cross-section for direct dark matter experiments. The *solid* lines exclude the parameter space above. The closed contours mark regions, in which signals where indicated. The *dashed* lines represent projected limits. The *yellow* shaded area marks the neutrino floor, which will be an irreducible background for future dark matter experiments.

1.4.4 Status of direct dark matter experiments

In fig. 1.7 a selection of results for the WIMP-nucleon cross-section measured by various direct dark matter experiments is shown. For a more complete collection of data the reader is referred to e.g. [17]. Although solid state detectors like CDMS-II Si [58], CoGent [41], CRESST-II [59] and DAMA/LIBRA [23] initially found indications for WIMP signal with low masses in the range $m_\chi \in [10,30]$ GeV/c^2, none of these signals have been verified to date or the signal regions have been ruled out by other experiments. However, based on theories about low-mass WIMPs, dark matter search experiments plan to extent their search to low-mass WIMPs with masses below 1 GeV/c^2. The experimental limits and projections in fig. 1.7 show, that especially solid state detectors have the potential to reach very low detection thresholds. Since for experiment like EDELWEISS, CDMS and CRESST, a lowering of the detection threshold down to $\approx$ 100 eV leads to the loss of discrimination power between electron and nuclear recoils, future experiments have to put more effort into background reductions and estimations. Especially the energy calibration has to be performed with great care.

The results on the WIMP-nucleon cross-section for liquid noble gas experiments clearly show, that they provide the best exclusion limits at WIMP masses above $10\,\mathrm{GeV/c^2}$. As the increase of the detector mass is relatively easy, they are expected to hold their leading sensitivity for standard WIMP masses in the future. The projected exclusion limits for XENONnT [60], LZ [61], DARWIN [62] show, that the sensitivity of actual dark matter experiments will soon reach areas, where the detectors become sensitive to neutrino backgrounds originating from solar and atmospheric neutrinos. As coherent neutrino scattering can produce nuclear recoils as well as electron recoils, new background rejection techniques have to be found, and will make the WIMP dark matter search even more challenging [63].

2. The HPGe detectors of the EDELWEISS experiment

The EDELWEISS experiment aims to detect dark matter WIMPs with High Purity Germanium (HPGe) crystals. Typically, these detectors have a mass of about 800 g and are operated at cryogenic temperatures ($T = 18\,\mathrm{mK}$) and low electric fields ($< 2\,\mathrm{V/cm}$). A WIMP candidate is expected to produce a nuclear recoil in the HPGe crystal by an elastic scatterin event with a Ge nucleon. The nuclear recoil creates electron/hole-pairs, which are separated by the electric field and measured as the ionization signal E_{ion}. In addition, the recoil leads to the production of phonons, which are measured as a temperature rise with a Neutron Transmutation Doped (NTD) Ge thermistor and define the heat signal. This hybrid detection of ionization and heat signal allows one to discriminate nuclear recoils from background electron recoils, mainly caused by γ- and β-radiation, as the number of created e^-/h^+-pairs per recoil energy depends on the recoil type. For this discrimination a full collection of the ionization and heat energy is mandatory. Hence, especially e^-/h^+-pairs created by recoils in the surface region are heavily affected by trapping, the HPGe detectors have a Fully Inter Digitized (FID) electrode design, which allows to discriminate surface events. A description of the FID800 detectors and the active background discrimination methods, as well as an explanation of the heat measurement with a NTD Ge thermistor is given in sections 2.1 - 2.4.

In fig. 1.7 the results from phase III (July 2014 until April 2015) of the EDELWEISS experiment were presented. The EDELWEISS collaboration was able to set upper limits on the WIMP-nucleon cross-section down to low-mass WIMPs of $4\,\mathrm{GeV/c^2}$ [21], which rules out existing claims of dark matter signals of various experiments. This success was based on the excellent technology of the FID800 detectors, which allows to discriminate nuclear and electron recoils and to reject surface events. The results for background rejection efficiencies are presented in sec. 2.5.

The goal for the next phase of the EDELWEISS experiment is to improve sensitivity for low-mass WIMPs with $m_\chi < 4\,\mathrm{GeV/c^2}$. It includes a further reduction of the detection threshold below 1 keV as well as the reduction of background events. The strategies to reach these goals include the usage of new low noise electronics, an improved understanding of charge migration processes, the evaluation of new parameters for the surface event discrimination like the rise time of ionization signals, the voltage-assisted calorimetric readout of charge signals and the reduction of the heat-only backgrounds. A discussion of these strategies is presented in sec. 2.6.

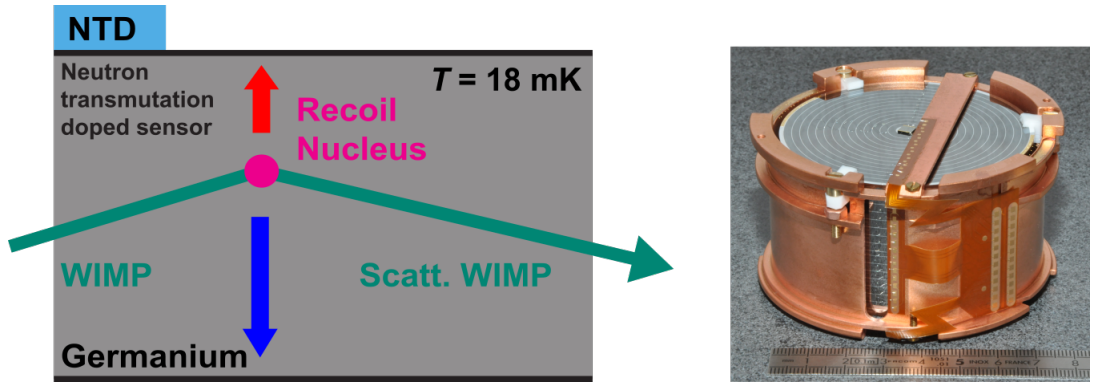

Figure 2.1: *Left:* Schematic illustration of the EDELWEISS detection principle. The aim is to measure the elastic scattering event of a WIMP with a Ge-nucleon simultaneously as a heat and ionization signal. The *blue* and *red* arrows mark the drift of electrons and holes to electrodes. The heat signal is measured with a NTD Ge thermistor. *Right:* Picture of a FID800 Ge detector in its copper casing. The crystal has a height of 4 cm and a diameter of 7 cm.

2.1 Hybrid detection of ionization and heat signals for electron and nuclear recoil discrimination

The detectors of the EDELWEISS experiment measure simultaneously the heat and ionization signal of an energy deposit in the detector. This enables the discrimination of electron recoils, caused by γ- and β-background radiation, from nuclear recoils, which are expected from WIMP candidates and neutrons.

The detectors consist of cylindrical HPGe crystals, which are operated in an electric field. If a particle scatters in the detector, the recoiling electron or nucleon creates electron/hole-pairs. These are separated by the electric field and measured as an ionization signal at a set of electrodes. In Ge the number of produced e^-/h^+-pairs per energy deposit depends on the recoil type. For electron recoils, the energy needed to produce one e^-/h^+-pair is $\varepsilon_{\mathrm{er}} \simeq 3.0\,\mathrm{eV}$, whereas for nuclear recoils it is significant larger. The dependence of the ionization signal on the recoil type can be expresses as

$$E_{\mathrm{ion}} = c_{\mathrm{ion}} \frac{E_{\mathrm{rec}}}{\varepsilon_{\mathrm{xr}}} = Q_{\mathrm{xr}} E_{\mathrm{rec}} \quad , \tag{2.1}$$

where c_{ion} is the calibration factor for the ionization channel, E_{rec} the recoil energy, ϵ_{xr} the energy to produce an e^-/h^+-pair and Q_{xr} the so-called ionization yield, where x stands for e or n in case of electron and nuclear recoil respectively.

Standardly with-in the EDELWEISS experiment, the ionization energy as well as the heat energy is calibrated according to bulk electron recoils created by interactions from a γ-ray calibration source. Therefore the unit is given in $\mathrm{keV_{ee}}$. Typically a ^{133}Ba source is used for calibration. It emits γ-rays with an energy of 356 keV, and as the penetration depth of 356 keV γ-rays in Ge is about 18 mm, it illuminates the detectors approximately uniformly. The calibration factor c_{ion} is then defined by the position of the 356 keV peak in

the ionization amplitude spectrum with $E_{\mathrm{ion}}(356\,\mathrm{keV}) = 356\,\mathrm{keV_{ee}}$. According to eq. 2.1, the ionization yield for electron recoils is then defined as $Q_{\mathrm{er}} = 1$ and for nuclear recoils it is smaller with $Q_{\mathrm{nr}} < 1$.

The ionization yield Q_{nr} for nuclear recoils depends on the recoil energy E_{rec}. For the EDELWEISS detectors this energy dependence was measured in a calibration experiment with a neutron source. The resulting parametrization

$$Q_{\mathrm{nr}} = 0.16 E_{\mathrm{rec}}^{0.18} \quad \text{for} \quad E_{\mathrm{rec}} \text{ in keV} \quad , \tag{2.2}$$

is in good agreement with a semi-empirical approach derived by Lindhard [64]. For a Ge nucleus, this would for example lead to an ionization yield $\approx 25\,\%$ with respect to an electron at a recoil energy of 10 keV.

Hence, the HPGe detectors measure the heat and ionization energy of an energy deposit and for low electric fields, the heat signal is approximately a direct measurement of the recoil energy with $H \approx E_{\mathrm{rec}}$ (a detailed discussion on the heat signal and the so-called Neganov-Trofimov-Luke effect follows in sec. 2.3), the ionization yield Q can be used to discriminate electron and nuclear recoils via

$$Q = \frac{E_{\mathrm{ion}}}{H} \approx \frac{E_{\mathrm{ion}}}{E_{\mathrm{rec}}} \quad . \tag{2.3}$$

Eventually this discrimination is limited by the resolution in the ionization channel. Especially for recoil energies below 200 eV, the number of created e^-/h^+-pairs (see eq. 2.5) is small as the production threshold for e^-/h^+-pairs is in the eV-range. Therefore the measurement of the ionization signal suffers from the small statistics of charge carriers. In comparison to that the heat channel is not limited by the statistics of phonons. The production threshold for individual phonons is only a few meV. Thus, the number of phonons produced per energy deposit is much higher than the number of e^-/h^+-pairs. Limitation in heat resolution follows more from parasitic heat capacities and athermal phonon losses, and will be discussed in sec. 2.4.

2.2 Interleaved electrode design for surface event discrimination

In the last section, we showed that the discrimination of electron and nuclear recoils with the HPGe EDELWEISS detectors is based on the ionization yield Q (see eq. 2.3). Clearly a full measurement of the ionization and heat signals is necessary to achieve a high discrimination factor. Especially e^-/h^+-pairs created in the near-surface region are affected by trapping and recombination, as will be described in sec. 3.3.4. Thus the measured ionization energy for energy deposits in this region can be reduced. Based on the short absorption lengths ($< 1\,\mathrm{mm}$) of background α-, β- and low energy γ-rays ($< 30\,\mathrm{keV}$) in Ge, surface events are mainly characterized by electron recoils. A reduced measurement of the ionization signal therefore leads to an ionization yield $Q < 1$ and consequently the event could be misinterpreted as nuclear recoil.

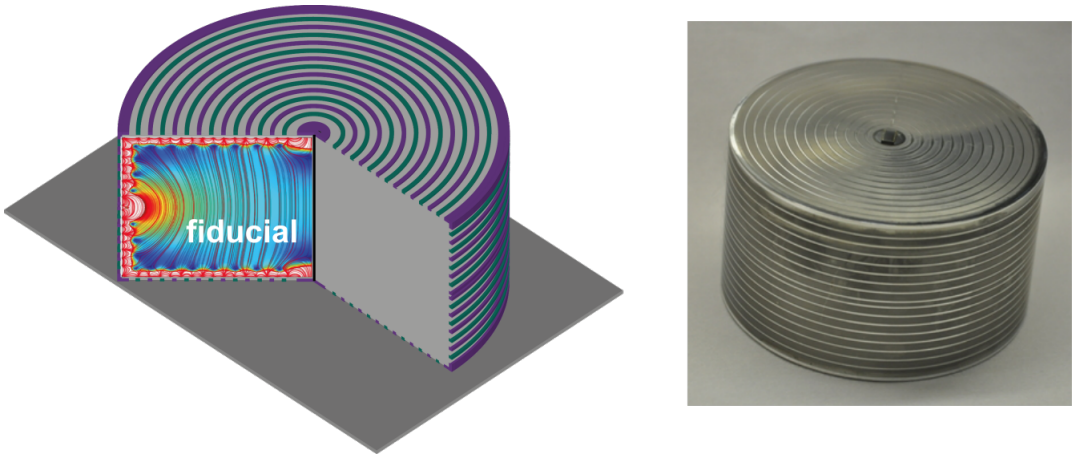

Figure 2.2: *Left:* Schematics of a Fully Inter Digitized (FID) detector, with 4 types of ring electrodes. The *green* rings represent the collecting and the *violet* the veto electrodes. Veto and collecting electrodes of the upper and lower half of the detector can be biased independently. A standard bias configuration is shown in fig. 2.3. In addition the electric field structure inside the detector is shown, where the *blue* colored region marks the fiducial volume. *Right:* Picture of an actual cylindric FID800 detector with a mass of 800 g, a diameter of 7 cm and a height of 4 cm.

In order to avoid misinterpretations of electron recoils as nuclear recoils, the EDELWEISS HPGe detectors have a Fully Inter Digitized (FID) electrode design, which is presented schematically in fig. 2.2 *left*. The cylindrical FID detectors are completely covered by ring electrodes made of aluminum with a typical width of 200 μm and a height of 100 nm. The ring electrodes are divided into 4 groups, which can be biased independently. The *top* electrodes cover the upper half of the detectors and the *bottom* electrodes the lower half. The ring electrodes at the top and the bottom are alternately connected by aluminum bonds, grouping the electrodes into 2 collecting and 2 veto electrodes (*green* and *violet* rings in fig. 2.2 *left*). For a standard detector operation, the collecting electrodes are biased with +4 V and −4 V, and the veto electrodes with a smaller bias with opposite

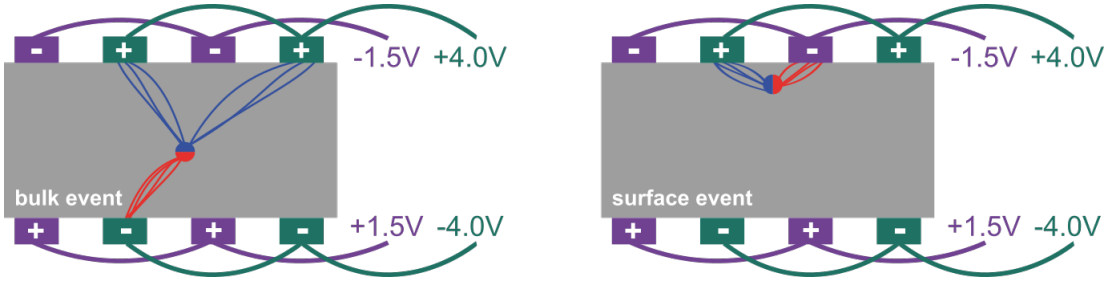

Figure 2.3: Schematic illustration of the surface event discrimination principle with a FID800 detector. As presented in fig. 2.2 the electric field lines in the inner part of the detector are parallel to the cylindric axis and therefore e^-/h^+-pairs created in this so-called bulk region are drifted to the top and bottom collecting electrodes, as shown in the *left* graphic. At the borders of the detectors the electric field lines are parallel to the surface and e^-/h^+-pairs created there drift to the collecting and veto electrodes on one side of the detector, as shown in the *right* graphic.

signs $-1.5\,\mathrm{V}$ and $+1.5\,\mathrm{V}$. The resulting electric field configuration is shown in fig. 2.2 *left*. In the near-surface area the electric field lines are parallel to the crystal border and in the bulk region parallel to the z-axis of the cylindrical detector. If we assume as a first approximation that electrons and holes drift along the electric field lines[1], e^-/h^+-pairs produced in the surface region of the detector are collected at a veto and a collection electrode and e^-/h^+-pairs created in the bulk region are collected at the two collecting electrodes (see fig. 2.3). Thus by measuring the ionization signals on the 4 types of electrodes, surface events can be discriminated from bulk events. The bulk region is called fiducial volume of the detector (*blue* area in fig. 2.2 *left*) and represents around 75 % of the total detector volume.

2.3 Neganov-Trofimov-Luke effect

In sec. 2.1 we discussed that the hybrid detection of ionization and heat signals in the FID800 detectors, allows one to discriminate electron and nuclear recoils, based on the ionization yield Q (see eq. 2.3). In a first approximation, we assumed that the heat energy is proportional to the recoil energy and independent from the ionization signal. Actually heat and ionization signals are not independent. Supplementary to the primary phonons produced by the recoil, electrons and holes create secondary phonons during their propagation to the electrodes. The creation of secondary phonons is called Neganov-Trofimov-Luke (NTL) [65, 66] effect and leads to an enhanced heat signal H according to

$$H = E_{\mathrm{rec}} + E_{\mathrm{NTL}} \quad \text{with} \quad E_{\mathrm{NTL}} = qN\Delta V \quad , \tag{2.4}$$

where E_{rec} is the recoil energy, N the number of produced e^-/h^+-pairs, q the electrical charge and ΔV the electrode bias between the electrodes on which a charge carrier is collected. The number of produced e^-/h^+-pairs follows from the recoil energy E_{rec} and the energy to produce one e^-/h^+-pair ϵ_{xr} via

$$N = \frac{E_{\mathrm{rec}}}{\epsilon_{\mathrm{xr}}} \quad . \tag{2.5}$$

As we discussed in sec. 2.1 the energy ϵ_{xr} to produce an e^-/h^+-pair in a HPGe crystal depends on the recoil type, with $\epsilon_{\mathrm{er}} = 3\,\mathrm{eV}$ for electron recoils and a significantly higher value for nuclear recoils. Moreover, ϵ_{nr} depends on the recoil energy according to eq. 2.2.

Eq. 2.4 clearly shows that for low electrode biases ΔV, the heat signal is dominated by the recoil energy E_{rec}. The typical bias for the collecting electrodes of the FID800 detectors in the EDELWEISS-III phase was $\Delta V = 8\,\mathrm{V}$. It was low enough to provide an efficient discrimination of electron and nuclear recoils [67]. Based on eq. 2.4 and 2.5, the heat energy H is described by

[1] A detailed discussion on charge migration in HPGe detectors follows in chap. 3. We will show that especially the electron transport properties are heavily affect by the crystal structure and electrons in the EDELWEISS crystals actually do not drift parallel to the electric field lines.

$$H = c_{\text{heat}} E_{\text{rec}} \left(1 + \frac{q\Delta V}{\epsilon_{\text{xr}}}\right) \quad , \tag{2.6}$$

where c_{heat} is the calibration factor of the heat channel and is chosen to fullfill $H = E_{\text{rec}}$ for electron recoils. The heat signal caused by an arbitrary recoil is then

$$H_{\text{xr}} = E_{\text{rec}} \left(\frac{1 + q\Delta V Q/\epsilon_{\text{er}}}{1 + q\Delta V/\epsilon_{\text{er}}}\right) \quad , \tag{2.7}$$

where Q is the ionization yield, with $Q \approx 1$ for electron recoils, whereas for nuclear recoils Q is energy dependent according to eq. 2.2. Combining eq. 2.3 and 2.7, the recoil energy of an event can be calculated from the heat and ionization energy measurement via

$$E_{\text{rec}} = H \left(1 + \frac{q\Delta V}{\epsilon_{\text{er}}}\right) - E_{\text{ion}} \frac{V}{\epsilon_{\text{er}}} \quad . \tag{2.8}$$

For the standard operation of the EDELWEISS detectors the NTL effect is distracting, as the measured heat energy has to be corrected according to eq. 2.8 in order to determine the recoil energy. On the other hand, the NTL effect can be used to amplify the ionization signal by applying high biases to the electrodes ($\Delta V = 100\,\text{V}$). In this case, the heat signal will be dominated by secondary phonons produced during the drift of electrons and holes in the applied electric field. Therefore the heat energy H is proportional to the ionization energy via

$$H = c_{\text{heat}} E_{\text{ion}} \quad , \tag{2.9}$$

where c_{heat} is the calibration factor, which is defined by calibration measurements with γ-sources, wherefore $[H] = \text{keV}_{\text{ee}}$. This operation mode allows one to lower the detection threshold to recoil energies $< 1\,\text{keV}$ and increases the sensitivity for low-mass WIMPs with $m_\chi < 5\,\text{GeV/c}^2$. However, the discrimination of electron and recoil based on the ionization yield Q is not possible any more, as from eqs. 2.3 and 2.9 it becomes clear that Q is always one. In addition, the baseline resolution in the ionization channels is typically around 1 keV and therefore higher than the resolution in the heat channel operated at high biases. It follows that for low energy deposits, significant pulses only show up in the heat channel. Thus, a surface event discrimination is not possible any more. On-going developments in EDELWEISS to use the NTL effect for the detection of low-mass WIMPs are discussed in sec. 2.6.

2.4 Calorimetric detection principle for a FID800 detector

In fig. 2.4 *left* a simplified schematic model of the calorimetric set-up for a FID800 detector is shown. It consists of a HPGe crystal, which functions as a target for WIMP candidates, and is in good thermal contact with a temperature sensor and weakly coupled to a thermal

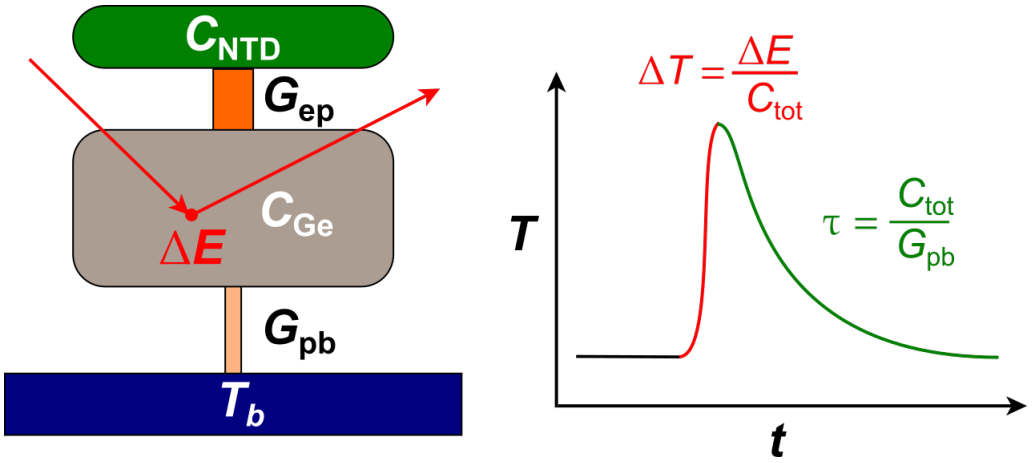

Figure 2.4: *Left:* Illustration of the calorimetric principle for a FID800 detector. The total heat capacity C_{tot} is the sum of the heat capacities of the HPGe crystal C_{Ge} and the temperature sensor C_{NTD}. G_{ep} and G_{pb} mark the thermal couplings between HPGe crystal and temperature sensor and between HPGe crystal and thermal bath. *Right:* Illustration of the general shape of a heat pulse. The relaxation time τ of the calorimetric system is determined by the thermal coupling G_{pb} and the total heat capacity C_{tot}.

bath with constant temperature T_{b}. An energy deposit ΔE in the HPGe crystal leads to a temperature rise ΔT of the detector with

$$\Delta T = \frac{\Delta E}{C_{\mathrm{tot}}} \quad , \tag{2.10}$$

where C_{tot} is the total heat capacity of the detector system, including the heat capacity of the HPGe crystal C_{Ge} and the heat capacity of the temperature sensor C_{NTD}. In case the total heat capacity is known, the energy deposit ΔE can be reconstructed from the measured temperature rise ΔT.

In order to measure a large temperature rise, the total heat capacity C_{tot} has to be low. For a FID800 detector, the total heat capacity is dominated by the phonon contribution from the HPGe crystal with

$$C_{\mathrm{Ge}} = \frac{12\pi^4 N k_{\mathrm{B}}}{5} \cdot \frac{T^3}{\Theta_{\mathrm{D}}^3} \quad , \tag{2.11}$$

where N is the number of atoms in the crystal, k_{B} the Boltzmann constant and $\Theta_{\mathrm{D}} = 373\,\mathrm{K}$ [68] the Debye temperature of Ge. As the heat capacity decreases with temperature, a large temperature rise requires an operation of the detector at low temperatures. Typically the FID800 detectors are operated at $T \approx 18\,\mathrm{mK}$. According to eq. 2.11, the heat capacity of a 800 g HPGe crystal at $T \approx 18\,\mathrm{mK}$ is $C_{\mathrm{Ge}} \approx 1.8\,\mathrm{nJ/K}$ [69] leading to a temperature rise of $\Delta T \approx 0.18\,\mu\mathrm{K/keV}$. The low temperatures needed for the operation of the FID800 detectors are provided by a ^{3}He/^{4}Hedilution refrigerator. A description of this cooling technique is given in sec. 4.2.

The temperature rise ΔT caused by an energy deposit ΔE, as well as the relaxation of the detector system to the base temperature T_b are time dependent. A schematic pulse shape is shown in fig. 2.4 *right*. Primary phonons created by a recoil are strongly athermal, meaning their energies are around a factor 10 to 100 times higher than the energies of the thermal phonons, determined by the operating temperature. The rise time of the heat pulse is therefore determined by the time, the athermal phonons need to thermalize with the temperature of the crystal lattice and is typically around 10 ms. The relaxation time is determined by the thermal coupling between the HPGe crystal and the thermal bath. For the FID800 detectors this thermal link is provided by gold bonds, leading to a relaxation time of $\tau \approx 100\,\mathrm{ms}$.

2.4.1 Neutron Transmutation Doped (NTD) Ge thermistors as temperature sensors

In EDELWEISS the temperature rise ΔT caused by a recoil in a FID800 detector is measured with a Neutron Transmutation Doped (NTD) Ge thermistor. Standardly, the FID800 detectors are equipped with two NTD Ge thermistors, which are glued to the center veto ring electrodes (see fig. 2.2 *right*) at the top and bottom of the HPGe crystals. As shown in eq. 2.10 the NTD Ge thermistor heat capacity contributes to the total heat capacity and therefore reduces the temperature rise ΔT. However with $C_\mathrm{NTD}(18\,\mathrm{mK}) \approx 0.2\,\mathrm{nJ/K}$ the NTD Ge thermistor heat capacity is small in comparison to heat capacity of the HPGe crystals with $C_\mathrm{Ge}\,(18\,\mathrm{mK}) \approx 1.8\,\mathrm{nJ/K}$.

NTD Ge thermistors belong to the category of semiconductor thermistors and make use of the strong temperature dependence of their electrical conductivity at low temperatures. In reality these semiconductor thermistors are almost exclusively made of silicon and germanium. The special production process for a NTD Ge thermistors is explained later. In the following, we explain the general principle of these devices.

In comparison to doped semiconductors[2] at room temperature, where most of the dopant impurities are ionized due to interactions with thermal phonons, at low temperatures the mean phonon energy is small and the fraction of ionized impurities is close to zero. In this low temperature regime, two types of conducting behaviors exist. If the dopant density exceeds a critical density, a so-called metal-insulator transition occurs, and the semiconductor conductivity goes to zero for zero temperatures. Different to that, semiconductor thermistors make use of doped semiconductors with a doping density below the metal-insulator transition. In this case even at zero temperature a finite conductivity exists (for more details see e.g. [70]). The charge transport in these devices can then be described very similar to amorphous materials [71]. Dopant impurities create a large distribution of localized energy levels close to the conduction band minimum and valence band maximum of the crystalline semiconductor. Therefore at sufficiently high temperatures, the conductivity is based on the hopping of charge carriers from one localized state to the nearest unoccupied state by interacting with a thermal phonon. At low temperatures the mean en-

[2] An introduction to semiconductors, band structures and dopant impurities is presented in chap. 3.

ergy of the phonons is decreased and so-called variable-range hopping is favored. A charge carrier hops to an unoccupied localized state with an energy level close to its initial energy level, which is not necessarily the neighboring localized state. The temperature dependent resistivity R of a semiconductor in the variable-range hopping regime can be described by

$$R(T) = R_0 \exp\left(\frac{T_0}{T}\right)^{-1/4} \quad , \tag{2.12}$$

where the value of T_0 is determined by the dopant density and R_0 can be calculated from the dopant density and the geometry of the semiconductor (see e.g. [72]).

Production of NTD Ge thermistors

NTD Ge thermistors are highly valuable devices as they can be produced with high reproducibility by irradiating germanium with reactor neutrons [73]. Natural Ge has four stable isotopes, where three of them (^{70}Ge, ^{74}Ge and ^{76}Ge) are the isotopes of interest as their reactions with neutrons produce the electrically active impurities ^{71}Ga, ^{75}As and ^{77}Se. The last two impurities are donors and ^{71}Ga is an acceptor. Based on the abundance of the different germanium isotopes and their cross-sections with neutrons, the NTD Ge thermistor created is p-type, although 32.2 % of the ^{71}Ga acceptor impurities are compensated by the ^{75}As and ^{77}Se impurities [74]. The advantage of neutron transmutation doping is, that it leads to a uniform distribution of dopant impurities in the Ge lattice as the primary distribution of the Ge isotopes is uniform. In addition, the neutron-Ge cross-section is low, wherefore large blocks of NTD Ge can be produced at once and cut into slices afterwards. Furthermore, the temperature dependence of the resistivity of a NTD Ge thermistor mainly depends on the net doping density, and uniform NTD thermistors with different characteristic can be produced by simply changing the neutron dose for the natural Ge block. Results for the characterization of NTD Ge thermistors can be found in [75].

NTD Ge thermistors have proven to be very attractive devices for temperature measurements at cryogenic temperatures, as they have very uniform and predictable properties. In addition, they can be produced in large numbers, which make them very valuable for large detector arrays not only for dark matter searches but also for other rare event searches like LUMINEU [76] and CUORE [77], which aim to measure the neutrinoless double beta decay. Another advantage is that NTD Ge thermistors are easy to read-out by using Field Effect Transistors (FET) (a typical read-out set-up is shown in sec. 4.3.2).

2.4.2 Other temperature sensors

There exist other techniques to measure the temperature rise in a calorimetric detector. In the following two are mentioned: Transition Edge Sensors (TESs) and Metallic Magnetic Calorimeters (MMCs).

TESs measure a temperature rise via the strong resistance change of a superconductor, operated close to its transition temperature to the normal state T_c (see e.g. [78]). In comparison to semiconductor thermistors with a logarithmic sensitivity $\alpha = \mathrm{d}\log T/\mathrm{d}\log R$ between 1 and 10, TESs can be produced with $\alpha > 1000$ (see e.g. [79]). They have shown to provide excellent performances in dark matter experiments like CRESST and CDMS but their production is much more complicated as the critical temperature of the fabricated devices is hardly reproducible. In addition, the electronic read-out is more complicated and involves SQUID electronics [80, 81].

MMCs measure a temperature rise as magnetic flux change created by a paramagnetic material, that is placed in an external magnetic field (see e.g. [82]). This technique is very promising as it provides excellent energy resolution (100 eV-range). In addition, in comparison to NTD Ge thermistors, MMCs are hardly affected by microphonic noise [83]. MMCs have not yet been used in dark matter experiments, however the KIT group of EDELWEISS in cooperation with the Heidelberg MMC group is developing a prototype detector.

2.5 Results for background discrimination with the HPGe detectors of EDELWEISS

As the scattering rate of WIMPs with baryonic matter is expected to be very low, actual dark matter experiments point to < 1 events/kg/year, it is crucial for dark matter experiments to operate their detectors in an as background free environment as possible. In addition, active background discrimination techniques are important to reject remaining background interactions.

In order to provide a low background environment, the detectors of the EDELWEISS experiment are shielded by different layers. First of all, the experiment is located in the Modane underground laboratory (LSM) in the French alps. The laboratory is covered by a 4800 m w.e. thick layer of rock, which reduces the cosmic muon flux down to 5 muons/m^2/day, which is a factor 10^6 less than at sea level [86]. Remaining cosmic muons are tagged with an active muon veto [87]. The reduction of the muon flux is important as muons can induce neutrons, which are not discriminable from WIMP candidates, as they also produce nuclear recoils in the detector.

Other background neutrons are produced by the natural decay chains of ^{238}U and ^{232}Th, which contaminate the rocks around the laboratory and (α,n) reactions. They are shielded with different layers of polyethylene.

In the EDELWEISS-III experiment, interactions from γ-rays provide the dominant background in the detectors. These originate from the natural radioactivity of ^{238}U and ^{232}Th, as well as from contaminations of ^{40}K, ^{60}Co and ^{137}Cs in the rocks of the laboratory. In order to reduce the amount of γ-background events, the EDELWEISS experiment is shielded with additional layers of lead, including a very low radioactive ancient roman lead shield close to the detectors. In addition, all components were screened before installation

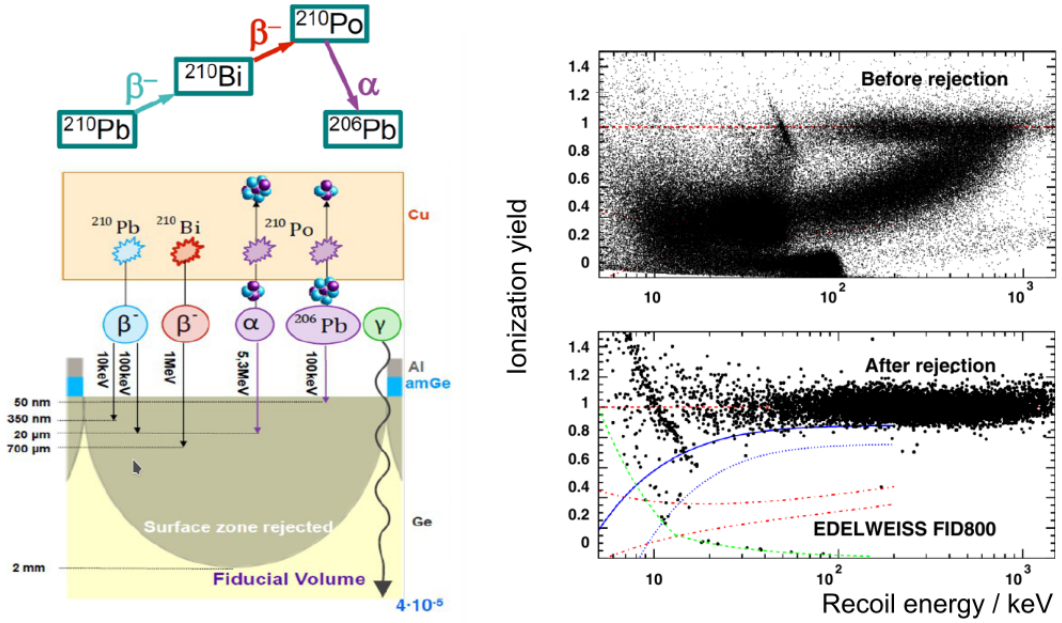

Figure 2.5: *Left:* Schematics of the surface region of a FID800 detector. The *grey* area marks the surface, the *yellow* one the fiducial region. α- and β-rays originate from the natural decay chain of ^{210}Pb, resulting from radon contaminations in the copper, and create energy deposits in the surface region. *Right:* Ionization yield versus recoil energy for a calibration experiment with a ^{210}Pb source. Although the primary interactions are electron recoils, a lot of events have a reduced ionization yield $Q < 1$, even leaking down into the nuclear recoil band (*top* graphic). After a surface cut (*bottom* graphic), only one event remains in the nuclear recoil band. Pictures from [84].

and only materials with low radioactive contaminations were used, e.g. the copper casings in which the detectors are held are made from ultra-pure copper. Beside interactions originating from external γ-background sources, EDELWEISS has to deal with internal γ-rays. Before the FID800 detectors were the installed in the Modane underground laboratory, they were stored at sea level. Hence, they were exposed to cosmic radiation. This led to long-lived isotopes in the detector with typical half-lives of 100 days. A detailed analysis of internal γ-ray sources within the EDELWEISS detectors can be found in [88]. It showed that the external γ-ray background is low enough to even measure the internal decay of tritium.

Another prominent background source follows from radon contamination of the materials in the experiment. The radon decay chain contains ^{210}Pb, which has a half-life of $T_{1/2} = 22.3$ years and creates β- and α-radiation. Like γ-rays, β- and α-rays produce electron recoils in the detector. However, the α- and β-particles have small absorption depths and interact mainly in the surface areas of the detectors (see fig. 2.5 *left*). As radon has a high mobility and is easily absorbed at surfaces, it is a very resistant background source [89]. In order to reduce the radon contamination, the whole EDELWEISS experiment is operated in a clean room and the remaining volumes in the cryostat are flushed with deradonized air on a regular basis.

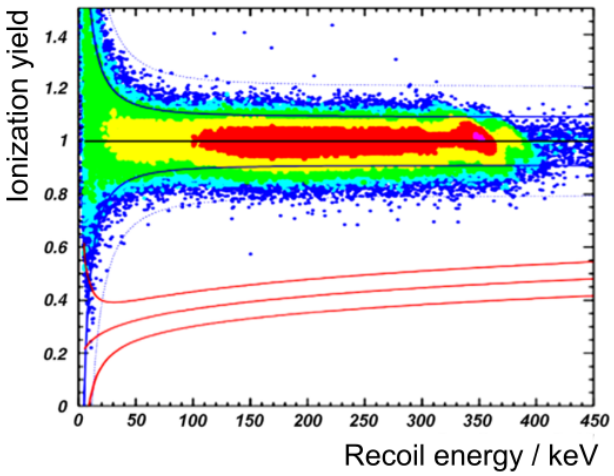

Figure 2.6: Ionization yield Q versus recoil energy for γ-ray interactions in the fiducial volume, originating from a ^{133}Ba calibration source. The solid lines mark the electron recoil (*black*) and the nuclear recoil band (*red*). Picture from [85].

The importance of an active discrimination technique for α- and β-interactions is shown in figure 2.5 *right*. The ionization yield of a FID800 detector was measured in a calibration experiment with a ^{210}Pb calibration source. It shows many events with reduced ionization yield, populating the electron recoil band as well as the nuclear recoil band. As all primary interactions were actually caused by electron recoils, the reduced ionization yields Q originate from trapping effects, which are especially strong at the surfaces. Events with reduced ionization yield due to trapping are very critical, as they can be misinterpreted as nuclear recoils and therefore as WIMP candidates. After applying the EDELWEISS surface cut (see sec. 2.2) to this data set, only one critical event above $E_{\mathrm{rec}} = 15\,\mathrm{keV}$ in the nuclear recoil band remained, allowing one to quantify the surface rejection factor [90] to

$$R_{\mathrm{surf}} < 4 \cdot 10^{-5}\,\mathrm{events/alpha}\ \ (90\,\%\ \mathrm{C.L.}) \quad . \tag{2.13}$$

The surface event rejection cut defines the fiducial volume of the detector. Remaining background interactions are caused by γ-rays, which can penetrate deeper into the crystal. As γ-rays produce electron recoils in the detector, they can be identified by the ionization yield Q (see sec. 2.1). Fig. 2.6 shows the results for a calibration run with a ^{133}Ba-source. This source produces γ-rays with an energy of 356 keV. They penetrate deeply into the crystal, but are also often scattered before they interact in the sensitive region of the detector. Therefore the measured recoil spectrum includes many events with a smaller energy than 356 keV. For the calibration run 425585 events were measured and no event leaked into the nuclear recoil band, resulting in a very powerful γ-ray rejection factor [90] of

$$R_{\gamma} < 6 \cdot 10^{-6}\,\mathrm{nuclear\ recoils}/\gamma\ \ (90\,\%\ \mathrm{C.L.}) \quad . \tag{2.14}$$

2.6 On-going developments for the next phase of the EDELWEISS experiment

The next phase of EDELWEISS, started in December 2016, and is dedicated to the search for low-mass WIMPs with $m_\chi < 5\,\mathrm{GeV/c^2}$. In this measurement phase, EDELWEISS detectors are operated at high electrode biases, which leads to an amplification of the charge signals in the heat channel and allows one to extend the detection thresholds significantly to recoil energies $E_\mathrm{rec} < 1\,\mathrm{keV}$. Moreover, additional strategies exist to improve the detector performance in order to lower the detection threshold, and are discussed in this section.

2.6.1 Low noise charge amplifiers

In case the EDELWEISS Ge detectors are operated in a low electric field, they allow to discriminate background electron recoils from nuclear recoils based on simultaneous measurements of ionization and heat signals (see sec. 2.1). The detection threshold in this operation mode is mainly limited by the resolution in the ionization channel and therefore directly connected to the noise in the used charge amplifiers. In order to lower the detection threshold significantly below $< 1\,\mathrm{keV}$, EDELWEISS is planning to use modern amplifiers with significantly reduced noise.

So far the ionization signals of the FID800 detectors are amplified by Junction Field Effect Transistors (JFETs), which are operated at $T \approx 100\,\mathrm{K}$ and allow a typical resolution for the baseline in the ionization channel of $\sigma_\mathrm{ion} \approx 300\,\mathrm{eV_{ee}}$. Recently, High Electronic Mobility Transistors (HEMTs) were developed at CNRS/LPN [91], which are operated at $T = 4\,\mathrm{K}$. Tests with a massive Germanium detector showed that HEMTs have a noise level around 3 times lower than JFETS and the baseline resolution in the ionization channel can be lowered to $\sigma_\mathrm{ion} \approx 91\,\mathrm{eV_{ee}}$ [92]. Examples of typical electronic read-out systems for ionization and heat signals are presented in sec. 4.3. An exact description of the electronics and read-out circuits in the EDELWEISS-III experiment can be found in [93].

2.6.2 Fast ionization read-out and pulse-shape analysis for improved surface event discrimination

The final results for the WIMP search with the 400-g interleaved Germanium detectors of the EDELWEISS-II experiment [94] showed, that for a total exposure of $427\,\mathrm{kg \cdot days}$ in the recoil energy range of $E_\mathrm{rec} \in [20{,}200]$ keV, 5 events were found in the nuclear recoil band, although only 3 were expected from background estimates [95]. In order to clarify, if these events are misinterpreted surface events, EDELWEISS developed the improved FID800 detectors, which consist of HPGe crystals which have additional ring electrodes at the lateral surfaces (see sec. 2.2). A second approach was to develop a Fast Ionization Channel (FIC) read-out card, which allows a sampling frequency of 40 MHz for the ionization signals instead of the standard sampling with 100 kHz. This enables one to measure the transient times of the ionization signals, which are typically between 50 ns and $1\,\mu\mathrm{s}$. Tests with

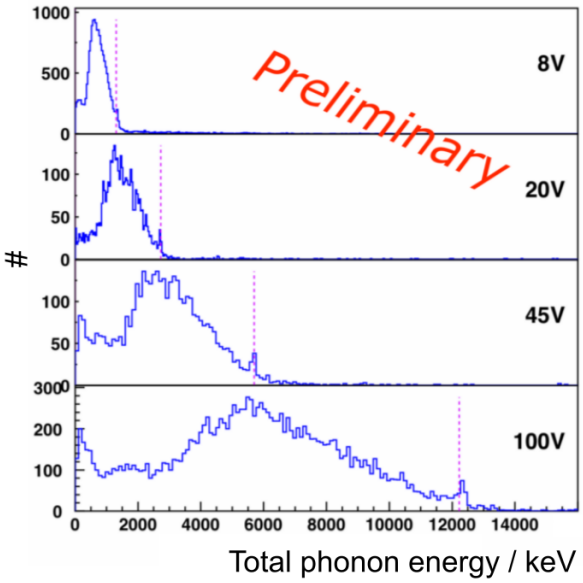

Figure 2.7: Total phonon energy spectrum for different electrode biases for a calibration run with a ^{133}Ba source. The red line marks the expected peak position of the 356 keV γ-rays calculated from its position at the lowest electrode bias with $\Delta V = 8\,\mathrm{V}$ (see eq. 2.4). Picture from [90].

EDELWEISS-type detectors have shown, that the pulse-shape analysis of these signals also allows to discriminate bulk and surface events [96, 97].

For the EDELWEISS-III run 309 (June 2015 - December 2015) a FIC prototype readout card was installed for one of the FID800 detectors and allowed one to record ionization signals on two collecting electrodes with a 40 MHz sampling frequency. Pulse-shape analysis of the ionization signals showed that the rise time allows to rejection of surface events with an efficiency of 95 % [98].

As the basis for the rise time analysis for the EDELWEISS-III ionization signals, an extensive pulse-shape analysis of ionization signals was performed in the framework of this thesis. Since the ionization signals are caused by drifting electron and hole pairs, the analysis of ionization pulse-shapes also allows one to study charge migration processes in HPGe. A comparison of simulation and data enables us to probe our understanding of electron and hole transport in the EDELWEISS detectors and to evaluate and improve the detector performance. The set-up for simulations and experiments, as well as the results for pulse-shape analyses of ionization signals will be presented in the chaps. 3, 4 and 5.

2.6.3 Amplification of the ionization signal based on the NTL effect

The current phase of the EDELWEISS experiment focuses on the extension of the detection threshold to recoil energies $E_{\mathrm{rec}} < 1\,\mathrm{keV}$ in order to improve the sensitivity for low-mass WIMPs. In sec. 2.3 we explained that this can be done by using the NTL effect. Electron and hole pairs, which are created by a recoil in the detector are separated in an electric field and produce secondary phonons while they migrate through the crystal. This additional heat signal is proportional to the electrode bias and therefore with increasing bias the detection threshold in the heat channel is lowered.

First results from Run 309, which was finished in March 2016, showed that some EDELWEISS detectors could hold voltages up to 100 V without a break down caused by leakage currents. The heat amplitude spectrum for one FID800 detector operated at different voltages is presented in fig. 2.7. The data were taken in a calibration experiment with a ^{133}Ba calibration source, which emitted γ-rays with an energy of 356 keV. The 356 keV peak showed the expected linear behavior based on the NTL effect (see eq. 2.4). In addition, an energy threshold of 150 $\mathrm{eV_{ee}}$ could be achieved for one of the detectors [98].

For Run 310, which started in December 2016, a long period low-mass WIMP search run is planned with 7 EDELWEISS detectors operated at high voltages. Based on these efforts, in the framework of this thesis, we performed an extensive calibration experiment with an EDELWEISS-type detector operated at high electrode biases in a ground experiment at CSNSM in Orsay, France. As the heat signal caused by drifting charge carriers is heavily affected by the transport properties of electrons and holes in the HPGe crystal, we made use of a hot carrier transport simulation in order to characterize and optimize the detector performance.

2.6.4 Influence of heat-only background events

The actual limits for the WIMP-nucleon cross-section retrieved from EDELWEISS experiments are based on data which was taken between July 2014 and April 2015 (Run 308), including data from 24 FID800 detectors with a total exposure of 496 kg $\cdot$ days. The results from an extended likelihood and a Boost Decision Tree (BDT) analysis showed that especially in the low-mass WIMP search region, the experiment is limited by heat-only events [21, 99].

The name heat-only events follows from the fact that they show a clear temperature rise in the NTD Ge thermistors, whereas no signal above the baseline fluctuations is measured in any of the 4 ionization channels. Although the actual origin of these events is not known so far and studies are on-going, several explanations have been suggested. Heat-only events caused by particle interactions in the NTD Ge thermistors can be excluded. The FID800 detectors are equipped with two NTD Ge thermistors placed on the top and bottom surface of the detector. If an interaction in one of the NDT Ge thermistors occurs, the other NTD Ge thermistor would show a much smaller signal. The asymmetry of the heat amplitudes can then be used to identify such events. As heat-only events survive the so-called asymmetry cut [100], they can not originate from NTD Ge thermistor-only events. Actually, EDELWEISS assumes that the heat-only events do not origin from actual particle interactions. This is reinforced by the observation that in Run 308 the heat-only event rate was nearly constant and showed no correlation between the detectors. The most favored explanation for this type of events is that they originate from the glue, which connects the NTD Ge thermistor with the HPGe crystal. Therefore studies are on-going to produce deported NTD Ge thermistors, which are already implemented in the electrode design and need no gluing.

As heat-only events eventually limit the low-mass WIMP search in EDELWEISS-III, we also performed a study of heat-only events within this thesis. Our approach was very practical. Although we also could not clarify the nature of these events, we made use of our high sampling frequency for the heat channel (20 kHz), which allowed us to record the pulse-shapes of the heat signals. A pulse-shape analysis showed that heat-only events differ in shape from regular events producing e^-/h^+-pairs. The pulse-shape analysis enabled us to reject about 96 % of the heat-only events (see sec. 6.5.3). However, in the actual EDELWEISS set-up a pulse-shape analysis is not possible, as the heat signals are stored with an effective sampling frequency of 500 Hz, which is not sufficient to resolve the heat pulse-shapes.

3. Hot carrier transport in germanium

The EDELWEISS dark matter detectors consist of High Purity Germanium (HPGe) crystals, which are operated at cryogenic temperatures. If operated at low electric fields, typically around 2 V/cm, the detectors allow to discriminate electron recoils, caused by γ- and β-background radiation, from nuclear recoils, expected from WIMP dark matter candidates, by the hybrid detection of ionization and heat signals, as the amount of ionization per recoil energy is higher for electron recoils than for nuclear recoils. Mandatory for a good discrimination is a full measurement of the ionization and heat energy. As the ionization signal is caused by e^-/h^+-pairs, which are separated by the electric field and drift to a set of electrodes, a full measurement of the ionization energy is equivalent to the full collection of all electrons and holes at the electrodes. Therefore the charge migration processes in HPGe crystals, especially the processes which prevent full charge collection, have a huge impact on the detector performance and discrimination power of electron and nuclear recoils.

In addition, the charge migration processes are also relevant if the detectors are operated at high electric field, typically around 50 V/cm as planned in EDELWEISS for the search of low-mass WIMPs. In this case, the heat signals are dominated by secondary phonons which are produced by drifting charge carriers. Consequently, heat signals then also suffer from an incomplete charge collection.

As the main goal of this thesis was to optimize the detector performance in respect to charge migration processes and to evaluate limitations for the detector performance originating from charge migration processes, the following chapter describes the main properties of charge migration in HPGe crystals at cryogenic temperatures. We discuss the consequences of the crystalline structure for electron and hole transport in section 3.1, followed by a description of impurities in HPGe crystals in sec. 3.2. In section 3.3, we present the main features of electron and hole transport, like the transport anisotropy of electrons, scattering effects and most important trapping effects reducing the collection of ionization signals. The charge migration properties in HPGe crystals described here, are selected by their relevance for the EDELWEISS detectors. All effects have been studied in special measurements.

In the second part of this chapter (sec. 3.4), a simulation tool for charge migration in the EDELWEISS detectors is presented. It is based on the charge migration properties discussed before. This tool allows one to simulate ionization and heat signals. It was used in the framework of this thesis to study charge migration processes by comparing simulations with experimental data.

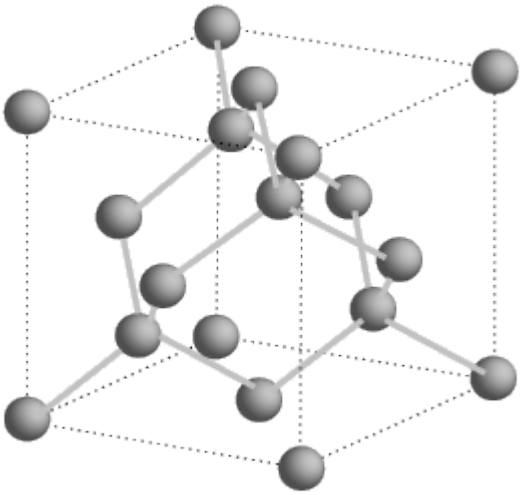

Figure 3.1: Unity cell of germanium, the atomes are shown as *greyish* spheres. The crystal has Diamond structure: Face center cubic with two base atoms (0,0,0) and (1/4,1/4,1/4). Figure adapted from [101].

3.1 Consequences of the crystalline structure

Germanium is a crystalline solid and is determined by the repetitive arrangement of its atoms. The smallest cubic unit in the crystal is the unit cell. In germanium it contains 8 atoms with a basis that is described by two atoms at the Cartesian coordinates (0,0,0) and (1/4,1/4,1/4) (see fig. 3.1). By repeating the unit cell many times along all three dimensions, it forms the crystal.

The periodic structure determines the allowed energy ranges for electrons in a crystals and is described by the band structure. The band structure for germanium is shown in fig. 3.2. The y-axis represents the electron energies and the x-axis the electron wave vectors. Generally, the electron wave vectors are expressed in terms of characteristic directions in the Brillouin zone[1]. For our purpose the important directions in the Brillouin zone are:

1. [100]-direction: This direction is parallel to the z-axis of the Brillouin zone and describes the orientation of the electric field in the EDELWEISS detectors. The X-point is the boundary point of the Brillouin zone in [100]-direction.

2. Γ-point: Center point of the Brillouin zone.

3. [111]-direction: The L-point is the boundary point of the Brillouin zone in [111]-direction. For Ge it describes the position of the conduction band mimima.

In germanium at zero temperatures, all states up to the maximum of the valence band are occupied by electrons, and the conduction band which is separated from the valence band by an energy gap $E_g = 0.67\,\mathrm{eV}$ is empty. This also holds for the temperatures at which the Ge detectors of the EDELWEISS experiment are operated which is typically at $T \approx 20\,\mathrm{mK}$. Germanium is a so-called semiconductor, as the energy gap is small and at

[1]The Brillouin zone is the unit cell of the reciprocal space, which is a concept to allow a reconstruction of crystal structures from spectroscopic measurements, e.g. with X-rays or neutrons.

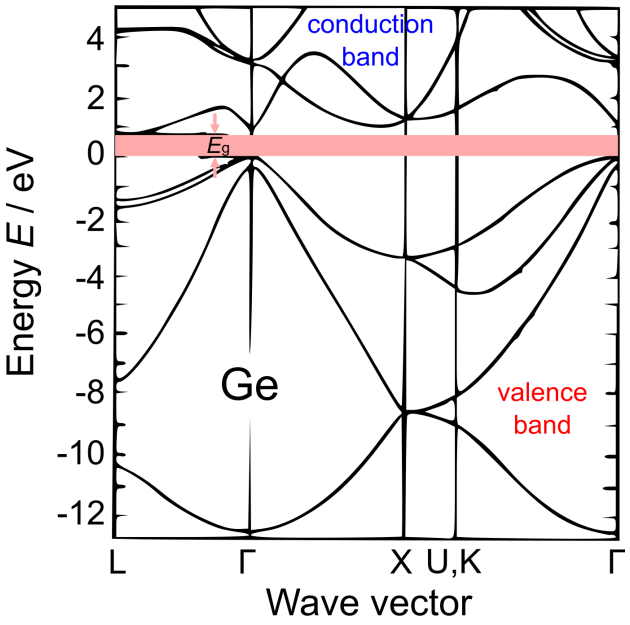

Figure 3.2: Energy band structure of Germanium. Germanium is an semiconductor with an indirect band gap of $E_g = 0.67\,\text{eV}$ at $T = 20\,\text{mK}$. The L wave vector is pointing in [111]-direction of the crystal. Figure adapted from [102].

room temperatures the thermal energy in the crystal is high enough that some electrons overcome the energy gap and contribute to the electric conductivity.In contrast to Ge, metals with high conductivity, typically 1000 times higher than semiconductors, have even at zero temperature partially filled energy bands, so that unoccupied energy states are easily reachable. In comparison to that the energy gaps of insulators are so large, typically above 5 eV , that even at room temperature the conductivity is close to zero.

Another characteristic property of a semiconductor is, that in case an electron is excited into the conduction band and contributes to the electrical conductivity, an empty state in the valence band is created, which is defined as hole and also contributes to the conductivity. Therefore, in case conductive charge carriers are produced in Ge, we talk of electron hole pair creation. Germanium is an indirect-gap semiconductor, which means the smallest gap between valence and conduction band is not vertical in $\boldsymbol{k}$-space (see fig. 3.2). In order to create an e^-/h^+-pair with minimal energy, in addition to the energy E_g to overcome the energy gap, the momentum $\boldsymbol{k}_g$ is necessary to transfer the electron from the valence band maximum at the Γ-point to the conduction band minimum at the L-point. As a consequence, the production of an e^-/h^+-pair by the absorption of a photon is only possible, if the momentum is provided by a phonon[2]. This follows from the conditions for energy and momentum conservation,

$$\hbar\omega_\gamma \pm \hbar\omega_q = E_g \quad and \quad \hbar\boldsymbol{k}_\gamma \pm \hbar\boldsymbol{q} = \boldsymbol{k}_g \quad , \tag{3.1}$$

where $\hbar\omega_\gamma$ is the photon energy, $\boldsymbol{k}_\gamma$ the photon momentum, $\hbar\omega_q$ the phonon energy, $\boldsymbol{q}$ the phonon momentum. As $\hbar\omega_q \ll E_g$ and $|k_\gamma| \ll |\boldsymbol{k}_g|$, the photon provides the energy for

[2]Phonons are quasi particles which describe the collective excitations in a crystal caused by the oscillation of the individual crystal atoms. For an introduction to solid state physics and semiconductor physics see e.g. [101], [103], [104]

the electron hole creation and the phonon provides the momentum. Actually, the phonon assisted photon absorption is not effective at cryogenic temperatures, as the energy and momentum of thermal phonons is very small according to the operation temperature.

In case the germanium crystals are used to measure an energy deposit via the number of created e^-/h^+-pairs, it is important to know the threshold for e^-/h^+-pair production. It turns out that it is $\epsilon_{\mathrm{er}} = 3.0\,\mathrm{eV}$ for electron recoils (see sec. 2.1) and therefore larger than the band gap energy $E_{\mathrm{g}} = 0.67\,\mathrm{eV}$. The "missing" energy of 2.33 eV flows into the creation of phonons. This is caused by the high non-equilibrium process that leads to the creation of e^-/h^+ pairs and is not so well understood. An idea of the involved processes is given in [105]. If we assume the primary interaction being caused by a γ-ray, this interacts with the electrons of the Ge atoms in the crystal, creating a primary free electron with a high kinetic energy. This electron interacts with the crystal and produces e^-/h^+-pairs via impact ionization, which involves the production of mainly optical phonons[3]. The secondary e^-/h^+-pairs produce additional charge carriers and phonons until the kinetic energy falls below the threshold of impact ionization. The produced e^-/h^+-pairs then are still hot and thermalize by emitting additional phonons, until they reach the equilibrium, where electrons have energies according to the conduction band minimum and holes have energies according to the valence band maximum. Although the kinetics of e^-/h^+-pair production processes are complicated, they have a straightforward consequence. The e^-/h^+-pairs are not created at one defined location in the crystal but in a creation volume around the interaction point of the primary radiation. This is included in the simulation code for carrier transport used in this work: The creation volume is assumed to be spherical, with an energy dependent radius r_{cr} as

$$r_{\mathrm{cr}} = 10^{-4} \cdot \frac{0.064\,\mathrm{g/cm^3}}{\rho} \cdot E_{\mathrm{dep}}^{1.68} \quad , \tag{3.2}$$

where $\rho = 5.36\,\mathrm{g/cm^3}$ is the density of Ge and E_{dep}, the deposited energy. In the simulation code the exact locations of the produced e^-/h^+-pairs are chosen randomly, using the Monte Carlo method.

3.2 Character of impurities in the EDELWEISS germanium crystals

The EDELWEISS experiment uses High Purity Germanium (HPGe) crystals which have a very low impurity density $\rho_{\mathrm{imp}} \lesssim 10^{10}\,\mathrm{cm^{-3}}$. Although the impurity density is very low, at cryogenic temperatures impurities have a huge influence on charge migration processes like scattering and trapping (see sec. 3.3.2 and 3.3.4). Therefore, in this section, we will discuss the nature of the impurities in the EDELWEISS detectors.

[3]The unity cell of Ge contains two basis atoms. In case a lattice excitations leads to a coherent movement of the two basis atoms, the phonon is called acoustic, in case the atoms move out of phase, it is called optical. Typically, optical phonons have higher energies than acoustic phonons.

In general, we distinguish two types of semiconductors according to the type of the dopant impurities. The n-type semiconductors contain donors, which are atoms that have at least one additional valence electron in comparison to the crystal atoms. The additional valence electron remains unbound in the crystal, and is easily ionized, leading to an additional electron in the conduction band and a charged donor impurity D^+ in the crystal. For Ge atoms with four valence electrons, typical donor impurities in the crystal are from the group V in the periodic system, e.g. As or P. In addition, there are p-type semiconductors, which contain acceptors. Acceptors are impurity atoms with at least one valence electron less than the crystal atoms. Therefore acceptor impurities in the crystal have an open bound to the crystal atoms. Thus, they can easily bound an electron from crystal the valance band crystal creating a hole at the valence band maximum and a charged acceptor impurity A^-. Typical acceptor impurities in p-type Ge crystals are from the group III in the periodic system, e.g. B or Al. Eventually, if we refer to the impurity density in a crystal, we mean the net donor or net acceptor density with $N_\mathrm{d} - N_\mathrm{a} > 0$ for a p-type or $N_\mathrm{a} - N_\mathrm{d} > 0$ for a n-type semiconductor, where N_d is the donor density and N_a the acceptor density.

The binding energies of the extra electrons and holes of dopant atoms are typically in the meV range [106]. Thus, at room temperature the thermal energy is high enough that normally all dopant atoms are ionized. This kind of impurities are called *shallow-level* impurities as their energy levels are close to the minimum of the conduction band (donors) or close to the valence band maximum (acceptors). However, the EDELWEISS detectors are operated at mK temperatures. Therefore the thermal emission of bounded electrons is very unlikely, which means the dopant atoms are in a neutral state.

In addition to the shallow-level impurities, their are other types of impurities, like crystal defects, often occurring at the surface due to detector processing (see sec. 4.1.2), or *deep-level* impurities. Deep-level impurities have binding energies in the range of the band gap and are normally very localized. Examples for this kind of impurities are metal atoms like gold, zinc or cadmium. Typically, their concentration is in the order of $10^9\,\mathrm{cm}^{-3}$ and they play a minor role for doped semiconductors. However for HPGe crystals with net dopant densities in the order of $10^{10}\,\mathrm{cm}^3$ they can affect charge migration processes like scattering (see e.g. [107]).

3.3 Main features of charge transport in Ge crystals

The band structure of germanium presented in sec. 3.1 has important consequences for the drift of electrons and holes in an electric field and differs from the behavior of the migration of free charge carriers in vacuum. In vacuum, the acceleration $\boldsymbol{\Gamma}$ of a charge carrier is parallel to the electric field $\boldsymbol{E}$ with

$$\boldsymbol{\Gamma} = (1/m)(q\boldsymbol{E}) \quad , \tag{3.3}$$

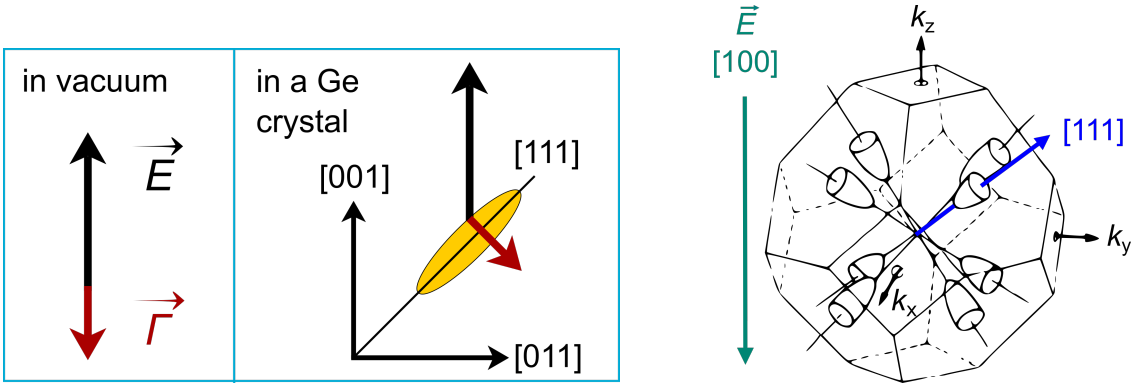

Figure 3.3: *Left:* Electron transport in an external electric field, in vacuum and in a germanium crystal. *Right:* First Brillouin zone of Ge. The surfaces of constant energies for electrons are located along the [111]-direction and have the shape of ellipsoids. The 8 L-points represent the conduction band mimima. The applied electric field in the Ge crystals of the EDELWEISS experiment points in [100]-direction as is marked by the *green* arrow.

	m^*_{l,e^-}	m^*_{t,e^-}	m^*_{heavy,h^+}	m^*_{light,h^+}
Germanium	1.64	0.082	0.28	0.044
Silicon	0.98	0.19	0.49	0.16

Table 3.1: Effective masses relative to the free electron masses. For electrons m^*_{l,e^-} and m^*_{t,e^-} mark the effective masses in transversal and longitudinal direction. For holes m^*_{heavy,h^+} and m^*_{light,h^+} are the effective masses of heavy and light holes. Data from [104].

where m is the mass of the free charge carrier and q the charge of the carrier. In a crystal the acceleration of electrons and holes is not necessarily parallel to the applied electric field as it is determined by the band structure. For a crystal the band structure is taken into account by replacing the free carrier mass m in eq. 3.3 with the effective mass

$$\left(\frac{1}{m^*}\right)_{ij} = \frac{1}{\hbar^2}\frac{\partial^2 E}{\partial k_i \partial k_j} \quad , \tag{3.4}$$

where $\partial^2 E/\partial k_\mathrm{i}\partial k_\mathrm{j}$ is the curvature of the energy band E in the $\boldsymbol{k}-$space (see fig. 3.2). It follows that the acceleration $\boldsymbol{\Gamma}$ actually becomes a tensor.

In the following the effects of band structure on the drift velocity for electrons (sec. 3.3.1) and holes (sec. 3.3.2) is discussed. Afterwards scattering (sec. 3.3.2) and trapping (sec. 3.3.4) effects, caused by the residual impurities in the crystal are presented.

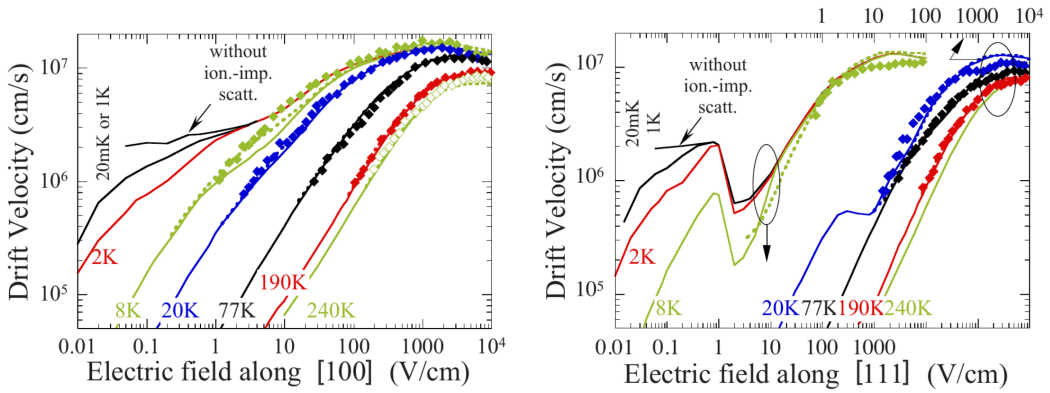

Figure 3.4: Electric field dependence of the drift velocity for electrons at different temperatures. *Left*: Field in [100]-, *Right*: Field in [111]-direction of the crystal. (Figure from [108]). Results from Monte Carlo simulation (*solid* lines), and experimental and theoretical results from [109] (symbols and *dashed* lines).

3.3.1 Transport anisotropy of electrons

In Ge crystals the surfaces of constant energy in k-space for the conduction bands are ellipsoids with major axis along the [111]-direction (see fig. 3.3 *right*). The surfaces of constant energy E can be expressed via

$$E = E_c + \hbar^2 \left[\frac{k_1^2 + k_2^2}{2m^*_{t,e^-}} + \frac{k_3^2}{2m^*_{l,e^-}} \right] \quad , \tag{3.5}$$

where E_c is the energy of the conduction band minimum. The k_1,k_2 and k_3 directions describe a Cartesian coordinate system with k_3 pointing in the [111]-direction of the crystal, and m^*_{l,e^-} and m^*_{t,e^-} are the effective masses in transversal and longitudinal direction. From the difference in the effective mass in transversal and longitudinal, it follows that the acceleration Γ for an electron in Ge crystal as well as it drift velocity depends on the direction of the electric field. Value for the effective masses are given in tab. 3.1. A comparison with silicon shows, that the difference of the effective masses in longitudinal and transversal direction is much larger in Ge crystal than in Si.

The results for simulations of the drift velocity for electric fields in [100]- and [111]-direction of an Ge crystal are presented in fig. 3.4. If we choose a low electric field of 2 V/cm and $T = 20$ mK, which is typical for an EDELWEISS detector, we see that the drift velocity in [100]-direction is about a factor 4 higher than for the [111]-direction. An additional property of electrons in Ge crystals manifests in the partial negative slope of th electric field dependency of the drift velocity in [111]-direction. The conduction band minima in [111]-direction split up in 4 so-called L-valleys[4], which are energetically equivalent (see fig. 3.3 *right*). It follows that an electron can be excited in any of these valleys. Therefore its drift velocity depends on the L-valley to which it belongs. In case an

[4]The four directions [111] are labeled: [111], [1$\bar{1}$1], [11$\bar{1}$] , [1$\bar{1}\bar{1}$]

electric field is applied in [100]-direction, excited electrons are uniformly distributed in all 4 L-valleys and have the same drift velocities. However, the L-valleys are not parallel to the electric field but at an angle of 35 ° and electrons drift under this angle with respect to the field direction. In case an electric field is applied in [111]-direction, one L-valley is parallel to the electric field, whereas the other three point in transversal directions to the field. As the transversal effective mass m_{t,e^-} is much smaller than the longitudinal effective mass m_{t,e^-} (see tab. 3.1), electrons in the transversal L-valleys are accelerated stronger with increasing electric field as electrons in the longitudinal L-valley (see eq. 3.3) and gain more kinetic energy. This process can be interpreted as a heating and electrons occupy states with higher energies in the transversal L-valleys. At a certain electric field strength their energy is high enough to perform an intervalley transition from the so-called hot valleys to the cold valley by emitting phonons. The start of this transition marks the negative slope of the field dependence of the drift velocity. With further increasing electric fields, all electrons accumulate in the cold longitudinal L-valley and the drift velocity increases again with field (for more details see [108] or [109]).

By explaining the dip in the drift velocity for electric field in [111]-direction, we already mentioned another important process for electron propagation in Ge crystals, which is the intervalley transition of electrons from one L-valley to another. This process will be discussed in section 3.3.2.

In the framework of this thesis, we will use the phrasing electron transport anisotropy to describe the dependence of the drift velocity from the electric field direction as well as the drift of the electrons in an angle of 35 ° to an electric field in [100]-direction.

The electric field dependence of electron drift velocities in the EDELWEISS detectors was extracted from special measurements [110], where the electric field was applied in [100]-direction. The results of these measurement are presented in figure 3.6 and show no dependence of the drift velocity on the net dopant impurity density.

3.3.2 Intervalley scattering of electrons

In the last section we described that conduction electrons in Ge crystals at cryogenic temperatures belong to 4 L-valleys. Since the electric field in EDELWEISS is applied in [100]-direction, electrons drift in an angle of 35 ° with respect to the electric field. In addition, electrons can interact with impurities and phonons, which leads to scattering. Generally, we distinguish two types of scattering. In case of intravalley scattering the electrons are only slightly distracted from a straight path and they stay in the same L-valley before and after the interaction. This leads to a diffuse path of the electrons along the direction of the L-valley, to which the electrons belong. In case of intervalley scattering, the interaction causes a transition of an electron from one L-valley to another and its drift direction changes completely.

The measured transition rates for intervalley scattering for EDELWEISS detectors with different dopant impurity densities at $T = 20\,\mathrm{mK}$ are presented in figure 3.5. We see that,

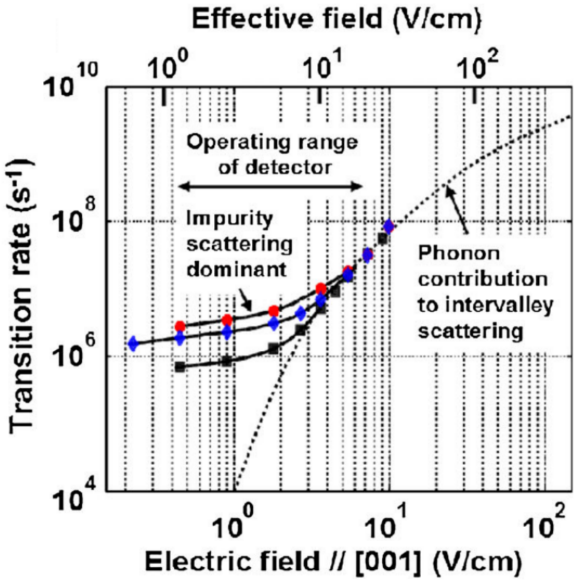

Figure 3.5: Intervalley transition rate versus applied electric field in [001]-direction for different EDElWEISS Germanium crystals (fig. from [111]). The *top* axis shows the effective field in the L-valleys. Experimental results for 3 different crystals are presented. *Red* circles: n-type with a net dopant density of $N_\mathrm{d} - N_\mathrm{a} \approx 10^{10}\,\mathrm{cm}^{-3}$, *Blue* diamonds: n-type with $N_\mathrm{d} - N_\mathrm{a} \approx 10^{11}\,\mathrm{cm}^{-3}$, *Black* squares: p-type with $N_\mathrm{a} - N_\mathrm{d} \approx 10^{10}\,\mathrm{cm}^{-3}$, $T = 20\,\mathrm{mK}$. The *dashed* line represents the expected contribution of phonons to the intervalley transition rate.

although the impurity concentration in HPGe crystals is very low ($\approx 10^{10}\,\mathrm{cm}^{-3}$), scattering by impurities has a significant effect at low temperatures and low electric fields. In addition we see, that the transition rates for fields $< 10\,\mathrm{V/cm}$ split up in three curves. Thus, the three detectors used for this measurements mainly differ in the net dopant density, we conclude that for low electric fields actually dopant impurities play the major role. At higher electric fields all three detectors show the same electric field dependence of the intervalley transition rate, which is consistent with phonon scattering. As the prototype detector used for this thesis was operated in an electric field range $E \in$ [1,50] V/cm, both contributions to the intervalley scattering rate, impurity and phonon scattering, are relevant.

The simulation code presented in this work includes both intravalley and intervalley scattering using a simplified approach. As intravalley scattering occurs on a time scale much smaller than intervalley scattering, both processes can be decoupled [112]. The actual diffuse path caused by intravalley scattering is not calculated. Instead the path is averaged by a discretization of the overall drift time in the ns-range. For every time step, the path of an electron in valley i is calculated as straight drift based on the field dependent drift velocity $v_\mathrm{i} = v_\mathrm{i}\,(E)$.

Intervalley transitions are treated as a random process, with a probability function based on the measurement of the transition rate depending on the electric field and presented in fig. 3.5. The decision whether an intervalley occurs is made after every discretized time step using the Monte Carlo method. In case no transition occurs for an electron, its probability for a transition will be increased after the next time step.

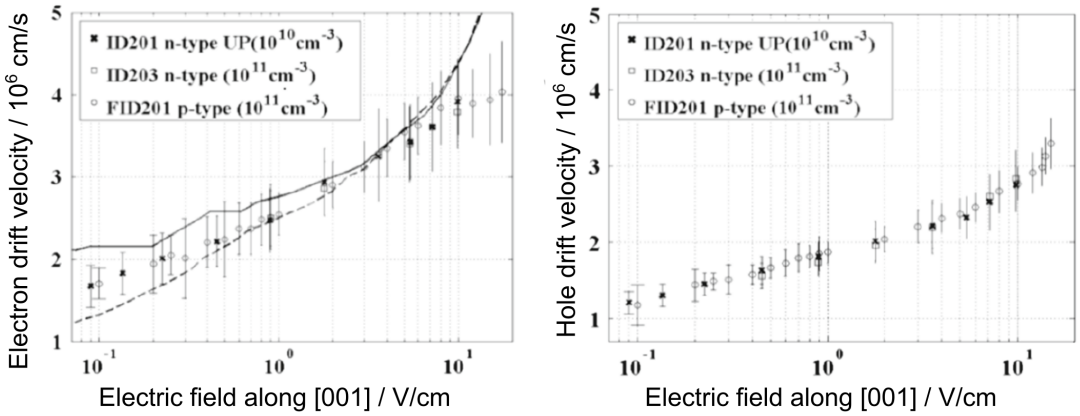

Figure 3.6: Measured drift velocities in projection along the [001]-direction, for *left* electrons and *right* holes, $T = 20\,\mathrm{mK}$. The three different measurements belong to three different detectors with different dopant densities (for more details see [110]).

3.3.3 Hole transport properties

As shown in figure 3.2 two valence bands converge in one maximum at the Brillouin zone center (Γ-point) and are called heavy and light hole band. The curvature of the heavy hole band is flatter (see eq. 3.4) than the light hole band and therefore has the higher effective mass (see tab. 3.1). At the Γ-point the heavy holes tend to dominate the hole propagation properties as the density of states per unity energy and volume is proportional to the effective mass. Actually, the number of light holes is only around 4% in comparison to the heavy holes (for more details see e.g. [113]). For that reason only heavy holes were considered for this work.

Like for electrons, the drift velocity of holes depends on the direction of the electric field, although the variation of the drift velocity with electric field direction is much smaller [114]. For low electric fields, as used for standard operation of the EDELWEISS detectors, the anisotropy of the hole drift velocity is nearly zero. Thus, the surface of equal energies of the valence band maximum is described by a nearly perfect sphere. However, especially at low temperatures, the anisotropy of the hole drift velocity increases with the electric field. At $T = 8\,\mathrm{K}$ and $E = 50\,\mathrm{V/cm}$ the drift velocity was measured to be about a factor 1.3 higher for the [100]- than for the [111]-direction [115]. Therefore this anisotropy is particularly important for the operation of the detectors at high electrode bias, as will be presented in chapter 6.

The simulation tool used in this thesis, does not take the hole transport anisotropy into account. Therefore, in the simulation holes follow strictly the electric field lines as expected from the propagation of free electrons in vacuum. The field dependence of the hole drift velocity is taken into account according to the measurements presented in fig. 3.6 *right*. Also no scattering processes leading to a diffuse path of holes along the electric field lines are included.

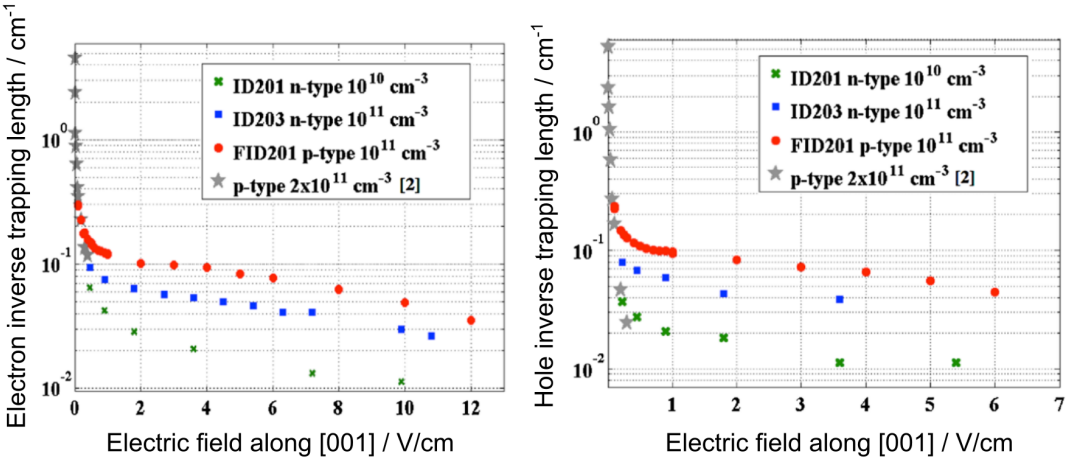

Figure 3.7: Measured electric field dependence of the trapping length in projection along the [100]-direction, for *left* electrons and *right* holes, $T = 20\,\mathrm{mK}$ [110]. The three different measurements were performed with the same three detectors as presented in fig. 3.5.

3.3.4 Bulk and surface trapping of electrons and holes

Interactions in the HPGe crystals of the EDELWEISS experiment lead to the creation of electron and hole pairs, which are separated by an electric field and collected as ionization signal at a set of electrodes. If the ionization signals are fully collected, they allow a reconstruction of the primary energy deposit. Effects that prevent a full measurement of the ionization energy are trapping and recombination and will be discussed in this section.

As electrons and holes propagate through a Ge crystal, they can be captured by localized states caused by impurities. Thus, they do not contribute to the ionization signal anymore. The captured carrier can be released after some time into crystal, in which case the capture center is called a trap. However the relaxation time of the trapped carrier is much longer than the collection time of an ionization signal and often the trapped charges are not released at all during normal operation times of the detector. In addition, a second carrier with opposite charge can be captured at the same localized state, in which case the pair annihilates, and the capture center is called a recombination center.

In this work, we will always refer to trapping, meaning both trapping and recombination, as the result is the same, a reduced ionization signal. In general, we distinguish between bulk and surface trapping, as the nature of impurities which cause the localized states are different in the two regions.

Bulk trapping

In section 3.2 we already discussed that the dominant population of impurities is equivalent to the dopant density. The fact that these dopant atoms act as trapping centers is confirmed by measurements of the field-dependent inverse trapping length for electrons and holes. In

figure 3.7 we see that the mean free path of electrons and holes depends on the net doping density of the crystal. It is longest for the crystal with the smallest net dopant density of $10^{10}\,\mathrm{cm}^{-3}$ (ID201).

We also discussed in sec. 3.2 that donor and acceptor atoms are in a neutral state, as the crystals are operated at low temperature, where intrinsic free charge carriers are. It follows that the trapping center are in a neutral state. Studies of charge trapping in the EDELWEISS Ge crystals have shown, that actually electrons are captured by acceptor atoms via $\mathrm{A}^0 + e^- \rightarrow \mathrm{A}^-$ and holes by donor atoms via $\mathrm{D}^0 + h^+ \rightarrow \mathrm{D}^+$ [110]. In addition, trapping leads to charged dopant atoms in the crystal and causes space-charge build-up. The space-charge alters the internal electric field in the crystal and also reduces the charge collection efficiency. In order to minimize the effect of charged trapping centers, a reset process is applied to the detector on a regular basis. Therefore the electrodes are grounded and the crystal is irradiated with γ-radiation. The produced e^-/h^+-pairs then drift to the charged trapping centers and neutralize them. A detailed description of the reset process is given in section 4.5.

In the simulation code for hot carrier transport used in this thesis, bulk trapping is treated as a random process, with a probability function based on the measurement of the electric field-dependent trapping length presented in fig. 3.7. If a charge carrier is trapped, it is removed from the simulated event. The net charge the trapped carrier induced on all electrodes is kept, whereas the charge-build up caused by the charged impurity atom is not taken into account. The crystal atoms are assumed to be always in an uncharged state.

Surface trapping

The main difference between bulk and surface trapping is, that the density of trapping centers at the surface is much higher than in the bulk region. In addition to the dopant impurities in the bulk region, at the surface, point defects, surface states, dangling bonds, and also localized mechanical stresses can act as trapping centers. Since the surfaces of the EDELWEISS detectors are polished and etched in order to reduce leakage currents, mechanical stresses and scratches are favored at the surface, as well as at small penetration depths in the order of μm. A detailed explanation of the surface treatment of the EDELWEISS detectors is found in sec. 4.1.2. A detailed description of surface effects for high purity Germanium crystals can be found in [116] or [117].

Additional losses of charge carriers at the surface can occur during the production process of e^-/h^+-pairs. In sec. 3.1 we explained that e^-/h^+-pairs created in a single energy deposit are created in a finite volume, which we approximated by a sphere. If we assume an interaction of 10 keV, the creation volume would have a radius of 600 nm. If this interaction takes place at a distance to the surface smaller than this radius, parts of the created charge carriers are produced either directly in the electrodes or in the amorphous Ge layer which covers the surface[5]. In both cases the charge carriers do not contribute to the

[5]The amorphous Ge layer is used for passivation. Open bonds of crystal atoms at the surface are closed

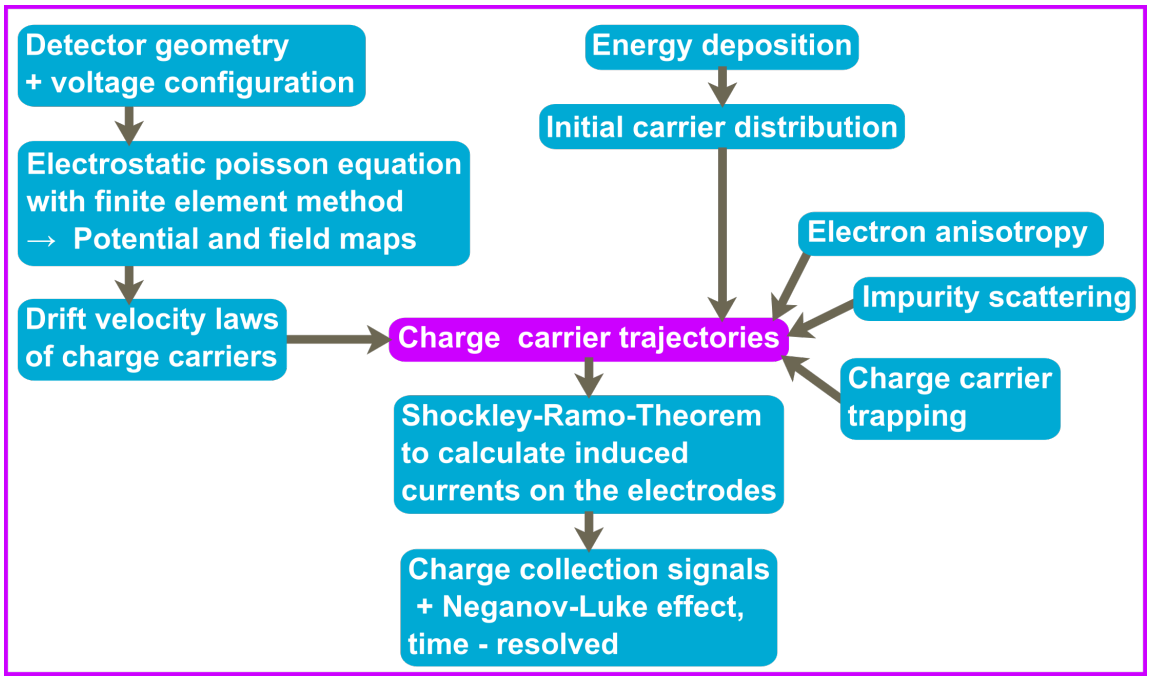

Figure 3.8: Structure of the simulation tool developed to describe the hot carrier transport in the EDELWEISS detectors.

ionization signal. For more details on the charge collection efficiency of the EDELWEISS detectors see e.g. [118].

The enhanced trapping at the surfaces, motivated the EDELWEISS collaboration to develop an interleaved electrode design which allows the discrimination of energy deposits in the surface region (see sec. 2.2).

The charge migration tool used in this thesis includes surface trapping in a simplified way. A charge carrier reaching the surface in areas uncovered by electrodes is treated as trapped. The carrier is removed from the simulation, while the net charge it induced on all electrodes is taken into account. Analog to bulk trapping, space-charge build-up based on charged trapping centers is not considered.

3.4 Modeling hot carrier transport in germanium

Figure 3.8 shows the structure of the Monte Carlo simulation tool for hot carrier transport in germanium used in this work. The MC package is a stand alone program based on Matlab [119] and was developed to describe charge migration in the EDELWEISS detectors [120]. Actually this tool is reviewed and adjusted to results from charge migration experiments within EDELWEISS on a regular basis. Especially within this work, we found that at high electric fields the holes transport anisotropy has a measurable effect on the

by atoms in the amorphous layer.

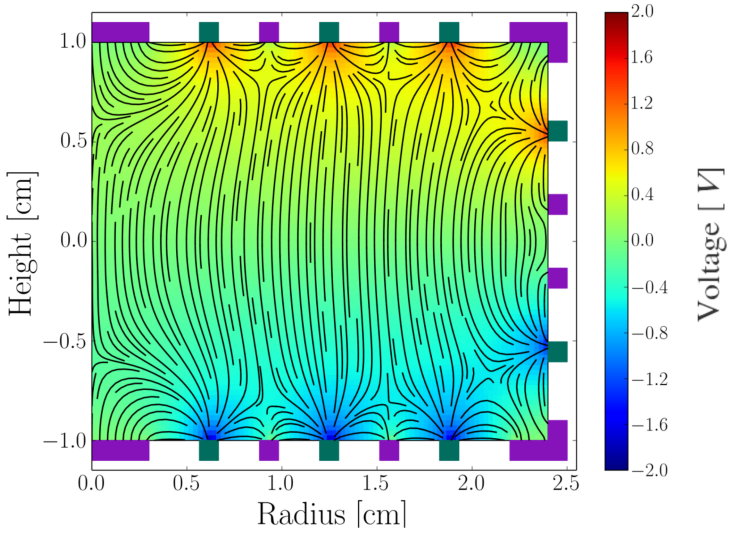

Figure 3.9: Results from electric field and potential simulations. The geometry of the detector is chosen according to the prototype detector. The electrodes are fully interleaved and the cylindric detector has a radius $r = 2.4\,\mathrm{cm}$ and a height $h = 2.0\,\mathrm{cm}$. As the detector is cylindric, it has rotational symmetry and a two-dimensional simulation with $r \geq 0\,\mathrm{cm}$ describes the whole set-up.

detector performance (see sec. 6.7.2). Therefore an implementation of the hole transport anisotropy is planned for the next version of the hot carrier transport tool.

The different parts of the simulation package are explained in this section. The software needs as input the actual geometry of the detector and the voltages that are applied to the electrodes. These informations allow a calculation of the electric potentials and electric fields in the germanium crystal. The calculation is based on the finite element method and is presented in sec. 3.4.1. The electric field maps are used to determine drift velocities, intervalley transition rates and trapping lengths of the charge carrier at every point in the crystal according the measurements presented in the last section. In addition, the maps of the electric potential of the individual electrodes, the so-called weighting potentials, allow to calculate the induced charges for each electrode by using the Shockley-Ramo theorem (sec. 3.4.2). An introduction to the calculation of the motion of the charge carriers is given in sec. 3.4.3. Examples for trajectories and ionization signals are presented in sec. 3.4.5. Eventually, the simulation calculates the heat signals based on the Neganov-Trofimov-Luke effect which is explained in sec. 3.4.6. In order to be able to compare the simulated ionization signal with experimental data, the locations of simulated energy deposits in the crystal have to agree with expectations from the experimental set-up. Since experimental results from a calibration experiment with an ^{241}Am are presented in this thesis, we simulated energy deposits according to this source. Details are explained in section 3.4.7.

3.4.1 Calculation of the electric field

The results for electric potentials and electric fields in our prototype detector are shown in figure 3.9. The EDELWEISS detectors have a cylindrical shape, and therefore a two-dimensional field map describes the complete set-up. The calculation was performe using the Partial Differential Equation Toolbox [121] of Matlab, which is based on the finite element method.

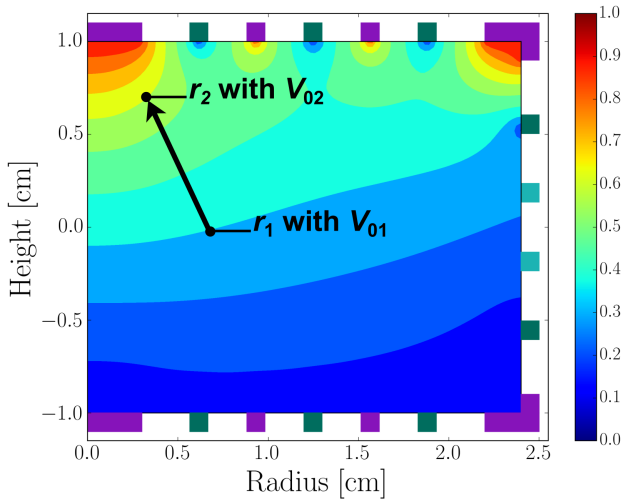

Figure 3.10: Illustration of the calculation of induced charge on an electrode with the Shockley-Ramo theorem. The induced charge on electrode A (*violet* rectangles for $h > 0\,\mathrm{cm}$) for a charge carrier q, moving from r_1 to r_2, is $\Delta Q_\mathrm{A} = -q\,(V_{01} - V_{02})$, where V_{01} and V_{02} are the potentials at the two positions. The color bar on the right represents the weighting potential, ranging from 0 to 1.

The prototype detector has the same fully interleaved electrode design (FID) as the EDELWEISS detectors installed in the Modane underground laboratory (see sec. 2.2). Ring electrodes cover all surfaces of the crystal and are interconnected leading to 4 types of electrodes. The electrode biasing was chosen similar to the configuration which is used for the standard WIMP search mode in EDELWEISS. This means that two electrodes are used as a veto to allow rejection of surface events and the electric field is kept in a low electric field range ($\approx 1\,\mathrm{V/cm}$). In figure 3.9 the *violet* rectangles on the upper half of the detector at heights $h > 0\,\mathrm{cm}$ are schematic for the top veto electrodes with a voltage $V_\mathrm{a} = 0.0\,\mathrm{V}$, the ones on the lower half at heights $h < 0\,\mathrm{cm}$ are the bottom veto electrodes with $V_\mathrm{c} = 0.0\,\mathrm{V}$. The *green* rectangles on the upper half represent the top collecting electrodes and were biased with $V_\mathrm{b} = +2.0\,\mathrm{V}$, the ones on the lower half are the so-called bottom collecting electrodes with $V_\mathrm{d} = -2.0\,\mathrm{V}$. This prototype detector is smaller than the FID800 detectors and has a radius $r = 2.4\,\mathrm{cm}$ and height $h = 2.0\,\mathrm{cm}$. In order to provide an adequate description of the experiment, the copper casing of the detector at ground potential was included in the finite element simulation. As the outer copper box is grounded, it affects the electric field lines at the surface of the detector. Only the electric field lines inside the crystal are shown in figure 3.9.

3.4.2 Application of the Shockley-Ramo theorem

The Shockley-Ramo theorem [122, 123] allows a straight forward way to calculate the induced Q on an electrode created by a moving charge q. Originally it was developed for the case of a charge carrier moving in a vacuum tube, but it can be extended to semiconductor detectors [124].

Two two basic equations connect the induced charge Q and the current I on an electrode by a moving point charge q with the weighting potential V_0 and the weighting field $\boldsymbol{E}_0$ via

$$Q = -qV_0(\boldsymbol{r}) \quad \text{and} \quad I = q\boldsymbol{v}\boldsymbol{E}_0(\boldsymbol{r}) \quad , \tag{3.6}$$

where $\boldsymbol{v}$ is the drift velocity of the charge at position $\boldsymbol{r}$. The weighting potential and the weighting field are calculated independently for every read-out electrode. As the prototype detector has 4 electrodes, we had to determine 4 weighting potential maps. The weighting potential and field of a specific electrode is calculated by simulating the electric fields and potential for a case where the potential of this electrode is set to a unit potential of 1 and all other electrodes are set to a potential of 0.

Figure 3.10 shows the weighting potential for the A electrode (*violet* rectangles in the upper half) of the detector. When a charge carrier moves from the position r_1 to r_2 and the weighting potential changes from V_{01} to V_{02}, the induced charge on electrode A is $\Delta Q_\mathrm{A} = -q\,(V_{01} - V_{02})$ (see eq. 3.6). In addition, the weighting potential map shows that the induced charge on an electrode is larger the smaller the distance between drifting charge carrier and electrode is. It also becomes clear that a moving charge carrier induces charge on all electrodes, regardless whether a charge carrier is collected at this electrode or not. The difference between electrodes that collect charges and electrodes which do not is, that the net amplitude of the ionization signal is only non-zero for electrodes which finally collect charges. Not that this statement only holds if no trapping occurs. In case a charge carrier is trapped, a net ionization signal remains even on electrodes which are not collecting any charge. The net ionization amplitude then again depends on the distance to the electrode in which the trapped carrier was drifted. In order to calculate the induced charge signal for a moving charge carrier, firstly one has to calculate the path of the carrier, which is then described by the positions r_1 to r_n, where n is the number of steps necessary for a carrier to reach the electrode or to be trapped. Secondly, the induced charge on an electrode is calculated for every step via

$$Q_{n+1} = -q\,(V_0(\boldsymbol{r}_{\mathrm{n}+1}) - V_0(\boldsymbol{r}_\mathrm{n})) \quad . \tag{3.7}$$

As the steps are discretized in propagation time for the charge carriers (see sec. 3.4.3), the induced electrode signal can be expressed in dependence of time. We see that the Shockley-Ramo theorem is a very powerful tool that solves the problem of a moving charge in an electric field by simplifying it to electrostatics at each path position of the charge carrier. A good overview, including some examples for the application, can be found in [125].

3.4.3 Extraction of the motion of electrons and holes

In the following an overview of the part of the simulation is given which processes the motion of electrons and holes. Details can be found in [126]. Initially the start positions of the e^-/h^+-pairs are chosen by randomly picking a position in a creation volume defined by eq. 3.2 around the location of the primary energy deposit. As no Coulomb interactions between the charge carriers are taken into account, every charge carrier is propagated independently. The carrier motion is discretized, and during one step the drift velocity

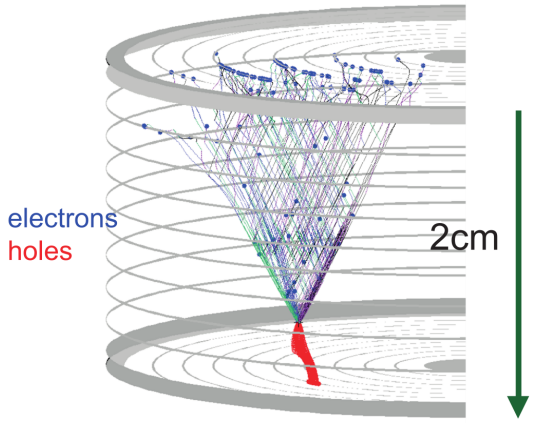

Figure 3.11: Example of simulated trajectories of electrons and holes in a fully interleaved EDELWEISS detector. The *gray* rings on top, bottom and lateral surface represent the detector electrodes. *Blue, green, violet, gray* lines represent the electron trajectories. The *blue* dots mark the locations of intervalley transitions. *Red* lines represent the hole trajectories. The *green* arrow points in the direction of the electric field ([100]-direction).

of the carrier is assumed to be constant. The typical time for one step is $\Delta t = 5\,\mathrm{ns}$, however the time intervals can be shortened if the drift velocity changes more than a certain threshold between two steps. Before and after every step, the positions of the charge carriers, the simulated time, the electric fields and the drift velocities are determined, as well as the induced charges on all electrodes according to eq. 3.7. In addition, the Monte Carlo method is used to decide whether an electron undergoes an intervalley transition or a charge carrier is trapped. If no transition or no trapping occurs, the probability for intervalley transition and trapping after the next step increases and is taken into account by the simulation. The simulation stops if at the end of a step, the carrier is located at an electrode or at the surface. Technically the simulation stops when the charge carriers are located within 200 nm distance from electrodes or surfaces. After the simulation is stopped, carrier paths, timing, induced charge signals, as well as the heat signal[6] and positions, where charges were trapped, are stored. This allows to reconstruct the time-resolved ionization signals.

Actually the simulation does not simulate each created charge carrier, as the number of computations would be huge. As we saw before, the energy needed to create an e^-/h^+-pair is 3 eV. Therefore, an energy deposit of 60 keV leads to the creation of 20000 e^-/h^+-pairs which would need a lot of computation time. Hence, charge carriers are treated as charge packages with a total charge of $q_{\mathrm{pack}} = N_{\mathrm{ca}}q$, where N_{ca} is the number of charge carriers per package. A typical number of packages created which has shown to be sufficient to describe the carrier motion in the crystal properly, is $N_{\mathrm{pack}} = 100$. It follows that for a 60 keV energy deposit one charge package typically contains $N_{\mathrm{ca}} = 200$ electrons or holes.

3.4.4 Trajectories of electrons and holes

Figure 3.11 shows an example of trajectories of electrons and holes in a FID EDELWEISS prototype detector. The charge carriers were created in an interaction in the bulk region of

[6] The heat signal is simulated according to the Neganov-Trofimov-Luke formula presented in eq. 2.4. No simulation of phonons is performed.

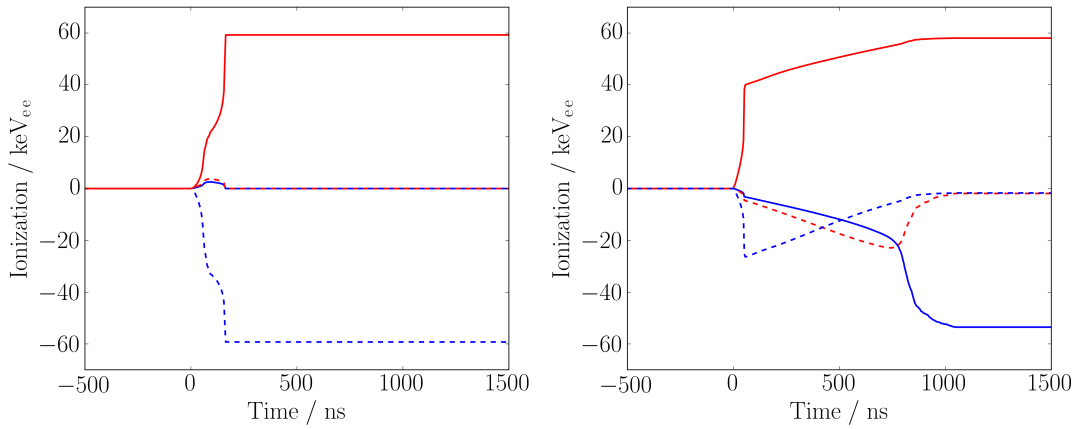

Figure 3.12: Simulated time-resolved ionization signals for the four interleaved electrodes A,B,C,D for the prototype detector used in this work. Voltage configuration on the electrodes was $V_A = V_C = 0\,V$ and $V_B = -V_D = +2.0\,V$. *Left:* surface event located at the bottom of the detector; *right:* bulk event. *Solid red* line: bottom collecting electrode D, *solid blue* line: top collecting electrode B, *dashed red* line: top veto (A), *dashed blue* line: bottom veto electrode (C). Further explanation see text.

the detector, where the electric field lines are parallel to the z-axis of the cylindric detector. We clearly see the effect of the electron transport anisotropy, as the electron trajectories approximately lay on the surface of a cone with an opening angle of $2 \cdot 35°$. The electron trajectories are marked by 4 different colors which represent the 4 different L-valleys of the conduction band. The actual color of a trajectory contains the information to which L-valley the electron belongs. Intervalley transitions of electrons are marked by the *blue* dots and, as discussed in sec. 3.3.2, they cause an instantaneous change of drift direction for the scattered electron. In this example, the transport anisotropy of electrons, as well as intervalley transitions, cause a collection of the signals on 6 ring electrodes. We stress, however that these 6 rings belong to one electrode, which is here the top collecting electrode named B throughout this thesis (see fig. 4.1). In comparison to the electron trajectories, the hole trajectories are straightforward (*red* lines) and they follow the electric field lines. Therefore holes are collected on one electrode ring which belongs to the bottom collecting electrode D.

3.4.5 Time-resolved ionization signal

In this section, we discuss the development in time of ionization signals on the four electrodes A,B,C,D, resulting from the charge migration simulation used in this thesis. We focus on two examples based on two energy deposit with a primary energy of 59.5 keV but at different locations in the cylindric detector. The voltage configuration at the electrodes was the same for both examples with $V_A = V_C = 0\,V$ and $V_B = -V_D = +2.0\,V$. The electric field and potential map resulting from this configuration was already shown in fig. 3.9.

The first example event is a surface event, where the e^-/h^+-pairs were created by an interaction close to the bottom surface, at a radius $r = 0.88\,\text{cm}$ and a height $h = 0.85\,\text{cm}$. In this region the electric field lines are parallel to the surface and inter-connect the C and D electrodes (see fig. 3.9). Therefore holes are collected at the C and electrons at the D electrode (see fig. 3.12 *left*). As no charge carrier are collected at the A and B electrode, the net ionization signal is zero, although a small bump occurs, as electrons and holes induce charge while they are drifted.

The second exemplary event is a bulk event, where the e^-/h^+-pairs were created by an interaction in the bulk region, at a radius $r = 0.72\,\text{cm}$ and a height $h = 0.79\,\text{cm}$. As the electric field lines in this region are parallel to the z-axis of the crystal, electrons and holes are drifted to the collecting electrodes B and D on the opposite sides of the detector. The actual shapes of the ionization signals in the B and D channels are consistent with the positions where the e^-/h^+- pairs were created. As shown in fig. 3.12 *right*, the ionization signal in the D channel has a steep slope at the beginning. Therefore the charge carriers were created closer to the D electrode than to the B electrode, as the induced charge per drift length of the carrier is larger close to an electrode (see sec. 3.4.2). We clearly see that the ionization signal in the B channel is steeper at the end of the signal, when the electrons start to drift closer to the B electrode. The net ionization amplitudes for this bulk event, reveals also the effect of trapping: The net amplitude in the D channel is $59.5\,\text{keV}_\text{ee}$, as expected from the simulated energy deposit. In contrast to that the net amplitude in the B channel is reduced to $57\,\text{keV}_\text{ee}$ and in addition the induced signal on the A and C electrodes also show small net ionization amplitude of about $1\,\text{keV}_\text{ee}$, although no charge carriers were collected by these electrodes.

If we compare the timing of the two signals in fig. 3.12, we see that the ionization signals of surface events have a much faster collection time than bulk events. In this case the charge of the surface event is collected after around 50 ns, whereas the collection time of the bulk event is around $1\,\mu\text{s}$. There are two reason for this difference in collection time. Firstly, e^-/h^+-pairs created by a surface event have to migrate a much shorter distance than e^-/h^+-pairs created by the bulk events. Secondly the drift velocities for electrons and holes are field dependent (see sec. 3.6). At the surface the electric field is $\approx 12\,\text{V/cm}$, whereas it is only about $\approx 2\,\text{V/cm}$ in the bulk. Therefore the drift velocities of electrons and holes are about a factor 1.5 higher, when they are drifted along the surface electric field lines than along the bulk field lines. In section 2.2, it was described that the net amplitudes on the different sets of electrodes can be used for surface event rejection. From the timing of the pulses shown here, we clearly see that also the collection time of ionization signals depends on the event location. Therefore the collection time and shape of the ionization signals can also be a parameter for surface event discrimination. The potential of such a pulse-shape analysis will be described in chapter 5.

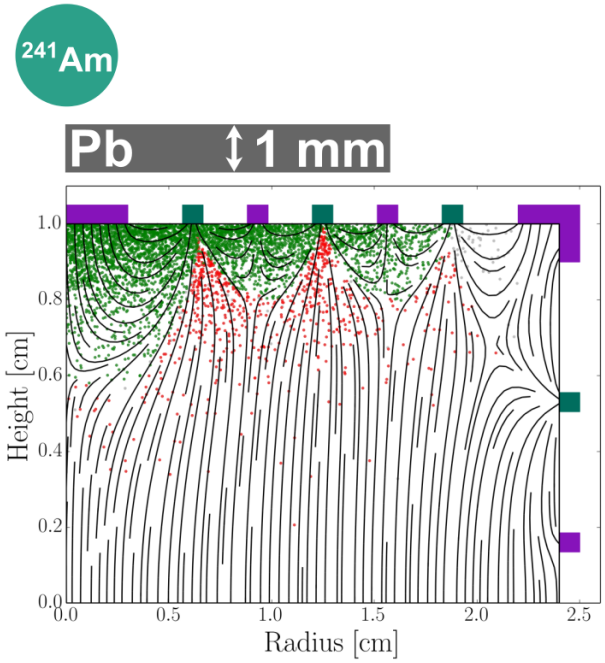

Figure 3.13: Schematic view of the experimental set-up with an ^{241}Am source with locations of energy deposits in the detector based Monte Carlo simulation. Field lines are shown for a voltage configuration with $V_A = V_C = 0\,V$ and $V_B = -V_D = +2.0\,V$. *Red:* bulk events, *green:* surface events. Details see text.

3.4.6 Heat signals extracted from charge migration simulations

As already mentioned, the simulation package presented in this chapter also allows to calculate the heat signals. Although it does not include any processes of phonon production and migration. It simply calculates the heat signal based on the Neganov-Trofimov-Luke formula (see eq. 2.4). Especially at high electric fields, the heat signals are dominated by the phonon signals originating from drifting electron hole pairs. Therefore the measurement of the heat signals is actually a measurement of the ionization energies, and charge migration processes affect the heat signals. Therefore a study of heat signals at high electric field is equivalent with a study of charge migration processes in HPGe crystals.

3.4.7 Modeling of γ-ray interactions

The analysis presented in this thesis is based on the comparison of simulations with experimental data. Thus, we had to implement the experimental set-up in our simulation tool. In figure 3.13 the schematic set-up is shown. Above the center electrode of the detector a ^{241}Am source was placed. Between source and crystal surface a lead layer with 1 mm thickness was placed in order to reduce the interaction rate in the detector to a level of 1 event/s. In addition, the lead layer nearly blocks all radiation of the ^{241}Am source, despite the 59.5 keV γ-rays.

The energy deposits caused by the ^{241}Am were simulated using simplified Monte Carlo method based on the following assumption[7]:

[7] Energy deposits can be modeled using simulation tools like GEANT4, which allow full tracking. However for our analysis the simplified model is sufficient.

- The ^{241}Am source is assumed to be point-like emitting 59.5 keV γ-rays isotropically. This assumption is justified, as radiation with smaller energy, is anyway blocked by the Pb layer.
- Only single energy deposits are allowed in the Pb layer and in the Ge crystal. As photoelectric absorption is dominant for γ-rays with energies below 100 keV (90 % [127] of all interactions), Compton scattering leading to multiple interaction can be neglected in a first approximation.
- The γ-rays can be stopped in the lead layer with a probability defined by the penetration depth of 59.5 keV γ-rays in lead which is $\lambda_{\mathrm{Pb}} \approx 0.18\,\mathrm{mm}$. If they are stopped, they are removed from the simulation.
- The locations of the γ-ray interaction in the Ge crystal are determined by using the penetration depth[8] of 59.5 keV γ-rays in Ge which is $\lambda_{\mathrm{Ge}} \approx 1\,\mathrm{mm}$.

As the energy deposits caused by the ^{241}Am are mainly located in the near surface region, we show only the upper half of the detector in figure 3.13. The simulated event locations are marked by *green* and *red* dots. The events where grouped in surface and bulk events according to the net ionization amplitudes on the 4 sets of electrodes:

- Surface event (*green* dots): $|\mathrm{A}| > 0.5\,\mathrm{keV_{ee}} \vee |\mathrm{C}| > 0.5\,\mathrm{keV_{ee}}$
- Bulk event (*red* dots): $|\mathrm{A}| < 0.5\,\mathrm{keV_{ee}} \wedge |\mathrm{C}| < 0.5\,\mathrm{keV_{ee}}$

In addition the electric field lines are shown which demonstrate nicely the connection between the shape of the electric field lines and the event categories. For bulk events the electric field lines connect top and bottom collecting electrode and for surface events the field lines connect veto and collecting electrode.

[8] The values for the penetration depths of 59.5 keV γ-rays in Pb and Ge are taken from [128].

4. Calibration experiment with a HPGe prototype detector

The aim of this thesis was to analyse charge migration processes in the High Purity Germanium (HPGe) crystals of the EDELWEISS experiment. We especially focused on time-resolved measurements of ionization signals and voltage-assisted heat detection with bias fields up to 50 V/cm. As both operations modes were not yet studied in detail for the EDELWEISS detectors in the Modane underground laboratory, we performed a calibration experiment with a HPGe prototype detector in a ground experiment at the *Centre de Sciences Nucléaires et de Sciences de la Matière* (CSNSM) in Orsay, France.

We mainly used an ^{241}Am calibration source which was shielded with a 1 mm lead layer. The lead layer was installed to reduce the event rate in the detector and to avoid pile-up pulses. The lead layer had the additional effect that almost exclusively 59.5 keV γ-rays could pass it, providing us with an almost monoenergetic source. In addition, energy deposits from 59.5 keV γ-rays are high enough to be detectable in the ionization and heat channels. Furthermore, the energy deposits occur in the surface region as well as in the bulk region which enabled us to study events originating from different regions of the detector.

The experimental set-up is shown in fig. 4.1 and the different parts are explained in this chapter. In sec. 4.1, we start with a description of the prototype HPGe detectors and it interleaved ring electrode design which is very similar to the FID800 EDELWEISS design. One of our main goals was to operate the detector at high electrode biases, which made a special surface treatment mandatory in order to avoid leakage current between neighboring electrodes. As the detector was also used as bolometer, it had to be operated at cryogenic temperature which was reached with a ^{3}He/^{4}He-dilution refrigerator (see sec. 4.2). The electronic read out circuits for the ionization channels and the heat channel, which measures the heat energy as temperature rise with a NTD Ge thermistor, are presented in section 4.3. As ionization signals, especially originating from surface events, can have very short physical transition time, the band-width limit of the ionization channels had to be considered for a final comparison of simulation and data. For the calorimetric detection, the bias current for the NTD Ge thermistor had to be optimized in order to provide the best Signal-to-Noise Ratio (SNR). The calibration sources are presented in sec. 4.4. We mainly used the ^{241}Am source but for some measurements also ^{109}Cd sources were installed. In order to provide a good detector performance, the detector was reset on a regular basis with LEDs (see sec. 4.5).

Finally, examples for measured time-resolved signals are shown in sec. 4.6. This thesis covers two measurement periods with different focus. The first measurements were performed to evaluate time-resolved ionization signals, wherefore a window triggered data acquisition system with a typical sampling frequency of 100 MHz was used, which was necessary to resolve the transient time. The second measurement period focused on heat signals. As heat pulses are slower than the ionization signals with typical rise and decay

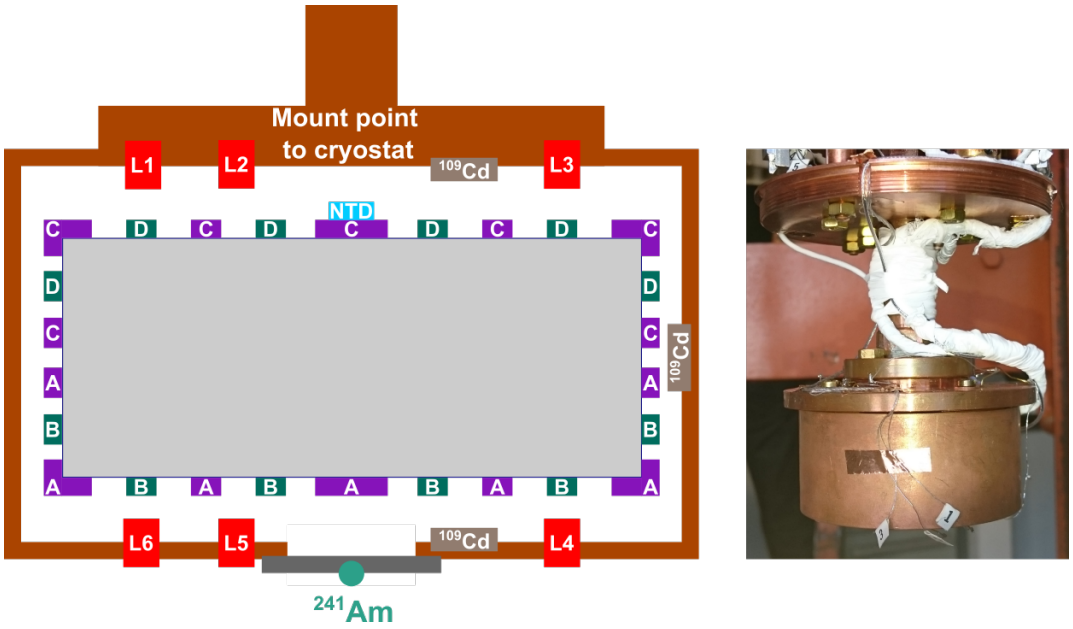

Figure 4.1: *Left:* Schematic of the detector set-up. The 4 types of electrodes are named A,B,C,D and can be biased separately. As the ^{241}Am calibration source, which we mainly used for the measurements presented in this work, faces the detector side covered by the A and B electrodes, we will refer throughout this work to the A and B electrodes as top electrodes. The detector is held in the copper casing by Teflon clamps, which are not shown here. In addition to the ^{241}Am source, partially three ^{109}Cd sources were installed. L1 to L6 refer to a set of LEDs, which were used for regeneration. The whole casing could be screwed to the experimental platform via a copper cylinder (*right*).

time in the ms-range, we used a data acquisition system with a lower sampling frequency of 20 kHz, which allowed us to store data continuously.

4.1 Electrode design and fabrication of a FID prototype detector

The HPGe prototype detector used in this work is smaller than the FID800 detectors used in the EDELWEISS-III phase (see chap. 2). It has a mass of 200 g and a cylindric shape with a radius of $r = 2.4$ cm and a height of $h = 2$ cm. However, the electrode design is very similar, and specific parameters are described in the following.

4.1.1 Fully Inter Digitized (FID) electrode design

As shown in figure 4.1 *left*, our FID200 prototype detector is surrounded by a copper casing, in which it is held by Teflon clamps. A copper cylinder on top of the casing, allows to screw the detector to the experimental platform of the cryostat (see fig. 4.1 *right*). The FID200 detector has the Fully Inter Digitized (FID) electrode design with ring electrodes covering top, bottom and lateral surfaces of the HPGe crystal (see fig. 4.2 *right*). The ring

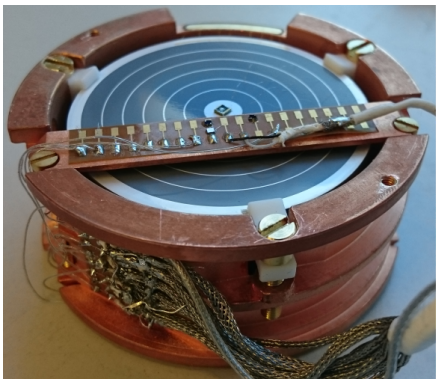
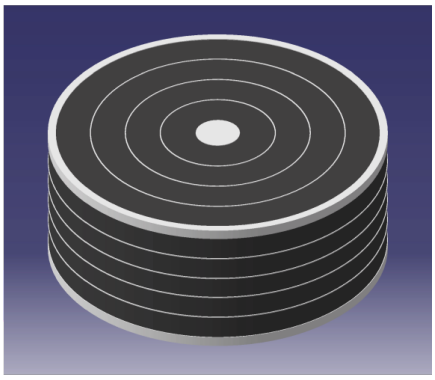

Figure 4.2: *Left:* Picture of the the FID200 prototype detector used in this thesis. The detector is hold in a copper casing by Teflon clamps. The NTD Ge thermistor is glued to the center C electrode ring. Ring electrodes and NTD Ge thermistor are connected via Aluminum bonds with the connector bridge to the cryostat. *Right:* Schematic of the FID electrode design (from [129]). For further details see text.

electrodes are made of aluminum and have a height of 200 nm. The typical width of a ring is $w = 150\,\mu$m, however the center and the corner electrodes are broader with a width in the order of 3 mm. The distance between the ring electrodes is $d \approx 5$ mm and therefore about a factor 2 larger than for the FID800 detectors. This change was made in order to avoid leakage currents in case the detector is operated at high electrode biases. Actually the FID200 detector could hold electrode biases up to $\Delta V = 100$ V (see sec. 6.4).

The ring electrodes form 4 types of electrodes A,B,C,D as shown in fig. 4.1 *left*, which can be biased individually. The ring electrodes of one type are connected by aluminum bonds and end at connector bridge to the cryostat as shown in fig. 4.2 *left*. This picture also shows the NTD Ge thermistor, which is used to measure the heat signal. It is glued to the center electrode of the C-type electrode.

4.1.2 Surface passivation and etching

As we wanted to use the FID200 prototype especially for calibration measurements at high electrode biases, we had to put attention to leakage currents. Particularly, neighboring ring electrodes are critical. Even small leakage currents can limit the detector performance as the inject noise in the ionization channels as well as in the heat channels. For leakage currents above typically 2 pA, we even observed a heating of or detector, which made operation impossible.

As mentioned in the last section, problems arising from leakage currents were already considered for the FID electrode design. The distances between the ring electrode of the FID200 detector are are larger than for the FID800 detectors. In addition, before the Al electrodes are evaporated, the surface is passivated with an amorphous Ge layer. However this passivation is mainly done to avoid open bonds of crystal atoms at the surface, which can act as trapping centers (see sec. 3.3.4). Effectively, some EDELWEISS detectors showed

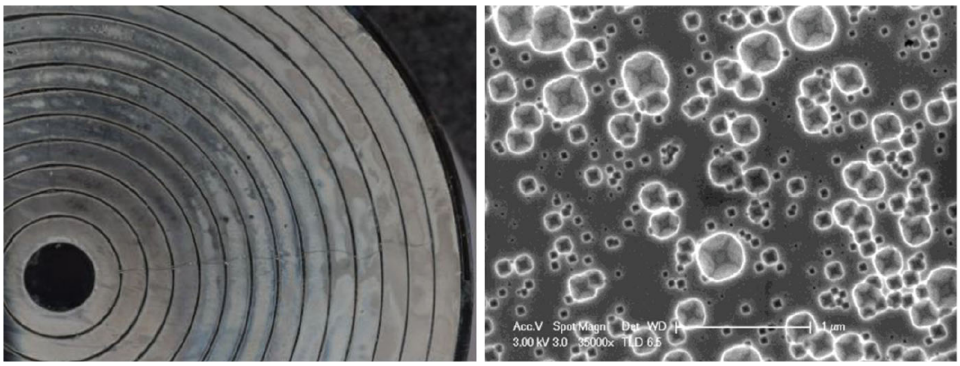

Figure 4.3: *Left:* Optical picture of the top surface of the presented FID prototype detector after XeF_2 dry etching. The surface is not shiny anymore. *Right:* Image of the germanium surface made with a scanning electron microscope. We mark the scratches and craters caused by the etching process. The scale is 1 μm. Pictures from [130] .

already significant leakage currents for electrode biases between two electrodes of 1 V [130]. Therefore the EDELWEISS collaboration developed a dry etching process with XeF_2, which was also applied to our FID200 detector. The complete detector, including the electrodes, is put in a vacuum and XeF_2 is injected in cycles. The main chemical reaction is

$$Ge + 2XeF_2 \rightarrow GeF_2 + 2Xe \quad , \tag{4.1}$$

where both products GeF_2 and 2Xe are in the gas phase and can be pumped out. By repeating the cycle the strength of the etching can be regulated. The limiting factor for this process is the thickness of the electrodes, as also aluminum is etched by $2XeF_2$, but the rate is much slower than for Ge. This technique has proved to be very sufficient for avoiding leakage current for the EDELWEISS detectors and 19 of 20 detectors dry etched with XeF_2 showed no leakage currents above 1 pA. In sec. 5.5, we show that dry etching also solved the problem of leakage currents in our detector.

However this etching technique reduces leakage currents, it is quite destructive. In figure 4.3 *left* an optical image of the surface of the FID200 detector after XeF_2 dry etching is shown and in comparison to our expectation of a shiny surface, the reflectivity is reduced. The image of the surface, made with a scanning electron microscope, (see fig. 4.3 *right*) reveals scratches and craters all over the surface. Some of the crater and scratches are quite large and may penetrate deeply in the crystal (mm-range). As they can act as trapping centers, they are very critical for the detector performance and their effect on charge migration processes is not known yet.

4.2 Dilution refrigerator

As already described in sec. 2.4, the temperature rise in a calorimeter caused by an energy deposit is inverse proportional to the heat capacity. As the heat capacity decreases with

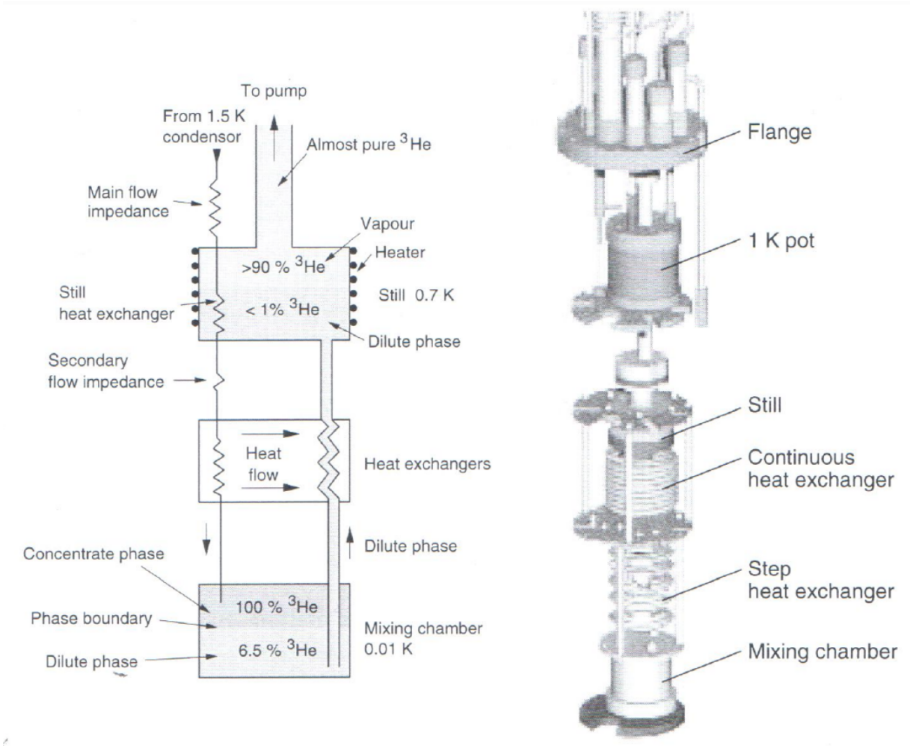

Figure 4.4: *Left:* Schematic of the inner part of a ^{3}He/^{4}He-dilution refrigerator. *Right:* Design of a commercial dilution refrigerator. Images from [70] and [131].

temperature, a low operation temperature in the mK-range is necessary to measure a significant temperature rise.

For our experiments, the former EDELWEISS-I cryostat [132], used for the WIMP search with a sapphire detector, was used. Currently, the base temperature of this cryostat is 21 mK, which allowed as a stable temperature regulation at $T = 23\,\mathrm{mK}$. The base temperature is actually expected to be lower, at least $T = 16\,\mathrm{mK}$, however loses of ^{3}Hedue to temporarily leaks in the ^{3}He/^{4}Hecircuit, have decreased the cooling power. The dilution refrigerator has to the advantage to be build on ultra radio pure materials and therefore provides a very low background radioactivity. As the cryostat is located in the ground laboratory at CSNSM in Orsay, France, it is not shielded against cosmic muons, which contribute to the background, especially at high energies (MeV-range). The cryostat is equipped anti shock system, significantly reducing the contribution of mechanical vibrations to the noise. In addition, the electric circuits are installed with great care to avoid noise from different electric masses.

The components and the working principle of a cryostat with a ^{3}He/^{4}He-dilution unit are explained in the following. The cryostat consists of several stages. The outer vessel contains liquid nitrogen, which cools the whole set-up to 77 K. It is followed by a liquid ^{4}Hecontainer, allowing a cool down to 4 K. By pumping the ^{4}He-liquid, the temperature can be further lowered to around 1.5 K. The most inner part contains the ^{3}He/^{4}He-dilution circuit and

can, depending on the specific performance, cool down the experimental platform to 5 mK. The minimal temperature reached with such a system was 1.75 mK [133].

A scheme of the the inner ^{3}He/^{4}He-circuit is shown in figure 4.4. The main parts contain the mixing chamber, where the minimal temperature is reached, the still and the counterflow heat exchanger. The whole cooling process is based on the property of ^{3}He/^{4}Hemixtures at $T = 0$ K to have two phases, which are separated by the so-called miscibility gap. There is the heavier phase, which consists of ^{4}He-liquid in which 6.5 % ^{3}He-liquid are dissolved. On top floats the lighter phase, which consists of pure ^{3}He-liquid. If the ^{3}Heconcentration in the mixed phase falls below 6.5 %, additional ^{3}He-liquid is dissolved from the pure ^{3}He-phase. This process has the same effect as a gas expanding in a vacuum (Joule-Thomson effect) and leads to cooling.

The cooling circle is driven by pumping on the still, which has a temperature around 0.7 K. As the vapor pressure of ^{3}Heis less than for ^{4}He, 90 % of the gas in the still consists of ^{3}Heatoms, whereas the liquid contains less than 1 % of liquid ^{3}He. The still is connected to the mixing chamber and pumping creates a concentration gradient for ^{3}Hebetween still and mixing chamber. As a consequence ^{3}Heis pumped to the still and reduces the ^{3}Hecontent in the mixed phase. Additional ^{3}He-liquid from the pure phase can then dissolve in the dilute phase and leads to a cooling effect. The almost pure ^{3}Hegas in the still is cleaned and then passed through a flow impedance so that it condenses. While flowing down to the mixing chamber, the liquid is pre-cooled by heat exchange with the still and the upcoming gas from the dilute phase. An important role is played by the heat exchanger. The down coming *warm* liquid flows in a pipe covered by a tube (continuous heat exchanger) with upcoming *cold* ^{3}Hefrom the dilute phase. In addition there are so called step heat exchanger with guarantee a high contact area between concentrated and dilute phase (see e.g. [134]).

4.3 Electronic set-up and noise spectrum

In the following a very brief introduction to the electronic circuits for ionization/charge and heat channels are given. For the ionization channel, we present the measurement of band-width, as this was necessary to compare rise time simulations with data (see sec. 5.2). For the heat channel, we show the results for the optimization of the NTD Ge thermistor bias current.

4.3.1 Charge measurement

The electronic read-out scheme for the charge signals is shown in figure 4.5. As preamplifiers field effect transitors (FETs)[1] are used. As the FETs were installed at the 4 K stage of the cryostat, we had to heat them via a heating resistance for around 1 min before operation. A re-coupling system is used to hold the detector at a constant bias. The connecting cables between the FETs at the 4 K stage to the outside of the cryostat are the critical parts of

[1] A detailed explanation and introduction to field effect transistors can be found in [136]

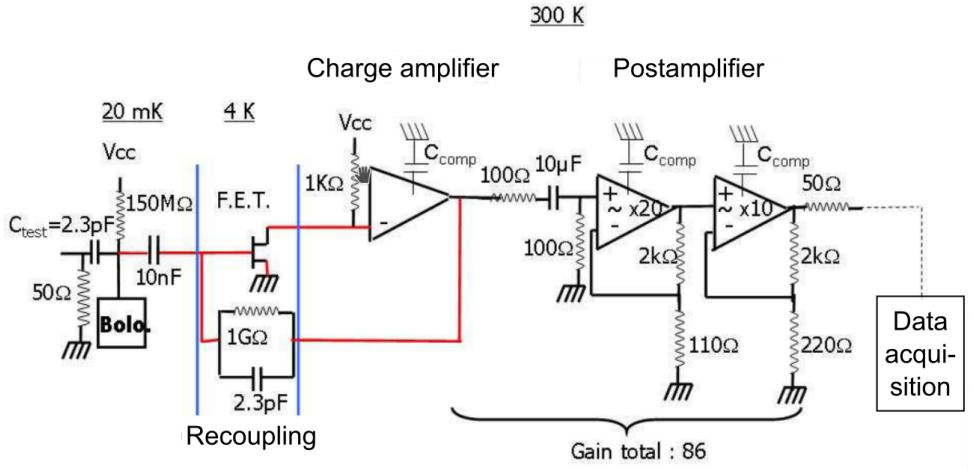

Figure 4.5: Schematic of the electronic read-out used for the charge signals, showing the different temperature stages of the cryostat. The detector is installed at the 20 mK stage, the Field Effect Transistors (FETs) follow at the 4 K stage. Charge amplifiers and post amplifiers are placed outside the cryostat at room temperature. Figure after [135] .

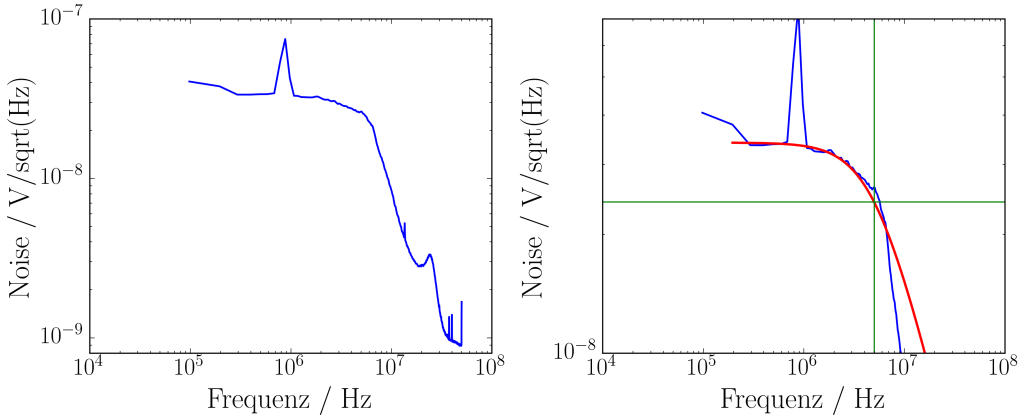

Figure 4.6: Noise spectrum for ionization channel B. *Left:* Overall spectrum based on the Fourier analysis of the part of the signals recorded before the transient region (see fig. 4.6.1). *Right:* Zoom in the region of the band-width limitation. In a first approximation the noise spectrum agrees with a first order Butterworth filter (*red* line) with a cut-off frequency of 5 MHz at −3 dB (*green* lines).

the experimental set-up, as no changes can be made while the cryostat is cooled down. Therefore they have to be treated very carefully. Post amplifiers are installed outside the cryostat before the signal is feed into a data acquisition system. The electrodes are biased by a battery source, which uses the cryostat as electric mass. The batteries are installed at room temperatures with cables going down to coldest stage of the cryostat, where the detector is installed.

The measured noise spectrum of the B ionization channel is shown in figure 4.6. Actually the noise spectra for the other channels look very similar. On the *left* the overall spectrum

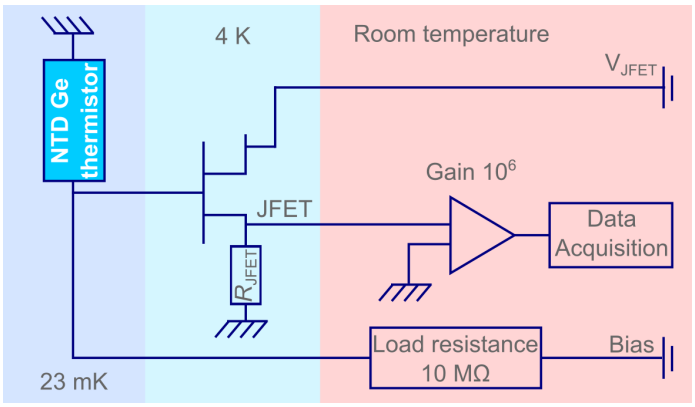

Figure 4.7: Schematic of the electronic read-out for the heat channel showing the different temperature stages of the cryostat.

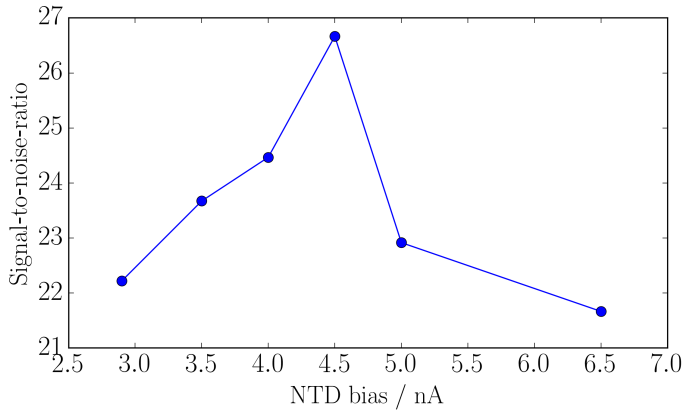

Figure 4.8: Measured Signal-to-Noise Ratio (SNR) versus NTD Ge thermistor bias I_{bias} at $T = 23\,\text{mK}$. The optimal bias with a maximal SNR was $I_{\text{bias}} = 4.5\,\text{nA}$.

is shown and on the *right* a zoom in the cut-off region. The shape as well as the position of the plateau is in good agreement with earlier measurements on the set-up [135]. In a first approximation the experimental noise spectrum follows the shape of a Butterworth low pass filter of first order. The *red line* is a fit to the experimental noise spectrum using a Butterworth filter with a cut-off frequency of 5 MHz. To know the band width of the experimental set-up is very crucial for this work. The aim of this work was to perform a pulse-shape analysis of the charge signals. In sec. 3.4.5, we saw that ionization signal from interaction close to the surface can have very short physical collection times in the order of 100 ns. In this case the band-width limitation of the experimental set-up will affect this signals. For the comparison of simulated ionization signals with experimental pulses, it is therefore important to take the band-width limitation into account. This is done by filtering simulated signals with the appropriate filter according to the measurement presented in figure 4.6. A detailed description of the electronics and the noise spectrum for experimental set-up can be found in [135]. In [93] the EDELWEISS electronics are described in detail.

4.3.2 Heat measurement

A schematic of the electronic set-up for the heat read-out is shown in figure 4.7. The NTD Ge thermistor is biased with a constant current, which is provided by a voltage source and a load resistance of 10 MOhm, which are both installed at room temperature. The JFET transistor is installed on the 4 K stage. This so-called DC biasing of the NTD Ge thermistor is different from the approach used for the EDELWEISS detectors in the Modane underground laboratory. The NTD Ge thermistors in EDELWEISS are biased with a square modulated current of 500 Hz. The advantage here is that the noise is not affected by this modulation and can be separated from the actual signals. For a detailed explanation see [93] and [98].

The sensitivity of the NTD Ge thermistor varies with the bias current and with the temperature of the device, as well as the read-out noise of the device. To determine the optimal operation parameters for the NTD Ge thermistor the Signal-to-Noise (SNR) in dependence of the applied current was measured for every operation temperature. The signal were generated by an LED with an absorption length of 1.67 μm, which is facing the center electrode of the top surface (see fig. 4.1). The LED is installed in-between the lead shield and the detector. As the detector was mainly operated at $T = 23$ mK, the sensitivity curve for this temperature is shown in figure 4.8. The optimal bias I_{bias} with maximal SNR at $T = 23$ mK was $I_{\text{bias}} = 4.5$ nA.

4.4 Calibration sources

The aim of this work was to study the prototype detector in the low energy regime $E_{\text{rec}} < 100\,\text{keV}_{\text{ee}}$. Therefore ^{241}Am and ^{109}Cd were used as calibration sources. The experimental set-up and the positions of the sources are shown in figure 4.1 *left*.

The ^{241}Am source is shielded by a 1 mm lead layer from the detector surface. This reduces the event in the detector to around 1 Bq and reduces the amount of pile-up pulses. ^{241}Am decays to 100 % via α-decay to ^{237}Np*. In 84.6 % of all cases the excited state of ^{237}Np* deexcites by emitting a 59.5 keV γ-ray. Their exists other deexcitation chains for ^{237}Np$*$, which lead to γ-rays with lower energy, but with decreasing energy the probability for absorption in the lead layer increases [137] and this γ-rays are absorbed before reaching the detector. The α particles, caused by the decay of ^{241}Am are as well shielded by the lead layer. For that reason ^{241}Am calibration source can be assumed to be mono energetic, producing nearly exclusively energy deposits of 59. keV in the detector. The 59.5 keV γ-rays can interact in Ge either via the photo electric effect and deposit there total amount of energy in one interactions (90 % of all interactions for γ-rays with an energy of 59.5 keV) or they interact more than once via the Compton effect (10 % of all interactions) [127]. The absorption depth for a 59.5 keV γ-ray in Ge is $\lambda_{\text{Ge}}(59.5\,\text{keV}) = 1$ mm [128]. Therefore the ^{241}Am source causes interactions in the surface and bulk region and allows to study events from different regions in the detector.

LED number	LED ref.	Wave length in μm	Aborption length
L1, L6	L7866	1.3 μm	$\approx 1\,\mu$m
L3, L4	L7850	1.45 μm	400 μm
L2, L5	L8245	1.65 μm	17 cm

Table 4.1: Wave length and absorption length for the different infrared LEDs used for regeneration. The LED number refers to position of the LED in the experimental set-up (see fig. 4.1). The LED reference numbers are the product numbers according to the company Hamamatsu. Data from [139].

For parts of the measurement three ^{109}Cd sources were installed facing the top, bottom an lateral surface (see fig. 4.1 *left*). The event rate for this sources was small in comparison to the ^{241}Am source (< 1 Bq), therefore pile-up events from this sources were not relevant. ^{109}Cd decays via electron capture: ^{109}Cd $\rightarrow^{109}$ Ag* $\rightarrow^{109}$ Ag. The excited ^{109}Ag* state is reached via $e^- + p \rightarrow n + \nu_e$ and a prompt X-ray with an energy of 22 keV or 25 keV is emitted [138]. The deexcitation of the ^{109}Ag$*$ releases γ-rays with an total energy of 88 keV, which can take different paths. In 4 % of the cases a single γ-ray with 88 keV is emitted. In the other cases the excitation energy is transfered to one of the electrons in the outer shells of the ^{109}Ag* atom and it is set free. This Auger electron has an energy according to the difference between the 88 keV excitation energy and the binding energy of the shell from which the electron is emitted. In 41 % of the cases the deexcitation of ^{109}Ag$*$ leads to an Auger electron with an energy of 62.5 keV originating from the K shell, in 45 % of the cases the Auger electron has an energy of 84 keV and originates from the L shell and in 10 % of the cases the Auger electron has an energy of 87 keV. The corresponding X-rays have energies of 25.5 keV, 4 keV or 1 keV. The sum of electron plus X-ray energy is always 88 keV. The absorption length of a 88 keV γ-ray in Ge is $\lambda_{\mathrm{Ge}}(88\,\mathrm{keV}) = 2.5$ mm [128].

4.5 Detector regeneration with infrared LEDs

A detector reset on a regular basis is important, as the detector performance degenerates over time. As described in sec. 3.3.4 electrons and holes can be trapped by neutral dopant impurities before they are collected by the electrodes. Besides a reduced ionization signal, this causes a charged impurity in the HPGe crystal. Therefore with operation time of the detector, more and more charged impurities occur and lead to space-charge build up and alters the electric field in the crystal. Clearly this reduces the charge collection efficiency and has to be avoided. An example for a measurement affected by degradation is discussed in sec. 5.5.

Therefore the detector is regenerated on a regular basis, typically after every measurement. All electrodes are shorted to ground and the detector is irradiated with infrared light from 6 LEDs (see tab. 4.1 and fig. 4.1 *left*). The photons emitted by the LEDs, produce e^-/h^+-pairs, which are then drifted in the electric field of the charged impurities and

neutralize them. The density of trapping centers varies for different detector regions and is especially high in the surface region. At the surface open bonds of Ge crystal atoms, as well as dislocations, e.g. scratches from the XeF_2-etching (see sec. 4.1.2), enhance the trapping center density in comparison to the bulk region, where only dopant impurities contribute. Therefore the used reset LEDs have different absorption lengths, especially allowing to efficiently neutralize space-charge build up in the surface region [139].

For the reset process the LEDs were operated one after the other. A function generator was used to generate LED pulses with an energy of $\approx 1\,\mathrm{MeV}$. This allowed a maximal repetition rate of $\approx 1\,\mathrm{ms}$. For higher rates the injected energy per time was so high that the detector heated up. The energy of the pulse was determined by the length of the pulse, typically in the range of a few hundred ns, and the applied voltage to the LED. During the reset the ionization signals on all channels were observed. If no significant ionization amplitudes was observed anymore the reset process was stooped. It typically took around 1 h to reach a sufficient space-charge cancellation. If before the reset, the detector was operated at high voltages, the reset took longer. The reset procedure was performed after every measurement. The longest periods without reset were overnight measurements, which lasted up to 12 h.

4.6 Data-acquisition of ionization and heat pulses

In this thesis two different analysis were performed. The first focused on pulse-shapes of the ionization signals and therefore required a high data sampling frequency in the MHz-range, as the transient times of the signals are in the 100 ns-range. The second part of this thesis focused on heat pulse and amplitude analysis at different electrode biases. Therefore a sampling frequency in the kHz was sufficient to reconstruct the signal amplitudes on all channels properly. The slower sampling frequency allows to resolve the shape of the heat pulses, which have rise and decay time in the ms-range. The data acquisition systems for the two parts and example pulses are shown in this section.

4.6.1 Window triggered data acquisition with MHz-sampling for time-resolved ionization measurements

The time-resolved charge signals were recorded with window triggered data acquisition system based on oscilloscopes and stored with a labview program. The oscilloscopes provide adequate sampling frequency of typical 100 MHz, which allowed to resolve the transient regions of the ionization signals. The time window for every ionization pulse consisted of 5000 points. Depending on the sampling frequency the points belonged to time intervals of 5 ns to 40 ns. In y-direction the oscilloscopes provided a 8 bit resolution. From that follow a discretization of the voltage amplitude of the charge signals in 256 points. The triggering was also done with the oscilloscopes. Standardly we triggered on ionization channel B. As electrode B is facing the ^{241}Am source (fig. 4.1 *left*)) most event take place close to this electrode. As channel B collects charge for surface event as well as for bulk events,

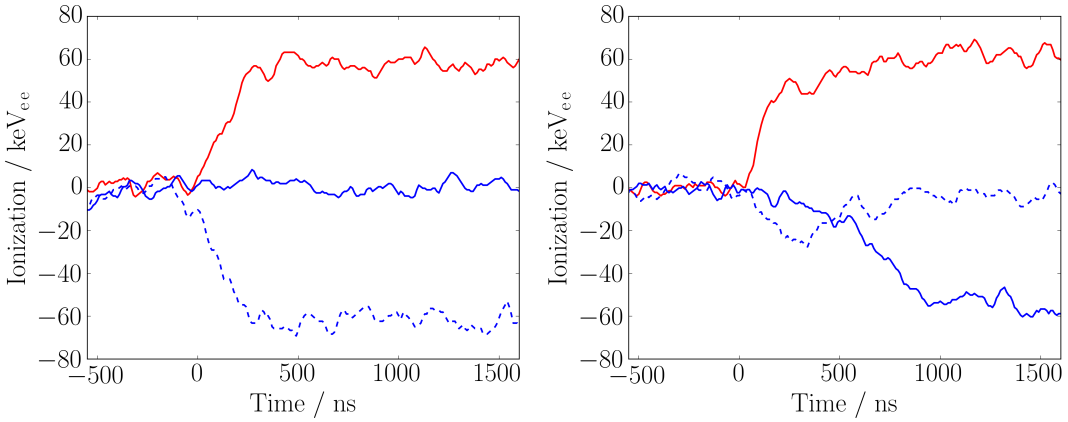

Figure 4.9: Time-resolved charge signals for 3 ionization channels: A (*dashed blue* line), B (*straight red*) line and D (*straight blue*) line. *Left:* surface event, *right:* bulk event. The voltage configuration was $V_A = V_C = 0\,V$ and $V_B = V_D = -2.0\,V$.

by triggering on channel B the maximal number of events is recorded in comparison to triggering on one of the other ionization channels. Triggering on heat was not reasonable here, as the heat signals were much slower than the ionization signals.

The time-resolved ionization signals recorded by channel A,B and D for two exemplary events are shown in figure 4.9. The time step was 10 ns and the detector was operated in a veto mode with $V_A = V_C = 0\,V$ and $V_B = V_D = -2.0\,V$. The ionization signals shown in the*left* graphic were caused by a surface event. e^-/h^+-pairs were drifted to the A and B electrodes, manifesting in a non-zero net amplitude in the A and B channels and zero net amplitude in the D channel. The ionization signals shown in the*right* graphic were caused by a bulk event. e^-/h^+-pairs were drifted to the B and D electrodes, manifesting in a non-zero net amplitude in the B and D channels. The net amplitude in the A channel is zero, although the induced signal by drifting electrons and holes showed up (see sec. 3.4.2).

In fig. 4.9 we see, that the ionization signals have a plateau before and after the transient region. As the transient regions of the pulses were adjusted to be in the center of every triggered time window (around point 2500), the net ionization amplitudes could be straightforward calculated from the difference of the mean value of the amplitudes of the first 2000 points and the last 2000 points. Actually the ionization signals relax exponentially but this did not show up as the relaxation times were much larger in size as the triggered time window.

The next chapter 5 will present the results of a pulse-shape analysis of ionization signals, with the rise time being the parameter of interest. The rise time was defined as the time between 10 % and 90 % of the net amplitude signal in every channel. It is obvious that a rise time can only be determined when the net signal amplitude is large than the amplitudes of the baseline fluctuations and therefore depends on the resolution in the ionization channels. Rise time extraction are typically possible for ionization amplitudes larger than 50 keV$_{ee}$ [96].

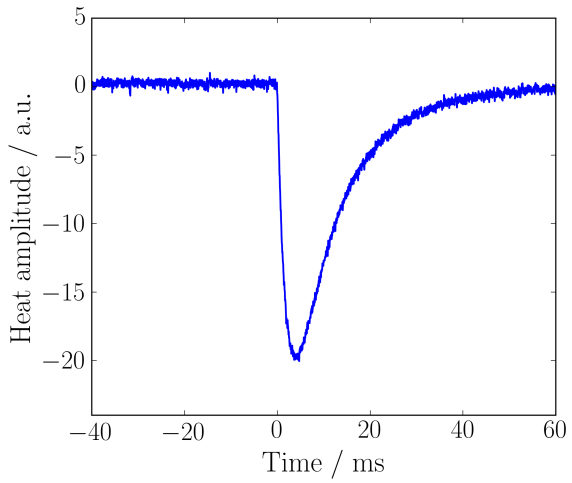

Figure 4.10: Uncalibrated time-resolved heat signal. The pulse originates from a 59.5 keV energy deposit of a γ-ray emitted by the ^{241}Am source. The detector was operated in planar mode with electrode biases $V_A = V_B = -V_C = -V_D = -50\,V$.

For the the time-resolved measurement of the ionization signals, the veto electrodes were always grounded to the cryostat mass. This was necessary as a strong leakage current occurred in case the C electrode was biased. In addition, the ionization channel C electrode appeared to be unconnected after cool down, so no data could be recorded for this channel. As the ^{241}Am source is facing the side with the A and B electrodes (see fig. 4.1), only few events would cause a net signal on the C veto electrode and therefore the missing channel was not crucial for our rise time study.

4.6.2 Continuous data acquisition with kHz-sampling at high electrode biases

The second part of this thesis was dedicated to the study of the performance of our prototype detector at high electrodes biases. In this case, we used a data acquisition system, which allowed us to take data continuously (data streaming). The sampling frequency was 20 kHz for all channels, which means the time intervals for the pulses was 50 μs. This frequency is obviously not high enough to resolve the transient regions of the ionization signals but sufficient to extract their amplitudes. For the heat pulses the 20 kHz sampling is high enough to resolve their pulse-shapes and also the transient regions. The advantages of the continuous data taking are that data accumulation is fast and triggering can be performed afterwards with different conditions. The most interesting trigger for this kind of experiments is the heat channel, as especially for high voltages trigger levels as small as 200 eV_{ee} were possible. In addition, triggering on heat provides the most complete data set, as the trigger includes all events independently at which combination of electrodes it was collected and also allows to study heat-only events with not signals in any ionization channels.

In figure 4.10 an example heat pulse is shown. It was recorded for an operation of the detector at high electrode biases, with the aim aim to study the Neganov-Trofimov-Luke (NTL) effect. The time scale is larger than for the charge signals. For our detector the rise time of the heat signal is in the order of 10 ms and much shorter than the ionization

signals with rise times between 100 ns and 1 μs. The rise time of the heat signals depends on the thermalization processes in the detector and the NTD Ge thermistor (see sec. 2.4). A study of the heat signals and a dedicated heat model for the EDELWEISS detectors can be found in [69]. The decay time of the heat signal depends on the coupling to the thermal bath. In this experiment gold wires were used for the connection and the decay time was around 20 ms.

5. Pulse-shape analysis of charge signals

The detectors of the direct dark matter search experiment EDELWEISS consist of High Purity Germanium (HPGe) crystals operated at cryogenic temperatures ($< 20\,\mathrm{mK}$) and typically at low electric fields ($< 2\,\mathrm{V/cm}$). A WIMP candidate is expected to elastically scatter with a crystal Ge-nucleus and the created nuclear recoil is measured simultaneously as heat and ionization signal. At low electric fields the heat energy H is proportional to the recoil energy E_{rec} and the ionization signal depends on the recoil type. Therefore, the ionization yield $Q = E_{\mathrm{ion}}/E_{\mathrm{rec}}$ can be used to discriminate nuclear recoils and electron recoils, which are created by γ- and β-background radiation. Clearly, this method depends on a full measurement of the ionization and heat energies. As especially in the near-surface region of the detector, the ionization signal, which is proportional to the number of electron/hole pairs created by the recoil, can be reduced by trapping effects and can lead to a misinterpretation of the recoil type, a rejection of surface events is crucial. Therefore, the EDELWEISS detectors have a special ring electrode design which allows the discrimination of surface events by an independent measurement of the ionization amplitudes on different sets of electrodes.

Clearly, the discrimination power of electron and nuclear recoils is strongly influenced by the charge collection efficiency in the HPGe crystals. For the collection efficiency, surface and bulk trapping, intervalley scattering and the drift velocities of electrons and holes play the main role. As these properties determine the time dependence of the ionization signals, pulse-shape analysis can be used to study charge migration processes in the HPGe crystal. Especially the rise time of ionization signals is a good parameter to study the quality of the detector performance and can even be used to discriminate surface events.

In this chapter, we present results of a study of electron and hole migration in the HPGe crystals of the EDELWEISS experiment. Furthermore we analyze the potential of a surface event discrimination based on ionization rise time. We make use of the comparison of hot carrier transport simulations with data measured with an EDELWEISS-type detector.In sec. 5.1, we describe the set-up for simulation and experiment, followed by a discussion on the optimal way to extract the rise times of the ionization signals in sec. 5.2. The results for the rise time distributions from simulations are discussed in sec. 5.3, as the connection between rise time and event location is straightforward in this case. Also the potential of a discrimination of surface events by using the rise times is presented in this section, allowing to reject 95 % of the surface events. Afterwards, the simulated rise times are compared with results from the experiment (sec. 5.4). We show that the rise time distributions for simulation and experiment are in very good agreement. Thus, we can conclude that charge migration processes included in the simulation tool for hot carrier transport in HPGe crystals provide an adequate description of charge transport in the EDELWEISS detectors. In addition, we show that a cut on the experimental rise times is as sufficient for surface events rejection as expected from simulation.

In section 5.5, we show that the rise time of the ionization signal is a more sensitive parameter for detector degradation and space-charge build-up than the ionization amplitudes. In addition, we show that leakage currents limit the detector performance at higher biases and explain that leakage currents can be significantly reduced by a dry etching with XeF_2.

Finally, in sec. 5.6 we present results for a rise time analysis of data taken with a FID800 prototype detector equipped with a Fast Ionization Channel (FIC) card, installed in the EDELWEISS-III experiment at the underground laboratory in Modane.

5.1 Description of the experimental set-up and Monte Carlo modeling of γ-ray interactions

The experiment was set up like presented in chapter 4 and a schematic is shown in figure 4.1. For the measurement discussed in the following the ^{109}Cd sources were not installed. Therefore the interactions in the detector are mainly caused by 59.5 keV γ-rays from the ^{241}Am source, allowing to study energy deposits in the surface and bulk region. The used detector was dry etched with XeF_2 and the 4 interleaved electrodes are structured as shown in figure 4.2. For data acquisition the window triggered acquisition system was used, where the trigger was set on the B channel with a threshold of around 20 keV (see sec. 4.6.1).

The Monte Carlo modeling of the γ-ray interactions was performed according to the description in sec. 3.4.7. As explained there, the energy deposits in the crystal are assumed to be single energy deposits and no Compton scattering in the crystal or in other parts of the set-up is taken into account.

Two voltage configurations were studied within this thesis. The first configuration was a low electric field configuration with $V_A = V_C = 0\,V$ and $V_B = V_D = -2.0\,V$. As the γ-rays emitted by the ^{241}Am source interact close to the surface which is covered with the A and B electrodes, the charge signals of bulk events are dominated by the charge migration of electrons drifting through the whole crystal to the D electrode. The second configuration was a high electric field configuration with $V_A = V_C = 0\,V$ and $V_B = V_D = +50.0\,V$. For the same reason as before, in this case charge collection for bulk events is determined by holes. Both configurations are called veto mode as the voltages on the A and C electrodes (veto electrodes) are lower than the voltages on the B and D electrodes (collecting electrodes).

5.2 Extraction of rise time from charge signals

The aim of our pulse-shape analysis of charge signals was to connect the rise time of a signal with the locations of an energy deposit and determine a discrimination of surface and bulk events based on a rise time cut. Actually, event locations are only directly accessible for simulations. Therefore, the discrimination of locations of energy deposits from

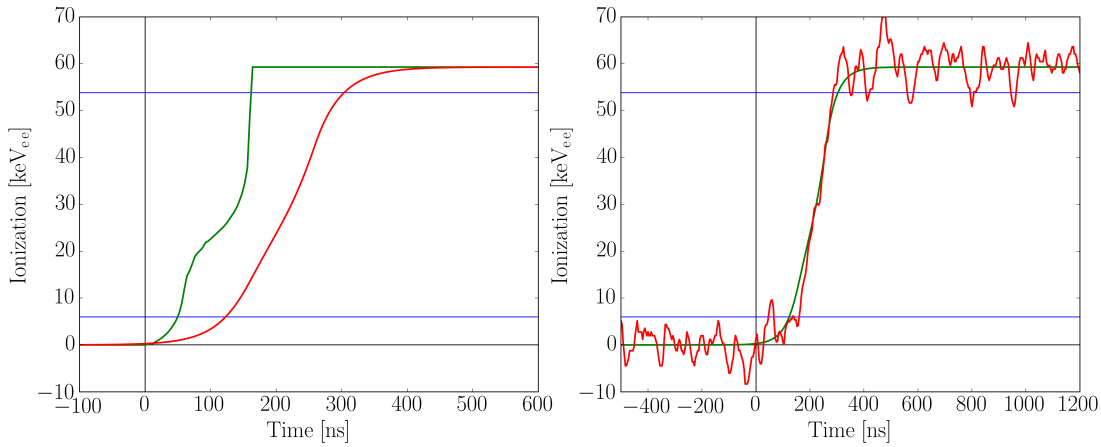

Figure 5.1: *Left:* Time-resolved charge signal for a typical surface event with a very short rise time. The *green* line represents the pure simulated signal, the *red* curve represents the simulated signal low pass filtered with a Butterworth filter of 1st order and 5 MHz roll-off (−3 dB). *Right:* Low pass filtered signal (*green* line) and low pass filtered signal plus actual experimental noise (*red* line). The *blue* line represents the 10 % and 90 % levels of the maximal signal amplitude. Their intersections with the signal mark the rise time. By applying a low pass filter to the surface event, the rise time is shifted from 110 ns for the pure signal to 160 ns.

experiment is based on a good agreement between rise time distributions from experiment and simulations. Furthermore, it is crucial to find an optimal process for the extraction of the pulse rise time out of an event trace by including experimental limitations into the simulations and by taking advantage of the knowledge about the shapes of the charge signals. In the following the influence of noise and band-width on the charge signals as well as the consequences of the Shockley-Ramo theorem for an optimal rise time extraction are presented.

5.2.1 Impact of the experimental band-width for simulated charge signals

The rise time of a charge signal was defined as the time interval between 10 % and 90 % of the maximal amplitude of the signal. The data sampling frequency had a typical value of 20 MHz leading to charge signals resembling step functions with around 1800 data points before and after the transient region (see sec. 4.6.1). Therefore, the maximal amplitude was defined as mean value of the data points after the signal transition.

The Monte Carlo tool treating charge transport in high purity Germanium presented in chapter 3 does not include effects on the charge signal originating from the experimental band-width. As shown in figure 5.1, these effects can have a large impact on the shape of the simulated charge signals. In the *left* graphic the *green* curve represents the charge signal of a typical surface event resulting from simulation. It has a short rise time of only 110 ns as the created charge carriers do not drift through the whole crystal but reach the veto and collecting electrode very fast. In our case the band-width of the read-out

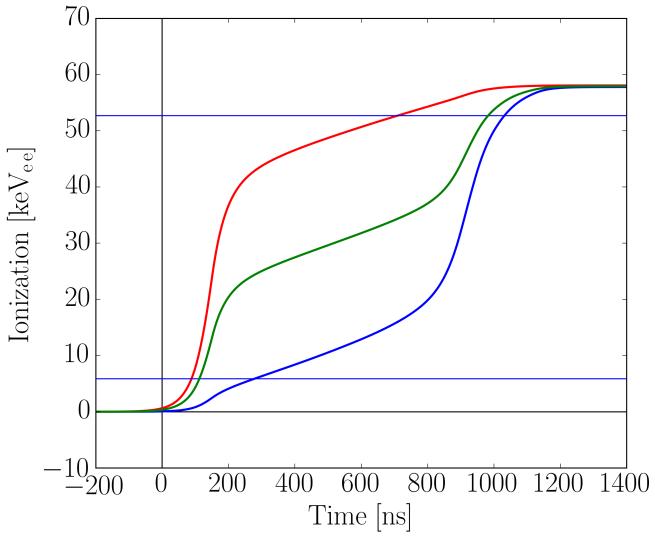

Figure 5.2: Induced ionization signals on the two collecting electrodes B (*red* line) and D (*blue* line) for an energy deposit in the bulk region, which occurred closer to the B electrode than to the D electrode. The *green* curve shows the charge signal based on the sum of the two signal, $(|\mathrm{B}| + |\mathrm{D}|)/2$ and allows an optimal rise time determination, because the 10 % to 90 % level of the maximal ionization amplitude (*blue* horizontal lines) fall in the region of a charge signal with large slope.

electronics is not fast enough to resolve the pure physical shape of the signals. Hence, finally we compare the simulated rise time with the experiment, we have to include the effect of band-width limitations in the simulation. Therefore, first of all the experimental band-width was measured as already explained in section 4.3.1 with the result that it can be described by a low pass filter of 1$^{\mathrm{st}}$ order with a 5 MHz roll-off at −3 dB. For that reason the pure simulated charge signals were filtered with the same low pass (fig. 5.1 *left, red* curve) before extracting the rise time. After filtering the rise time increased significantly from 110 ns to 160 ns. The band-width mainly affects surface events which have a much shorter rise time. Signals from bulk events are only slightly altered by the low pass filter as the charge carriers migrate through the whole crystal leading to rise times up to 1 μs.

In addition to the low pass filtering, actual noise extracted from the measured signals was added to the simulated signals. A typical signal trace is presented in figure 5.1, *right*.

5.2.2 Application of the Shockley-Ramo theorem for pulse-shape analysis

In the last section it was explained that bulk signals originating from electrons and holes drifting through the whole crystal are minor affected by the band-width limitation of the electronic read-out. However, they are strongly affected by the shape of the Shockley-Ramo potentials for the top (B) and bottom (D) collecting electrodes. In section 3.4.2 we explained that the induced signal on an electrode by a charge carrier drifting the distance Δr is proportional to the change of the weighting potential between these two position (eq. 3.6). In addition, the change of the weighting potential for a track Δr increases with the distance to electrode on which the signal is induced. Therefore, charge signals have a steep slope when the charge carriers are drifted close to the recording electrode and a flat slope when the carriers are drifting far away.

In figure 5.2 two exemplary charge signals are shown, created by an energy deposit that was located close to the B (top collecting) electrode but far enough away from the surface to be collected at the B and D electrodes. The *red* curve marks the charge signal on the B electrode with a sharp increase at the beginning, as the charge carriers are drifted close to this electrode and a flat gradient at the end. The charge signal at the D electrode, represented by the *blue* curve has the opposite shape with a high slope at the end. Also shown in the graphic is the 10 % and 90 % level of the maximal ionization amplitude. It is obvious that the rise time is much better defined in the regions where the charge signals are steep. As we wanted to have the best possible estimator for the rise time, we combined both signals by summing the charge signals according to $(|\mathrm{B}| + |\mathrm{D}|)/2$. The resulting curve (*green* line) profits from two steep parts at the beginning and the end of the charge signal and allows a well defined rise time extraction.

Although the shape of the wighting potentials affect mainly the bulk events, we conclude that the most uniform way to extract the rise time of an event is based on the sum of all signals on all four electrodes according to $(|\mathrm{A}| + |\mathrm{B}| + |\mathrm{C}| + |\mathrm{D}|)/2$. In this case one does not have to make any decision on the nature of the event before the determination of the rise time.

5.3 Analysis of simulated charge signals

In section 2.2 we described how events are categorized for the FID EDELWEISS detectors by using the net amplitude signals on the four set of electrodes. This categorization was necessary to discriminate surface events which are more affected by trapping effects and incomplete charge collection and therefore are critical for the discrimination of electron and nuclear recoils.

The rise time of the charge signals also contains information about the location of an interaction in the detector and can be reconstructed for experimental and simulated charge signals. We will start our analysis by categorizing event locations by the net ionization amplitudes on the various electrodes and then connect these categories with the rise time of the events. As the connection between event locations, net ionization amplitudes and rise times is straight forward for simulated γ-ray interactions, we present results from simulation before comparing them to the experimental data.

5.3.1 Localization of γ-ray interactions by ionization amplitudes

In the following, event categories are presented based on the net ionization amplitudes on the A, B, and D electrodes. The events are created by 59.5 keV γ-interactions from an ^{241}Am source facing the top surface of the crystal, which is covered by the A and B electrodes. The C electrode is not considered here, because the net amplitude spectrum would be centered around 0 $\mathrm{keV_{ee}}$ as the interactions all take place close to the A and B electrodes. Sine the electrodes are biased in veto mode with $V_\mathrm{A} = V_\mathrm{C} = 0\,\mathrm{V}$ and

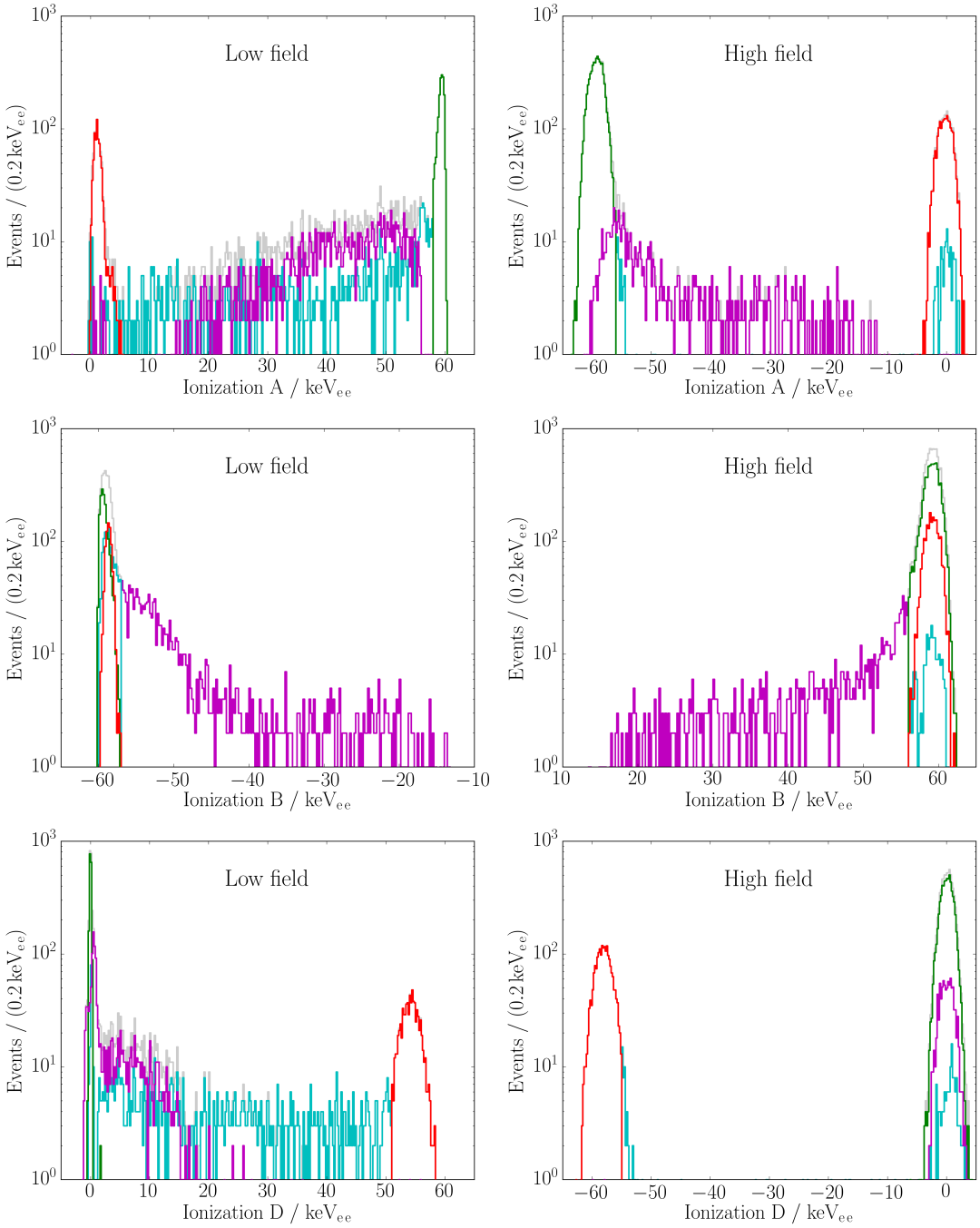

Figure 5.3: Net simulated amplitude spectra of the ionization signals of the A, B and D electrodes. The color code is: *gray* for all simulated events, *red* for bulk events, *green* for surface events, *cyan* for shared events, *magenta* for events with incomplete charge collection. For the detailed definitions see text. The signs of the amplitude spectra are caused by the type of charge carriers which are collected. The voltage configurations are $V_A = V_C = 0\,V$ and for the low field case presented on the *left* side $V_B = -V_D = -2.0\,V$ with hole collection on B and electron collection on D and for the high field case presented on the *right* $V_B = -V_D = +50.0\,V$ with hole collection on D and electron collection on B.

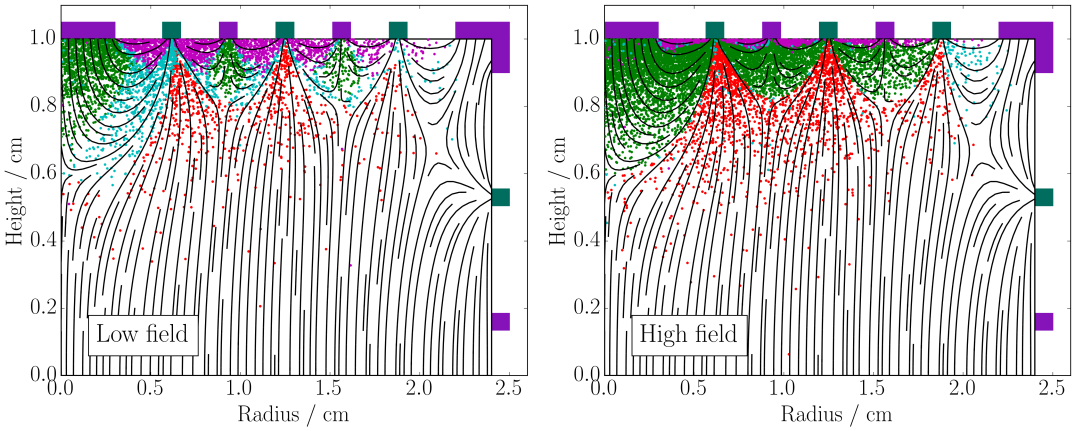

Figure 5.4: Cross-section through upper half of detector, showing two sets of electrodes A,B (*purple*, *dark green*) (C,D are on the opposite site and not shown here). Electric field lines are shown as black lines. Simulated energy deposits created by 59.5 keV γ-rays from an ^{241}Am source are represented as dots, where the color code is: *red* for bulk events, *green* for surface events, *cyan* for shared events, *magenta* for events with incomplete charge collection. The voltage configuration on the electrodes is $V_A = V_C = 0\,V$, *left:* $V_B = -V_D = -2.0\,V$ (low field with electron collection on B) and *right:* $V_B = -V_D = +50.0\,V$ (high field with hole collection on D).

$V_B = -V_D = -2.0\,V$ or $V_B = -V_D = +50.0\,V$, no charge collection on the C electrode will occur.

The amplitude spectra for the A, B and D electrodes in case of the two voltage configurations are presented in figure 5.3. The various colors mark the events that fall in one of four event categories listed in the following:

1. Bulk: Full charge collection on the B and D electrode.
2. Surface: Full charge collection on the A and B electrode.
3. Shared: Full charge collection on B and the sum of A and D.
4. Incomplete: No full charge collection on one of the electrodes.

Events are defined as full charge collection, if they belong to the $5\,\sigma$ region around the 59.5 keV_{ee} peak in the spectrum of the specified channel after fitting a Gaussian function to the peak.

In addition to the amplitude spectra of the ionization signals for low and high electric fields shown in fig. 5.3, in fig. 5.4 the associated locations of the energy deposit are presented. The obvious qualitative difference between the low field and the high field configuration is that there are more shared events (*cyan* line/dots in fig. 5.3 and 5.4) in the low field case. This is caused by the different types of charge carriers which dominate charge collection in the two cases. As presented in figure 5.4, γ-rays from the ^{241}Am source, deposit energy near the top surface area covered by the A and B electrodes. Therefore, in

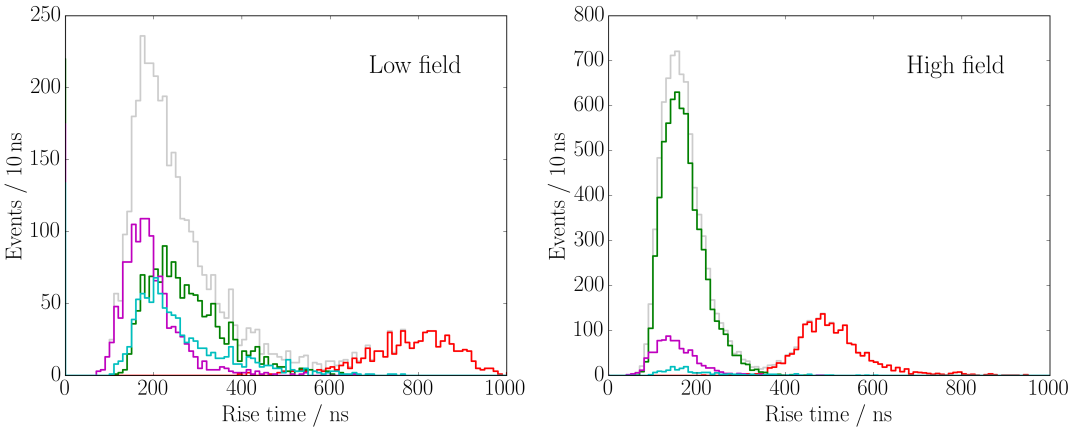

Figure 5.5: Simulated rise time distribution for the low and high electric field case. The voltage configurations on the electrodes are $V_A = V_C = 0\,V$, *left:* $V_B = -V_D = -2.0\,V$ (low field) and *right:* $V_B = -V_D = +50.0\,V$ (high field).

case an interaction is deep enough in the crystal that the produced electrons and holes are drifted to the electrodes on the opposite sites of the detector, the charge transport is dominated by either holes or electrons.

In the high field case the B electrode is biased with $V_B = +50.0\,V$. Therefore charge transport is dominated by hole transport as electrons are collected very fast at the B electrode. As the simulation of holes assumes no transport anisotropy the holes are drifted very strictly along the field lines and in the critical region where the electric field lines change from connecting B and D electrodes to connecting A and B electrode, holes follow the shape of the electric field lines and interactions either belong to the surface category or the bulk category. Therefore shared event are strongly suppressed and do hardly show up in fig. 5.3 *right* and 5.4 *right* (*cyan* histogram/dots).

In the low field case the B electrode is biased with $V_B = -2.0\,V$ and charge transport is dominated by electrons. As electrons have a transport anisotropy (see sec. 3.3.1) they do not drift along the electric field line but in an 35 ° angle, leading to an extended area in the crystal between the bulk and surface event regions, where part of the electrons are drifted to A and D electrode (*cyan* dots in fig. 5.4 *left*) and causing charge sharing between A and D electrodes (*cyan* histogram in fig. 5.3 *left*). Therefore this major difference between the low and high field case can be understood by the different transport properties of electrons and holes.

5.3.2 Combination of event categories and rise time distributions

After categorizing the energy deposits created by 59.5 keV γ-rays from an ^{241}Am source based on the ionization amplitude, we study the rise time distribution for these categories. The results for the rise time distributions are presented in figure 5.5 and show a significant difference in the rise time for bulk and all other events. For the bulk events, we note

a difference in the rise time from the low field to the high field case, which reflects the field dependence of the drift velocity of electrons and holes. We can use the bulk rise time distribution for cross checking our simulation: In the low field case the rise times for bulk events are distributed around 800 ns. For bulk events, charge carriers have to drift through the whole crystal. We can than approximate the mean drift velocity to $2\,\mathrm{cm}/800\,\mathrm{ns} = 2.5 \cdot 10^6\,\mathrm{cm/s}$. As the electric field is 2 V/cm in the low field case and charge migration is dominated by electrons, we can compare the drift velocity with the special measurements presented in figure 3.6. There we find $v_{\mathrm{el,drift}}(2\,\mathrm{V/cm}) \approx 2.9 \cdot 10^6\,\mathrm{cm/s}$ which agrees rather well with our approximation. In addition it confirms that the bulk rise time distribution is consistent with the assumption electrons are drifted at an electric field of 2 V/cm. The same agreement is given for the high field case: The distribution of rise times for bulk events around 500 ns leading to a drift velocity of $4 \cdot 10^6\,\mathrm{cm/s}$. This is consistent with hole transport at an electric field of 50 V/cm with $v_{\mathrm{ho,drift}}(2\,\mathrm{V/cm}) \approx 4.1 \cdot 10^6\,\mathrm{cm/s}$ (values extrapolated from 3.6 *right*).

As the goal of our pulse-shape analysis and of the EDELWEISS fast ionization channel approach is to perform a surface event rejection based on the rise time of the charge signals, we performed a rise time cut and determined the efficiency of such a cut by comparing the remaining events with the event categories based on the ionization amplitudes defined in the last section 5.3.1. The results are summarizes in table 5.1. We note that in the low field case we can rejects 95.3 % of the events in the combined category of (surface+shared+incomplete) with a rise time cut of 600 ns. In the high field case 99.7 % of theses event are rejected by a rise time cut of 400 ns. That the rise time cut is more efficient for the high field case is based on the fact charge collection improves with increasing fields as especially the probability for bulk trapping decreases.

In conclusion, we could show that the simulation is consistent with our expectation how the charge transport in HPGe crystal works. Clearly, we are able to connect rise time with event locations in the detector. A rise time cut based on the simulated charge signals shows promising results. A comparison of simulated and experimental data will be shown in the next section, testing the reliability of the simulation tool.

5.4 Comparison of experimental and simulated rise time distributions

After discussing the simulation of our prototype set-up, where we connected the locations of γ-ray interactions with event categories based on the charge amplitudes on the interleaved electrodes and then presented the difference for bulk events and all other events in rise time, we now compare the simulations with measured data. Therefore we performed the same analysis backwards, by starting with the rise time distributions and then comparing the event categories, which allows us then to conclude about the primary interaction locations. Finally we performed the same rise time cut as explained in the section 5.3.2.

The rise time distributions presented in figure 5.6 show that the simulations well reproduce the experimental data for the low and high field case. Therefore we can conclude that

	LF: Sim.	LF: Exp.	HF: Sim.	HF: Exp .
t_{cut} in ns	600	600	400	400
ϵ_{bg} in %	95.3	97.4	99.7	98.5
ϵ_{bulk} in %	3.6	9.5	6.2	10.1

Table 5.1: Cut efficiencies for a rise time cut in the low field (LF) and high field (HF) case. The cut efficiency ϵ_{bg} is defined as $\epsilon_{\mathrm{bg}} = (N_{\mathrm{sur}}(t < t_{\mathrm{cut}}) + N_{\mathrm{shar}}(t < t_{\mathrm{cut}}) + N_{\mathrm{in}}(t < t_{\mathrm{cut}}))/(N_{\mathrm{sur}} + N_{\mathrm{shar}} + N_{\mathrm{in}})$, where N_{sur}, N_{shar} and N_{in} are the number of events in the categories surface, shared and incomplete. The cut efficiency ϵ_{bulk} is defined as $\epsilon_{\mathrm{bulk}} = N_{\mathrm{bulk}}(t < t_{\mathrm{cut}})/N_{\mathrm{bulk}}$, where N_{bulk} is number of events in the bulk category (see sec. 5.3.1). The experimental results are discussed in sec. 5.4.

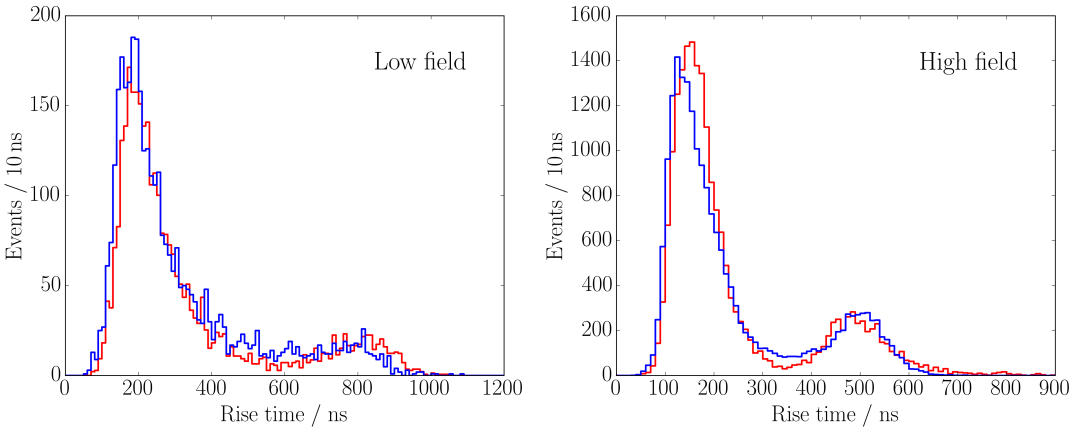

Figure 5.6: Rise time distribution for the low and high electric field case. Measured (*blue* histograms) and simulated (*red* histograms) data are shown.

the charge migration processes included in the modeling tool provide an adequate description of the experiment. The good agreement also shows that there is a clear separation between bulk and all other events, so that one can connect rise time from the experimental study with event locations as presented in figure 5.4.

In order to compare the experiment and the simulation on a qualitative basis, we also categorized the charge signals from experiment by the ionization amplitudes as presented in sec. 5.3.1 for the simulations. The relative contribution to the different event categories are shown in table 5.2. Especially in the low field case there is a good agreement between simulation and experiment. In contrast to that, in the high field case the agreement is not quite as good. Notably the number of surface events is overestimated by the simulation and the shared and incomplete events are underestimated. As the agreement of this contribution with the simulation is impressive in the low field case, we can conclude about the origin of the discrepancy in the high field case. In the low field case the charge migration is dominated by electrons, which show a transport anisotropy (see sec.3.3.1). Therefore, shared event occur in the region where the electric field lines change from connecting A and

		Bulk	Surface	Shared	Incomplete
Meas / Sim	low field	0.10 / 0.15	0.33 / 0.34	0.22 / 0.22	0.35 / 0.29
	high field	0.19 / 0.21	0.53 / 0.68	0.09 / 0.02	0.19 / 0.09

Table 5.2: Fraction of events in the four event categories (Meas/Sim).

B electrodes to connecting B and D electrodes. Therefore, as this transport anisotropy of electrons is included in the modeling, the agreement of simulation and data is very good. For holes no transport anisotropy is included. As a consequence shared events in the high electric field case, where charge signals are dominated by hole transport are strongly suppressed by the simulation. However, holes also have a transport anisotropy. It is much smaller than than for electrons (see sec.), wherefore it was not implemented in the simulation so far. Thus, the anisotropy for holes increases with electric field and our result show that it is not negligible and should be implemented in a future charge modeling tool.

Based on the experimental rise time distribution, we performed the same cut as presented in the last section. The results are shown in table 5.1. Obviously, the efficiency of rejecting surface, shared and incomplete events from the bulk region is close to what is expected from simulation. Also the amount of bulk events that is lost by such a cut is in the same order of magnitude. The high rejection efficiencies for near-surface events (LF: 97.4 %/HF: 98.5 %) show that the rise time is an event discrimination parameter which can be used independently from the amplitude based rejection with the FID electrodes. An application for the FID800 detectors in EDELWEISS is presented in sec. 5.6. However pulse-shape analysis are only efficient for signals large enough in comparison to the baseline fluctuations and for EDELWEISS detectors typically for event with ionization amplitude above 40 keV [96]. Furthermore the good agreement between simulation and data shows that charge migration simulations are a very meaningful tool to test and optimize HPGe detectors. The potential of these simulation studies will stressed further in chapter 6 by analyzing the detector performance for the low-mass WIMP search.

5.5 Ionization signal rise time as indicator for space-charge build-up

In section 4.1.2, we explained the surface treatment for our prototype detector which is based on a final XeF_2 dry etching process in order to avoid leakage currents. In the following, we describe the experimental verification that this surface treatment is really necessary. We show the results of an experimental study to confirm that the rise time of ionization signals is a good estimator for degradation and charge build-up during detector operation.

For this study, an additional prototype HPGe crystal was used which had the same dimensions, the same interleaved electrode design and the same net dopant densities as the detector used for the pulse-shape analysis presented before. However it was not dry etched with XeF_2.

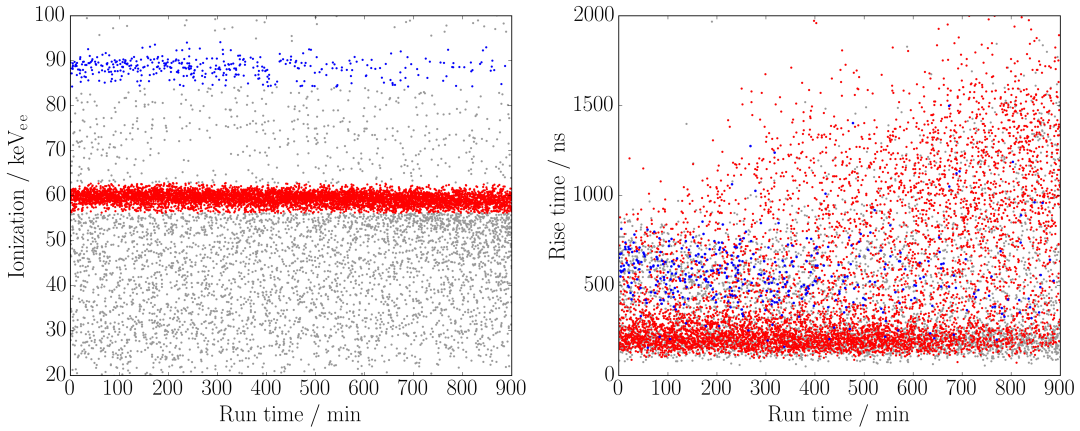

Figure 5.7: Degradation of charge collection in ionization amplitude (*left*) and in rise time (*right*). Energy deposits of 59.5 keV γ-rays from the ^{241}Am source, facing the top surface, are highlighted by the *red* dots. Energy deposit of 88 keV γ-rays are produced by three ^{109}Cd sources facing the top, bottom and lateral surface of the detector (*blue* dots). As the different types of sources are located at different positions, trapping effects in the case of 59.5 keV and 88 keV photons create different counter-fields, which is a possible explanation for the difference in the kinetics of degradation for the two lines. Voltage configuration: $V_B = -V_D = -4.0\,V$ and $V_A = -V_C = +1.5\,V$.

The experimental set-up was according to the schematic already shown in fig. 4.1. In addition to the ^{241}Am source emitting 59.5 keV γ-rays, three ^{109}Cd sources were installed facing the top, bottom and lateral surface and emitting 88 keV γ-rays. In figure 5.7 the results for a degradation study of the ionization amplitude and rise time are shown. The *left* graphic shows a clear degradation of the 88 keV-line (*blue* dots) after around 400 min of measurement time. For the 59.5 keV-line (*red* dots) the degradation is not so easy to identify and starts around 600 min. The comparison with the rise time for the ionization signals of the same data set (fig. 5.7 *right*) shows that the degradation is more obvious in the rise time data. In the beginning the rise time distribution extends to a maximal value around 1000 ns and then gradually broadens to values up to 2000 ns. Especially for the 59.5 keV γ-ray interactions marked as *red* dots, the degradation is much more evident and already starts at around 200 min of run time. For the 88 keV γ-ray energy deposits the degradation was already very clear from the ionization signal distribution and is less evident in the rise time distribution. As the observed degradation is caused by the trapping of charge carriers leading to counter electric fields in the HPGe crystal which opposite charge migration, the difference in the kinetics of degradation for the 88 keV and 59.5 keV line is based on the different positions of the ^{109}Cd sources in comparison to the ^{241}Am source. The ^{109}Cd source also creates energy deposits in the lateral surface region.

As we already discussed, degradation is caused by charge trapping. However, the degradation build-up was very fast and strong for our detector. Therefore, we performed further measurements to find the reason for the degradation. We performed a degradation study at different electrode biases and found the degradation to increase with the collecting voltage. In addition, we observed that the experimental platform started to heat for electrode

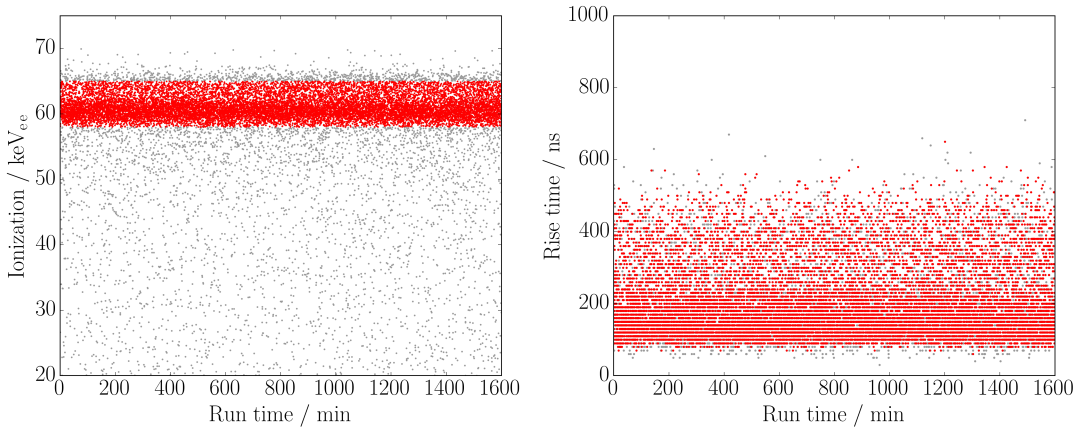

Figure 5.8: Stable charge collection in ionization amplitude (*left*) and in rise time (*right*). Energy deposits of 59.5 keV γ-rays from the ^{241}Am source, facing the top surface, are highlighted by the *red* dots. Before operation the detector was dry etched with XeF_2, which was not done for the crystal presented in fig. 5.7. Voltage configuration: $V_B = -V_D = +50.0\,V$ and $V_A = -V_C = 0\,V$.

biases above $\Delta V = 10\,V$. Special leakage current measurements showed also increased values with electrode bias. This strongly suggested that the observed degradation correlated with carrier injection from the electrode contacts, leading to an increased carrier injection and stronger degradation with voltage. Therefore, a test of the detector for high voltage measurements in order to use the Neganov-Trofimov-Luke amplification of the charge signals to lower the detection threshold for low-mass WIMP search, was not possible. Instead we concluded that we need an improved surface treatment of the detector that resolves the leakage current problem. This was achieved by dry etching our HPGe detectors surfaces with XeF_2. The prototype detector we used for the pulse-shape study presented here, as well as for the study of the detector performance at high bias (see chap. 6) was dry etched with XeF_2. In figure 5.8 we show, that the performance of this detector was stable even at high biases of $\Delta V = 100\,V$ and no degradation was observed for operation times up to 26 hours.

We conclude that the XeF_2 dry etching is a necessary treatment to reduce leakage current and the rise time is a good estimator for evaluating the detector stability.

5.6 Summary and outlook: The EDELWEISS-III fast ionization channels

The pulse-shape analysis of ionization signals showed that the charge migration processes in the HPGe detectors of the EDELWEISS experiment are well understood. Especially the rise time distributions retrieved from simulation and data showed a good agreement. The slight discrepancies for ionization signals dominated by hole transport could be explained by a missing implementation of hole transport anisotropies in the simulation. In addition, we could show that the rise time is a very sensitive parameter for detector degradation, even

more sensitive than the ionization amplitude. Furthermore, the clear separation of rise time for bulk and surface events supported the hypothesis that surface event discrimination is possible with pulse-shape analysis. A rise time cut for events measured with the prototype detector allowed us to reject more than 95 % of all non-bulk events.

The potential of pulse-shape analysis was also tested for a detector in the EDELWEISS-III phase. Therefore, a Fast Ionization read-out Card (FIC) which allowed one a sampling frequency of 40 MHz for the ionization channel was developed at KIT. The FIC was installed for one of the FID detectors in the underground laboratory in Modane, providing one with a time-resolved measurement of charge signals for two collecting electrodes of this prototype FID800 detector. In Run 309, which lasted from April 2014 to January 2015, first data were taken in a calibration run with a ^{133}Ba source. Analog to the pulse-shape analysis presented in this section, the rise time of the ionization signals was extracted. A surface discrimination cut based on the rise time was defined and allowed us to a reject of 95.6 % of the surface events, while only 5.75 % of actual bulk events were also rejected. Further analysis of the rise time data in comparison with charge migration simulations based on the software presented in chap. 3 even allowed one to extract the event position along the z-axis of the detector with a precision of $\Delta z = 0.28\,\mathrm{cm}$. Assuming a realistic improved noise level in the FIC channels, a precision of $\Delta z = 0.05\,\mathrm{cm}$ should be in reach. The development of the fast ionization channel, as well as the analysis of the rise time data was performed in the frame work of a PhD thesis and the details of this work can be found in [98].

6. Neganov-Trofimov-Luke amplification of charge signals

In December 2016, the next phase of the EDELWEISS dark matter experiment started, operating the HPGe detectors at high electric fields (up to 100 V/cm) in order to lower the detection thresholds for recoil energies below 1 keV increasing the sensitivity for low-mass WIMPs with $m_\chi < 5\,\mathrm{GeV/c^2}$. With this, EDELWEISS enters a new regime for the operation of its detectors. The original FID800 detector design was developed for an operation at low electric fields ($\approx 2\,\mathrm{V/cm}$). The hybrid detection of ionization (electron/hole-pairs) and heat (phonons) allowed a powerful discrimination of electron recoils (γ-, β-background) and nuclear recoils (WIMPs, neutrons) sincce in the low field case, the heat energy is approximately proportional to the recoil energy E_rec and therefore the ionization yield $Q = E_\mathrm{ion}/E_\mathrm{rec}$ depends on the recoil type. In addition, the FID interleaved ring electrode design, based on two collecting and two veto electrodes, allowed to reject surface events based on the independent measurement of the ionization signals on this four sets of electrodes. Surface events are critical as the charge collection efficiency for electrons and holes created in the surface regions is often decreased due to trapping and recombination effects. This leads to a reduced measurement of the ionization energy and can cause misinterpretations of electron recoils as nuclear recoils.

By increasing the bias field of the detector, its performance changes as the heat signals start to be dominated by secondary phonons produced by drifting electrons and holes (Joule heating [140]). Nowadays this heating is known as the Neganov-Trofimov-Luke (NTL) effect [65, 66] based on the observation that the amount of secondary phonons produced by a drifting charge carrier linearly increases with the operation voltage. The additional heating has two effects: It allows to amplify the charge signals linearly with the applied voltage in the heat channel and provides very low detection thresholds. Tests of the CDMS collaboration with a HPGe detector have reached a detection threshold of $56\,\mathrm{eV_{ee}}$ [47]. On the other hand, the discrimination power of the hybrid detection of heat and ionization signals is lost as both signals are now determined by the migration of charge carriers. Furthermore the surface event discrimination based on ionization signals is lost for low energy recoil events since the detection threshold of the ionization channels is typically limited to a few $100\,\mathrm{eV_{ee}}$. Beside a slight improvement on the charge collection efficiency, the higher electric field has no significant effect on the ionization energy threshold.

Therefore, especially for the operation of FID800 detectors at high electric fields, the question arises, how they should be optimally operated to still allow a proper energy calibration, although the ability to discriminate electron and nuclear recoils as well as surface events is not provided any more. In addition, due to the interleaved ring electrode design, the detectors could be affected by leakage currents between neighboring electrodes. First results from Run 309, which was finished in March 2016, showed that the EDELWEISS detectors could hold voltages up to 100 V without any measurable effect of leakage currents. In addition, the analysis of heat data from a calibration experiment with γ-rays

showed the expected linear NTL amplification of the heat signal with increasing electrode voltage. Furthermore, already an energy threshold of $150\,\mathrm{eV_{ee}}$ could be achieved for one of the detectors [98].

Based on these promising results for the EDELWEISS detectors, we performed an extensive calibration experiment with an EDELWEISS-type prototype detector aiming to understand and optimize its performance for this new operation mode. As the heat signals caused by drifting charge carriers are heavily affected by the transport properties of electrons and holes in the HPGe crystals, we made use of the comparison of hot carrier transport simulations with data. This allowed us to evaluate and understand the influence of charge carrier trapping which compromises a full signal measurement and a proper energy calibration of the detector. Especially, we will show that the electrode geometry has a huge impact on the detector performance and that simpler electrode designs are favored at high electric fields.

This chapter is structured in the following way: The experimental set-up for the calibration experiment in the ground laboratory at CSNSM is described in sec. 6.1, followed by a presentation of the software tool (sec. 6.2) used for data processing and analysis. The prototype detector had the same interleaved electrode design as the FID800 EDELWEISS detectors with a set of 4 interleaved ring electrodes A,B,C,D which in general allowed us to discriminate surface events for recoil energies in the keV-scale. As the surface discrimination is not available any more for recoil energies far below 1 keV, we performed measurements with electrodes operated in a planar mode with $V_\mathrm{A} = V_\mathrm{B}$ and $V_\mathrm{C} = V_\mathrm{D}$ for neighboring electrodes on the top and bottom surfaces. The calibration process for an operation in planar mode and possible challenges based on the interleaved electrode design are presented in sec. 6.3.

After verifying that the NTL amplification of the charge signals in the heat channel increases as expected linearly with voltage (sec.6.4), a detailed analysis of the detector performance at low and high electrode biases is presented in sec. 6.5 and 6.6. The analysis includes a characterization of the charge migration processes in the detector based on the comparison of simulation and data. In addition, heat-only events are discussed, which are at the moment the limiting background in EDELWEISS-III and their origin is not known so far. We present a very practical approach to reject these events based on a pulse-shape analysis of the heat signals.

In sec. 6.7, we show that the hot carrier transport simulation tool used in this thesis provides an adequate description of electron and hole propagation in the EDELWEISS detectors. In addition, we show that the operation of the prototype detector at high voltages is limited by carrier trapping at surfaces uncovered by electrodes. In sec 6.8, we discuss strategies to reduce the effect of surface trapping. We use the charge migration simulation tool to optimize the electrode configuration. The results are summarized in sec. 6.9.

6.1 Description of the experimental set-up

The experimental set-up was already described in chapter 4 and the schematics of the set-up were presented in fig. 4.1. The detector was equipped with an ^{241}Am source which faced the top detector side covered by the A and B electrodes. There were no ^{109}Cd sources installed. In order to read out the heat signals a NTD Ge thermistor was used. It was glued on the center C electrode which was located at the bottom of the detector. In contrast to the data used for pulse-shape analysis of the ionization signals, the data for this part of the work were recorded as continuous stream for all five measuring channels (4 ionization channels A,B,C,D + 1 heat channel).

The sampling frequency was chosen to be 20 kHz. Therefore one data point was taken every 50 μs. This sampling frequency was high enough to resolve the pulse-shapes of the heat signals, which have a typical rise time of 10 ms and a decay time of 20 ms. As the rise time of the ionization signals is much faster, with a maximal transient time around 1 μs (see chap. 5), it can not be resolved by a sampling frequency of 20 kHz. However, the reconstruction of the signal amplitudes of the ionization channels is perfectly feasible. These amplitudes are the necessary parameters for the analysis performed in this work. In addition, a sampling with 20 kHz kept the amount of data stored per measurement on a practical level, not exceeding 2 Gbit per run.

6.2 Description of a software tool for processing streamed data

The data processing is done using a software tool developed at CSNSM in Orsay, France. This software is also used for data analysis within the LUMINEU experiment which studies the neutrinoless double β-decay. A detailed description of the software tool can be found in [141]. In the following an overview of the functionality of the program is given. As an example the data processing for the heat signals is described, although the same processing is performed for the charge signals of the A,B,C and D electrodes. For this kind of study always triggering on the heat signal was used, as especially in case of high electrode biasing a much lower energy threshold can be achieved for the heat channel in comparison to the ionization channels.

6.2.1 Triggering on the heat channel

In this work, triggering on the heat channel was chosen, as it allows a lower energy threshold and allows to study heat-only events (see sec. 6.5.3), with no signal above the baseline noise in any of the the four ionization channels, typically $E_{\mathrm{ion}} < 3\,\mathrm{keV_{ee}}$.

The triggering process involves the following steps:

1. **Reference pulse**: The user manually scans the streamed data file and selects about 30 pulses on which the software builds a mean pulse. An example for a typical mean

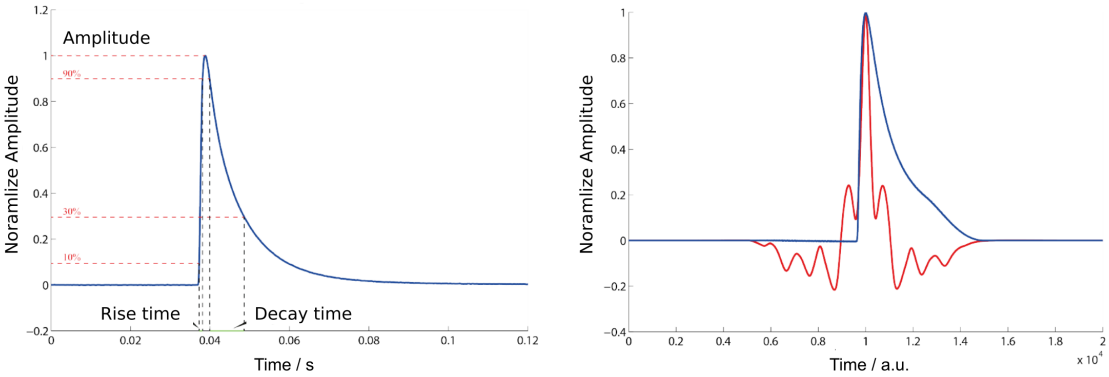

Figure 6.1: *Blue:* Reference pulse. *Left:* A typical heat pulse is shown. The definitions for amplitude, rise and decay time are shown. *Right:* The reference pulse before and after applying the Gatti-Manfredi filter is shown. The amplitude of the pulse is given as the maximum of the *red* curve. Figures from [141].

pulse is shown in figure 6.1 *left*. The rise time of the signal is determined by the thermalization time in the calorimetric detector and the decay time by the coupling between detector set-up and thermal bath (see sec. 2.4).

2. **Noise power spectrum:** The user selects parts of the streamed data without signal and the software algorithm builds a noise power spectrum.

3. **Optimal filter:** The triggering algorithm as well as the analysis algorithm presented in the next section are designed to provide an optimal extraction of the amplitude of a pulse. Therefore a Gatti-Manfredi-filter [142] is used. This filter is a so-called matched-filter, which is based on a Fourier transformation algorithm, which reduces the noise contribution to the amplitude extraction process, but does not affect the pulse amplitude. The basic input parameters for building this filter are the reference pulse and the noise power spectrum. In fig. 6.1 *right* the *red* curve represents the filtered reference pulse. The amplitude of the signal is then defined as the maximum of this curve.

4. **Trigger threshold and baseline resolution:** The trigger threshold is chosen to be typically between 3σ and 5σ of the baseline resolution. The baseline resolution is determined by selecting again parts of the data stream without pulses. A Fast Fourier Transformation is performed with the selected data and subsequent the optimal filtered reference pulse is fitted to the transformed data. The amplitude spectrum is distributed around zero and fitted with a Gaussian function. The baseline resolution is calculated independently for all 5 channels (4 ionization channels + 1 heat channel) before triggering.

5. **Triggering and pulse-shape analysis:** A step wise optimal filtering is performed on the complete heat data stream. Structures with an amplitude above the trigger threshold are fitted to the filtered reference pulse and the correlation between this

pulses is calculated. The correlation parameter c is sensitive to the shape of the filtered pulses and in case $c \to 1$ the shape of the actual pulse and the reference pulse match very well. For correlations $c \to 0$ the pulse shape do not match. In our experiment, $c \to 0$ can be caused by pile up pulses, where a second pulse occurs while the first has not relaxed yet, or by high energy deposits caused by cosmic rays, which lead to a signal that is out of the voltage range of the data acquisition system. Other events with a low correlation parameter are heat-only events and will be discussed in section 6.5.3. The software tool allows us to set either a fixed correlation value, above which the signal is accepted and triggered or leave the correlation variable. In the latter case the user can manually decide if the shape of a pulse is matching the reference pulse. The software adjusts then the c value according to the decision, and afterwards only pulses with c values above that value are accepted. The positions of the maximal heat amplitude of triggered pulses in the heat data file is stored to the so-called trigger file. The position in the data file also allows to reconstruct the real time at which the event was triggered.

6.2.2 Evaluation of triggered pulses

After the triggering the positions of the signals in the streamed data were known and the analysis algorithm included in the software could be used to evaluate the properties of every triggered pulse. The algorithm evaluates the data streams of the channels separately and as input it needs the reference pulse and the noise power spectrum for every channel (4 ionization channels + 1 heat channel) and the trigger file. For the ionization channels, the data streams have to be synchronized with the heat data stream. The ionization signals are much faster than the heat signals. Therefore they are expected to reach the data acquisition system earlier. However, this difference in the timing manifests itself as a constant offset between the pulse positions for heat and ionization channels. Thus, before evaluating the ionization signals according to the heat trigger file, the user has to define this offset. As the offset can vary slightly the user defines a fixed offset plus a range of typical 3 data points around this offset position, in which the algorithm then searches for the maximal amplitude in the filter data stream. Actually, the algorithm looks for the maximal amplitude or the minimal amplitude and choses which absolute value is larger, as the sign of ionization signals depends on the type of charge carriers an electrode collects. For the heat channel the pulses are always positive.

The output parameters of the triggered pulses are explained in the following, mentioning only the parameters used for this work:

1. Trigger position: Position of the triggered pulse in the stream data file.
2. Raw amplitude: Maximum or minimum of the raw pulse.
3. Filtered amplitude: Maximum or minimum of the filtered pulse.
4. Fitted amplitude: The unfiltered reference pulse is plotted against the triggered

pulses and a linear function is fitted to this plot. The slope of this linear fit defines the signal amplitude.

5. Correlation parameter: Correlation between reference and triggered pulse.

6. Rise and decay time of the pulse: These parameters are defined as shown in fig. 6.1 *left*.

7. Baseline resolution: Gaussian fit to filtered amplitude spectra of a part in the stream without any signal. It is determined directly from the streamed data before the triggering and therefore independent of the triggering process.

6.3 Calibration of data from the prototype detector operated at high biases in planar mode

The aim of an operation of a HPGe detector at high electrode biases is to lower the energy threshold. In general, this implies that a low signal regime is entered, where the energy resolutions on the ionization channels are not good enough to measure any signal. Therefore, an operation of the electrodes in a veto mode with a bias difference between veto and collecting electrode, which is normally used to discriminate surface events (see sec. 2.2) based on the ionization signals, can not be used for surface event discrimination any more. As a consequence, the prototype detector studied in this thesis was operated in planar mode. The A and B electrode on the top surface were biased with the same voltages and the C and D electrodes on the other site with the opposite values. In this case only one NTL amplification factor occurs and leads to an uniform amplification of the charge signals in the heat channel. A discussion on the biasing of the electrodes in veto mode can be found in section 6.8.1.

The experiment was equipped with an ^{241}Am source. Therefore, energy deposits in the detector were mainly caused by 59.5 keV γ-rays. The advantage of this source was, that the recoil energies cause by the γ-rays were high enough to be detectable with the ionization and the heat channels. As the ionization signals contain a lot of information about the charge transport in the HPGe detector, the analysis presented here is based on all detection channels. However, our final conclusions take into account that in a real low-mass WIMP search experiment, the signals on the ionization channels are too small to be detectable.

In the following the procedure for calibrating the prototype detector in a planar mode is shown, using as an example a measurement where the electrodes were biased with $V_\mathrm{A} = V_\mathrm{B} = -V_\mathrm{C} = -V_\mathrm{D} = +50\,\mathrm{V}$. This was the highest bias we could apply to the prototype detector with $V_\mathrm{A} > 0\,\mathrm{V}$ (see sec. 6.4). For the opposite polarization, a stable detector performance was also possible for voltages up to $V_\mathrm{A} = -50\,\mathrm{V}$.

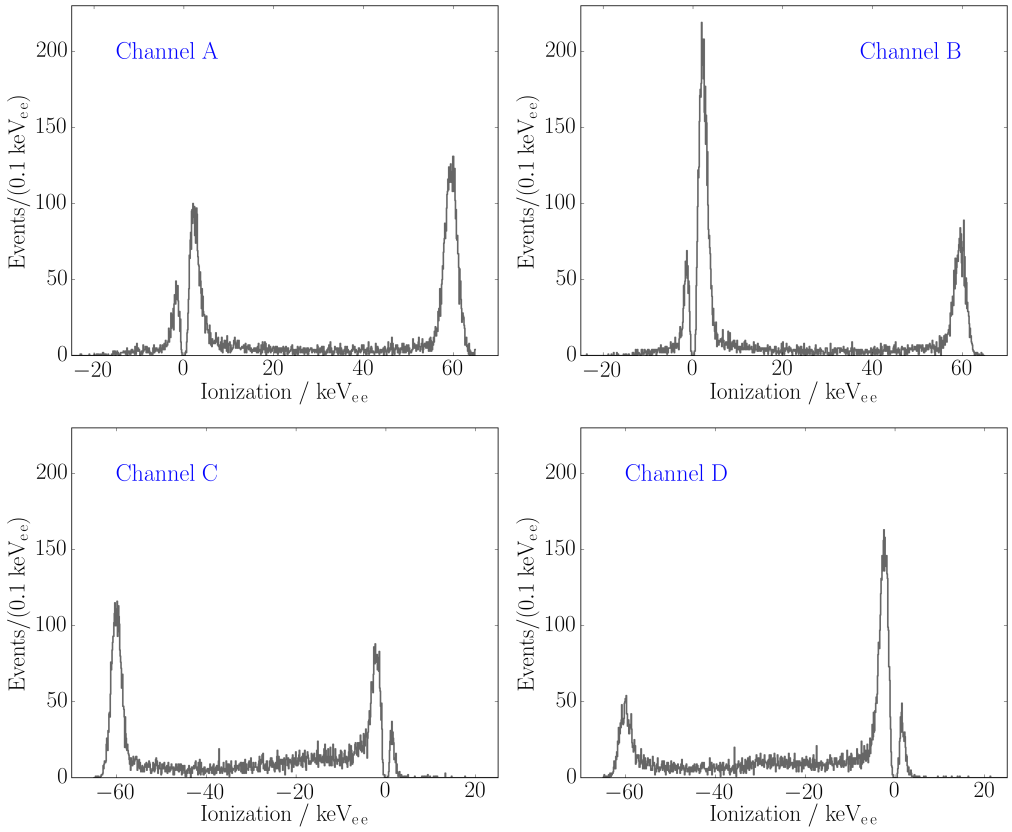

Figure 6.2: Calibrated ionization amplitude spectra for the four ionization channels A, B, C, D. The prototype was operated in planar mode with a high bias configuration: $V_A = V_B = -V_C = -V_D = +50\,V$.

6.3.1 Results from the calibrated ionization amplitude spectra

In fig. 6.2 calibrated ionization spectra for the four electrodes A,B,C,D are shown. The calibration was performed by fitting a Gaussian function to the filtered amplitude spectra retrieved from the software presented in sec. 6.2.2. The different signs for the 59.5 keV-peak originate from the fact that the A and B electrodes collected electrons and C and D collected holes. The fitting results for baseline resolution and resolution on the 59.5 keV-peak are summarized in tab. 6.1. We find that the baseline resolution and the resolution on the 59.5 keV-peak are in good agreement, differing maximal up to 30 %. That means our the experiment was mainly limited by electronic noise. Charge migration processes as trapping played a minor role. The prototype experiment was located at ground level and was not optimized for an actual WIMP search. Therefore the baseline resolutions are clearly higher than the resolutions achieved with the detectors installed at the Modane underground laboratory. Still the resolutions were sufficient to study the detector performance and charge migration properties at high biases.

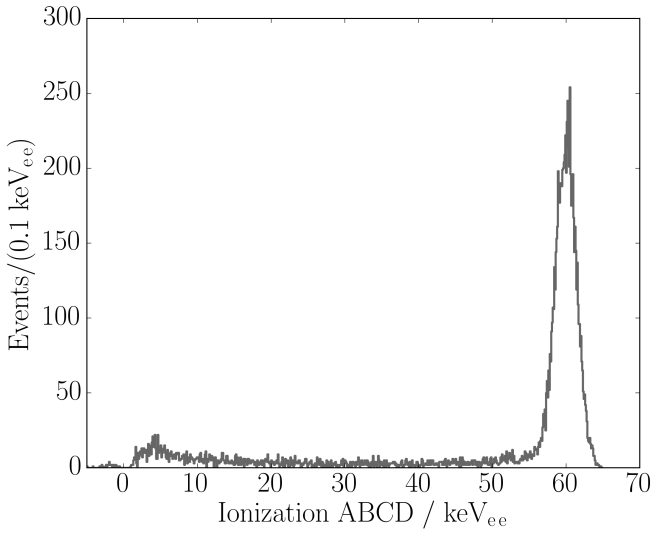

Figure 6.3: Calibrated charge spectrum after summing up the signals from the four ionization channels: (A+B-C-D)/2. This is the best estimator for signals with full charge collection.

Channel	A	B	C	D	ABCD
FWHM(59.5 keV) in keV$_{ee}$	3.536 ±0.095	3.225 ±0.418	2.824 ±0.128	3.300 ±0.232	3.450 ±0.008
FWHM(0 keV) in keV$_{ee}$	3.201 ±0.082	2.386 ±0.059	2.381 ±0.065	2.400 ±0.042	2.593 ±0.071

Table 6.1: Results the energy resoultions in the ionization channels A,B,C and D in planar mode with $V_A = V_B = -V_C = -V_D = +50\,V$. ABCD marks the summed ionization channel as defined in eq. 6.1.

The double peak structure around zero reflects the baseline fluctuations and is expected to be a single Gaussian with mean 0. However, we observe a dip at zero which has a simple technical reason: For pulse triggering we used the heat channel. Hence, as described in sec. 6.2.2, the timing of the pulses in the data streams of heat and ionization channels is different, we had to synchronize the channels. The synchronization process includes the definition of a fixed range in which the software searches for the maximal or minimal signal amplitude in case the heat channel triggered a pulse. In case, the actual ionization signal is zero the software still searches for the maximum or minimum, resulting in the observed dip at zero. For our purpose the double peak structure at zero ionization amplitude is not important as the baseline resolution is determined any way on pure baseline data before the triggering process (see sec. 6.2).

The calibrated ionization spectra already allow us to draw some general conclusion about charge collection in the detector. First of all, the majority of events ($\approx 38\,\%$) with an energy of 59.5 keV are collected on th A and C electrodes. This results from the fact that the ^{241}Am source is installed above the A center electrode causing a lot of energy deposits

located below this electrode. Secondly, the amount of events with ionization amplitudes in the range $|E_{\mathrm{ion}}| \in [15{,}55]$ keV$_{\mathrm{ee}}$ is $\approx 30\,\%$ for the C and D channels and therefore higher than for the A and B channel with $\approx 14\,\%$. This is a clear sign for charge transport effects. The energy deposits occur close to the top surface covered by the A and B electrodes. Therefore electrons are collected after migrating a short distance, whereas holes migrate through the whole crystal and can either be trapped or partially be collected on the C and D electrodes. A third interesting group of events are interactions with negative amplitudes in the A and B channels ($\approx 5\,\%$ of all events), which are not consistent with baseline fluctuations ($E_{\mathrm{ion}} < -8\,\mathrm{keV_{ee}}$). In section 6.7 we will show that these events have reduced ionization signals in C and D and are connected with trapping.

The top electrodes A and B, as well as the bottom electrodes C and D are biased with the same voltage. Thus, generally, charge sharing can occur. In order to identify events with full ionization amplitude, we defined a new estimator for the energy collected in the ionization channel by summing up the ionization amplitudes via

$$\mathrm{ABCD} = \frac{\mathrm{A} + \mathrm{B} - \mathrm{C} - \mathrm{D}}{2} \quad , \tag{6.1}$$

where A,B,C and D are the ionization amplitudes measured at the four electrodes, taking into account the polarity of the signals.

The resulting ionization spectrum is shown in figure 6.3. A comparison with the spectra of the individual channels in figure 6.2 shows: For channel C and D, about $\approx 30\,\%$ of the measured events have an amplitude in the range $|E_{\mathrm{ion}}| \in [15{,}55]$ keV$_{\mathrm{ee}}$, whereas for ABCD only 13 % occur in this range. Therefore we can already conclude that there exists charge sharing. In addition, events with reduced ionization amplitude in the ABCD channel are likely originating from trapping effects.

6.3.2 Heat signal calibration based on event categories defined by charge signals

In the last section, we showed the ionization amplitude spectra for the prototype detector equipped with an ^{241}Am source. In this section, we describe the calibration process for the heat channel for the same measurement with a planar voltage configuration at the electrodes: $V_{\mathrm{A}} = V_{\mathrm{B}} = -V_{\mathrm{C}} = -V_{\mathrm{D}} = +50\,\mathrm{V}$.

In figure 6.4 we present the uncalibrated heat spectrum. The peak at an amplitude of ≈ 2500 a.u. corresponds to the 59.5 keV-peak and shows a clear broadening, especially when zooming into its region as shown in fig. 6.4 *right*. Its shape can be understood as two overlapping peaks at slightly different positions. By using the ionization amplitude spectra, we could analyze this structure in more detail. First of all, we defined events present in the $5\,\sigma$ region around the position of the 59.5 keV peak in the summed ionization amplitude spectrum ABCD as events with full charge collection. This means all electron/hole-pairs created by an interaction of an 59.9 keV γ-ray in the detector were collected. Secondly, we selected all events which fulfilled the same $5\,\sigma$ criterion in the ionization amplitude spectra

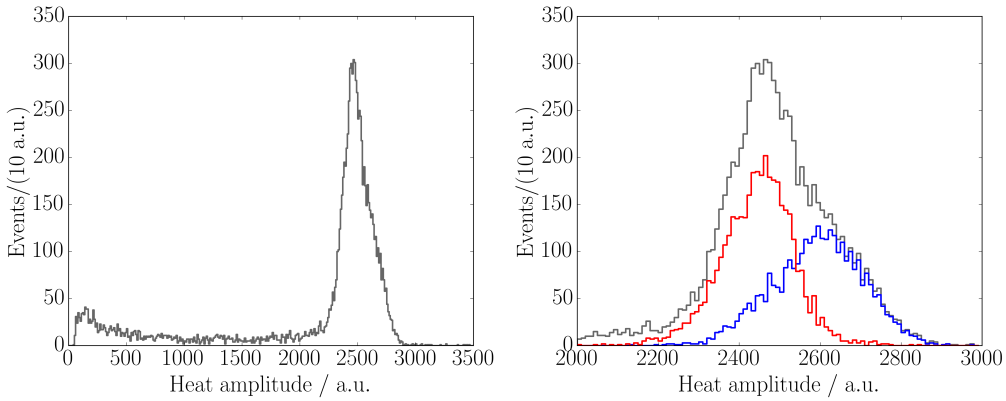

Figure 6.4: Spectra of the uncalibrated filtered heat amplitudes based on a measurement in planar mode with $V_A = V_B = -V_C = -V_D = +50\,V$. *Left:* Overall spectrum. *Right:* Zoom into the region of the 59.5 keV-peak originating from the ^{241}Am source. The overall spectrum is shown in *black*. The *blue* curve represents events which show full charge collection on the A and C electrode. The *red* curve stands for all other events with full charge collection with various combinations of the A,B,C,D electrodes (for further explanation see text).

of the A and C channels. The *blue* curve in fig. 6.4 represents all events, that fullfill the full charge collection criterion on the summed signal ABCD and the individual criteria of full charge collection on the A and C electrode. The *red* curve marks events with full charge collection events according to ABCD, but not on the A and C electrode. Clearly, the 59.5 keV-peak in the total heat amplitude spectrum splits into two peaks with different positions and different resolutions.

An explanation for the different positions of the two peaks can be that the NTL factor varies for the electrodes. This is at first sight quite unexpected, as all electrodes were supposed to be biased with the same absolute voltage of $V = 50\,V$. A reasonable explanation assumes that there is a resistance leak of one of the electrodes to ground. A detailed description will be given in section 6.3.3. For the calibration of the heat spectrum, we took this electrode-dependent NTL factor into account by calibrating the heat spectrum according to event categories defined by the ionization amplitudes.

Event categories based on the charge signals

It was described before, that the NTL amplification factor was not uniform for all events and therefore the heat spectrum differed for events collected at different combination of electrodes. The calibration process of the heat spectrum was adjusted to this behavior by categorizing all events according to all possible combinations of charge collection on the set of the four electrodes A,B,C and D. Afterwards the heat spectrum was calibrated independently for all event categories. In total there are 10 event categories which are listed in tab. 6.2. If we compare these 10 event categories with the heat spectrum shown in fig. 6.4 *right*, the *blue* curve describes the events that belong to the first category (AC). The *red* curve is a joined spectrum of the categories 2 to 9.

Category	Logic	N_j	FWHM(59.5 keV) in $\mathrm{keV_{ee}}$
1: AC	ABCD $\wedge$ A $\wedge$ C $\wedge$!B $\wedge$!D	3211	5.886 ± 0.383
2: BD	ABCD $\wedge$ B $\wedge$ D $\wedge$!A $\wedge$!C	1554	3.949 ± 0.711
3: AD	ABCD $\wedge$ A $\wedge$ D $\wedge$!B $\wedge$!C	-	-
4: BC	ABCD $\wedge$ B $\wedge$ C $\wedge$!A $\wedge$!D	-	-
5: A(C+D)	ABCD $\wedge$ A $\wedge$!B $\wedge$!C $\wedge$!D	1278	4.727 ± 1.125
6: B(C+D)	ABCD $\wedge$ B $\wedge$!A $\wedge$!C $\wedge$!D	812	3.567 ± 0.423
7: C(A+B)	ABCD $\wedge$ C $\wedge$!A $\wedge$!B $\wedge$!D	45	-
8: D(A+B)	ABCD $\wedge$ D $\wedge$!A $\wedge$!B $\wedge$!C	12	-
9: (A+B)(C+D)	ABCD $\wedge$!A $\wedge$!B $\wedge$!C $\wedge$!D	965	4.562 ± 1.531
10: Reduced	!ABCD	2773	-
All events		10650	4.864 ± 0.004

Table 6.2: Description of the 10 event categories based on ionization amplitudes. The logic characters represent *full charge collected on electrode X*. Full charge means, the amplitude of an event falls into the $5\,\sigma$ region of the 59.5 keV-peak of the specified channel X. The table also lists the number of events N_j in the different categories for a measurement with $V_\mathrm{A} = V_\mathrm{B} = -V_\mathrm{C} = -V_\mathrm{D} = +50\,\mathrm{V}$. The values for the FWHM(59.5 keV) refer to the energy resolution of the 59.5 keV-peak in the heat channel for the various categories $1-9$. Categories with too few events (3,4,6,7) and events with reduced ionization amplitude (10) are finally calibrated with an effective calibration factor c_eff (see eq. 6.2).

After calibrating the heat amplitude spectra individually for all event categories, they were superimposed in one spectrum. However, the number of events in the AD, BC, B(C+D) and D(A+B) categories were too small to be calibrated individually (see tab. 6.2). In addition, events with reduced charge collection could not be classified any further. Therefore an effective calibration factor c_eff was used for these events with

$$c_\mathrm{eff} = \sum_\mathrm{j} c_\mathrm{j} \cdot \frac{N_\mathrm{j}}{N_\mathrm{total}} \quad , \tag{6.2}$$

where N_j is the number of events in one category j and N_total the total number of events that deliver full charge on the sum of the charge signals ABCD.

The results for the heat spectrum calibration are shown in table 6.2. Events categories with low statistics and the events in the reduced charge collection category were calibrated using the calibration factor defined in eq. 6.2. In sec. 6.2 we explained that the baseline resolution of the channels is retrieved from intervals in the data streams without pulses.

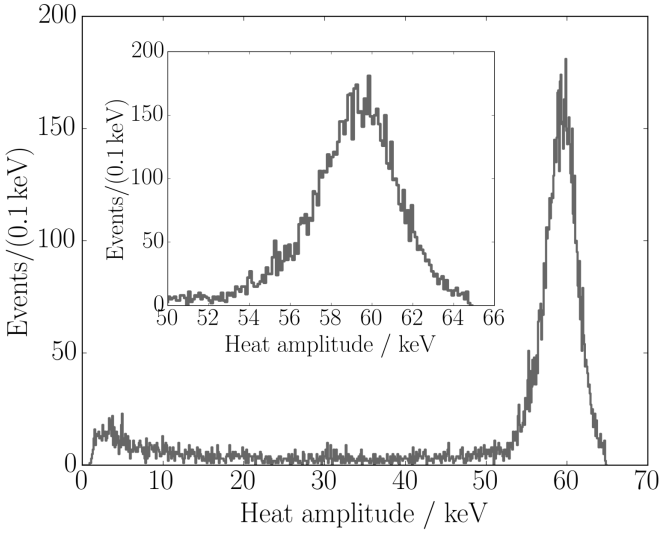

Figure 6.5: Calibrated heat spectrum. The *outer* graph shows the overall spectrum up to 65 keV and the *inner* graph a zoom into the region of the 59.5 keV peak.

The baseline amplitude spectrum is distributed around zero and the resolution can be determined by fitting a Gaussian function to it. For the heat channel, the baseline resolution FWHM(0) was calibrated with the effective calibration factor c_{eff} calculated via eq. 6.2. We find

$$\text{FWHM}\,(0) = 212\,\text{eV} \pm 1\,\text{eV} \quad . \tag{6.3}$$

The overall calibrated heat spectrum is shown in fig. 6.5. No double peak structure as in fig. 6.4 is visible. The results from a Gaussian fit to the 59.5 keV-peak show a resolution of $\text{FWHM}(59.5\,\text{keV}) = 4.864\,\text{keV} \pm 0.004\,\text{keV}$ (see also tab. 6.2) which is around 15 % better than the resolution of the 59.5 keV-peak in the uncorrected spectrum presented in fig. 6.4.

We remark that the baseline resolution (eq. 6.3) of the heat channel is around a factor 14 better than the resolution on the 59.5 keV-peak, which opens the question why the peak resolution is so enhanced in comparison to the baseline. In addition, we observe that the peak resolution in the heat channel is worse than the peak resolution in the summed ionization amplitude channel ABCD, $\text{FWHM}_{\text{ABCD}}(59.5\,\text{keV}) = 3.450\,\text{keV} \pm 0.008\,\text{keV}$ (see tab. 6.1). As the heat signal at high biases is dominated by phonons created by drifting charge carriers, the resolution of the heat channel should be limited by the charge migration properties of electrons and holes. Therefore the peak resolution in the heat channel should be at least as good as the resolution in the ABCD spectrum. Both observations point in the direction that this behavior is connected to the calorimetric part of the detector and is not a charge transport issue [143]. Actually, a study of the heat signals performed for the FID800 detectors in EDELWEISS showed that the simple thermal model of a calorimetric detector, presented in sec. 2.4 is not valid for these detectors [69]. The thermal model which actually describes the heat pulses is based on a 6 body system, which is affected by a huge parasitic heat capacity, which causes 76 % of the deposited energy of an interaction to be undetectable with the NTD Ge thermistors. A detailed study on this additional heat capacity is on-going and likely explains also our increased heat resolution.

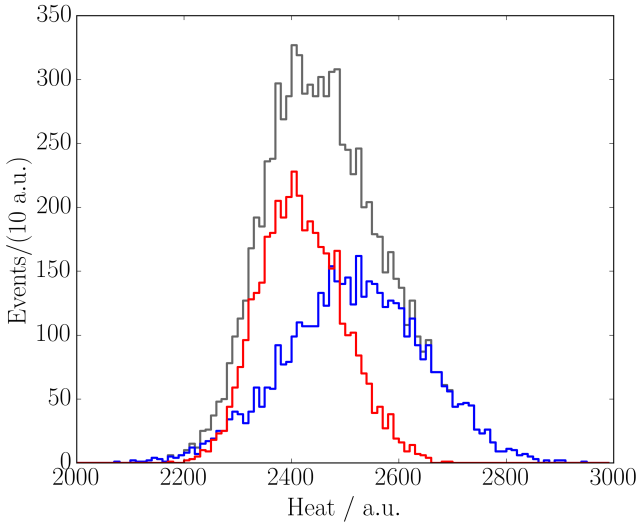

Figure 6.6: Simulated heat spectrum for a voltage configuration with $V_A = +50\,V$, $V_B = +45\,V$, $V_C = V_D = -50\,V$. The *black* curve represents all simulated events, the *blue* curve marks events with full charge collection on the A and C electrode and the *red* curve represents all other events with full charge collection.

We further remark that the peak energy resolution for events in the AC category is significant worse than for the other channels. This may be related to the loss of phonons to an additional NTD Ge thermistor, which was glued on top of the A electrode, but could not be read-out due to a problem with the cabling.

6.3.3 Discussion of different NTL amplification factors in planar mode

A straightforward explanation for the broadening of the 59.5 keV-peak in the heat spectrum caused by different NTL factors for charge collection on the various electrodes (see fig. 6.4) is that the electrode biasing is actually not planar and one of the electrodes is biased with a voltage $V < 50\,V$.

This assumption was tested by using the hot carrier transport simulation tool presented in chapter 3. The results from the heat spectrum showed that the NTL amplification factor was higher for AC events. Therefore we assumed the voltage drop to occur at the B electrode leading to an actual bias of $V_B = +45\,V$. For the simulation we assumed the source to be monoenergetic, and to emit γ-rays isotropically, leading to energy deposits of 59.5 keV according to a penetration depth of 1 mm in the HPGe (see sec. 3.4.7). The output of the simulation contained the ionization amplitudes as well as the NTL amplified heat amplitudes. The simulated events were categorized according to the ionization amplitudes into two groups as for the spectra shown fig. 6.4 *right*. The first category contains all events with full charge collection on the A and C electrodes, the second category all other events with full charge collection. The heat spectra for both event categories were smeared with the experimental resolution of the 59.5 keV-peaks with $\mathrm{FWHM_{AC}} = (6.5 \pm 0.3)\,\mathrm{keV_{ee}}$ and $\mathrm{FWHM_{others}} = (3.5 \pm 0.1)\,\mathrm{keV_{ee}}$. In fig. 6.6 the simulated heat spectrum is shown. The *blue* curves mark the events in the AC category and the *red* curve all other events. The amplitudes were scaled to match the uncalibrated experimental heat spectrum in fig. 6.4.

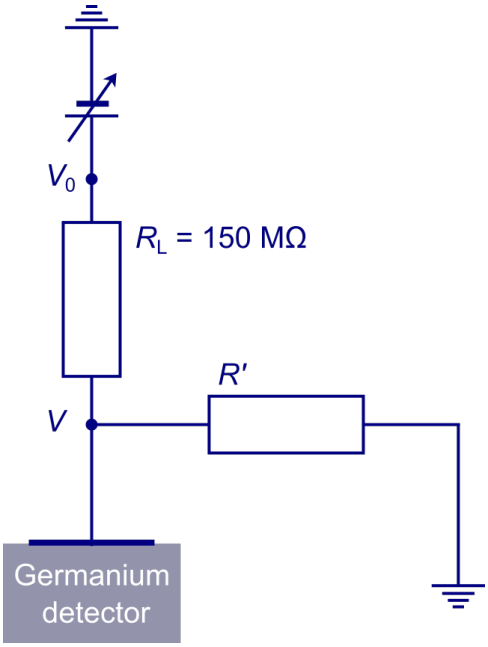

Figure 6.7: Schematic view of the electrode bias circuit. In case of a resistance leakage R' to the ground, the applied voltage V_0 is different from the actual voltage V at the electrode on the detector. R_L is the load resistance of an electrode.

Clearly, there is a good agreement of simulation and data (see fig. 6.4) for the 59.5 keV-peak (see fig. 6.6 *right*). Therefore, we can confirm that the shape of the 59.5 keV peak in our experimental heat spectrum is caused by an reduced voltage on the B electrode.

The scheme in fig. 6.7 represents a bias circuit for the electrodes which can explain an unexpected voltage drop on one of the electrodes. At the level of the batteries, the same voltage V_0 is provided and measured for all electrodes. As the biasing is actually achieved by using a load resistance of $R_L = 150\,\mathrm{M\Omega}$, a leakage resistance R' to the ground would cause a voltage drop at the stage of the electrodes. Therefore, V depends on the leak resistance to ground and can be calculated via

$$V = \frac{V_0 R'}{(R' + R_L)} \quad . \tag{6.4}$$

To get an idea how the leakage resistance influences the electrode bias, we assume a realistic leakage of $R' = 2\,\mathrm{G\Omega}$. For an applied voltage of $V_0 = 50\,\mathrm{V}$, eq. 6.4 predicts a voltage at the electrode $V = 46.5\,\mathrm{V}$. This is very close to the value we used for the B electrode, $V_B = 45\,\mathrm{V}$, to reproduce the experimental heat spectrum with the simulation. Therefore the leakage resistance to the ground is an appropriate explanation of the phenomenon of having two NTL amplification factors in a mode that is otherwise expected to be planar.

6.4 Linearity of the NTL amplification factor

The first step, in order to analyze the performance of the HPGe prototype detector towards high voltages was to evaluate the linearity of the NTL effect and study the behavior of the Signal-to-Noise Ratio (SNR). As a reminder, we chose a planar voltage configuration for all measurements in order to have only one NTL amplification factor.

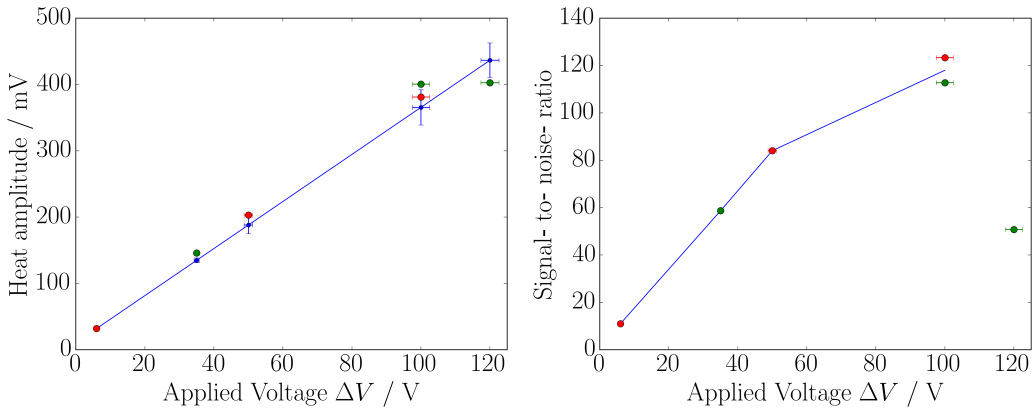

Figure 6.8: *Left:* Amplitude of the 59.5 keV-peak in mV versus electrode bias ΔV. The *blue* curve and dots mark the amplitudes of the 59.5 keV-peak expected from a linear NTL effect (see eq. 2.4) extrapolating from the peak measurement at $\Delta V = 6$ V. The *red* and *green* dots represent the actually measured positions of the 59.5 keV-peak at the given biases. *Right:* Signal-to-Noise-Ratio (SNR) versus electrode bias ΔV. The *blue* curve connects the data points. In both plots the *red* dots represent measurements with $V_A = V_B > 0$ V and the *green* dots measurements with $V_A = V_B < 0$ V. The uncertainties of the data points are dominated by the uncertainty in the electrode bias described in sec. 6.3.3. For the measured amplifications, the error bars are smaller than the marker size.

The *left* plot in fig. 6.8 shows that the 59.5 keV-peak amplitude in the heat channel of our prototype detector is linearly amplified according to our expectation from the NTL effect up to an electrode bias of $\Delta V = 100$ V. There is a trend that the actually measured heat amplitudes of the 59.5 keV-peak (*green* and *red* dots) are higher than expected from the extrapolation of the measured peak position at $\Delta V = 6$ V (*blue* curve and dots). This can be explained by the uncertainty of the actual electrode bias described in the last section.

The measured 59.5 keV-peak amplitude at $\Delta V = 120$ V is the first data point with a lower value as expected from the linear extrapolation from the measurement at $\Delta V = 6$ V. This is caused by a starting break down of the detector originating from the build-up of leakage currents between the electrodes. It becomes obvious by analyzing the SNR as shown in fig. 6.8 *right*. The SNR increases as expected with the electrode bias up to $\Delta V = 100$ V. For the next higher electrode bias $\Delta V = 120$ V, the SNR is reduced by more than a factor of 2 in comparison to $\Delta V = 100$ V, although the NTL amplification factor is only slightly reduced in comparison to the linear expectation. We conclude that the SNR is a much better indicator for a starting break down of the detector than the NTL amplification factor.

The SNR does not show a pure linear behavior as noise levels differ from measurement to measurement and experimental conditions are not exactly reproducible. In these measurements no significant difference for the linearity of the NTL effect and the SNR was observed by changing the polarity on the detector from $V_A = V_B > 0$ V (*red* dots) to $V_A = V_B < 0$ V (*green* dots).

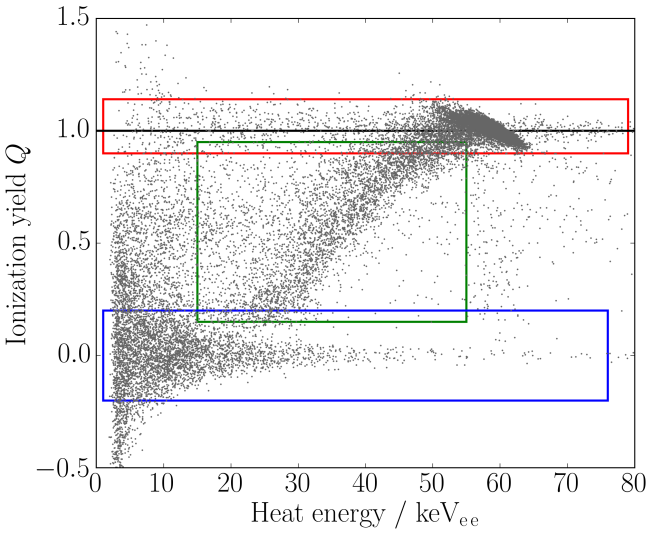

Figure 6.9: Ionization yield Q versus heat energy in $\mathrm{keV_{ee}}$ for a low electric field configuration with $V_\mathrm{A} = V_\mathrm{B} = -V_\mathrm{C} = -V_\mathrm{D} = +3\,\mathrm{V}$. The three colored boxes mark the main structures of events in this plot. **1** / *red:* Events with full charge collection, **2** / *green:* Events with incomplete charge collection, **3** / *blue:* Events with no charge signal above the baseline noise.

6.5 Study of the detector performance for a low electric field configuration

By using the FID800 EDELWEISS detectors in an operation mode with high electric fields, the experiment enters a complete new area of detection. First tests with these detectors showed promising results, as the NTL amplification showed a linear behavior and some detectors could hold voltages up to $\Delta V = 100\,\mathrm{V}$ [90]. The aim of this work is to get a deep inside in the detector operation at different voltages, including the analysis of charge transport effects as well as developing pratical solutions to identify and eventually suppress the unknown heat-only event background.

Therefore the detector was first studied in case of a low electric field with an electrode bias of $V_\mathrm{A} = V_\mathrm{B} = -V_\mathrm{C} = -V_\mathrm{D} = +3\,\mathrm{V}$, where the expected performance is close to the standard operation mode in EDELWEISS.

6.5.1 Ionization yield in the low electric field limit

In sec. 6.4, we showed that the NTL amplification behaves linearly as we expected. Based on these results, a more detailed analysis of the detector performance was performed at different electrode biases.

The study of the performance of the prototype detector at an electrode bias of $V_\mathrm{A} = V_\mathrm{B} = -V_\mathrm{C} = -V_\mathrm{D} = +3\,\mathrm{V}$ is based on the analysis of the ionization yield Q, which is the ratio of the measured ionization signal E_ion and the recoil energy E_rec (see sec. 2.1). As the detector was operated at a low electrode voltages the NTL amplification factor was small and the energy measured in the heat channel H is approximately proportional to the recoil energy E_rec of an interaction (see eq. 2.3). In addition, our experiment was equipped with an ^{241}Am source emitting γ-rays which cause electron recoils in Ge and

create more electron/hole-pairs than nuclear recoils, originating from neutrons or WIMP candidates with the same energy. In general, the ionization yield is normalized to the number of e^-/h^+-pairs created by electron recoils. Therefore, as in our case the detector was irradiated with γ-rays, we expect an ionization yield $Q = 1$.

The results for the ionization yield Q in the studied low electric field case is shown in fig. 6.9. It is defined as the ratio of the calibrated summed ionization amplitude spectrum ABCD and the calibrated heat spectrum according to section 6.3.2. Clearly, not only events at $Q = 1$ but also at $Q < 1$ show up.

The large majority of events occurs at $Q \approx 1$ as highlighted by the *red* box. The actual elliptical shape of the distribution is caused by the energy resolutions in the ionization and heat channels. The majority of events in the *red* box have an energy of $H = 59.5\,\mathrm{keV_{ee}}$ as expected for γ-rays from the ^{241}Am source. Events with $Q \approx 1$ deliver the same amount of energy in the heat and ionization channel, which means all created e^-/h^+-pairs are collected at the electrodes. Therefore we can classify the events marked by the *red* box as events with full charge collection. There are additional events outside the $59.5\,\mathrm{keV_{ee}}$ region which also have $Q \approx 1$ and therefore are also events with full charge collection. These event originate from γ-rays that already lost some of their primary energy in other parts of the detector before they interacted in the sensitive area or from events which only deposited parts of their energy in the sensitive area and then escaped.

The *green* box marks all the events, where the ionization amplitude is reduced in comparison to the heat amplitude. These events are clearly connected to the phenomenon of charge trapping, where electrons and holes created in the primary interaction are either bound to impurities on their way to the electrodes or reach surface regions which are not covered by an electrode. This hypothesis of charge trapping will be discussed in detail and verified in sec. 6.5.2 by comparing the experimental results to the output of the charge migration simulation tool explained in chap. 3.

There is a third group of events which is highlighted by the *blue* box. These events have very low Q-values which are consistent with no signal amplitude larger than the baseline noise for the ionization channel ABCD ($E_{\mathrm{ion}} < 3\,\mathrm{keV_{ee}}$), whereas the heat signal amplitude clearly exceeds the baseline noise. These events are so-called heat-only events, as they deliver only a signal in the heat channel. The origin of these events is not understood so far and represents one of the main background sources in the EDELWEISS experiment in the Modane underground laboratory (see sec. 2.6.4). Although we could not find the origin for these events either, we made use of the analysis tool presented in sec. 6.2.2. We found that the shape of the heat-only signals differs from the shape of heat signals that also showed a significant signal on at least one of the ionization channels. Based on the shape parameters of the heat signals, we could discriminate the heat-only events from the other events. The details of this analysis are presented in sec. 6.5.3.

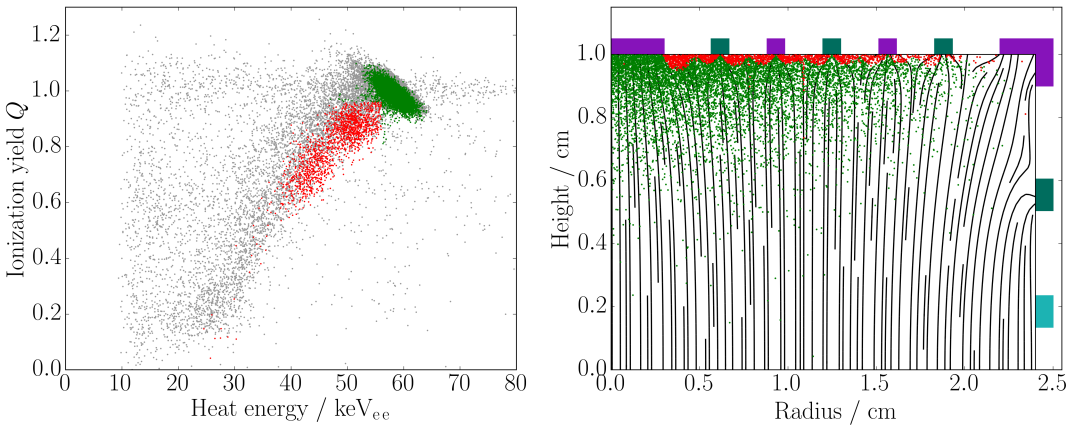

Figure 6.10: *Left:* Ionization yield Q versus heat energy in keV$_{ee}$. The *grey* dots represent the experimental data for $V_A = V_B = -V_C = -V_D = +3\,V$. The *green* and *red* dots mark the results from MC simulation. *Green* dots highlight events with full charge collection and therefore $Q \approx 1$, *red* dots highlight events with reduced $Q < 1$ due to trapping. *Right*: Event locations in the upper half of the detector retrieved from simulation. *Violet* and *green* rectangles mark the electrodes A and B. The electric field lines are shown as *solid* lines. Events affected by trapping (*red* dots) are located close to the surface and in-between the electrodes. For the simulation a monoenergetic source emitting isotropically 59.5 keV γ-rays and producing single energy deposits in the crystal was assumed. For the experimental data events which show no signal above the baseline noise in the summed ionization ABCD (heat-only events) are not shown.

6.5.2 Qualitative analysis of charge trapping effects in experiment and simulation

To confirm that the events occurring in the *green* box in fig. 6.9 are event with reduced ionization amplitudes due to trapping, we performed a simulation of the experimental set-up using the MC tool presented in chap. 3 which also takes into account the trapping of charge carriers. In order to compare the ionization yield Q from simulation with data, the simulated ionization and heat amplitudes were smeared with the experimental resolutions on the 59.5 keV$_{ee}$-peak with $\sigma_{ABCD} = 0.78\,keV_{ee}$ and $\sigma_{Heat} = 1.54\,keV_{ee}$. In fig. 6.10 the experimental results already shown in fig. 6.9 for the ionization yield Q (*gray* dots) are now displayed together with results from the Monte Carlo simulation tool (*green* and *red* dots).

Although the assumptions in the MC tool strongly simplify the experimental set-up, e.g. events interacting multiple times in the detector are ignored as well as events caused by radiation that already deposited some amount of energy in other parts of the experiment, there is a qualitatively good agreement between Q-values from simulation and data. Both data sets show the majority of events distributed around $Q \approx 1$ and heat energies around $H = 59.5\,keV_{ee}$, which represent events with full charge collection (*green* dots). In addition, both data sets show events with reduced Q-value, which in case of the simulation (*red dots*) can only be caused by trapping.

In figure 6.10 *left* we classified the simulated events into two groups: *Green* dots highlight events with full charge collection ($Q > 0.95 \wedge H > 56\,\mathrm{keV_{ee}}$) and *red* dots highlight events with reduced charge collection due to trapping. This allows us to identify the locations of the events affected by trapping. In figure 6.10 *right* we clearly see that events affected by trapping are located in the surface region and in-between the ring electrodes. Furthermore, 99.6 % of the events affected by trapping are located within 0.5 mm distance from the surface. We conclude that surface trapping, caused by charge carriers that reach the surface at regions which are not covered by an electrode, is the dominant process leading to reduced ionization amplitudes and therefore reduced Q-values.

A closer look shows that the experimental data extend to much lower ionization yields Q than the data retrieved from MC simulation. It looks like trapping effects in the experiment are stronger than expected from simulation. This is likely the case as the simulation does not treat charge build-up and detector degradation: For every event, the electric field configuration is assumed to be only defined by the voltages applied on the electrodes. Charged impurities caused by trapped charge carriers are not considered, however the reduced ionization and heat amplitudes caused by the stopped charge carriers is taken into account (see sec. 3.3.4). In the experiment the charged impurities should by avoided by a proper reset of the detector (see sec. 4.5). However, even after a long regeneration there are still some charged impurities remaining and an operation of the detector at low electric field favors a fast build-up of charged impurities.

There is an additional group of events in the experimental data which does not occur in the simulation. For these events $Q \approx 1$ holds, but the heat energy is below 59.5 keV. These events are simply not considered in the simulation as they originate from radiation that deposited some energy via Compton scattering in other parts of the set-up before interacting in the sensitive area or only deposited parts of their energy and escaped afterwards.

Furthermore the results from simulation show that no heat-only events are expected for interactions caused by a γ-ray source. Therefore we can conclude that the heat-only events are not caused by charge migration processes in HPGe detectors and the origin of these events must lay somewhere else. The heat-only events are discussed in the next section.

6.5.3 Investigation of discrimination of heat-only events

Up to now the origin of heat-only events in the EDELWEISS-III detectors is not known. However, they are the dominant background and studies are on-going to clarify their origin (see sec. 2.6.4). Heat-only events are not exclusively connected to the EDELWEISS-III set-up as our experimental results (see fig 6.5.1 *blue* box) also showed a significant population of heat-only events. However, in contrast to the set-up in the Modane underground laboratory, our data acquisition system allowed a sampling frequency of 20 kHz and provided us with the required resolution for the shape of the heat signals. Based on shape parameters provided by the analysis framework presented in section 6.2, we developed a method to discriminate heat-only events.

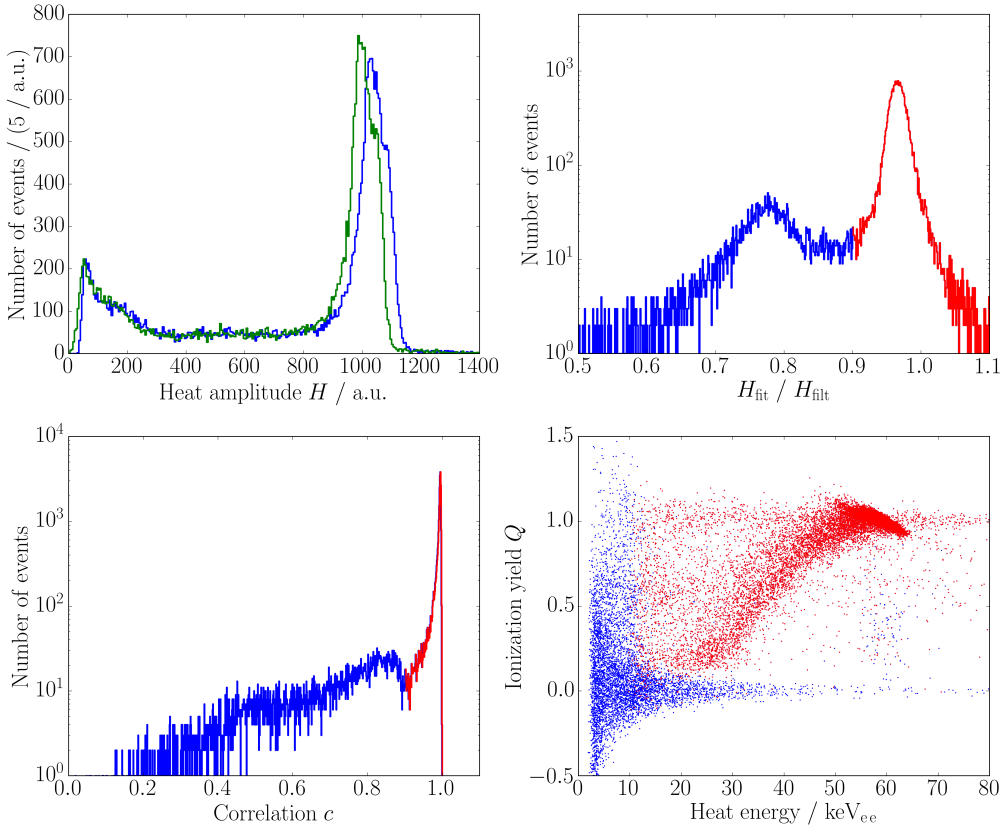

Figure 6.11: *Top left:* Uncalibrated heat amplitude spectra, the *blue* is based on the maxima of the filtered pulses, the *green* is extracted from a linear fit of the filtered pulses against the reference pulse. *Top right:* Ratio of filtered amplitudes to fitted amplitudes, *red* represents H_{fit} / $H_{\mathrm{filt}} > 0.9$ and *blue* H_{fit} / $H_{\mathrm{filt}} \leq 0.9$. *Bottom left:* Correlation of filtered pulse to reference pulse, *red* marks $c > 0.9$ and *blue* $c \leq 0.9$. *Bottom right:* Ionization yield Q versus heat energy in $\mathrm{keV_{ee}}$, *red* dots mark events after applying a cut with H_{fit} / $H_{\mathrm{filt}} > 0.9 \wedge c > 0.9$, *blue* dots mark the remaining events.

As already explained in sec. 6.2 the signal amplitudes for the measured pulses are determined in different ways. The heat amplitude parameter we have used so far is the filtered heat amplitude H_{filt}, which is retrieved from an optimal filter. As discussed before, the optimal filter used here, maximizes the signal to noisr ratio and is rarely affected by the shape of the heat pulse. The analysis tool provides a second method to extract the heat amplitude by plotting the reference pulse against the actual pulse, and fitting a linear function to this plot. The slope of this linear function then defines the fitted heat amplitude H_{fit} of the pulse and is clearly affected by the agreement of the shapes of the two pulses.

In fig. 6.11 *upper left*, the heat amplitude spectra for the filtered H_{filt} and fitted heat amplitudes H_{fit} are shown. A clear shift of the 59.5 keV-peaks of the two spectra can be observed. By plotting the ratio H_{fit} / H_{filt} (*upper right* graphic), this shift can be identified as a two peak structure describing two event populations with different pulse-

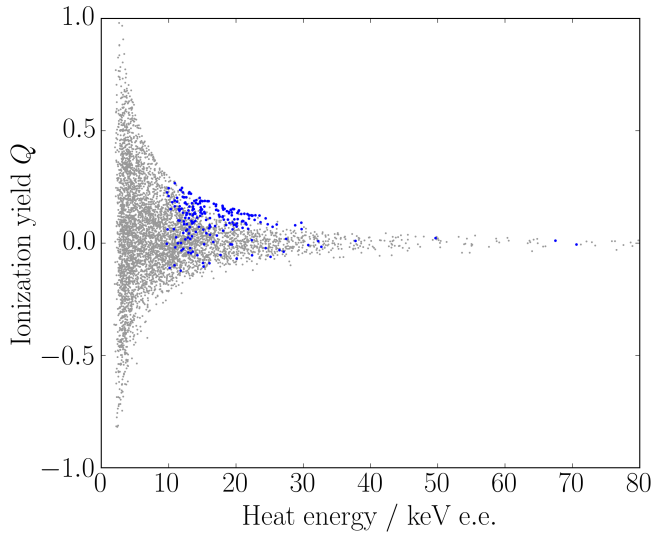

Figure 6.12: Ionization yield Q versus heat energy. The *grey* dots represent all events where the ionization amplitude ABCD is smaller than the baseline amplitude spectrum with (ABCD $< 3.0\,\mathrm{keV_{ee}}$). The *blue* dots mark events that are not rejected by $H_{\mathrm{fit}} \,/\, H_{\mathrm{filt}} > 0.9 \wedge c > 0.9$. The rejection efficiency for heat-only events is 95.6 %.

shape parameters. In order to discriminate heat-only events, we defined a cut accepting all events with $H_{\mathrm{fit}} \,/\, H_{\mathrm{filt}} > 0.9$ (*red* line) as regular pulses and rejected the other events as being from type heat-only (*blue* line).

We studied a second pulse-shape parameter, which is the correlation c between a triggered pulse and the reference pulse. It is calculated for every triggered pulse and converges to $c = 1$, in case the pulse-shape of the single pulse and reference pulse are in good agreement. The *lower left* graphic in figure 6.11 shows the distribution of the correlation c for the measured pulses. We observe two contributions, one with c close to 1 and another extending down to $c = 0.1$. For our analysis we accepted all heat signals with a correlation $c > 0.9$ as regular pulses (*red* line) and rejected all other events as being from type heat-only (*blue* line).

Finally we combined the two criteria and accepted only pulses that fullfill $H_{\mathrm{fit}} \,/\, H_{\mathrm{filt}} > 0.9 \wedge c > 0.9$. With this cut we split the events in two categories as shown in the *lower right* graphic of fig. 6.11. The *red* dots represent accepted events and the *blue* dots rejected events. As one can directly see, most of the heat-only events can be discriminated by this procedure. The fact that also some of the low energy events with a Q-value close to one are rejected, is caused by the energy resolution in the heat channel. The smaller the heat amplitude of a pulse is in comparison to the amplitude spectrum of the baseline noise, the less sensitive is any pulse-shape parameter as the shape of the pulse is dominated by noise. Consequently, in our case we can define our pulse-shape based heat-only discrimination method as efficient for energies above $10\,\mathrm{keV_{ee}}$.

The efficiency of our heat-only event rejection method is shown in figure 6.12. The events marked by the *gray* dots were selected based on the ionization amplitude ABCD. They are classified as heat-only events as their ionization amplitude ABCD is smaller than $3.0\,\mathrm{keV_{ee}}$ which is the FWHM of the baseline amplitude spectrum. After applying the cut presented in this section, all events but the events marked by the *blue* dots are rejected, illustrating a rejection efficiency for heat-only events of 95.6 %.

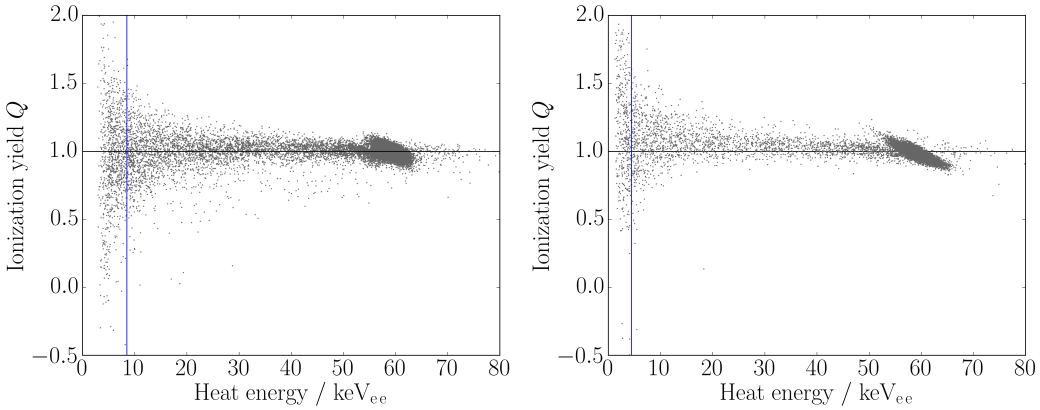

Figure 6.13: Ionization yield Q versus heat energy for two voltage configurations, *left:* $V_A = V_B = -V_C = -V_D = 25\,V$ ($\Delta V = 50\,V$), *right:* $V_A = V_B = -V_C = -V_D = 50\,V$ ($\Delta V = 100\,V$). The *blue* vertical lines are explained in sec. 6.6.2.

This study makes clear that the recording and analyzing of the full shape of the heat signal can be a very helpful tool to lower the effect of heat-only background events. A possible rejection method for heat-only events is not limited by only considering the two pulse-shape parameters presented here. There are additional parameters like the rise and decay times of the signals, which are also sensitive to the pulse-shape and could help to improve the rejection method.

6.6 Study of the detector performance for high electric field configurations

In the last section we showed that the ionization yield Q is a good parameter to characterize the detector performance in our calibration experiment, showing that the major limiting effects on its performance are caused by charge trapping and heat-only events. In this section we focus on the detector performance with increasing voltage. We will show that especially the interpretation of the Q-value changes and is not a good estimator for the detector performance any more.

6.6.1 Ionization yield in the high electric field limit

In fig. 6.13 the results for ionization yield Q versus the heat energy for two voltage configurations are presented. The *left* graphic shows the results from a measurement with an electrode bias of $\Delta V = 50\,V$ and the *right* one for a measurement with $\Delta V = 100\,V$. We clearly see that the distribution of Q-values is more narrowed around 1 when increasing the electrode bias, which owes to the fact, that the energy resolution improves with increasing bias as charge collection is more efficient for higher electric fields.

If we compare the ionization yield Q shown in fig. 6.13 with the results for the measurement at low electric field presented in fig 6.9, we mark two differences: In the high electric field configurations the two populations with $Q < 1$ are missing in contrast to the low electric field case were we associated these populations to events affected by charge trapping and heat-only events. Actually, these populations did not really disappear but the interpretation of the Q-value changes dramatically for high voltages.

As already explained in sec. 2.3 with increasing electrode bias the heat signal is more and more dominated by the phonons produced during the drift of the electrons and holes (NTL effect) than by the phonons created in the primary interaction. Therefore the relation between heat signal and recoil energy $H \approx E_{\mathrm{rec}}$ does not hold any more and has to be replaced by $H \approx E_{\mathrm{ion}}$. With increasing electric field the Q-value converges then to 1 for all interactions and events that are affected by charge migration will also have a Q-value of 1. Thus, interactions where trapping was involved do not disappear but show up at smaller heat energies in the Q-plot, as the heat amplitude per unit energy deposit is reduced in comparison to events with full charge collection.

In conclusion, for high electric fields the ionization yield Q can not be used to study charge trapping effects. However, trapping is very critical for the detector performance and can lead to a misinterpretations of the recoil energy. Therefore we used a different approach to study charge trapping at high electrode biases based on the MC simulation tool for charge migration in HPGe crystals presented in chap. 3. The fact that charge trapping effects are represented in an adequate way in the simulation was already shown for the low electric field case (sec. 6.5.2). For high biases, trapping will be discussed in sec. 6.7.3, as it is a very important background and has to be considered for the optimization of the detector performance (see sec. 6.8).

In fig. 6.13, we saw that apparently also the heat-only event populations are missing for the high electric field cases. This is caused by the operation of the detector in the NTL amplified mode and will be discussed in the next section.

6.6.2 Heat-only events in the case of high electric fields

In order to explain the missing population of heat-only events in fig. 6.13, we analyzed the data of a measurement at medium electrode bias with $\Delta V = 35\,\mathrm{V}$. The results for the ionization yield Q are presented in figure 6.14. We see a population of heat-only events, although their maximal heat energy is below $15\,\mathrm{keV_{ee}}$ in comparison to the low electric field case, where we found events with heat energies up to $70\,\mathrm{keV_{ee}}$ (see fig. 6.9).

This artifact is caused by the fact that the measured heat signal per unit deposited energy H/E_{rec} in case of a proper interaction in the detector, producing electron/hole-pairs, depends on the electrode bias via $H/E_{\mathrm{rec}} = (1 + \Delta V/\epsilon)$, with $\epsilon = 3$ for electron recoils (see sec. 2.3). In contrast to that the signals of the heat-only events are not amplified by the electrode bias since no ionization is produced. To show that this explains the missing heat-only event population in the high electric field cases, we present a simple example:

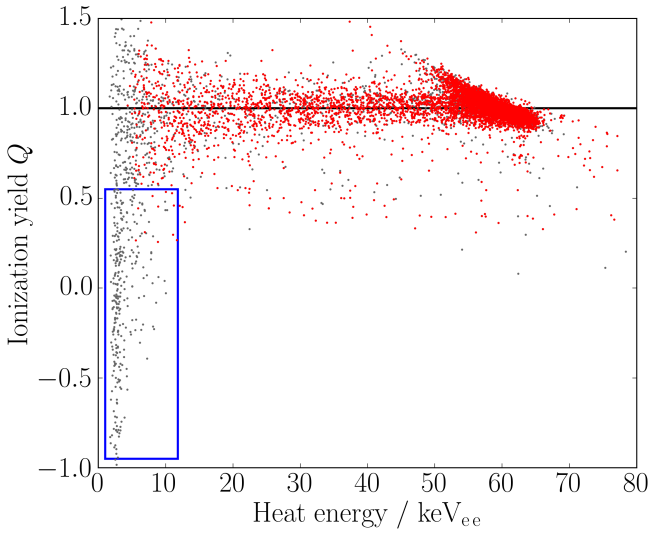

Figure 6.14: Ionization yield Q versus heat energy for $V_A = V_B = -V_C = -V_D = 17.5\,V$ ($\Delta V = 35\,V$). Few events are located in the *blue* box where heat-only events are expected to occur. For details see sec. 6.6.2.

In the low electric field case presented in fig. 6.9, the heat energies of heat-only events with a significant statistic range up to around $50\,keV_{ee}$ (*blue* box). Based on the NTL amplification factors $f_{NTL} = (1 + \Delta V/3)$ for $\Delta V = 6\,V$ with $f_{NTL1} = 3$ and for $\Delta V = 35\,V$ with $f_{NTL2} \approx 12.7$, we can calculate the expected upper energy bound for heat-only events for $\Delta V = 35\,V$ via $50\,keV_{ee} \cdot f_{NTL1}/f_{NTL1} \approx 11.8\,keV_{ee}$. A box with an upper limit of $11.8\,keV_{ee}$ is drawn in fig. 6.14 and clearly marks the population of heat-only events. We can now calculate the upper bound for heat-only event amplitudes expected at $\Delta V = 50\,V$ and $\Delta V = 100\,V$ and we get upper bounds to be about $4.4\,keV_{ee}$ and $8.5\,keV_{ee}$. These are represented by the lines in fig. 6.13. As the resolution of the ionization yield Q is mainly defined by the ionization amplitude resolution and this only slightly improves for high biases according to the more efficient charge collection, the heat-only events are hidden in the wide distribution of Q-values at low heat amplitudes. In the case of $\Delta V = 50\,V$ we can still classify a few events as heat-only with very small Q-values but not for $\Delta V = 100\,V$.

In order to test the heat-only event rejection method presented in sec. 6.5.3, we applied the same rejection criteria to the events measured at $\Delta V = 35$. In fig. 6.14, we see that the accepted events (*red* dots) are free of heat-only events.

Eventually, our observations of heat-only events support the statement that heat-only events are not events affected by poor charge collection. They are either produced by interactions outside the HPGe crystal, e.g. the NTD Ge thermistor or they are not connected to particle interactions at all. In case their origin can not be found, a pulse-shape analysis is a viable tool to reduce the effect of these background events on low-mass WIMP searches with the EDELWEISS detectors.

6.7 Charge transport and charge trapping in a HPGe detector at high electric fields

In order to optimize the EDELWEISS detector for the operation with high electrode biases, it is very important to have a good understanding of the detector performance. Since at high electric field the ionization signals as well as the heat signals are determined by the charge transport of electrons and holes, the key to optimize the detector performance is to understand the charge transport. Especially charge trapping is a limiting factor and leads to miscalculation of the primary recoil energy by an interacting particle.

In order to evaluate our understanding of charge migration in the prototype detector, we analyzed the detector for different high bias conditions using the persuasive power of a comparison of simulation and data. An important tool for our analysis are the event categories based on the ionization amplitudes presented in sec. 6.3, as they contain information about scattering, trapping and transport anisotropies of electrons and holes.

The calibration experiment was equipped with an ^{241}Am source, which produced near-surface interactions. Therefore we could study the individual charge migration properties of electrons and holes in different measurements by simply switching the polarity of the electrode biases. The results are presented in sec. 6.7.1 and sec. 6.7.2. In addition, the nature of trapping effects is analyzed in section 6.7.3.

6.7.1 Detector signals in case of long electron tracks

The analysis results presented in this section make use of all 5 detection channels (4 ionization channels + 1 heat channel), as especially the ionization amplitudes contain valuable information about the charge transport in the detector. For this study we focused on experimental and simulated data with an electrode bias of $V_A = V_B = -V_C = -V_D = -50\,V$. The ^{241}Am calibration source (see fig. 4.1) faced the top surface of the detector covered with the A and B electrode. It emitted 59.5 keV γ-rays which mainly interacted close to the surface of the detector and produced e^-/h^+-pairs close to the A and B electrode. Hence, $V_A = V_B = -50\,V$, holes are collected quickly at the A and B electrodes and the charge transport for this experiment is dominated by electrons, which have to migrate through the whole crystal and are collected at the bottom electrodes C and D. The electric field lines for such an operation in planar mode are shown in fig. 6.17.

Qualitative comparison of simulated and experimental ionization amplitudes

The first step of our analysis was to compare the ionization amplitudes on the four sets of electrodes retrieved from simulation and data for the calibration experiment with a monoenergetic source emitting 59.5 keV γ-rays.

The results for the signal amplitudes on the four ionization channels A,B,C and D are shown in figure 6.15. We clearly see that the main structures in the experimental data are

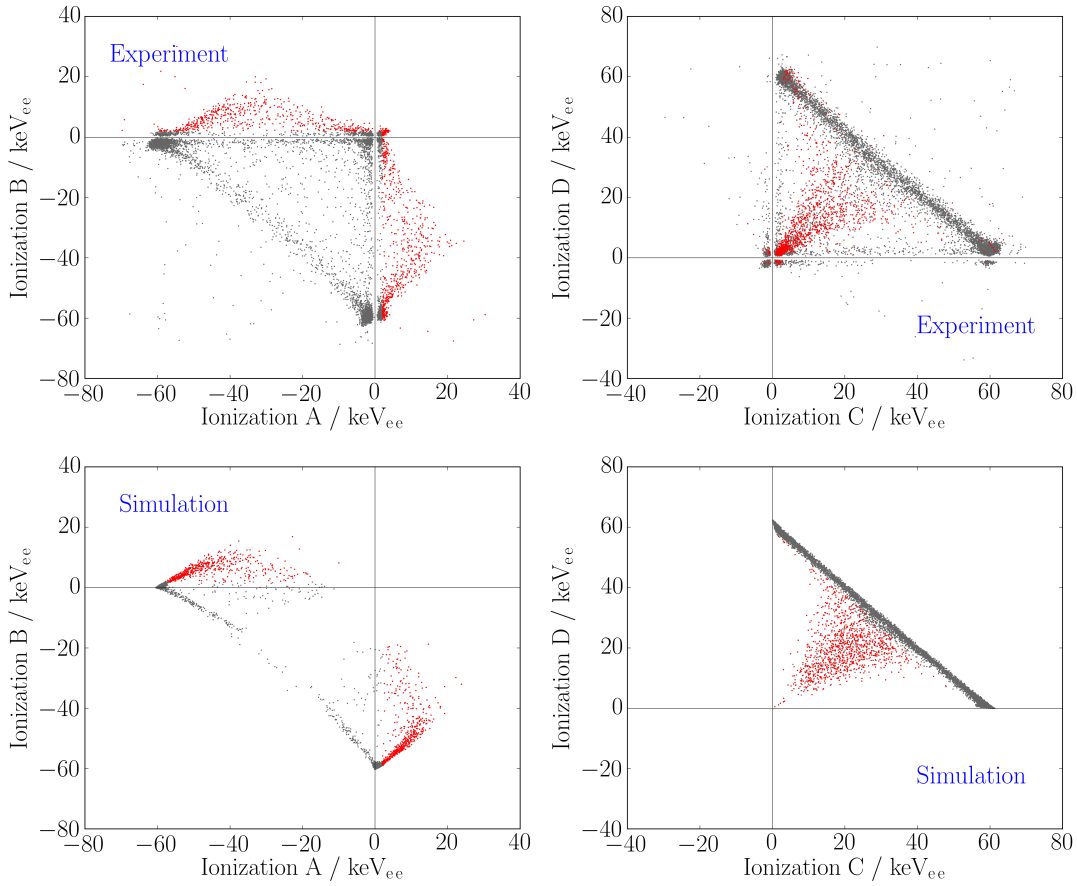

Figure 6.15: *Left:* Ionization signals of channel A versus channel B. *Right:* Ionization signals of channel C versus channel B. The signs of the signal amplitudes indicate the carrier type which is collected. A and B collect holes and the signals have negative amplitude. C and D collect electrons and the signals have positive amplitude. Special events with an ionization signal opposite to the expectation from the carrier type to be collected are marked by *red* dots. The figures at the *top* show the results from experiment, the *bottom* figures from simulation. The voltage configuration was $V_A = V_B = -V_C = -V_D = -50\,V$. For explanations see sec. 6.7.1.

reproduced in the simulation and we mark 4 dominant populations of events:

1. Events with a maximal ionization amplitude around $-59.5\,keV_{ee}$ in the A or B channel[1] and events with a maximal ionization amplitude around $59.5\,keV_{ee}$ in the C or D channel.

2. Events with an ionization amplitude in the A and B channel (events along the line connecting ionization A $\approx -59.5\,keV_{ee}$ / ionization B $\approx 0\,keV_{ee}$ and ionization A $\approx 0\,keV_{ee}$ / ionization B $\approx -59.5\,keV_{ee}$) and events with an ionization amplitude in

[1]The negative sign here contains the information about the charge of the collected carries. In this case the electrode bias was $V_A = V_B = -V_C = -V_D = -50\,V$ and therefore the A and B electrodes collect holes and the ionization amplitudes on these electrodes are negative.

the C and D channel (events along the line connecting ionization C $\approx 59.5\,\mathrm{keV_{ee}}$ / ionization D $\approx 0\,\mathrm{keV_{ee}}$ and ionization C $\approx 0\,\mathrm{keV_{ee}}$ / ionization D $\approx 59.5\,\mathrm{keV_{ee}}$). We note that the population of events with shared signals on C and D is larger than the population of events with shared signals on A and B.

3. Events with an ionization amplitude larger than $0\,\mathrm{keV_{ee}}$ on A or B, which is surprising as A and B collect holes, which create negative signal amplitudes. These events show a reduced signal amplitude in the C and D channel and are marked by the *red* dots.

4. Events with ionization amplitudes along the zero axis of ionization amplitude A and B, as well as C and D. This event population does only appear in the experimental data.

Since we know the properties of electron and hole transport in the HPGe crystal which are implemented in the MC charge transport model, we can characterize the 4 main populations:

1. All electrons drift either to the C or D electrode and all holes drift either to the A or B electrode according to our expectation from the shape of the electric field lines (see fig. 6.17 *top left*).

2. Electron collection is shared between the C and D electrodes and hole collection is shared between the A and B electrodes. The population of shared events on the C and D electrode is larger than for A and B as electrons have a strong transport anisotropy (see sec. 3.3.1) and are drifted in an angle of $35\,^\circ$ to the electric field. In contrast to that, in the simulation, no transport anisotropy is implemented for the holes and they drift strictly along the electric field lines.

3. The events marked as *red* dots in fig. 6.15 are caused by charge carrier trapping. These events deliver a shared signal on the C and D electrode, which is in total smaller than $59.5\,\mathrm{keV}$. The C and D electrode are biased with a voltage $V_\mathrm{C} = V_\mathrm{D} > 0\,\mathrm{V}$. Therefore, they collect electrons and the trapped charge carriers are electrons. While charge carriers drift through the crystal, they induce charge on all electrodes and the induced charge signal is larger the closer to an electrode the charge carriers are migrating (see sec. 3.4.2). In our case, the charge carriers are produced close to the A and B electrodes and therefore electrons induce a large signal with positive sign on the A and B electrode. In case of full charge collection the contribution of induced charge to the net ionization amplitude on the A and B electrodes is zero as the induced signal returns to zero after the electrons are collected on the C and D electrodes. In our case parts of the electrons were trapped and therefore the induced part of ionization signal on the A and B channels did not return to zero. A net ionization amplitude with a sign opposite to the expectation from hole collection remains. We did not find events with negative ionization amplitudes on C and D, as holes are drifted far away from these electrodes and therefore even in case trapping occurs, the induced charge signal on the C and D electrodes was negligible.

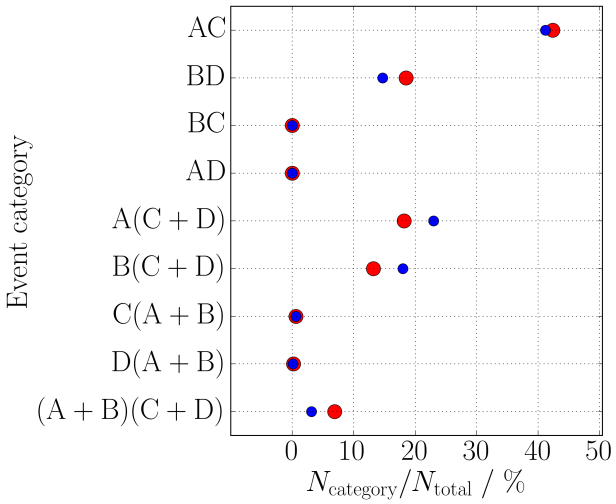

Figure 6.16: Number of events in event category N_{category} normalized to the total number of events with full charge collection N_{tot}. The voltage configuration is planar with $V_{\text{A}} = V_{\text{B}} = -V_{\text{C}} = -V_{\text{D}} = -50\,\text{V}$, which means signals are mainly influenced by electron migration. The *red* dots represent the results from experiment, the *blue* dots the results from simulation. The statistical uncertainties are smaller than the marker sizes.

4. Events with ionization amplitudes along the zero axis of the ionization amplitude A and B, as well as C and D. These events are also characterized by full charge collection on the A and B, C and D electrodes but they do not originate from primary interaction with an energy deposit of 59.5 keV. They are mainly caused by γ-rays from the ^{241}Am source, which already deposited energy in other parts of the detector before they interact in the HPGe crystal or deposited part of their energy in the detector and then escaped. Other contributions to this population of events originate from background radiation caused by radioactive materials in the experimental set-up, as well as from cosmic muon backgrounds. Thus, these interactions are not considered in the simulation, where we assumed a monoenergetic source emitting 59.5 keV γ-rays, this event population did not show up in the simulation.

The ionization amplitudes for our calibration experiment retrieved from experiment and simulation agree very well on a qualitative basis. Therefore we conclude, that the MC simulation tool for charge migration contains the main properties of electron transport in HPGe crystals also for rather high bias fields. This is not surprising since the simulation already described well the case for low fields, where trapping issues are more prominent than in high field configurations. The next step was then to study the charge migration processes on a quantitative level, as we finally wanted to use the charge migration tool to optimize our detector performance.

Quantitative comparison of simulated and experimental ionization amplitudes

After giving a general description of the effects of charge migration processes in Ge for the detector performance at high electric fields, in the following we present the results from a quantitative analysis of the detected events originating from our ^{241}Am source. It is again based on the comparison of simulation and data.

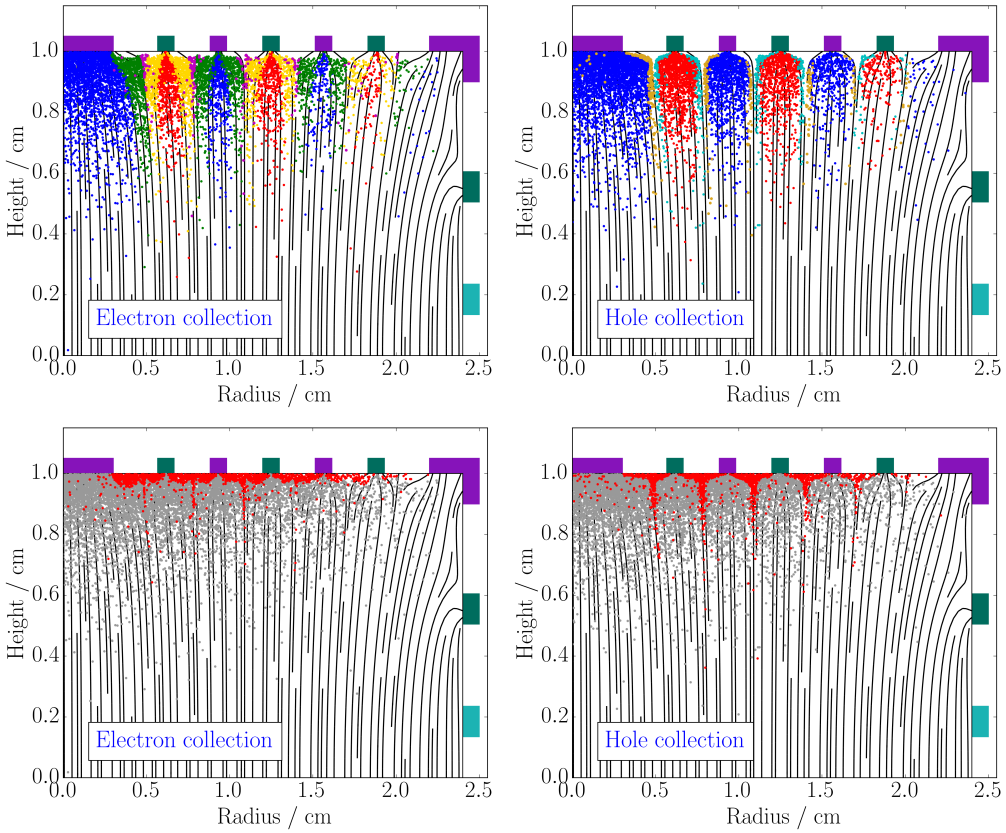

Figure 6.17: Simulation results for the locations of energy deposits in the prototype detector facing an ^{241}Am source. *Left:* Electron transport dominates charge collection as $V_A = V_B = -V_C = -V_D = -50\,V$. *Right:* Hole transport dominates charge collection as $V_A = V_B = -V_C = -V_D = +50\,V$. *Top:* Events with full charge collection. The color of the dots marks the event categories to which the events belong: AC *blue*, BD *red*, A(C+D) *green*, B(C+D) *yellow*, C(A+B) *dark yellow*, D(A+B) *cyan*, (A+B)(C+B) *magenta*. *Bottom:* Events with full charge collection are shown as *gray* dots. In addition, events with reduced charge signals due to trapping are represented by the *red* dots.

In section 6.3 we discussed that the interactions caused by the ^{241}Am source can be categorized according to the ionization amplitudes on the set of the four electrodes A,B,C and D, leading to 10 different event categories. In this section, we discuss the categories 1 to 9, which are characterized by full charge collection on the summed ionization amplitude ABCD. In our experimental set-up the ^{241}Am is approximately a monoenergetic source for γ-rays with an energy of 59.5 keV, full charge collection is defined by events with an ionization amplitude in the 5σ region of the 59.5 keV$_{ee}$ peak in the ionization amplitude spectrum. The category 10, which is connected to charge trapping, is discussed in sec. 6.7.3.

The first step of this analysis was to extract all events with full charge collection on ABCD. This was done for the simulated data as well as for the experimental data. After extracting the number of events with full charge collection N_{total}, the events were further classified and the number of events in every category $N_{category}$ was determined. The results

for the relative contributions of events in the various categories $N_{\text{category}}/N_{\text{total}}$ retrieved from simulation and experiment are shown in figure 6.16. We see, that the number of events in the different categories extracted from data (*red* dots), are in general in good agreement with the simulations *blue*). Therefore we can conclude, that the charge migration processes included in the simulation provide an adequate description of the experimental set-up. Slight variations between simulation and experiment are not surprising as the simulation was very simplified only taking single energy deposits into account and also no noise was included in the analysis of the simulated data set.

Based on the good agreement between event categories from experiment and simulation, we can now discuss the charge migration processes for electrons in more details. In fig. 6.17 *top left*, the simulated locations of energy deposits caused by 59.5 keV γ-rays are presented and the colors mark the events according to the category to which they belong. The different categories are discussed in the following:

1. The majority of events belong to the event categories AC or BD. In this case the interaction took place close below the A or B electrodes and the created electrons and holes were drifted to the C or D electrode, as expected from the shape of the electric field lines (*blue* and *red* dots).

2. Another large population of events belongs to the A(C+D) or B(C+D) event category. The simulation shows, that in this case the interaction are located in-between the A and B electrodes (*green* and *yellow* dots). As the transport anisotropy of the electrons is affecting the charge collection and electrons drift in an angle of 35° to the electric field, especially in this case, it is very likely that electrons created in one interaction are partially collected on the C and D electrodes. However, simulation and data show the same trend for the populations of theses categories, the simulation overestimate the number of events in theses categories. This will discussed in bullet 6.

3. As neither the shape of the electric field lines nor the transport anisotropy of electrons lead to pure charge collection on the A and D or B and C electrodes, no events contribute to the categories AD and BC.

4. Events in the categories C(A+B) and D(A+B) do not show up for two reasons. Electron hole pairs are created close to surface covered by the A and B electrodes, so holes have a minor effect on the ionization amplitude spectra as they only drift a short distance and are collected very quickly.

5. The simulation shows, that events in the category (A+B)(C+D) are located very close to the middle in-between the A and B electrodes (*magenta* dots). According to the simulation, electrons and holes are created in a finite volume(see sec. 3.1). In this case, e^-/h^+-pairs are partially created in the area were the electric field lines connect the A and C electrode and in the area were they connect the B and D electrode. In this way, the simulation allows shared collection of holes on the A and B electrodes. However, the simulation underestimates the number of events in this category and is discussed in the following.

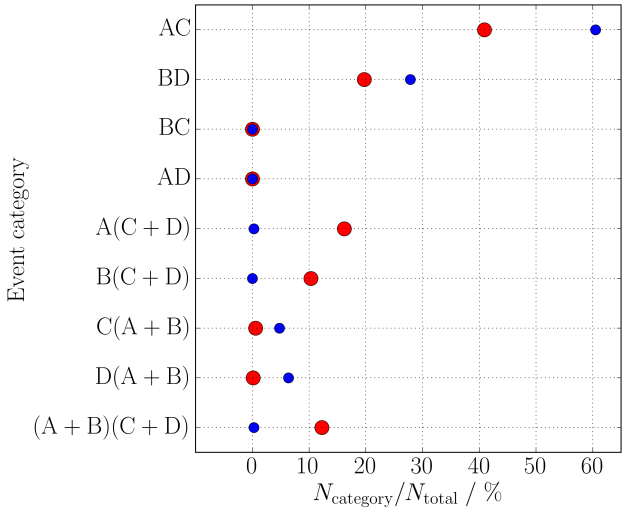

Figure 6.18: Number of events in event category N_{category} normalized to the total number of events with full charge collection N_{tot}. The voltage configuration is planar with $V_{\text{A}} = V_{\text{B}} = -V_{\text{C}} = -V_{\text{D}} = +50\,\text{V}$, which means signals are mainly influenced by hole migration. The *red* dots represent the results from experiment, the *blue* dots the results from simulation. The statistical uncertainties are smaller than the marker sizes.

6. The simulation underestimates the number of events with shared charge collection on (A+B)(C+D) and overestimates the amount of events in category A(C+B) and C(D+B). These are the first hints for a missing implementation of a hole transport anisotropy, which will be discuss in detail in sec. 6.7.2. In the simulation the holes strictly follow the electric field lines and therefore even if they occur in-between electrodes, shared collection on A and B is strongly suppressed. If we assume a small transport anisotropy, especially the events with e^-/h^+-pair production in-between electrodes will be affected. These events belong to the categories A(C+D), B(C+D), (A+B)(C+D) (*green*, *yellow*, *magenta* dots in fig. 6.17 *top left*). The hole transport anisotropy enhances charge sharing on A and B. Thus, more events show up in category (A+B)(C+D) and less in the categories A(C+D),B(C+D) is reduced, which is consistent with the experimental data. However, the hole transport plays a minor role for electron dominated charge signals.

The event categories based on the ionization amplitudes are a very powerful tool to analyze the effect of charge transport in Ge on the detector performance, especially when comparing data with simulation based on hot carrier transport. We saw that when the detector response is dominated by the charge collection of electrons, the electron transport anisotropy favors shared charge collection on at least 3 electrodes. We will see in section 6.7.3, that this also favors electron trapping at the surfaces and is therefore a fundamental limit for the charge collection in a FID detector.

6.7.2 Detector signals in case of long hole tracks

In the following the results from an analysis of our calibration experiment, equipped with an ^{241}Am source emitting 59.5 keV γ-rays with an electrode bias $V_{\text{A}} = V_{\text{B}} = -V_{\text{C}} = -V_{\text{D}} = +50\,\text{V}$ is presented. In this case, as the energy deposits are located close to the A and B electrodes, the detector signals are dominated by the charge migration of holes.

In figure 6.18 the results for the number of events in the different event categories is shown, retrieved from simulation and experiment. Similar to the analysis of electron transport, we focus here on events with full charge collection. Thus, we focus on events where the summed ionization amplitude ABCD falls into the 5σ region of the 59.5 $\mathrm{keV_{ee}}$-peak. We note that the populations of the different event categories do not agree as well as in the case where the charge transport was dominated by electron transport (see sec. 6.7.1).

The results presented in fig. 6.18 show significantly less events that delivered full charge on the AC and BD electrodes as predicted from simulation. In addition, the simulation predicts no events with shared charge collection on the C and D electrode (event categories A(C+D), B(C+D) and (A+B)(C+D)), which are clearly observed in the experiment. Finally, events with shared charge collection on A and B (event categories C(A+B), D(A+B)) are expected by the simulation and are not measured in the experiment.

We can interpret this discrepancy in the populations of events in the different categories by comparing it to the case where electrons dominated the charge collection. We see in fig. 6.17 *top right* that the events which belong to the event categories A(C+D) and B(C+D) are located in-between the electrodes and favor charge sharing on the C and D electrode. This follows from the electron transport anisotropy which causes the electrons to migrate in an angle of 35° to the electric field lines. In the case of hole transport no transport anisotropy is included in the simulation. Therefore also holes created in the region in-between the A and B electrodes strictly propagate along the electric field lines and charge collection is favored on the electrodes A and C or B and D. However, the experimental data show a significant amount of events with charge sharing on the C and D electrodes and as in case of electron transport charge sharing is caused by electron transport anisotropy, we can conclude that the hole transport anisotropy plays an important role for our detector. Hence, it is not implemented in the simulation, we well understand the difference between simulation to data.

To conclude, although the transport anisotropy for holes in Ge crystals is much smaller than for electrons - the drift velocity for electron varies more than 100 % for an electric field along the [100]-direction of the crystal in comparison to the [111]-direction (see sec. 3.3.1), whereas it only varies around 30 % for holes (see sec. 3.3.3)- it has a measurable effect on the detector signals in our FID prototype detector. Therefore it is planned in a next step to implement the hole transport anisotropy in the hot carrier transport simulation. An approach, how this can be done, is found in [144] and is considered for further developments of the hot carrier transport simulation tool used for this thesis.

6.7.3 Effect of charge trapping on the detector signals

In the sections 6.7.1 and 6.7.2, we discussed the detector performance resulting from charge migration in HPGe crystals and found that especially in the case signals are dominated by electron transport, the hot carrier transport simulation tool used for this thesis provides an excellent description of our experimental set-up. Therefore, for the discussion of the

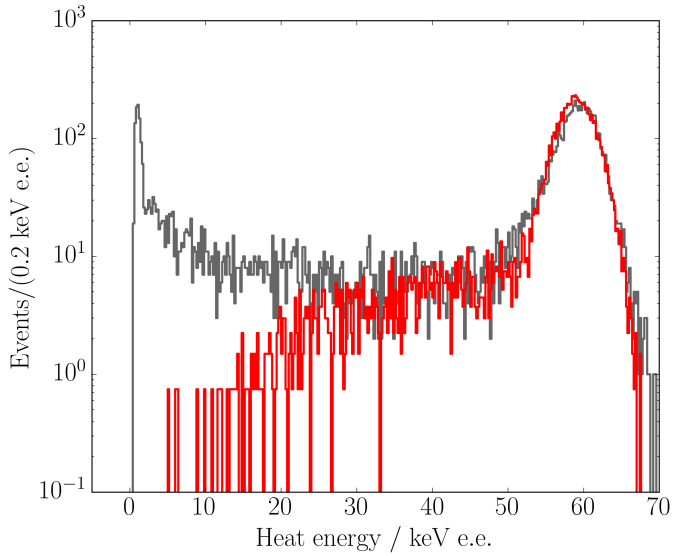

Figure 6.19: Heat energy spectrum in $\mathrm{keV_{ee}}$ for a planar high voltage configuration with $V_\mathrm{A} = V_\mathrm{B} = -V_\mathrm{C} = -V_\mathrm{D} = -50\,\mathrm{V}$. The *black* curve describes the experimental data, the *red* curve the simulation. The simulated spectrum was smeared with Gaussian noise based on the 59.5 keV-peak resolution in the experiment $\sigma = 2.30\,\mathrm{keV_{ee}}$ and scaled to the experimental data according to the maximal height of the 59.5 keV-peak.

effect of charge trapping on the detector performance, we will focus on simulation and data, retrieved from an electrode biasing with $V_\mathrm{A} = V_\mathrm{B} = -V_\mathrm{C} = -V_\mathrm{D} = -50\,\mathrm{V}$, where the charge collection is dominated by electron tracks. However, all results also apply to the case where hole tracks dominate the signals, especially as we found that the amount of events affected by trapping in the simulation only varies slightly from 15.4 %for electrons to 12.9 % for holes.

Thus, the transport anisotropy of electrons in Ge crystals favors shared charge collection on the C and D electrodes, it also favors trapping on the crystal surfaces, as electrons much more easily drift to surfaces which are not covered by an electrode. The effect of charge trapping is discussed based on the heat amplitude spectrum. Eventually for high biases, in order to detect recoil energies below 1 keV, it would be the only detection channel, because the ionization channels are limited by read-out noise in combination with the low statistics for the created e^-/h^+-pairs.

In figure 6.19 the *black* histogram represents the heat energy spectrum measured with an electrode bias of $\Delta V = 100\,\mathrm{V}$. In addition to the $59.5\,\mathrm{keV_{ee}}$ peak there are events leaking down to energies around $1\,\mathrm{keV_{ee}}$ which is the heat trigger level. In the following we will analyze this spectrum in comparison to the results from simulation. The heat energy spectrum based on the simulation of a monoenergetic source emitting 59.5 keV γ-rays is represented by the *red* line. The simulated heat energy spectrum is smeared with the energy resolution on the 59.5 keV-peak in the experimental spectrum. The scaling of both spectra is performed according to the maximal height of the 59.5 keV-peak in simulation and experiment. This scaling procedure is appropriate, as we showed in the section 6.7.1 that the event categories in simulation and data based on the ionization amplitudes for events with full charge collection agree very well.

In figure 6.19, we see that the simulated and experimental heat energy spectrum agree very well down to heat amplitudes of $25\,\mathrm{keV_{ee}}$. Thus, the only effect that can lead to a reduction of the heat amplitude implemented in the simulation is trapping, we can conclude that at least down to $25\,\mathrm{keV_{ee}}$ charge trapping explains the shape of the experimental spectrum. Furthermore, bulk trapping depends on the electric field and is negligible at an electrode bias of $\Delta V = 100\,\mathrm{V}$ (see fig. 3.7). Therefore the only reason for trapping that is implemented in the simulation is surface trapping. The positions of the primary interactions in the detector, where the created e^-/h^+-pairs are affected by surface trapping, are shown as *red* dots in fig. 6.17 *bottom* and support the hypothesis of surface trapping. These events are located in-between the electrodes and in combination with the transport anisotropy favor charge trapping at an uncovered free surface of the detector.

An obvious explanation for the discrepancy of the heat amplitude spectra from simulation and experiment at amplitudes lower than $20\,\mathrm{keV_{ee}}$ is the fact that primary energy deposits below $59.5\,\mathrm{keV}$ are not taken into account for the simulation. Actually, γ-rays emitted by the ^{241}Am source can scatter in other parts of the experimental set-up before they interact in the sensitive region of the detector. In addition the trigger level was set very low and therefore the peak in the experimental spectrum near zero is likely caused by triggering on baseline fluctuations without any signal.

We state that in our calibration experiment with an ^{241}Am source, which creates mainly interactions in the near-surface region below the A center electrode, 21.1 % (Sim: 15.4 %) of the events in the energy range from $20\,\mathrm{keV_{ee}}$ up to $70\,\mathrm{keV_{ee}}$ are affected by surface trapping. At an eventual operation of the detector for low recoil energies, no discrimination of surface events will be possible. Therefore events with reduced amplitudes due to surface trapping will lead to a misinterpretation of the primary energy deposit of an interaction and provide a fundamental limit for the detector performance. Therefore, the optimization of the detector design in respect to surface trapping is important for the next generations of low threshold dark matter detector. Hence, trapping is well included in the simulation tool, we can use the simulation tool to find an optimal detector configuration, providing as little surface trapping as possible. The results of these studies of different detector geometries for the massive HPGe detectors of EDELWEISS are presented in the next sections.

6.8 Optimization of the detector configuration at high electric fields

The analysis of results from the calibration experiment presented in the last sections made use of the advantage that our calibration experiment hosted a source producing γ-rays causing energy deposits, which were large enough to be detectable in the heat and the ionization channels. It allowed us to verify that the MC simulation tool for charge transport in HPGe crystals provides an adequate description of the experimental set-up. In addition it showed that surface trapping limits the charge collection at high electrode biases and reduces the quality and reliability of the resulting heat amplitude spectrum.

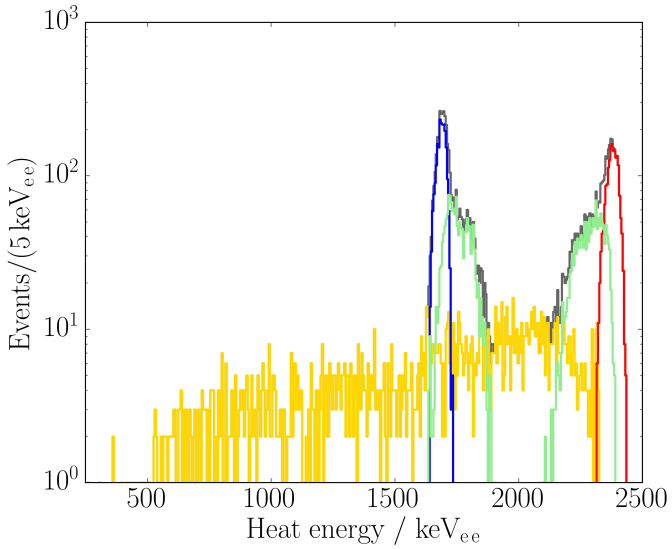

Figure 6.20: Heat amplitude spectrum (*black*) from simulation with $V_A = -V_C = -35\,V$ and $V_B = -V_D = -50\,V$. The input energy deposit distribution was based on a mono- energetic source, emitting 59.5 keV γ-rays. The colored histograms represent contributions based on the charge amplification from different electrode biases: $\Delta V_{AC} = 70\,V$ (*blue*); $\Delta V_{BD} = 100\,V$ (*red*); combination of A,B, C and D (*green*); charge amplification reduced by trapping (*yellow*).

In this section we use the charge migration simulation tool to study strategies to reduce surface trapping and to find an optimal detector configuration. For the optimization, we made use of the full information retrieved from the ionization and heat channels, but also considered that eventually the Germanium detectors are operated at high electrode biases, allowing to detect recoil energies below $1\,keV_{ee}$ in the heat channel, whereas the signals are too small be detectable in the ionization channel.

6.8.1 FID detector operated in veto mode

Actually, the FID detectors in EDELWEISS-III were designed to be able discriminate surface events. Therefore a straightforward question is whether there is a way to profit from a FID detector at high electrode biases operated in a veto mode with $V_A \neq V_B$, although finally we will not be able to detect any ionization signal at the electrodes for very small signals.

The primary idea of such a detection mode would be that the charge signals of events at the surface are amplified by a smaller NTL amplification factor, based on the smaller difference of the electrode bias $\Delta V_{AB} \ll \Delta V_{BD}$ with an ultimate amplification being so small, that the resulting heat signal is below the detection threshold.

Therefore a large difference for the NTL amplification for the neighboring electrodes A,B and C,D is favored. As the maximal voltage difference will be limited by leakage currents between the neighboring electrodes, we tested our prototype and found that the maximal voltage difference without leakage in our experiment for $V_B = V_D = -50\,V$ was $\Delta V_{AB} = \Delta V_{CD} = 15\,V$, which is consistent for measurements with the FID800 detectors.

An example for a simulated heat spectrum in an veto mode, caused by a source emitting mono energetic γ-rays as presented in the last section, at high bias $V_A = -V_C = -35\,V$

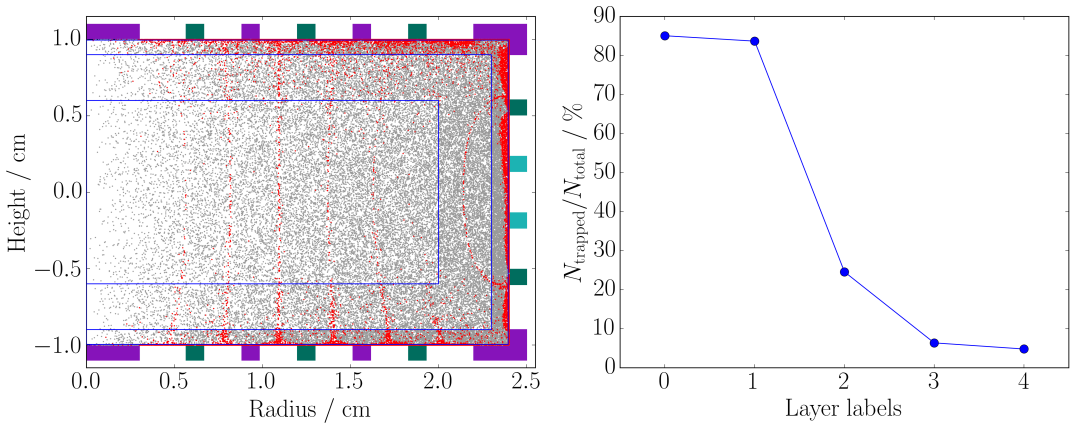

Figure 6.21: *Left:* 2-D projection of event locations simulated in a HPGe detector with a FID-type electrode design (interleaved electrodes are marked by the *magenta* and *green* rectangles). The interaction points were assumed to be distributed uniformly in the detector in order to study effects from surface trapping from all regions of the detector. Events were simulated in layers with different distances from the surface (*blue* boxes). The *gray* dots mark all locations of events, which are not affected by surface trapping and the *red* dots represent events affected by surface trapping. *Right:* Amount of trapped charges for interactions located in layers with different thickness and distance from the surface (*blue* boxes in the *left* graphic). The labels on the x-axis represent different layers with **0**: 200 nm to 1 μm; **1**: 1 μm to 40 μm; **2**: 40 μm to 1 mm; **3**: 1 mm to 4 mm; **4**: $>$ 4 mm.

and $V_{\text{B}} = -V_{\text{D}} = -50\,\text{V}$ is shown in figure 6.20. The contributions from the different NTL amplification factors based on charge amplification by the different electrodes A,B,C and D are shown. In contrast to our assumption, the heat spectrum does not split up according to the NTL amplifications $\Delta V_{\text{AB}} = 15\,\text{V}$ and $\Delta V_{\text{BD}} = 100\,\text{V}$. The two peaks we observe belong to the NTL amplifications $\Delta V_{\text{AC}} = 70\,\text{V}$ and $\Delta V_{\text{BD}} = 100\,\text{V}$. Therefore with this configuration, we can not discriminate surface and bulk events. In addition, events with mixed amplification (*green* histogram) occur and make the heat spectrum quite complicated. A proper energy calibration would be hard here and so far we can not recommend an operation in this veto mode.

An operation at higher voltage differences between A and B is not possible at the moment due to leakage currents. In addition it would oppose the primary idea to have a large difference in the NTL factor for surface and bulk events. Therefore, in the following we focus on detector configuration that are simpler and do not involve different NTL factors.

6.8.2 FID detector operated in planar mode

In case of a low-mass WIMP search, where the detection threshold is lowered to recoil energies below 1 keV by using the NTL effect, signals from low energy background radiation will also be detected with higher efficiency. Hence, the absorption depth for radiation originating for any type of background particle decreases with energies, most of these particles from external background will interact in the near-surface region of the detector.

Therefore, their signals will be strongly affected by surface trapping, making it very hard to reconstruct the recoil energy of an interaction.

The aim of this section is to quantify the effect of surface trapping in dependence on the absorption depth of background electron recoils for a FID-type EDELWEISS detector operated in planar mode with $\Delta V = 120\,\mathrm{V}$. This voltage configuration was chosen based on the results from high voltage tests with the EDELWEISS-III detectors, allowing the detectors to be biased up to $\Delta V = 100\,\mathrm{V}$ without being affected by leakage currents. The results which are presented in the following hold for all electrode biases in the same order of magnitude.

In order to study the effect of surface trapping, we performed a simulation, where interaction points were chosen to happen in various layers with various distances from the detector surface. The decision for the thickness of these layers and the distance from the surface was based on the already known EDELWEISS-III background from the natural decay chain of ^{210}Pb (see sec. 2.5). We simulated interactions in 5 layer with the following dimensions: **0**: 200 nm to 1 μm; **1**: 1 μm to 40 μm; **2**: 40 μm to 1 mm; **3**: 1 mm to 4 mm; **4**: > 4 mm.

The layer closest to the surface of the detector (layer 0) starts at a distance of 200 nm and represents the minimal distance between an electron or hole and the surface before it is treated as already collected at an electrode or the surface. For each of these layers an uniform distribution of interaction positions in the detector was assumed. In addition, all interactions are treated as single energy deposits with a fixed amount of energy. In general, the primary energy affects only the size of the creation volume(see eq. 3.2) for electron/hole-pairs and is chosen to be 10 keV.

In figure 6.21 *left* the center positions of the creation volumes of the simulated e^-/h^+-pairs for all simulated events are shown. The *red* dots represent events, where some electrons and holes were trapped on the way to the electrodes. Events are defined as influenced by surface trapping according to the heat amplitude spectrum. Thus all interactions have a primary energy of 10 keV, the heat amplitude spectrum has a peak at 10 $\mathrm{keV_{ee}}$. Finally, events are classified as influenced by surface trapping if they have a heat amplitude smaller than the 5σ region of a Gaussian fit to the 10 keV-peak. The *gray* dots mark all events that are not affected by surface trapping. We observe that the number of events affected by trapping increases strongly with decreasing distance of the energy deposits to the detector surface. In addition, also events in the bulk region are affected by trapping, especially along the z-axis and in-between the ring electrodes. This clearly shows the large influence of the electrode design on the charge collection.

In figure 6.21 *right* we present the number of events with reduced heat amplitude due to trapping according to the 5 different layers with different distances to the surface. The relative number of trapped events $N_{\mathrm{trapped}}/N_{\mathrm{total}}$ is defined independently for every layer, based on the total number of simulated events in this layer N_{total}. We clearly see that the closer an interaction is located to the surface, the more likely parts of the produced electrons and holes are trapped. For the layer closest to the surface, we find that 87 % of

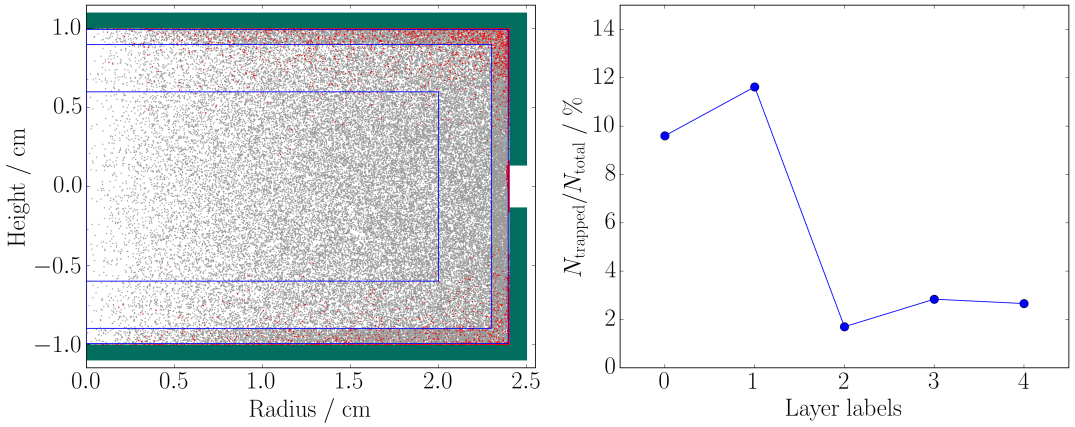

Figure 6.22: *Left:* 2-D projection of event locations simulated in a HPGe detector with planar electrode design (*green* rectangles). The interaction points were assumed to be distributed uniformly in the detector in order to study effects from surface trapping from all regions of the detector. Events were simulated in layers with different distances from the surface (*blue* boxes). The *gray* dots mark all locations of events, which are not affected by surface trapping and the *red* dots represent events affected by surface trapping. *Right:* Amount of trapped charges for interactions located in layers with different thickness and distance from the surface (*blue* boxes in the *left* graphic). The labels on the x-axis represent different layers with **0**: 200 nm to 1 μm; **1**: 1 μm to 40 μm; **2**: 40 μm to 1 mm; **3**: 1 mm to 4 mm; **4**: $>$ 4 mm.

the events are affected by surface trapping. If we combine the results from all simulated layers, we still end up with 42.3 % of the detector volume leading to events being affected by surface trapping.

The results from the analysis of surface trapping in case of near-surface background interactions strikingly shows the problematic, which occur from an operation of a FID detector in planar mode. It is thus obvious that an optimized detector design significantly reducing surface trapping, has to be different as will be presented in the next section.

6.8.3 A new planar electrode design based on two electrodes covering top, bottom and lateral surfaces of the detector

Based on the results from the last section, we present another possible design for a massive HPGe detector, which provides a much better detector performance in the terms of surface trapping. Instead of an interleaved electrode design, a configuration with only two electrodes covering the top and bottom surfaces is chosen (see fig. 6.22). This design has the clear advantage that surface trapping caused by uncovered areas at top and bottom surfaces of the detector are excluded. In order to avoid the loss of charge carriers due to trapping at lateral surfaces, the planar electrodes are extended to the lateral surface. Therefore only one area critical for surface trapping remains, which is the area of the gap between the two electrodes. However, in this region occur the highest electric fields, and therefore the gap has to be chosen wide enough to allow electrode biases up to $\Delta V \approx 100$ V

without effects from leakage currents in order to gain advantage from the NTL effect. The gap size chosen here is quite conservative with 3 mm. We expect that a detailed experimental study of the leakage current in dependence of the electrode bias would likely result in a smaller gap size.

In figure 6.22 the results of a study of surface trapping for the new planar electrode design is presented. The simulation parameters were chosen to be exactly the same as in section 6.8.2. The improvement in the number of trapped events at the detector surface for this electrode configuration is large. There still exists an increase of the amount of events influenced by trapping with decreasing distance to the surface. However, in contrast to a FID-type detector operated in planar mode, where in the maximum case very close to the surface 87 % of the events are affected by trapping, we only find 12 % of events to be affected by surface trapping. If we consider all simulated energy deposits in the detector, we find that 7.3 % of the detector volume is affected by surface trapping in comparison to 42.3 % in the case of a FID-type detector.

Therefore, we conclude that it is worth to change the electrode design to a planar configuration with only two electrodes covering top, bottom and also lateral surfaces of the HPGe crystal. Especially at high electrode bias, this design significantly reduced the effect of surface trapping on the detector performance and the reconstruction of the primary energy deposits. In addition, this new design is much simpler than the FID electrode design and the the production process of such an detector is straightforward. For the actual run of the EDELWEISS experiment started in December 2017, one of the detectors is already equipped with such an electrode design and will be tested at high voltages.

Another possibility, which is very close to the approach here, are point contact detectors. They are already used in dark matter experiments like CoGent [41] and CDEX [145], where the recoil energies of particle are only measured via one channel, the ionization channel. These detectors have one very small electrode, that is biased as high as possible and the rest of the detector is covered by an electrode, which is grounded. Similar to the electrode design presented in this work, the influence of charge trapping is determined by the dimension of the surface area not covered by the electrodes.

6.9 Conclusion

In this chapter a detailed study on the detector performance of an EDELWEISS prototype detector towards the operation at high voltages was presented. In order to study the effects of electron and hole transport in HPGe crystals on the detector signals, we compared results from a calibration experiment with a FID prototype detector with simulations. We could show, that for electrons the transport anisotropy has a large effect on the detector signals and is adequately implemented in the simulation tool. For hole transport, we found slight discrepancies, which occur from a missing implementation of the hole transport anisotropy in the simulation tool. Overall the agreement between the results of the charge transport simulation and the experimental data was very good. This allowed us to conclude, that

a HPGe detector at high electrode biases is mainly limited in its performance by surface trapping caused by electrons and holes that do not reach one of the electrodes but are stuck on the surface.

Based on the results from comparing simulation and experiment, we performed an optimization of the detector geometry and found that a detector with full cover electrodes reduces the amount of surface trapping and is in addition easy to handle. Another solution which is very close to the proposed design are point-contact detectors.

Thus, the low-mass WIMP search in EDELWEISS-III showed that it was mainly limited by heat-only events, therefore by events which did not deliver any ionization signal, we developed a rejection method for these events. This rejection method was based on pulse-shape analysis of the heat signals and allowed us to reject 95.6 % of all measured heat-only events. However, in order to use heat-pulse shape analysis of heat signals from FID800 detectors, a much higher sampling frequency of the heat signal in contrast to the actual read-out in EDELWEISS is necessary, requiring substantial changes in the read out system.

7. Conclusion

This thesis was performed in the framework of the EDELWEISS dark matter experiment, which searches for Weakly Interacting Massive Particles (WIMPs) with High Purity Germanium (HPGe) detectors. Although WIMP theory favors a mass of dark matter candidates in the range $m_\chi \in [10, 1000]$ GeV/c^2, hints of WIMP signatures close to the detection thresholds of direct dark matter experiments like CDMS-II Si [58], CoGent [41], CRESST-II [59] and DAMA/LIBRA [23], as well as the observation of a possible dark matter annihilation signal from the Galactic Center [13] have inspired theories based on low mass dark matter candidates. Especially low-mass WIMPs, which can have masses < 5 GeV/c^2 are very promising candidates. The trend to search for low-mass dark matter candidates has particularly affected experiments based on solid state detectors, as these detectors can provide very low detection thresholds < 1 keV and allows us to probe WIMP masses down to a few GeV/c^2.

The core of the EDELWEISS experiment are cylindrical HPGe crystals with masses around 800 g, which are operated in an electric field and at low temperatures, typically $T = 18$ mK. WIMP dark matter candidates are expected to elastically scatter with the Ge nuclei of the crystals, creating nuclear recoils with energies in the keV-range for standard WIMPs and in the sub-keV-range for low-mass WIMPs. The recoiling nucleon then creates electron/hole pairs, which are separated in the electric field and collected as an ionization signal E_{ion}. In addition, the recoil creates phonons and the heat signal H can be measured as a temperature rise in the detector. If the HPGe crystals are operated at low electric fields, typically around 2 V/cm, the heat energy is almost proportional to the recoil energy $H \propto E_{\mathrm{rec}}$. Since the number of created e^-/h^+-pairs depends on the type of the recoil, electron recoils caused by γ- and β-background radiation produce more e^-/h^+-pairs per recoil energy than nuclear recoils, the ionization yield $Q = E_{\mathrm{ion}}/E_{\mathrm{rec}}$ can be used to discriminate electron and nuclear recoils. Clearly, a high discrimination efficiency requires a full measurement of the heat and especially the ionization signal. This can be compromised by e^-/h^+-pairs created in the surface region, as the density of trapping centers is very high there, and charge carriers can easily recombine or can be trapped before they are collected at the electrodes. This leads to a reduced ionization signal and can cause a misinterpretation of the recoil type of an event. Therefore EDELWEISS developed the Fully Inter Digitized (FID) electrode design, which contains 4 sets of interleaved electrodes, which can be biased and read out independently. Depending on the combination of measured ionization signals on the 4 electrodes, this detector-type allows the rejection of surface events and defines a fiducial volume in the bulk region of the detector, which is less affected by trapping. The excellent performance of these detectors was proven in phase III of the EDELWEISS experiment. The analysis of data from 24 HPGe detectors, operated well shielded against cosmic muons in the Modane underground laboratory, has successfully set limits on the WIMP-nucleon cross-section down to WIMP masses of 4 GeV/c^2 [100, 99].

In the current data taking phase of the EDELWEISS experiment, having started in December 2016, the goal is to test the FID detectors in a new operation mode, where in contrast to the standard operation of the detectors, the crystals are operated at high electric fields up to 50 V/cm. In this case, drifting electrons and holes create many additional phonons on their way to the electrodes and enhance the heat signal. By using this so-called Neganov-Trofimov-Luke (NTL) effect, which is proportional to the applied electrode bias and the number of created e^-/h^+-pairs, the detection threshold can be significantly lowered. In the CDMS experiment a massive HPGe detector was tested at high bias and could reach a detection threshold of 56 eV [47]. At high electrode biases the heat signal H is dominated by secondary phonons, and therefore proportional to the ionization signal $H \propto E_{\mathrm{ion}}$. In this case, the ionization yield Q can not be used anymore for the discrimination of electron and nuclear recoils. In addition, especially for a detection threshold < 100 eV, the baseline resolution in the ionization channels is not good enough to detect events above baseline fluctuations. Therefore the 4 FID electrodes can not be used anymore for surface event discrimination, and the signal channels are reduced to a single heat channel.

At low electric fields, as well as at high electric fields, the detector signals are heavily affected by the charge migration of electrons and holes in the HPGe crystal. Hence, a good detector performance is directly connected to a full charge collection and a good understanding of carrier transport in the HPGe crystals. This thesis is dedicated to understanding the charge migration processes of electrons and holes in the HPGe EDELWEISS crystals at low temperatures. The analysis presented in this work is founded on the simulation of hot carrier transport in HPGe crystals and on a comparison of simulations with experimental data. We performed a calibration experiment with a prototype FID HPGe detector at ground level at the CSNSM laboratory in Orsay, France. The experimental set-up was equipped with an ^{241}Am calibration source, which emits 59.5 keV γ-rays, causing energy deposits in the near-surface region of our detector (penetration depth $\lambda_{\mathrm{Ge}}(59.5\,\mathrm{keV}) \approx 1$ mm). This experimental set-up was implemented in a standalone Monte Carlo simulation package of charge transport, which was developed according to special charge transport measurements with the EDELWEISS detectors. The main ingredients are listed in the following: The electron transport is heavily affected by the consequences of the band structure of HPGe. The electric field in EDELWEISS is applied along the [100]-direction of the crystal and the conduction band minima point in the [111]-direction. Thus, electrons do not migrate along the electric field lines but along an angle of 35 °. In addition, 4 energetically equal conduction band minima occur in the 4 [111]-directions (L-valleys). Electrons can undergo transitions between the L-valleys with the consequence that they change the drift direction. For holes, a transport anisotropy also exists but is much smaller and was not taken into account in the simulation tool used in this work. An important part of the simulation code is the inclusion of trapping processes. In the crystals' bulk region dopant impurities with a net dopant density of $\approx 10^{10}\,\mathrm{cm}^{-3}$ exist and can act as trapping centers. In the surface region, additional trapping centers caused by open bonds and dislocations occur and can reduce the ionization signals.

The first analysis part focused on the study of ionization signals. As electrons and holes start to drift in an electric field, they induce charges on all electrodes. This ends when all charge carriers are collected or stopped by trapping. Therefore the pulse-shapes of the ionization signals are a direct consequence of electron and hole migration and allow to study charge transport properties. The prototype detector used in this thesis has the FID electrode design and was therefore equipped with 4 sets of electrodes A,B,C,D. These 4 channels could be read out independently. We used a window triggered data acquisition system with triggering on B and a sampling frequency of 100 MHz, which was sufficient to resolve the transient regions of the ionization signals. We analyzed two voltage configurations. In both cases the veto electrodes where grounded with $V_A = V_C = 0\,V$, whereas the collecting electrodes where biased with i) $V_B = -V_D = -2\,V$ and ii) $V_B = -V_D = +50\,V$. The used ^{241}Am source led to γ-ray interactions in the near-surface region of the A and B electrodes. Hence, the voltage configurations i) and ii) allow us to distinguish between surface events collected on the A and B electrodes from bulk events collected at the B and D electrodes. In addition we can study the effects of electron and hole propagation separately as for configuration i) the bulk events are dominated by electron transport as holes are quickly collected at the B electrodes and electrons propagate through the whole crystal to the D electrode. For configuration ii) bulk events are dominated by hole transport. Our pulse-shape analysis was based on the evaluation of the rise time of the ionization signals, which was defined as the time between 10 % and 90 % of the maximal signal amplitude. Results from simulated and experimental data showed, that the rise time distributions agree very well and therefore the charge migration processes included in the simulation provide an adequate description of the experiment. In addition, a clear separation of rise times for surface and bulk events occurred in the rise time distributions. Bulk events for the low electric field configuration i) showed rise times distributed around 800 ns, whereas for the high electric field configuration ii) the rise times were distributed around 500 ns. The difference is caused by the increasing drift velocity of electrons and holes with the electric field. Surface events in both cases are distributed around a rise time of 200 ns. Based on the observation of a clear separation in rise time for bulk and surface events, we performed a rise time cut: $t_{rise} > 600\,ns$ allowed to reject 97.5 % of the surface events for configuration i) and $t_{rise} > 400\,ns$ allow to reject 98.5 % of the surface events for configuration ii). The difference in the rejection efficiency was mainly based on the reduced effect of bulk trapping at high fields. We found a slight discrepancy between the populations of events categorized by the ionization amplitudes in channel A,B,C,D in simulation and experiment for configuration ii). Events with shared charge collection on the A,B and D electrodes were strongly suppressed in the simulation. This is connected to a missing implementation of the hole transport anisotropy in the simulation and was discussed in more detail in the second part of this work. In addition, we showed that the rise time parameter can also be used to characterize the degradation and space-charge build up in the detector. It turned out, that it is even more sensitive to degradation than the ionization amplitudes, indicating the degradation at earlier times in the measurements.

The second analysis part of this thesis was dedicated to the study of the Neganov-Trofimov-Luke (NTL) effect. Starting in December 2016, the EDELWEISS collaboration

takes data with HPGe crystals biased up to 70 V, in order to search for low-mass WIMPs with $m_\chi < 5\,\mathrm{GeV/c^2}$. In this operation mode, no discrimination of electron and nuclear recoils, as well as no discrimination of surface events is possible. Therefore it is necessary to have a good understanding of the detector performance and the background, in order to calibrate the detector properly. The heat signals at high biases are dominated by phonons created by drifting electrons and holes. As a consequence charge migration processes like trapping are influencing both ionization and heat signals. We used the same FID prototype detector equipped with an ^{241}Am source, as we used for the pulse-shape analysis of the ionization signals. The 59.5 keV energy deposits caused by this γ-source result in detectable signals in the 4 ionization channels as well as in the heat channel. Our analysis made full use of the fact that we had 5 measuring channels, keeping in mind that for an eventual search for low-mass WIMPs, the ionization signals would be too small to be distinguishable from noise, and therefore only one detection channel, the heat channel, would exist. In comparison to the time-resolved measurements of the ionization signals, we used a data acquisition unit, which allowed us to store data continuously. We chose a sampling frequency of 20 kHz, which was sufficient to resolve the pulse-shapes of the heat signals[1]. Triggering could then be done off-line and was based on the heat channel, as it provided the lowest energy threshold.

To allow for a uniform amplification of the heat signals H for all events according to $H \propto \Delta V$, the FID detector was operated in planar mode with $V_\mathrm{A} = V_\mathrm{B} = -V_\mathrm{C} = -V_\mathrm{D}$ and $\Delta V = |V_\mathrm{B} - V_\mathrm{D}|$. The calibration process for the heat spectrum at $\Delta V = 100\,\mathrm{V}$ revealed a typical challenge for a FID-type detector. In the heat spectrum, the 59.5 keV-peak was broadened. A selection of events according to the ionization amplitudes showed that events collected at the A and C electrodes were distributed around a center peak position 7 % higher than all other events. We could reproduce the experimental results with the MC charge migration simulation tool by assuming a voltage drop of 10 % on the B electrode ($V_\mathrm{B} = +45\,\mathrm{V}$). This deviation from the planar mode causes different NTL amplification factors for different collection electrodes. In addition, we calculated that a voltage drop of 10 % is consistent with a realistic leaking resistance to the ground on the order of 2 GΩ. Based on these results, the heat signals were calibrated independently for all different combinations of charge collection on the 4 electrodes, allowing us to narrow the FWHM of the 59.5 keV-peak by about 15 %.

For $\Delta V = 100\,\mathrm{V}$, we found the following resolutions in the heat channel: $\mathrm{FWHM_{BF}} = 212\,\mathrm{eV_{ee}} \pm 0.1\,\mathrm{eV_{ee}}$ for baseline fluctuations and $\mathrm{FWHM_{59.5\,keV}} = 4.864\,\mathrm{keV_{ee}} \pm 0.004\,\mathrm{keV_{ee}}$ for the 59.5 keV-peak. This clearly showed that the peak resolution at 59.5 keV was not limited by the baseline noise. In addition, we evaluated the resolution of the 59.5 keV-peak in the ionization channel[2], which was $\mathrm{FWHM^{ion}_{59.5\,keV}} = 3.450\,\mathrm{keV_{ee}}$ and better than the peak resolution in the heat channel. We concluded that the resolution at high bias is not yet limited by charge migration processes but by the calorimetric read-out, as otherwise

[1] The 20 kHz sampling was not enough to resolve the transient times of the ionization signals.

[2] We chose the best estimator for the ionization energy here, which is the sum of the ionization amplitudes $E_\mathrm{ion}(\mathrm{ABCD}) = \left(E_\mathrm{ion}(A) + E_\mathrm{ion}(B) - E_\mathrm{ion}(C) - E_\mathrm{ion}(D)\right)/2$.

the resolutions of heat and ionization channels should be the same. Optimization of the heat signals in EDELWEISS is on-going. First results already showed that the heat signals are largely affected by an additional parasitic heat capacity, which can lead to a reduction of the heat signals of about 76 % [69].

The measurement of the heat amplitude of the 59.5 keV-peak with increasing electrode bias ΔV showed that it increased linearly according to the NTL effect up to $\Delta V = 100\,\mathrm{V}$. At $\Delta V = 120\,\mathrm{V}$, we found a slight reduction of the 59.5 keV heat amplitude of about 5 % in comparison to our expectation from the NTL effect. This reduction was connected to a starting break down of the detector due to the injection of leakage currents from the electrodes, as confirmed by the analysis of the Signal-to-Noise Ratio (SNR): The SNR increased up to $\Delta V = 100\,\mathrm{V}$. At $\Delta V = 120\,\mathrm{V}$, it was suddenly reduced by a factor ≈ 2 in comparison to $\Delta V = 100\,\mathrm{V}$. We conclude that a detector breakdown primarily manifests itself in a large increase of the baseline fluctuations and not in a reduced NTL factor.

We started the detailed analysis of the detector performance for a low electric field configuration in planar mode with $\Delta V = 6\,\mathrm{V}$. At this voltage, the NTL amplification of the heat signals is small and the heat energy H is approximately proportional to the recoil energy E_{rec}. Therefore a discrimination of electron and nuclear recoils based on the ionization yield $Q = E_{\mathrm{ion}}/E_{\mathrm{rec}}$ is in principle possible. As we used a γ-source, which causes electron recoils in the HPGe crystal, we expected our detected events to be distributed around $Q = 1$. The actual measurement showed a dominant event population at $Q = 1$, but also additional populations with $Q < 1$. Events with $Q \in [0.2,0.8]$ are present in both experimental and simulated data, and we could explain this by charge trapping. The simulated data allowed us to reconstruct the locations of the primary interaction. We found that 99.6 % of the events affected by trapping were located within a 0.5 mm distance from the surface and especially in-between the ring electrodes. Therefore we concluded further that they are caused by surface trapping. Surface trapping occurs when charge carriers reach surfaces, which are not covered by electrodes and therefore do not contribute to the ionization signal amplitudes.
The second population of events with $Q \lesssim 0.2$ contained typical heat-only events. The ionization amplitudes $E_{\mathrm{ion}}(\mathrm{ABCD})$ for these events were smaller than the FWHM of the baseline fluctuations $E_{\mathrm{ion}}(\mathrm{ABCD}) < 3.0\,\mathrm{keV_{ee}}$, whereas the heat amplitudes were significantly above the baseline with $H > 1\,\mathrm{keV_{ee}}$. Heat-only events are very critical for the performance of EDELWEISS detectors and have shown to be the limiting background at low recoil energies [100]. Their exact origin is unknown so far, although they are suspected to be caused by a glued connection between the NTD Ge thermistor and the FID detector. For our prototype FID detector we showed that a heat pulse-shape analysis could reject 95.9 % of all heat-only events. The pulse-shape analysis was based on two parameters, where the first one was retrieved from the comparison of different methods for the heat amplitude reconstruction and the second one was the correlation of triggered pulses with a reference pulse. A limitation of this rejection method is of course the baseline resolution in the heat channel.

In a next step, we analyzed the detector performance at high electric fields, and studied data from an operation at the maximal electrode bias of $\Delta V = 100\,\mathrm{V}$. In this case, the heat signal is dominated by secondary phonons, which are created along the drift of electrons and holes, and is therefore proportional to the ionization energy, $H = c_{\mathrm{heat}} E_{\mathrm{ion}}$. In this case the Q-value is always 1 and can not be used to analyze events affected by trapping. However, heat-only events should still show-up with a reduced Q-value. At $\Delta V = 100\,\mathrm{V}$, we found no significant population of heat-only events, wherefore we analyzed data from a measurement at lower electrode bias with $\Delta V = 35\,\mathrm{V}$. At this bias, we could identify heat-only events but the population was strongly reduced in comparison to the measurements at $\Delta V = 6\,\mathrm{V}$. In addition the maximal energy of heat-only event at $\Delta V = 35\,\mathrm{V}$ was $16\,\mathrm{keV_{ee}}$, whereas it was $70\,\mathrm{keV_{ee}}$ at $\Delta V = 6\,\mathrm{V}$. This reduction is in agreement with different NTL amplification factors for the two measurements and confirms the nature of the heat-only events: They originate from events with no charge collection and therefore their signals are not amplified by the NTL effect. With heat-only events spread in energy up to around $70\,\mathrm{keV_{ee}}$ in the case of $\Delta V = 6\,\mathrm{V}$, we could calculate their amplitudes at higher electric fields according to the NTL effect. For $\Delta V = 100\,\mathrm{V}$ we expect an upper bound for heat-only amplitudes of $4.4\,\mathrm{keV_{ee}}$. At these energies the Q-value is already widely spread according to the resolution in the ionization channel. Thus, heat-only events are not distinguishable anymore from other events close to the detection threshold in heat. This then explains the missing population of heat-only events. In view of the heat-only events in the EDELWEISS WIMP search, this finding undoubtedly confirms, that heat-only events are not accompanied by charge creation and are therefore not events whose charge signal may have been missed.

Our next goal was to study the charge migration processes at high electric fields. We started with the analysis of events, which delivered the full energy of $59.5\,\mathrm{keV}$ in the summed ionization channel ABCD. The γ-rays from the ^{241}Am source caused energy deposits in the top near-surface region covered by the A and B electrodes. Consequently, the polarization on the electrodes defined, if either the created electrons or holes dominated the charge collection. For $V_{\mathrm{A}} = V_{\mathrm{B}} < 0\,\mathrm{V}$ holes drift only a short distance before they are quickly collected on A and B, whereas electrons drift through the whole crystal to the C and D electrodes. Obviously, for $V_{\mathrm{A}} = V_{\mathrm{B}} > 0\,\mathrm{V}$ it is the other way around. For that reason, we could study the detector performance separately for electron and hole transport. The analysis was organized in the following way: Events belonging to the $59.5\,\mathrm{keV_{ee}}$ peak in the summed ionization amplitude spectrum ABCD were further categorized by their signal amplitudes in the individual channels A,B,C,D. This led to 9 event categories, which were defined by electrodes on which the charges were collected, e.g. AC (charge collection on A and C), A(C+D) (charge collection on A and (C+D)), etc. The population of events in these categories was then compared to simulations.
In case of signals dominated by electron transport ($V_{\mathrm{A}} = V_{\mathrm{B}} = -50\,\mathrm{V}$), we found a very good agreement between simulation and experiment. 38 % of events with shared charge collection on C and D were measured in the experiment, and the simulation predicted 44 %. This confirmed that the transport anisotropy of electrons, causing them to drift along an angle of 35 ° to the field applied in [100]-direction, has a measurable effect on the ionization

signal, favoring events with shared charge collection.
In case of signals dominated by hole transport ($V_A = V_B = +50\,V$), the agreement of simulation and experiment was not as good as for electrons. The number of events with charge collection on C and D was strongly underestimated by the simulation, expecting only a few events in this category (around 2 % of all events), whereas the measured population was 40 %. As the shared events, in case of electron transport, were favored by the electron transport anisotropy, we concluded that the missing implementation of the hole transport anisotropy in the simulation causes the discrepancy. In the simulation, holes strictly follow the electric field lines, and therefore shared charge collection is very unlikely. An implementation of the hole transport anisotropy in the hot carrier transport simulation tool is planned in the future.

After analyzing events in the 59.5 keV-peak of the heat spectrum, connected with full charge collection, we studied events with reduced heat amplitudes $H < 55\,keV_{ee}$[3]. Since the agreement between simulation and experiment had been excellent for electron transport ($V_A = V_B = -50\,V$) and events with full charge collection, we studied this case. Note that all results also apply to the case where hole collection dominated the signal, especially as we found that the amount of events affected by trapping in the simulation only varies slightly from 15.4 % for electrons to 12.9 % for holes. After scaling the simulated heat spectrum to the experimental one according to the peak height of the 59.5 keV-peak, we found a good agreement of the shape of the simulated and experimental spectra down to $20\,keV_{ee}$. In addition, the number of events in the heat energy range $H \in [20,55]$ keV_{ee} agreed rather well: Sim 15.4 % / Exp 21.1 %. For the simulated data, we assumed a monoenergetic source, causing single energy deposits. Thus, only trapping of charge carriers could cause reduced heat signals. We concluded, that trapping is the reason for heat amplitudes down to energies of 20 keV_{ee}. The simulated events clearly showed that events affected by trapping are close to the surface area, and in-between the electrodes. As we had seen before in the low field case, surface trapping and therefore the configuration of the detector electrodes is limiting the detector performance. Events with heat amplitudes $< 20\,keV_{ee}$ did show up in the experiment but not in simulation. Likely, these event are caused by low energy γ-rays, which already deposited some parts of their energy outside the sensitive region of the detector. Such events were not taken into account in the simulation.

Based on the finding that surface trapping limits the detector performance and that our simulation tool describes the effects of surface trapping properly, we performed an optimization of the detector performance using simulations.
We discussed an operation of the ring electrodes in veto mode with $V_A < V_B$, as used at low electrode biases in EDELWEISS to reject surface events. Eventually, this is not recommended for two reasons: Firstly, the bias difference between neighboring ring electrodes is strongly limited by leakage currents. Secondly, the heat spectrum becomes much more complex, as the NTL amplification depends on the electrode on which the charge carriers are collected. As the ionization signals at low energy deposits < 1 keV are not

[3] With $H < 55\,keV_{ee}$, events are outside of the 5σ-region of a Gaussian fit to the 59.5 keV-peak in the heat amplitude spectrum.

detectable anymore, no discrimination is available and it becomes very difficult to perform a proper energy calibration of the heat channel. In a next step we investigated a planar bias mode with 2 sets of electrodes, i.e. $V_A = V_B = -V_C = -V_D$. In order to find the critical parts of the detector when operated in this mode, we simulated events uniformly distributed in the detector in layers with different thickness and distance from the surface. The layer dimensions were chosen according to a typical background source for dark matter search experiments, which is the natural decay chain of ^{210}Pb. It produces β- and α-rays, which interact close to the surface. However our results apply to all kinds of backgrounds, especially to γ-rays, which also interact close to the surface with decreasing energy. We established that the limiting factor is surface trapping. In case the interaction took place in the layer closest to the surface with a range $d \in [200\,\text{nm}, 1\,\mu\text{m}]$, 87 % of events showed reduced heat amplitudes due to surface trapping. In case we considered all simulated events uniformly distributed in the entire crystal, we found that 42.3 % of these events were affected by surface trapping.

Based on these results, we designed an optimized electrode system, which consists of only two electrodes, which fully cover the top, bottom and lateral surface of the detector. The only uncovered region in this case is a small gap on the lateral surface, that separates the top and bottom electrode. The limit for this design is then defined by the gap size, as surface trapping can only occur there. For our simulation, we chose a very conservative gap size of 3 mm, which was consistent with our experimental experience that it allowed electrode biases up to $\Delta V = 100\,\text{V}$ without leakage currents. The simulations showed that with this design the amount of events affected by trapping in the layer closest to the surface with $d \in [200\,\text{nm}, 1\,\mu\text{m}]$ could be reduced to 12 %. The total amount of events within this modified geometry affected by surface trapping was reduced to 7.3 %.

The results we presented in this thesis show, how powerful the comparison of data retrieved from hot carrier transport simulation and experiments is, especially in the case of a well defined calibration experiment. The good agreement of rise time distributions confirmed the proper implementation of charge migration processes of electrons and holes in the HPGe crystals of EDELWEISS. In addition, we could evaluate the rise time as an additional analysis parameter for the discrimination of surface events. Actually, in Run 309, which lasted from April 2014 to January 2015, the first FID800 detector in the Modane underground laboratory was read out with a Fast Ionization Card (FIC), allowing one to sample two electrodes with a frequency of 40 MHz. Results from calibration data, taken with a ^{133}Ba γ-source, allowed to reject 98.4 % of the surface events with a rise time cut. The comparison of simulated and experimental data even allowed to extract the event position along the z-axis of the detector with a precision of $\Delta z = 0.28\,\text{cm}$. Assuming a realistically improved noise level in the FIC channels, a precision of $\Delta z = 0.05\,\text{cm}$ should be in reach.

The analysis of the prototype detector at high electrode biases performed in this thesis showed that even in this new detection regime, where the detectors are operated at high electric fields up to 50 V/cm and more, we have a good understanding of charge migration. In the searches for low-mass WIMPs with semiconductor detectors, voltage-assisted

calorimetric amplification of heat signals will lead the path to higher sensitivity. In this endeavor, understanding the charge transport and avoiding charge trapping becomes an even more important issue.

In December 2016, data taking resumed in the EDELWEISS laboratory, specifically focusing on testing the HPGe detector performance at high biases. Besides FID-type detectors, also a HPGe crystal with our modified surface trapping reducing design was installed. With these measurements EDELWEISS joins the new era for solid state dark matter detectors, probing WIMP nucleon cross-sections down to masses below $1\,\mathrm{GeV/c^2}$.

Bibliography

[1] P. A. R. Ade, N. Aghanim, M. I. R. Alves et al.. *Planck 2015 results. I. Overview of products and scientific results.* Astronomy & Astrophysics, 571:A1, 2015. ISSN 0004-6361. doi:10.1051/0004-6361/201321529.

[2] F. Zwicky. *Republication of: The redshift of extragalactic nebulae.* General Relativity and Gravitation, 41(1):207–224, 2009. ISSN 00017701. doi:10.1007/s10714-008-0707-4.

[3] P. A. R. Ade, N. Aghanim, M. Arnaud et al.. *Planck 2015 results. XIII. Cosmological parameters.* Astronomy & Astrophysics, p. 1502.01589, 2015. ISSN 0717-6163. doi:10.1007/s13398-014-0173-7.2.

[4] A. Penzias and R. W. Wilson. *A Measurement of Excess Antenna Temperature at 4080 Mc/s.* The Astrophysical Journal, 142:419, 1965. ISSN 0004-637X. doi:10.1086/148307.

[5] R. A. Alpher, H. Bethe and G. Gamow. *The Origin of Chemical Elements.* Physical Review, 73(803-804), 1948. ISSN 05717132. doi:10.1103/PhysRev.73.803.

[6] NASA. *1E 0657-56: NASA Finds Direct Proof of Dark Matter (Credit: X-ray: NASA/CXC/CfA/M.Markevitch et al.; Optical: NASA/STScI; Magellan/U.Arizona/D.Clowe et al.; Lensing Map: NASA/STScI; ESO WFI; Magellan/U.Arizona/D.Clowe et al.).* 2006.

[7] K. G. Begeman, A. H. Broeils and R. H. Sanders. *Extended rotation curves of spiral galaxies: dark haloes and modified dynamics.* Monthly Notices of the Royal Astronomical Society, 249(3):523–537, 1991. doi:10.1093/mnras/249.3.523.

[8] V. C. Rubin and J. Ford, W. Kent. *Rotation of the Andromeda Nebula from a Spectroscopic Survey of Emission Regions.* The Astrophysical Journal, 159:379, 1970. ISSN 0004-637X. doi:10.1086/150317.

[9] J. F. Navarro, C. S. Frenk and S. D. M. White. *The Structure of Cold Dark Matter Halos.* The Astrophysical Journal, 462:563, 1996. ISSN 0004-637X. doi:10.1086/177173.

[10] Y. Sofue. *Grand Rotation Curve and Dark-Matter Halo in the Milky Way Galaxy.* Publications of the Astronomical Society of Japan, 64(4):75, 2012. ISSN 0004-6264. doi:10.1093/pasj/64.4.75.

[11] J. L. Feng. *Dark Matter Candidates from Particle Physics and Methods of Detection.* Annual Review of Astronomy and Astrophysics, 48(1):495–545, 2010. ISSN 0066-4146. doi:10.1146/annurev-astro-082708-101659.

[12] C. Alcock, R. A. Allsman, D. R. Alves et al.. *MACHO Project Limits on Black Hole Dark Matter in the 1-30 Solar Mass Range.* The Astrophysical Journal, 550(1):L169–L172, 2001. ISSN 0004637X. doi:10.1086/319636.

[13] D. Hooper and L. Goodenough. *Dark matter annihilation in the Galactic Center as seen by the Fermi Gamma Ray Space Telescope.* Physics Letters, Section B: Nuclear, Elementary Particle and High-Energy Physics, 697(5):412–428, 2011. ISSN 03702693. doi:10.1016/j.physletb.2011.02.029.

[14] B. W. Lee and S. Weinberg. *Cosmological lower bound on heavy-neutrino masses.* Physical Review Letters, 39(4):165–168, 1977. ISSN 00319007. doi:10.1103/PhysRevLett.39.165.

[15] L. D. Duffy and K. Van Bibber. *Axions as dark matter particles.* New Journal of Physics, 11, 2009. ISSN 13672630. doi:10.1088/1367-2630/11/10/105008.

[16] K. Petraki and R. R. Volkas. *Review of Asymmetric Dark Matter.* International Journal of Modern Physics A, 28(19):1330028, 2013. ISSN 0217-751X. doi:10.1142/S0217751X13300287.

[17] T. M. Undagoitia and L. Rauch. *Dark matter direct-detection experiments.* Journal of Physics G: Nuclear and Particle Physics, 43(1):013001, 2016. ISSN 0954-3899. doi:10.1088/0954-3899/43/1/013001.

[18] E. Armengaud, Q. Arnaud, C. Augier et al.. *Axion searches with the EDELWEISS-II experiment.* Journal of Cosmology and Astroparticle Physics, 2013(11):067–067, 2013. ISSN 1475-7516. doi:10.1088/1475-7516/2013/11/067.

[19] Z. Ahmed, D. S. Akerib, S. Arrenberg et al.. *Search for Axions with the CDMS Experiment.* 0902.4693, (July):2–6, 2009. doi:10.1103/PhysRevLett.103.141802.

[20] J. D. Lewin and P. F. Smith. *Review of mathematics, numerical factors, and corrections for dark matter experiments based on elastic nuclear recoil.* Astroparticle Physics, 6(1):87–112, 1996. ISSN 09276505. doi:10.1016/S0927-6505(96)00047-3.

[21] L. Hehn. *Search for Dark Matter signals in EDELWEISS-III with a multidimensional maximum likelihood method.* PhD Thesis (KIT, IKP), 2016.

[22] S. Cebrián, E. García, D. González et al.. *Sensitivity plots for WIMP direct detection using the annual modulation signature.* Astroparticle Physics, 14(4):339–350, 2001. ISSN 09276505. doi:10.1016/S0927-6505(00)00124-9.

[23] G. Savage, G. Gelmini, P. Gondolo et al.. *Compatibility of DAMA/LIBRA dark matter detection with other searches.* Journal of Cosmology and Astroparticle Physics, 2009. doi:10.1088/1475-7516/2009/04/010.

[24] A. M. Green. *Astrophysical uncertainties on direct detection experiments.* Modern Physics Letters A, 27(03):1230004, 2011. ISSN 0217-7323. doi:10.1142/S0217732312300042.

[25] F. J. Kerr and D. Lynden-Bell. *Review of galactic constants.* Monthly Notices of the Royal Astronomical Society, 221(4):1023–1038, 1986. ISSN 0035-8711. doi:10.1093/mnras/221.4.1023.

[26] M. C. Smith, G. R. Ruchti, A. Helmi et al.. *The RAVE survey: Constraining the local Galactic escape speed.* Monthly Notices of the Royal Astronomical Society, 379(2):755–772, 2007. ISSN 00358711. doi:10.1111/j.1365-2966.2007.11964.x.

[27] CMS Collaboration. *The CMS experiment at the CERN LHC.* Journal of Instrumentation, 3:285, 2008. ISSN 1748-0221. doi:10.1088/1748-0221/3/08/S08004.

[28] ATLAS-Collaboration. *The ATLAS Experiment at the CERN Large Hadron Collider.* Journal of Instrumentation, 3(08):S08003–S08003, 2008. ISSN 1748-0221. doi:10.1088/1748-0221/3/08/S08003.

[29] ATLAS Collaboration. *Observation of a new particle in the search for the Standard Model Higgs boson with the ATLAS detector at the LHC.* Physics Letters B, 716(1):1–29, 2012. ISSN 03702693. doi:10.1016/j.physletb.2012.08.020.

[30] CMS Collaboration. *Observation of a new boson at the LHC with the CMS Experiment.* Nuclear Physics B - Proceedings Supplements, 251-252:129–134, 2014. ISSN 09205632. doi:10.1016/j.nuclphysbps.2014.04.022.

[31] A. Abramowski, F. Acero, F. Aharonian et al.. *Search for photon-linelike signatures from dark matter annihilations with H.E.S.S.* Physical Review Letters, 110(4):1–6, 2013. ISSN 00319007. doi:10.1103/PhysRevLett.110.041301.

[32] J. Aleksić, E. A. Alvarez, L. A. Antonelli et al.. *Searches for dark matter annihilation signatures in the Segue 1 satellite galaxy with the MAGIC-I telescope.* Journal of Cosmology and Astro-Particle Physics, 06:035, 2011. ISSN 1475-7516. doi:10.1088/1475-7516/2011/06/035;.

[33] B. Zitzer. *The VERITAS Dark Matter Program.* Proceeding of the Fifth International Fermi Symposium, pp. 2–7, 2015.

[34] M. G. Aartsen, R. Abbasi, Y. Abdou et al.. *Search for dark matter annihilations in the sun with the 79-string icecube detector.* Physical Review Letters, 110(13):1–7, 2013. ISSN 00319007. doi:10.1103/PhysRevLett.110.131302.

[35] K. Choi, K. Abe, Y. Haga et al.. *Search for Neutrinos from Annihilation of Captured Low-Mass Dark Matter Particles in the Sun by Super-Kamiokande.* Physical Review Letters, 114(14):1–7, 2015. ISSN 10797114. doi:10.1103/PhysRevLett.114.141301.

[36] O. Adriani and Others. *Observation of an anomalous positron abundance in the cosmic radiation.* Nature, 458:607–609, 2009. ISSN 0028-0836. doi:10.1038/nature07942.

[37] L. Accardo, M. Aguilar, D. Aisa et al.. *High statistics measurement of the positron fraction in primary cosmic rays of 0.5-500 GeV with the alpha magnetic spectrometer on the international space station.* Physical Review Letters, 113(12):1–10, 2014. ISSN 10797114. doi:10.1103/PhysRevLett.113.121101.

[38] M. Klasen, M. Pohl and G. Sigl. *Indirect and direct search for dark matter.* Progress in Particle and Nuclear Physics, 85:1–32, 2015. ISSN 01466410. doi:10.1016/j.ppnp.2015.07.001.

[39] R. Bernabei, P. Belli, A. Bussolotti et al.. *The DAMA/LIBRA apparatus.* Nuclear Instruments and Methods in Physics Research. Section A, Accelerators, Spectrometers, Detectors and Associated Equipment, 592(3):297–315, 2008. doi:10.1016/j.nima.2008.04.082.

[40] S. C. Kim, H. Bhang, J. H. Choi et al.. *New limits on interactions between weakly interacting massive particles and nucleons obtained with CsI(Tl) crystal detectors.* Physical Review Letters, 108(18):1–5, 2012. ISSN 00319007. doi:10.1103/PhysRevLett.108.181301.

[41] C. E. Aalseth, P. S. Barbeau, J. Colaresi et al.. *CoGeNT: A search for low-mass dark matter using p-type point contact germanium detectors.* Physical Review D - Particles, Fields, Gravitation and Cosmology, 88(1):1–20, 2013. ISSN 15507998. doi:10.1103/PhysRevD.88.012002.

[42] X. Defay, A. Broniatowski, a. Juillard et al.. *Cryogenic Ge detectors for dark matter search: Surface event rejection with ionization signals.* Journal of Low Temperature Physics, 151(3-4 PART 2):896–901, 2008. ISSN 00222291. doi:10.1007/s10909-008-9762-1.

[43] Z. Ahmed, D. S. Akerib, S. Arrenberg et al.. *Search for weakly interacting massive particles with the first five-tower data from the cryogenic dark matter search at the Soudan Underground Laboratory.* Physical Review Letters, 102(1):1–5, 2009. ISSN 00319007. doi:10.1103/PhysRevLett.102.011301.

[44] J. Cooley. *Results from the CDMS II Experiment.* Science, 327:1619–1621, 2010. ISSN 1095-9203. doi:10.1126/science.1186112.

[45] V. Mandic, W. Rau, D. Akerib et al.. *Position dependence in the CDMS II ZIP detectors.* AIP Conference Proceedings, 1:509–512, 2002. ISSN 0094243X. doi:10.1063/1.1457697.

[46] R. Agnese, A. J. Anderson, D. Balakishiyeva et al.. *Demonstration of surface electron rejection with interleaved germanium detectors for dark matter searches.* Applied Physics Letters, 103(16):1–5, 2013. ISSN 00036951. doi:10.1063/1.4826093.

[47] R. Agnese, A. J. Anderson, T. Aramaki et al.. *New Results from the Search for Low-Mass Weakly Interacting Massive Particles with the CDMS Low Ionization Threshold*

Experiment. Physical Review Letters, 116(7):1–6, 2016. ISSN 10797114. doi:10.1103/PhysRevLett.116.071301.

[48] G. Angloher, C. Bucci, P. Christ et al.. *Limits on WIMP dark matter using scintillating CaWO4 cryogenic detectors with active background suppression.* Astroparticle Physics, 23(3):325–339, 2005. ISSN 09276505. doi:10.1016/j.astropartphys.2005.01.006.

[49] X. Defay, E. Mondragon, M. Willers et al.. *Cryogenic silicon detectors with implanted contacts for the detection of visible photons using the Neganov-Luke Effect.* Journal of Low Temperature Physics, 2015. ISSN 1573-7357. doi:10.1007/s10909-016-1534-8.

[50] G. Angloher, A. Bento, C. Bucci et al.. *Results on light dark matter particles with a low-threshold CRESST-II detector.* European Physical Journal C, 76(1):1–8, 2016. ISSN 14346052. doi:10.1140/epjc/s10052-016-3877-3.

[51] M. G. Boulay. *DEAP-3600 Dark Matter Search at SNOLAB.* Journal of Physics: Conference Series, 375(1):012027, 2012. ISSN 1742-6596. doi:10.1088/1742-6596/375/1/012027.

[52] K. Abe, K. Hieda, K. Hiraide et al.. *XMASS detector.* Nuclear Instruments and Methods in Physics Research, Section A: Accelerators, Spectrometers, Detectors and Associated Equipment, 716:78–85, 2013. ISSN 01689002. doi:10.1016/j.nima.2013.03.059.

[53] M. G. Boulay and A. Hime. *Technique for direct detection of weakly interacting massive particles using scintillation time discrimination in liquid argon.* Astroparticle Physics, 25(3):179–182, 2006. ISSN 09276505. doi:10.1016/j.astropartphys.2005.12.009.

[54] J. Angle, E. Aprile, F. Arneodo et al.. *Constraints on inelastic dark matter from XENON10.* Phys. Rev. D, 115005:1–8, 2009. doi:10.1103/PhysRevD.80.115005.

[55] XENON100 Collaboration, E. Aprile, J. Aalbers et al.. *XENON100 Dark Matter Results from a Combination of 477 Live Days.* Phys. Rev. D, 122001:1–12, 2016. ISSN 2470-0010. doi:10.1103/PhysRevD.94.122001.

[56] D. S. Akerib, S. Alsum, H. M. Araújo et al.. *Results from a search for dark matter in LUX with 332 live days of exposure.* arXiv:1608.07648, pp. 1–8, 2016.

[57] C. Fu, X. Cui, X. Zhou et al.. *Spin-dependent WIMP-nucleon cross section limits from first data of PandaX-II experiment.* arXiv:1611.06553, pp. 1–5, 2016.

[58] R. Agnese, Z. Ahmed, A. J. Anderson et al.. *Silicon detector dark matter results from the final exposure of CDMS II.* Physical Review Letters, 111(25):19–24, 2013. ISSN 00319007. doi:10.1103/PhysRevLett.111.251301.

[59] G. Angloher, M. Bauer, I. Bavykina et al.. *Results from 730 kg days of the CRESST-II Dark Matter search.* European Physical Journal C, 72(4):1–22, 2012. ISSN 14346052. doi:10.1140/epjc/s10052-012-1971-8.

[60] XENON Collaboration, E. Aprile, F. Agostini et al.. *Lowering the radioactivity of the photomultiplier tubes for the XENON1T dark matter experiment.* European Physical Journal C, 75(11):1–10, 2015. ISSN 14346052. doi:10.1140/epjc/s10052-015-3657-5.

[61] D. C. Malling, D. S. Akerib, H. M. Araújo et al.. *After LUX: The LZ Program.* p. 9, 2011.

[62] J. Aalbers, F. Agostini, M. Alfonsi et al.. *DARWIN: towards the ultimate dark matter detector.* p. 36, 2016. ISSN 14757516. doi:10.1088/1475-7516/2016/11/017.

[63] C. A. J. O'Hare, A. M. Green, J. Billard et al.. *Readout strategies for directional dark matter detection beyond the neutrino background.* Physical Review D - Particles, Fields, Gravitation and Cosmology, 92(6), 2015. ISSN 15502368. doi: 10.1103/PhysRevD.92.063518.

[64] J. Lindhard, V. Nielsen, M. Scharff et al.. *Integral equations governing radiation effects.* Det Kgl. Danske Viden., 33(10), 1963.

[65] B. Neganov and V. Trofimov. *Method of calorimetric measurement of ionizing radiation.* Otkrytiya Izobret, 146:215, 1985.

[66] P. N. Luke. *Voltage-assisted calorimetric ionization detector.* Journal of Applied Physics, 64(12):6858, 1988. ISSN 00218979. doi:10.1063/1.341976.

[67] Q. Arnaud, J. Billard and A. Juillard. *Optimizing Cryogenic Detectors for Low-Mass WIMP Searches.* Journal of Low Temperature Physics, 184(1-2):308–315, 2016. ISSN 15737357. doi:10.1007/s10909-015-1463-y.

[68] G. R. Stewart. *Measurement of low-temperature specific heat.* Review of Scientific Instruments, 54(1):1–11, 1983. ISSN 00346748. doi:10.1063/1.1137207.

[69] J. Billard, M. de Jesus, A. Juillard et al.. *Characterization and Optimization of EDELWEISS-III FID800 Heat Signals.* Journal of Low Temperature Physics, 184(1):1–9, 2016. ISSN 15737357. doi:10.1007/s10909-016-1500-5.

[70] C. Enss and S. Hunklinger. *Low-temperature physics.* Springer-Verlag Berlin Heidelberg New York, 2005.

[71] N. F. Mott. *Introductory talk; Conduction in non-crystalline materials.* Journal of Non-Crystalline Solids, 8-10(C):1–18, 1972. ISSN 00223093. doi:10.1016/0022-3093(72)90112-3.

[72] D. McCammon. *Semiconductor Thermistors.* In C. Enss, ed., *Cryogenic Particle Detection*, chap. 2, pp. 35–62. Springer Berlin Heidelberg, 2005. ISBN 978-3-540-31478-3. doi:10.1007/b12169.

[73] E. E. Haller, N. P. Palaio, M. Rodder et al.. *NTD Germanium: A Novel Material for Low Temperature Bolometers*, pp. 21–36. Springer US, Boston, MA, 1984. ISBN 978-1-4613-2695-3. doi:10.1007/978-1-4613-2695-3_2.

[74] N. P. Palaio, M. Rodder, E. E. Haller et al.. *Neutron-Transmutation-Doped Germanium Bolometers*. pp. 933–943, 1983.

[75] N. Wang, F. C. Wellstood, B. Sadoulet et al.. *Electrical and thermal properties of neutron-transmutation-doped Ge at 20 mK*. Physical Review B, 41(6):3761–3768, 1990. ISSN 01631829. doi:10.1103/PhysRevB.41.3761.

[76] E. Armengaud, Q. Arnaud, C. Augier et al.. *Development and underground test of radiopure ZnMoO4 scintillating bolometers for the LUMINEU $0\nu2\beta$ project*. Journal of Instrumentation, 10(05):P05007–P05007, 2015. ISSN 1748-0221. doi:10.1088/1748-0221/10/05/P05007.

[77] C. Arnaboldi, F. T. Avignone, J. Beeman et al.. *CUORE: A cryogenic underground observatory for rare events*. Nuclear Instruments and Methods in Physics Research, Section A: Accelerators, Spectrometers, Detectors and Associated Equipment, 518(3):775–798, 2004. ISSN 01689002. doi:10.1016/j.nima.2003.07.067.

[78] K. D. Irwin and G. C. Hilton. *Transition-Edge Sensors Preprint of chapter in Cryogenic Particle Detection Transition-Edge Sensors*, vol. 149. 2005. ISBN 3540201130.

[79] S. J. Smith, S. R. Bandler, A. D. Brown et al.. *Characterizing the superconducting-to-normal transition in Mo/Au transition-edge sensor bilayers*. Journal of Low Temperature Physics, 151(1-2 PART 1):195–200, 2008. ISSN 00222291. doi:10.1007/s10909-007-9619-z.

[80] S. Henry, N. Bazin, H. Kraus et al.. *The 66-channel SQUID readout for CRESST II*. Journal of Instrumentation, 2:P11003–P11003, 2007. ISSN 1748-0221. doi:10.1088/1748-0221/2/11/P11003.

[81] D. S. Akerib, P. D. Barnes, P. L. Brink et al.. *Design and performance of a modular low-radioactivity readout system for cryogenic detectors in the CDMS experiment*. Nuclear Instruments and Methods in Physics Research, Section A: Accelerators, Spectrometers, Detectors and Associated Equipment, 591(3):476–489, 2008. ISSN 01689002. doi:10.1016/j.nima.2008.03.103.

[82] A. Fleischmann, C. Enss and G. M. Seidel. *Cryogenic Particle Detection*. vol. 99 of *Topics in applied physics*, chap. Metallic M, pp. 151–216. Springer-Verlag Berlin Heidelberg, 2005.

[83] M. Loidl, M. Rodrigues, X. F. Navick et al.. *Concept of metallic magnetic calorimeters for rare event search in the LUMINEU project*. Journal of Low Temperature Physics, 176(5-6):624–630, 2014. ISSN 15737357. doi:10.1007/s10909-013-1023-2.

[84] J. G. N. Bastidon. *The EDELWEISS-III Project and the Rejection Performance of Its Cryogenic Germanium Detectors.* Journal of Low Temperature Physics, pp. 870–875, 2014. doi:10.1007/s10909-014-1096-6.

[85] A. Juillard. *Status and Prospects of the EDELWEISS Direct WIMP Search Experiment.* Journal of Low Temperature Physics, pp. 1056–1062, 2012. doi:10.1007/s10909-012-0512-z.

[86] B. Schmidt, E. Armengaud, C. Augier et al.. *Muon-induced background in the EDELWEISS dark matter search.* Astroparticle Physics, 44:28–39, 2013. ISSN 09276505. doi:10.1016/j.astropartphys.2013.01.014.

[87] C. Kéfélian. *Search for dark matter with EDELWEISS-III excluding background from muon-induced neutrons.* PhD Thesis (UCBL and KIT), 2016.

[88] E. Armengaud, Q. Arnaud, C. Augier et al.. *Measurement of the cosmogenic activation of germanium detectors in EDELWEISS-III.* arXiv:1607.04560, pp. 1–38, 2016.

[89] E. Armengaud, C. Augier, A. Benoit et al.. *Background studies for the EDELWEISS dark matter experiment.* Astroparticle Physics, 47:1–9, 2013. ISSN 09276505. doi:10.1016/j.astropartphys.2013.05.004.

[90] J. Gascon. *Run 309: Results so far ! (Internal note).* Tech. Rep., 2016.

[91] Q. Dong, Y. X. Liang, D. Ferry et al.. *Ultra-low noise high electron mobility transistors for high-impedance and low-frequency deep cryogenic readout electronics.* Applied Physics Letters, 105(1), 2014. ISSN 00036951. doi:10.1063/1.4887368.

[92] A. Phipps, A. Juillard, B. Sadoulet et al.. *A HEMT-Based Cryogenic Charge Amplifier with sub-100 eVee Ionization Resolution for Massive Semiconductor Dark Matter Detectors.* arXiv:1611.09712v1, 2016.

[93] B. Censier, A. Benoit, G. Bres et al.. *EDELWEISS read-out electronics and future prospects.* Journal of Low Temperature Physics, 167(5-6):645–651, 2012. ISSN 15737357. doi:10.1007/s10909-012-0568-9.

[94] A. Broniatowski, X. Defay, A. Juillard et al.. *Cryogenic Ge detectors with interleaved electrodes: Design and modeling.* Journal of Low Temperature Physics, 151(3-4 PART 2):830–834, 2008. ISSN 00222291. doi:10.1007/s10909-008-9754-1.

[95] E. Armengaud, C. Augier, A. Benoît et al.. *Final results of the EDELWEISS-II WIMP search using a 4-kg array of cryogenic germanium detectors with interleaved electrodes.* Physics Letters B, 702(5):329–335, 2011. ISSN 03702693. doi:10.1016/j.physletb.2011.07.034.

[96] A. Broniatowski, B. Censier, A. Juillard et al.. *Cryogenic germanium detectors for dark matter search: Surface events rejection by charge measurements.* Nuclear Instruments and Methods in Physics Research Section A: Accelerators, Spectrometers,

Detectors and Associated Equipment, 559(2):378–380, 2006. ISSN 01689002. doi: 10.1016/j.nima.2005.12.015.

[97] N. Foerster, A. Broniatowski, K. Eitel et al.. *Pulse-Shape Analysis of Ionization Signals in Cryogenic Ge Detectors for Dark Matter.* Journal of Low Temperature Physics, pp. 1–7, 2016. ISSN 0022-2291. doi:10.1007/s10909-016-1532-x.

[98] B. Siebenborn. *Discrimination of surface events with time resolved ionization channels in the EDELWEISS dark matter search.* PhD Thesis (KIT, IKP), 2016.

[99] E. Armengaud, Q. Arnaud, C. Augier et al.. *Constraints on low-mass WIMPs from the EDELWEISS-III dark matter search.* Journal of Cosmology and Astroparticle Physics, 2016(05):019–019, 2016. ISSN 1475-7516. doi:10.1088/1475-7516/2016/05/019.

[100] L. Hehn, E. Armengaud, Q. Arnaud et al.. *Improved EDELWEISS-III sensitivity for low-mass WIMPs using a profile likelihood approach.* The European Physical Journal C, pp. 1–11, 2016. ISSN 14346052. doi:10.1140/epjc/s10052-016-4388-y.

[101] C. Kittel. *Introduction to Solid State Physics.* John Wiley and Sons Ltd, 8th edn., 2004. ISBN 978-0471415268.

[102] C. Persson and S. Mirbt. *Improved electronic structure and optical properties of sp-hybridized semiconductors using LDA+USIC.* Brazilian Journal of Physics, 36(2):286–290, 2006. ISSN 0103-9733. doi:10.1590/S0103-97332006000300014.

[103] N.W. Ashcroft; N.D. Mermin. *Solid State Physics.* Saunders College, Philadelphia, 1976.

[104] S. Hunklinger. *Festkörperphysik.* Oldenbourg-Verl., München, 2., verb. edn., 2009.

[105] C. A. Klein. *Bandgap dependence and related features of radiation ionization energies in semiconductors.* Journal of Applied Physics, 39(4):2029–2038, 1968. ISSN 00218979. doi:10.1063/1.1656484.

[106] E. M. Gershenzon, G. N. Gol'tsman and A. P. Mel'nikov. *Binding energy of a carrier with a neutral impurity atom in germanium and in silicon*, 1971.

[107] H. Grimmeiss. *Deep Level Impurities in Semiconductors.* Annual Review of Material Science, 7:341–376, 1977.

[108] V. Aubry-Fortuna and P. Dollfus. *Electron transport properties in high-purity Ge down to cryogenic temperatures.* Journal of Applied Physics, 108(12):123706, 2010. ISSN 00218979. doi:10.1063/1.3520656.

[109] C. Jacoboni, F. Nava, C. Canali et al.. *Electron drift velocity and diffusivity in germanium.* Physical Review B, 24(2):1014–1026, 1981. doi:10.1103/PhysRevB.24.1014.

[110] M. C. Piro, A. Broniatowski, S. Marnieros et al.. *Hot carrier trapping in high-purity and doped germanium crystals at millikelvin temperatures.* Journal of Low Temperature Physics, 176:796–801, 2014. ISSN 15737357. doi:10.1007/s10909-014-1088-6.

[111] A. Broniatowski. *Intervalley scattering of hot electrons in germanium at millikelvin temperatures.* Journal of Low Temperature Physics, 176(5-6):860–869, 2014. ISSN 15737357. doi:10.1007/s10909-014-1091-y.

[112] M. I. Nathan. *Anisotropy of the Conductivity of n-Type Germanium at High Electric Fields.* Physical Review, 130(6):2201–2204, 1963. doi:10.1103/PhysRev.130.2201.

[113] K. Seeger. *Semiconductor Physics.* Springer, 9th edn., 2004. ISBN 3-540-21957-2.

[114] C. Canali, G. Ottaviani and G. Majni. *Hot Hole Anisotropic Effects in Silicon and Germanium.* Solid State Communication, 15:1213–1216, 1974.

[115] L. Reggiani, C. Canali, F. Nava et al.. *Hole drift velocity in germanium.* Physical Review B, 16(6):2781–2791, 1977. doi:10.1103/PhysRevB.16.2781.

[116] R. H. Kingston. *Review of germanium surface phenomena.* Journal of Applied Physics, 27(2):101–114, 1956. ISSN 00218979. doi:10.1063/1.1722317.

[117] E. E. Haller, W. L. Hansen and F. S. Goulding. *Physics of ultra-pure germanium.* Advances in Physics, 30(1):93–138, 1981. ISSN 0001-8732. doi:10.1080/00018738100101357.

[118] A. Broniatowski, B. Censier, A. Juillard et al.. *Dead layer and degradation effects in cryogenic germanium detectors for dark matter search.* Nuclear Instruments and Methods in Physics Research, Section A: Accelerators, Spectrometers, Detectors and Associated Equipment, 559:402–404, 2006. ISSN 01689002. doi:10.1016/j.nima.2005.12.172.

[119] The MathWork Inc. *MATLAB (R2013b).* 2013.

[120] A. Broniatowski. *A simulation code for the ionization and heat signals in low-temperature germanium detectors for Dark Matter research.* Nuclear Instruments and Methods in Physics Research, Section A: Accelerators, Spectrometers, Detectors and Associated Equipment, 520(1-3):178–181, 2004. ISSN 01689002. doi:10.1016/j.nima.2003.11.287.

[121] The MathWork Inc. *Partial Differential Equation Toolbox 1.3.*

[122] W. Shockley. *Currents to Conductors Induced by a Moving Point Charge.* Journal of Applied Physics, 9(10):635, 1938. ISSN 00218979. doi:10.1063/1.1710367.

[123] S. Ramo. *Currents induced by electron motion.* Proceedings of the IRE, (11):0–1, 1939.

[124] G. Cavalleri, E. Gatti, G. Fabri et al.. *Extension of Ramo's theorem as applied to induced charge in semiconductor detectors.* Nuclear Instruments and Methods, 92(1):137–140, 1971. ISSN 0029554X. doi:10.1016/0029-554X(71)90235-7.

[125] Z. He. *Review of the Shockley-Ramo theorem and its application in semiconductor gamma-ray detectors.* Nuclear Instruments and Methods in Physics Research Section A: Accelerators, Spectrometers, Detectors and Associated Equipment, 463(1-2):250–267, 2001. ISSN 01689002. doi:10.1016/S0168-9002(01)00223-6.

[126] A. Broniatowski. *Preliminary: A Monte Carlo tool for hot carrier tranport simulation in semiconductors.* To be published, 2017.

[127] G. Chapman. *Gamma-ray attenuation coefficients for germanium.* Nuclear Instruments and Methods, 52:101–103, 1967. doi:10.1016/0029-554X(67)90563-0.

[128] Nist. *http://physics.nist.gov/PhysRefData/FFast/html/form.html.*

[129] S. Marnieros. *Detector Schematic, private communication.* Tech. Rep., 2015.

[130] S. Marnieros, L. Bergé, A. Broniatowski et al.. *Controlling the Leakage-Current of Low Temperature Germanium Detectors Using XeFl2 Dry Etching.* Journal of Low Temperature Physics, 176(3-4):182–187, 2014. ISSN 0022-2291. doi:10.1007/s10909-013-0997-0.

[131] F. Pobell. *Matter and methods at low temperatures.* Springer, Berlin ; Heidelberg [u.a.], 1992. ISBN 3-540-53751-1 ; 0-387-53751-1 ; 978-0-387-53751-1 ; 978-3-540-53751-9.

[132] A. De Bellefon, I. Berkes, C. Bobin et al.. *Dark matter search with a low temperature sapphire bolometer.* Astroparticle Physics, 6(1):35–43, 1996. ISSN 09276505. doi:10.1016/S0927-6505(96)00040-0.

[133] D. Cousins, S. Fisher, A. Guénault et al.. *An advanced dilution refrigerator designed for the new Lancaster microkelvin facility.* Journal of Low Temperature Physics, 114(5):547–570, 1999. ISSN 0022-2291. doi:10.1023/A:1021862406629.

[134] G. Frossati. *Experimental Techniques : Methods for Cooling Below 300 mK.* Journal of Low Temperature Physics, 87, 1992.

[135] X. Defay. *Recherche de matiere noire au sein de l'expérience EDELWEISS avec des bolometres germanium a double composante Ionisation/Chaleur, rejet des evenements de surface avec la voie ionisation*, 2008.

[136] P. Horowitz and W. Hill. *The Art of Electronics.* 2nd edn., 1989. ISBN 0-521-37095-7.

[137] M. Bé, V. Chisté, C. Dulieu et al.. *Table of Radionuclides (Vol. 2 - A = 151 to 242).* Bureau International Des Poids Et Mesures, 2, 2008.

[138] M.-M. Bé, V. Chisté, C. Dulieu et al.. *Table of Radionuclides (Vol. 1 - A = 1 to 150)*. Bureau International Des Poids Et Mesures, 1, 2004.

[139] E. Olivieri, A. Broniatowski, J. Domange et al.. *Space-and-surface charge neutralization of cryogenic Ge detectors using infrared LEDs*. pp. 310–313, 2009. doi: 10.1063/1.3292566.

[140] J. P. Joule. *On the Mechanical Equivalent of Heat*. Philosophical Transactions of the Royal Society of London, 140:61–82, 1850.

[141] M. Mancuso. *Development and optimization of scintillating bolometers and innovative light detectors for a pilot underground experiment on neutrinoless double beta decay*. PhDThesis (Université Paris-Saclay), 2016.

[142] E. Gatti and P. F. Manfredi. *Processing the signals from solid-state detectors in elementary-particle physics*. La Rivista del Nuovo Cimento, 9(1):1–146, 1986. ISSN 0393697X. doi:10.1007/BF02822156.

[143] A. Broniatowski, M.-C. Piro, S. Marnieros et al.. *Voltage-Assisted Calorimetric Detection of Gamma Interactions in a Prototype Cryogenic Ge Detector of the EDELWEISS Collaboration for Dark Matter Search*. Journal of Low Temperature Physics, 184(1-2):330–335, 2016. ISSN 0022-2291. doi:10.1007/s10909-016-1471-6.

[144] B. Bruyneel, P. Reiter and G. Pascovici. *Characterization of large volume HPGe detectors. Part I: Electron and hole mobility parameterization*. Nuclear Instruments and Methods in Physics Research, Section A: Accelerators, Spectrometers, Detectors and Associated Equipment, 569(3):764–773, 2006. ISSN 01689002. doi:10.1016/j.nima.2006.08.130.

[145] W. Zhao, Q. Yue, K. J. Kang et al.. *Search of low-mass WIMPs with a p -type point contact germanium detector in the CDEX-1 experiment*. Physical Review D - Particles, Fields, Gravitation and Cosmology, 93(9):1–12, 2016. ISSN 15502368. doi:10.1103/PhysRevD.93.092003.

Acknowledgement

Obwohl man eine Doktorarbeit letztendlich selber schreiben muss, ist die Durchführung ohne die Unterstützung von Kollegen, Freunden und Familie nicht möglich. Bei diesen bedanke ich mich ganz herzlich. Ihr wart ein großer Rückhalt.

Zunächst danke ich Herrn Prof. Dr. Dr. h.c. Johannes Blümer, der mir meine Doktorarbeit am Institut für Kernphysik in Karlsruhe ermöglicht hat. Desweiter gilt mein Dank Herrn Prof. Dr. Christian Enss vom Kirchoff-Institut für Physik in Heidelberg, der meine Arbeit als Korreferent betreut hat.

Ich danke meinen Betreuern Dr. Klaus Eitel und Alexandre Bronitawoski, PhD, für die Unterstützung meiner Arbeit am KIT, sowie für die Möglichkeit Experimente am CSNSM in Orsay, Frankreich, durchzuführen. Ein großes Dankeschön geht an alle EDELWEISS Kollegen in Karlsruhe: An Dr. Geertje Heuerman and Silvia Scorza, PhD, für die vielen hilfreichen und unterstützenden Gespräche, an Dr. Bernhard Siebenborn der mir in der Schreibphase immer gern geholfen hat. Desweiteren danke ich Dr. Valentin Kozlov, Dr. Lukas Hehn, Dr. Cécile Kéfélian und Dr. Benjamin Schmidt für die gute gemeinsame Zeit.

I like to thank the EDELWEISS collaboration, especially the members that contributed to and helped with my experimental studies in Orsay. I like to thank again Alexandre Bronitawoski, PhD, and Stephanos Manieros, PhD, for enabling me to perform my own lab experiments. Special thanks goes to Michele Mancuso, PhD, who helped me to optimize data acquisition and analysis. I am grateful for all the experimental support by the CSNSM laboratory people. Thank you for your friendly and welcoming nature. Thanks to Maurice Chapellier, PhD, Andrea Giuliani, PhD, Emiliano Olivieri, PhD, Xavier Defay, PhD, Louis Dumoulin, PhD, Denys Poda, PhD, and Valentina Novati.

Ein großes Dankeschön geht an meine Famile: meine Eltern, meine Schwester und Matthias. Danke für eure Unterstützung, eurer Verständnis und die vielen Ermutigungen. Besonders danke ich Vanessa Graber, PhD, für das Korrekturlesen meiner Doktorarbeit und für die lange Freundschaft. Ich danke den Kollegen von Katrin und der Theoretischen Teilchenphysik, dem tollen X-Ment Team und allen Freunden, die mich in den letzten Jahren begleitet haben.